Linear and nonlinear optics of metallic nanoparticles film

Yara El Harfouch

N° 179-2009 Année 2009

THESE DE L'UNIVERSITE DE LYON

Délivrée par

L'UNIVERSITE CLAUDE BERNARD LYON 1

ECOLE DOCTORALE

DIPLOME DE DOCTORAT

(arrêté du 7 août 2006)

soutenue publiquement le 19 Octobre 2009

par

EL HARFOUCH Yara

TITRE : Optique linéaire et non linéaire de films de nano particules métalliques

Directeur de thèse : Mr. Pierre François BREVET

JURY : M **Emmanuel BENICHOU,** Co-Encadrant
M **Leonard BERLOUIS,** Invité
M **Pierre François BREVET,** Directeur de thèse
M **Remi CARMINATI,** Rapporteur
M **Fabrice CHARRA,** Rapporteur
M **Christophe DUJARDIN,** Président du jury
M **Martti KAURANEN,** Examinateur
M **Eric VAUTHEY,** Examinateur

UNIVERSITE CLAUDE BERNARD - LYON 1

Président de l'Université	**M. le Professeur L. Collet**
Vice-président du Conseil Scientifique	M. le Professeur J-F. Mornex
Vice-président du Conseil d'Administration	M. le Professeur G. Annat
Vice-président du Conseil des Etudes et de la Vie Universitaire	M. le Professeur D. Simon
Secrétaire Général	M. G. Gay

UFR SANTE

Faculté de Médecine Lyon Est – Claude Bernard	Directeur : M. le Professeur J. Etienne
Faculté de Médecine Lyon Sud – Charles Mérieux	Directeur : M. le Professeur F-N. Gilly
UFR d'Odontologie	Directeur : M. le Professeur D. Bourgeois
Institut des Sciences Pharmaceutiques et Biologiques	Directeur : M. le Professeur F. Locher
Institut des Sciences et Techniques de Réadaptation	Directeur : M. le Professeur Y. Matillon
Département de Formation et Centre de Recherche en Biologie Humaine	Directeur : M. le Professeur P. Farge

UFR SCIENCES ET TECHNOLOGIE

Faculté des Sciences et Technologies	Directeur : M. Le Professeur F. Gieres
UFR Sciences et Techniques des Activités Physiques et Sportives	Directeur : M. C. Collignon
Observatoire de Lyon	Directeur : M. B. Guiderdoni
Institut des Sciences et des Techniques de l'Ingénieur de Lyon	Directeur : M. le Professeur J. Lieto
Institut Universitaire de Technologie A	Directeur : M. le Professeur C. Coulet
Institut Universitaire de Technologie B	Directeur : M. le Professeur R. Lamartine
Institut de Science Financière et d'Assurance	Directeur : M. le Professeur J-C. Augros
Institut Universitaire de Formation des Maîtres	Directeur : M R. Bernard

To my family, and my husband…

Acknowledgement:

A Phd is the fruit of a group work, discussions and most of all support and encouragement. Today is the time to say to all those who helped me accomplish this work, each by his own way, a thank you from the bottom of my heart.

I would like to start by thanking the lasim laboratory and his director Mr Chirsitian Bordas.

First of all I would like to thank Pierre Francois Brevet for these wonderful and fruitful three years of PhD within his lovely group ONLI. I want to thank him for his scientific interest and advices, for his availability for discussions and for giving me faith in my experiments. I want also to thank him for his friendship and care.

I want to thank deeply Emmanuel Benichou for all kind of help and encouragement that he gave me during my PhD. I want to thank him for teaching me all the technical utilities and being always available for any kind of help, as well as being so friendly.

I want also to thank Len Berlouis that I had the chance to work in collaboration with. I want to thank him for his friendship and all the interest that he showed to transmit his knowledge in electrochemistry to me.

I want also to thank all the permanent members of the group, Isabelle, Guillaume, Franck and Christian.

I would also like to thank Gaelle, Jerome and Chawki for their friendship and for their special passage within the group, as well as Lin Pu.

Now comes the time to thank my road partner in this long journey Julien with whom I had excellent discussions, starting sometimes by science and ending up with the French laws. I want to tell him thanks for these special three years and for his great friendship that I hope will last.

I would also like to thank the jury members, Pr. Remi Carmnati and Dr Fabrice Charra for accepting to report my work, Pr. Eric Vauthey, Pr. Martti Kauranen, Pr. Christoph Dujardin, and Dr Len Berlouis for judging my work.

I want also to thank all the LASIM members, especially all those who are, or were in the same boat as me: Maya, Myriam, Houssam, Cycilia, Cyril, Nadia, Renaud, Amandine, Jeremy,...

During all my studies, I've been through lots of phases until achieving my PhD, and throughout the road real precious diamonds were always there shining. I want to thank these diamonds: Samar, Rolla, Samer, Rami, Abbass, Sandra, Nisrine, Majdy, Nour, Judy, Zainab,...and all the rest. A very big thanks isn't sufficient to say how much I am grateful to have you in my life.

A big thanks goes to my family, my father and mother first of all for all their help and support, for all their encouragement and for all the good that is in me. I want to thank them for giving me such a chance in life and raising me in such a way that made me achieve all these goals. I owe you more than a simple thanks, and words can't express how much I do owe you. I love you both. I want to thank my brothers Fayssal and Mohammad for their presence and for their eternal love. I want to thank my little angel Carla for all her love and encouragement. I want to thank my second family too, my father and mother in law Ahmad and Sofie and my aunt in law Kaemla.

At last, I want to thank my husband Wassim for all his love and care during these three years of thesis. I want to thank him for supporting me during the hardest times and for sharing with me the most special moments of my life. Finally, with love everything is possible.

OUTLINE

Introduction

Ever since the discovery of nonlinear optics, it has been used in vast fields of study. A nonlinear response is named so when the dielectric polarisation $\boldsymbol{P}$ responds nonlinearly to the electric field $\boldsymbol{E}$ of the light. This nonlinearity is only observed at very high light intensity provided by lasers. Second Harmonic Generation is one of several nonlinear processes possible to take place. It is the conversion of two photons at fundamental frequency ω into one photon at harmonic frequency 2ω, i.e. twice the energy and half the wavelength of the fundamental photon. In centrosymmetric bulk materials such as gold and silver, SHG is forbidden in the dipole approximation because of the inversion symmetry while it doesn't vanish at interfaces where this inversion symmetry is broken. For this reason, this process is highly surface specific for interfaces between two centrosymmetric media. More recently it has also been used to investigate the nonlinear optical properties of metallic particles dispersed in a liquid solution. In this case, the method of choice bears the name of Hyper Rayleigh Scattering (HRS) namely the scattering of harmonic light, because no coherent light at the harmonic frequency may be generated. HRS is an incoherent phenomenon where the total detected intensity is the incoherent superposition of the SHG intensities scattered by each nonlinear source present in the studied sample.

In this work SHG process is used to study silver and gold nanoparticles film at liquid interfaces. Silver and gold nanoparticles are gaining increasing attention owing to their unique electronic and optical properties. They exhibit a strong surface plasmon resonance absorption band in the visible spectrum corresponding to the collective excitation of the conduction band electrons. These properties are strongly dependent on the particle form and size. These nanometric particles are being the building blocks for several technological applications. Progressive research activities are exploring more about the nanoscale world and aim to use nanotechnologies in optics, electronics, biology, and healthcare to mention a little.

The aim of this thesis is to study the linear and nonlinear optical properties of metallic films formed at liquid interfaces. Using nonlinear optics, we want to monitor the formation of the film, the interaction between the particles in such films and finally the metallic behaviour. To

perform such studies Second Harmonic Generation (SHG) has been employed. First incoherent SHG also named HRS was used to give a particular emphasis on the effect of the surfactants on the quadratic hyperpolarisability of the particle. Thiol derivatized silver and gold nanoparticles were tested in order to investigate the role of surfactants adsorbed at the particle surface in the breaking of symmetry of the particles. After characterisation of the nanoparticles, they were used to form metallic nanoparticles film at the liquid interfaces. These films were studied using coherent SHG technique in order to monitor the film formation and the interactions between the particles leading to an expected phase transition once the interparticle distance is less than a critical value. The distance between the particles is controlled thanks to the Langmuir technique. These studies were complemented with experiments performed at the liquid/liquid interface and at the glassy carbon/electrolyte interface to examine in details the role of roughness on the SHG response.

Chapter 1 presents the methods used to synthesise the various nanoparticles studied during this work along with the techniques used to characterise these synthesised particles. In order to study the linear and nonlinear optical properties of metallic nanoparticles, several synthetic methods have been followed yielding several particles shape and size. Our study was focused on spherical and nanorods form. One of the main aims of this work was to prepare self assembled metallic film using the Langmuir technique. In order to form such films, the nanoparticles should be functionalised by organic molecule in order to prevent particle aggregation and also to ensure the nanoparticles float on the subphase surface. Alkanethiol molecules were chosen to cap the metallic nanoparticles studied at the interface. These surfactants play an essential role in the control of the interaction between the particles.

In the second chapter of this work the nonlinear optical properties of the various nanoparticles used to form metallic film at the interface were studied using Hyper Rayleigh Scattering. The hyperpolarisability of silver and gold spherical and nanorods nanoparticles stabilised with various surfactants were determined. The aim of these experiments was to deduce whether the capping layer plays an enhancing role or a quenching one on the hyperpolarisability value.

In chapter 3 the hydrodynamic model was used to get the expressions for the different nonlinear polarisation contributions from both the interface and the bulk. An overview of the three layer model is also presented from which the effective tensor elements and the polarisation equations are given. A relation between the effective susceptibility tensor

elements and the Rudnick and Stern parameters is presented. These theoretical calculations are to be used to fit the experimental data obtained upon the film formation at the interface.

After the characterisation of the nanoparticles in chapter 2, the particles were used to form a nanoparticle film at the air/water interface. Chapter 4 and 5 provide information about the linear and nonlinear optical response of metallic nanoparticles film at the air/water interface. Both spherical and nanorods particles were used to form the film aiming to examine the optical response of different forms of nanoparticles. The linear studies were performed to emphasize the modifications in the linear response of the film due to the interaction between the particles upon compression and to monitor a possible transition of the system from insulator to metal. These linear studies were followed by a detailed nonlinear study where the evolution of the second harmonic signal upon the film formation is detailed. A polarisation study accompanied the film formation aiming to deduce the dominant contribution of the nonlinear response in such films.

Chapter 6 presents the study of a metal liquid like film (MELLF) formed from aggregated silver nanoparticles supported at the water/Dichloroethane (DCE) interface. The film kinetics was performed using UV-visible absorption spectroscopy. The evolution of the SHG signal upon the film formation was studied together with a polarisation study at various stages of the film formation allowing the study of the evolution of the film from a rough one into a smoother one once reorganisation takes place after a certain time of the film formation.

In order to underline the difference in the SHG response of rough and smooth films, a detailed study of the growth of a silver film using an electrochemical method is given in the last chapter. This method was chosen since it provides more control of the film growth. These experiments were performed in order to address both the problem of field enhancement and random roughness at such surfaces and to deduce whether the SH signal is enhanced or quenched upon the combination of a nanoscale surface roughness and electric polarisation.

Chapter 1
Synthesis and characterisation of metallic nanoparticles

1.1. Introduction

Metallic nanoparticles have gained increasing attention due to their unique optical and electronic properties [1]. Several synthetic methods of silver [2-5] and gold [6-10] particles with variable shapes and sizes [11] have been developed since years. In 1951, Turkevich *et al.* developed the preparation of gold particles using citrate as a reducing agent, yielding stable nanoparticles solutions of low polydispersity [12]. Ever since, considerable efforts have been devoted to develop new synthetic methods aiming to achieve better control of the size, shape, and distance between the particles for the purpose of nanoparticle assembly [13]. To characterise the particles, many different techniques have been used, transmission electron microscopy (TEM) and absorption spectroscopy in particular.

The optical properties of small metal nanoparticles reflect the electronic structure which depends strongly on their size [14, 15], shape [16, 17], environment [18], interactions between the particles [19, 20] and the adsorbed species on the surface [21]. Their optical response is dominated by the surface plasmon resonance (SPR) corresponding to the collective oscillation of the free electrons in the conduction band of the particle. Monodispersity of nanoparticle solutions is one of the important goals in improving the methods of synthesis, in order to study particles with desired shapes and sizes. In this work we are interested in the synthesis of both spherical and nanorods nanoparticles. Nanorods shape have been used in various fields of study due to their unique optical properties [22-24]. Indeed, the UV-visible absorption of a nanorod has two SPR: a longitudinal one associated with the long axis of the nanorod and a transverse one associated with the short axis while the spherical nanoparticles exhibit only one SPR. Gold nanorods have been synthesised in many laboratories by a seed-mediated, surfactant-assisted approach that was first reported in 2001 [8] and has been widely studied

and improved [25, 26]. Nonetheless, the reproducibility of the synthesis in terms of the nanorod size, shape and yield has been a persistent challenge facing the technique. This difference in reproducibility has been attributed to a wide variety of factors including seed aging time and nanorod growth time. Very recently, it has been reported that a very dilute impurity in the CTAB (cetyl-trimethylammonium bromide) can greatly affect nanorods formation [27].

In order to study the linear and nonlinear optical properties of metallic nanoparticles, several synthetic methods have been followed yielding several particles shape and size. One of the main aims of this work is to prepare self assembled metallic film at the air-water interface using the Langmuir technique. Self assembly of both spheres and nanorods particles has been an important direction besides the synthesis [13, 28]. In order to form Langmuir metallic films, the nanoparticles should be functionalised by organic molecules in order to prevent particle aggregation and also to ensure the nanoparticles float on the subphase surface. Alkanethiol molecules are usually used to cap the metallic nanoparticles studied at the interface. These surfactants play an essential role in the control of the growth and the shape of the particles as well as the extend of aggregation [29, 30]. Thiol derivatized particles have been synthesised and are proved to be highly stable [6, 31]. Besides its amphiphilic character, the alkanethiol thiol chain can be varied from C_3 to C_{18}, thereby varying the minimum inter-particles spacing, thus the interaction between adjacent particles [32].

The aim of this chapter is to detail the methods used to synthesise the various nanoparticles studied during this work along with the techniques used to characterise them. First of all the characterization techniques are presented. Two techniques are discussed in this chapter: the UV-vis absorption spectroscopy and the Transmission Electron Microscopy (TEM). In the second part, we will present the particle synthesis and the main properties for each kind of particles.

1.2. Characterisation techniques

Two techniques were used to characterize the colloidal solution of the nanoparticles synthesized. The first is the Transmission Electron Microscopy (TEM) which allows an easy determination of the form and size of the nanoparticles and the second is the ultra violet

visible absorption spectroscopy which allows the determination of the linear optical properties of the particles, and besides, gives indication on the aggregation of the particles.

1.2.1. Transmission Electron Microscopy (TEM)

This technique allows us to observe the nanoparticles directly. It gives details about the size and the shape of the nanoparticles observed. Through the imaging of a large number of these particles, the probability distribution is deduced. A drop of the colloid solution was taken by a micro pipette and spread on a carbon coated-copper grid. The drop was left to dry up before taking the transmission electron microscopic images of the colloidal solution. The electronic microscope used is a high voltage TOPCON 002B microscope (120 KV). The images obtained gave information about the shape and size of the particles. The size distribution is obtained out of these TEM images. In Figure 1.1 is a TEM image of a sample of gold nanoparticles solution and its corresponding size distribution. The histogram in Figure 1.1b is obtained out of the different particles diameter presented in Figure 1.1a. Out of Figure 1.1b, the average diameter and the standard deviation are obtained. In all the samples that will be presented successively in this chapter a size distribution around 10 % and 30 % was obtained.

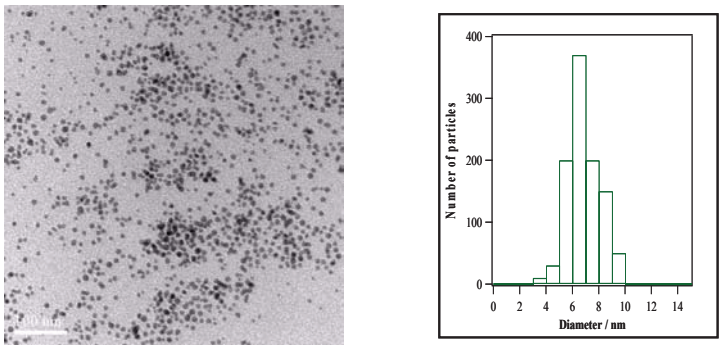

(a) (b)

Figure 1.1: TEM image of a sample of gold nanoparticles solution stabilised with citrate and its size distribution.

1.2.2.UV-Visible Absorption Spectroscopy

This spectroscopic technique relies on measuring the extinction of a light beam traversing a distance *b* of the sample solution at all frequencies of the visible spectrum. This technique permits us to obtain the absorbance of the sample since the scattering cross section is negligible for the small sizes of the particles investigated.

The absorbance of the solution follows the Beer Lambert law:

$$A = \log_{10}\left(\frac{I_0}{I}\right) = \varepsilon\, b\, C \tag{1.1}$$

where A is the absorbance (unitless), I_0 and I are the incident and transmitted light intensities, ε is the molar extinction coefficient also named molar absorbtivity with units of $L.mol^{-1}.cm^{-1}$, the latter depending on the nature of the solute, solvent, temperature and wavelength, b is the path length of the sample, that is the thickness of the solution, often given in centimeters. C is the concentration of the compound solution, expressed in mol L^{-1} . The experimental setup light source is the white light beam of a Halogen Deuterium lamp. The light beam is sent to the sample solution through an optical fiber. Another fiber collects the transmitted beam to the spectrometer (USB2000, Ocean optics) connected to a computer where the spectra are visualized using SW5 software.

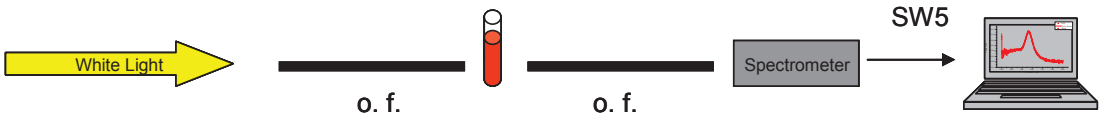

Figure 1.2 : UV-vis Experimental set-up.

First, the UV-Visible spectrum of the reference is registered. The reference is the solvent in which the nanoparticles synthesised are dispersed. The solvents used were hexane, chloroform and pure water (Millipore 18.2 MΩcm). This reference corresponds to the transmitted intensity of the cell in the absence of the nanoparticles. Then the UV-visible transmission spectrum of the nanoparticles solution is registered and the absorbance extracted using equation (1.1). This spectrum allows us to characterize the nanoparticles, determine the SPR position and also verify the absence or the presence of aggregation depending on the broadening of the spectrum. Moreover, the surfactants stabilizing the particle can shift the SPR position.

1.3. Synthesis and characterisation of Spherical nanoparticles

Since the aim of this work is to study the linear and nonlinear optical properties of metallic nanoparticles several synthesis have been done to control the size, the form and the nature of the particles to be placed at the interface. Soluble and insoluble nanoparticles were synthesised in our laboratory or through collaboration.

1.3.1. $NaBH_4$ Reduction

Materials: Sodium Borohydride (99%), Silver Nitrate, and sodium citrate were purchased from Aldrich. MilliQ water (18.2MΩ.cm) from Millipore was used in each preparation. All glassware was cleaned prior to use with detergent solutions followed by rinsing with milliQ water.

Silver nanoparticles with small sizes (diameter equals 8 nm) were synthesised using the Sodium Borohydride method [33]. Two solutions were prepared, the first one containing 10.3 mg silver nitrate ($AgNO_3$) and 14.7 mg sodium citrate ($Na_3C_6H_5O_7$) diluted in 200 mL of distilled water. Sodium citrate was used as a protective agent to stabilise the silver nanoparticles, control their size, and prevent their coalescence into large ensembles owing to their negative charge. The second solution contained 38 mg Sodium Borohydride ($NaBH_4$) diluted in 10 mL of water. $NaBH_4$ was used since it is a strong reducing agent yielding small diameter nanoparticles. 6 mL of the second solution were added to the first solution. The solution was then placed in an ice bath. The reaction mixture was stirred for half an hour. The final color was dark yellow with a concentration 4.38×10^{16}particles/L. The UV-visible absorption spectrum of the solution presented in Figure 1.3 exhibits the strong surface plasmon resonance band at 400 nm that is characteristic of colloidal silver. The plasmon resonance position is in agreement with the theoretical calculation using the Mie theory (quasi-static approximation) [34].

The broadening of the resonance is attributed to the size and shape distributions of the synthesized particles as compared to perfect sphere used in the Mie theory. From the TEM image, see Figure 1.4, the shape of the particles is quasi spherical of diameter equals 8 nm.

The size distribution is ~ 15%. This large size distribution is clearly noticed in the TEM image where we notice the presence of large particles probably due to aggregated particles.

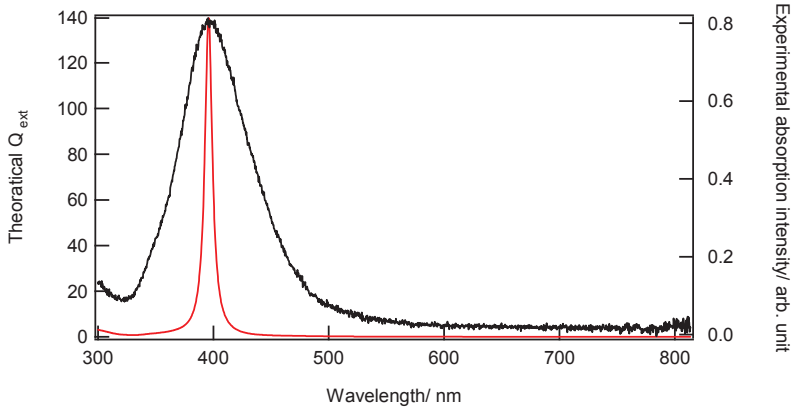

Figure 1.3 : UV-visible spectrum of the silver colloidal solution stabilized with citrate with a particle diameter of 8 nm (black) compared to a Mie calculation in the quasi static approximation(red).

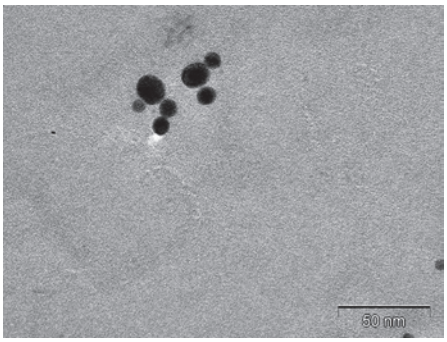

Figure 1.4 : TEM image for silver nanoparticles of diameter equals 8 nm in water solution

1.3.2. Synthesis of hydrophobic alkanethiol capped silver nanoparticles of small diameter (8 nm).

Materials: Silver nitrate, dodecanethiol, tetraoctylammonium bromide, and sodium borohydride were purchased from Aldrich, chloroform, ethanol were purchased from Roth.

Many methods have been used to synthesize metallic particles with control of the size, the shape and the hydrophobic or hydrophilic character. To obtain the hydrophobic property of the metallic nanoparticles, capping with alkanethiol molecules is usually performed, see figure 1.5.

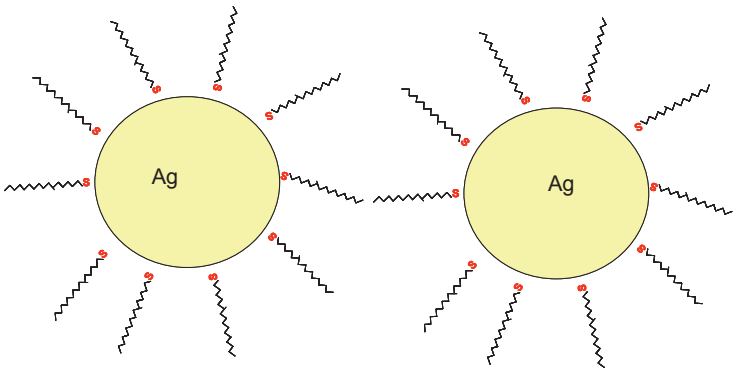

Figure 1.5: Schematic of silver nanoparticles capped with alkanethiol.

Surfactants are used to provide a hydrophilic/hydrophobic character and are responsible for particle stabilization [1]. Particles are thus stabilized against irreversible agglomeration. The two-phase Arrested Growth Method for the capping silver nanoparticles is based on the work of Brust and co-workers [31] for gold nanoparticles and is detailed in the work of Korgel [13] for silver ones. The name is derived from the use of two liquid phases due to the fact that silver nitrate ($AgNO_3$) does not dissolve directly in chloroform. Therefore the metallic salt is first dissolved in pure water and then silver ions are transferred into the organic phase using a phase transfer catalyst tetraoctylammonium bromide (TOAB). After that step the organic phase containing the nanoparticles is separated from the aqueous phase.

Thirty milliliters of an aqueous silver ion solution containing 0.153 g of $AgNO_3$ was combined with 20.4 mL of a chloroform solution of the phase transfer catalyst containing 2.227 g of TOAB and stirred vigorously for one hour. The organic phase was collected and 0.16 g of dodecanethiol ($C_{12}H_{25}$ SH) was added, the mixture being stirred for 15 minutes. Then 24 mL of an aqueous sodium borohydride solution containing 0.390 g of $NaBH_4$ was added. The reaction mixture was stirred for 12 hours, and then washed twice with water. The organic nanocrystal rich phase was collected and 300 mL of ethanol added. The solution was left at temperature of -18°C until precipitation took place. The phase was filtrated while being washed with ethanol and water to remove the phase transfer catalyst, excess thiol and reaction by-products. The powder was collected and weighted. Its weight was 50 mg. In all of the future works, the exact concentration used to perform the experiment is essential. For these synthesized particles, this exact concentration was determined from the last step of the

synthesis which is the filtration. The filtrated powder of the nanoparticles was weighted then redispersed in a known volume of chloroform giving the solution a concentration of 1.82×10^{17} particles/L. The experimental error on this value arises from the weighting of the dispersed powder, presence of residues of the free thiols, and a probable bad dispersion of the powder in the chloroform thus favouring sedimentation.

The C_{12} dodecanethiol capped silver nanoparticles were considered capped with an average length of carbon chain. The same synthesis was used with shorter or longer chain length. The length of the alkanethiol chains may vary from C_3 to C_{18} in commercially available products, thereby varying the minimum inter-particles spacing. Particles coated with long-chain thiol were stable and had a high hydrophobic character whereas the short-chain ones were instable. This instability may be attributed to the disordered nature of the alkyl chains, short chain thiols not forming a crystalline environment and possessing a large number of gauche defects [1]. C_{12} chains were considered as a good compromise, the edge-to-edge distance between particles being approximately equal to the length of a single chain [1]. Moreover, as the chain length increases, the inter-particle spacing (or edge-edge distance) increases. This can be explained by the change in the chain conformation despite the possible increase in defects. Nevertheless, as the length of the carbon chain increases and so will the interparticle distance, the interaction between the particles decreases. For this reason, this same procedure was used to cap the particles with different chain length. Silver nanoparticles capped with octadecanethiol, hexanethiol and propanethiol were synthesized following the same procedure and giving particles of about 8 nm diameter. The same procedure was also followed for the synthesis of gold capped particles where the silver ions were replaced by gold ions. Figure 1.6 shows the TEM image for a dodecanethiol silver nanoparticles colloidal solution where the particles have a rather spherical shape and a diameter of about 8±1 nm.

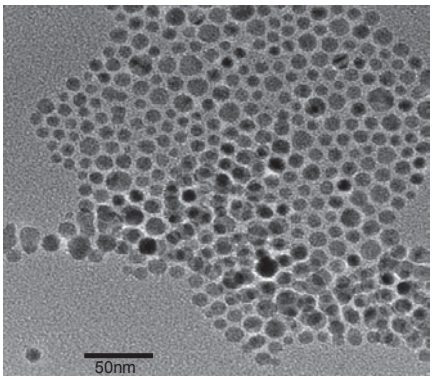

Figure 1.6 : Image of nanoparticles obtained by TEM microscopy for the silver nanoparticles capped with dodecanethiol of diameter equal 8nm.

In some of the TEM image, we noticed the presence of aggregation that could have taken place during the deposition of the droplet of the solution in the grid. In order to differentiate between the aggregation taking place while performing the deposition and the aggregation already present in the synthesized solution, UV-Visible absorption spectroscopy was performed. Figure 1.7 presents the experimental and the theoretical absorption spectra for the dodecanethiol silver spherical nanoparticles of diameter equal 8nm. The experimental absorption is broader than that of the theoretical one. The broadening of the experimental resonance was attributed to the size and the shape distributions as well as the possible aggregation of the solution.

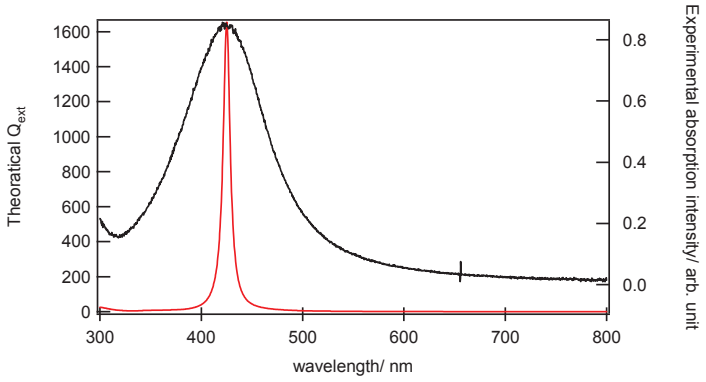

Figure 1.7: Theoretical (red) and experimental (black) absorption spectra versus wavelength of silver synthesized nanoparticles capped with dodecanethiol of diameter 8nm.

Nevertheless, the large size distribution was one of the inconvenient points of this synthesised nanoparticles solutions. Hence, commercially available dodecanethiol nanoparticles with a smaller size distribution were purchased where the diameter is about 10 nm. These nanoparticles were purchased from Aldrich Company (667838-25ML). The UV-visible

absorption spectrum of such a commercial solution is given in Figure 1.8. The broadening of the experimental resonance is attributed to the size distribution and the deformation in the spherical shape of the synthesized particles, even though the distributions are narrower for this solution. The concentration for the commercial nanoparticles was 3.03×10^{17} particles/L.

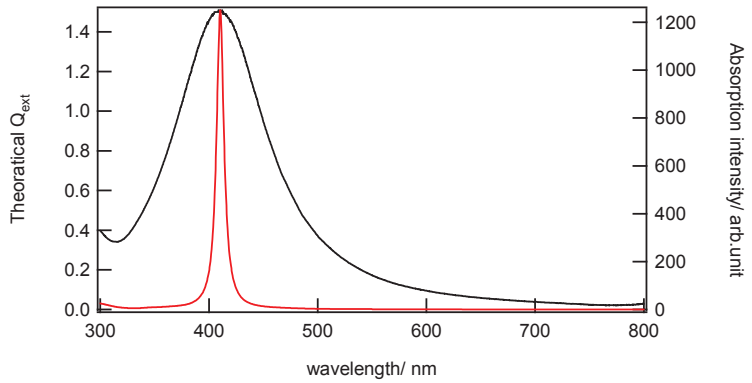

Figure 1.8: Theoretical (red) and experimental (black) absorption spectra versus wavelength of silver commercial nanoparticles capped with dodecanethiol of diameter 10nm.

1.3.3. Synthesis of hydrophobic alkanethiol capped gold nanoparticles of 18 nm diameter

Materials: $HAuCl_4.3H_2O$, $NaBH_4$, Ascorbic acid (AA), CTAB (cetyl-trimethylammonium bromide) (Aldrich 855820) and AgNO3 were used as purchased from Sigma-Aldrich. MilliQ water with resistivity 18.2 MΩ.cm was used. Glassware was cleaned with detergent solution prior to use followed by rinsing with MilliQ water.

1.3.3.1. Preparation of the gold seeds

0.1mL of an aqueous 2.5×10^{-2} M solution of $HAuCl_4.3H_2O$ was added to 7.5 mL of a 0.10 M CTAB solution in a test tube. The solutions were gently mixed by inversion. The solution appeared bright brown-yellow in color. Then 0.6 mL of an aqueous 0.01 M cold $NaBH_4$ solution (temperature 4°C) was added all at once to the solution, followed by rapid inversion mixing for 2 minutes. Gas evolved during this mixing and special care was taken to allow the escape of the gas during mixing. The solution then acquired a pale brown-yellow color. The test tube was then kept in a water bath maintained at 25°C for 2 hours before being used. This solution could still be used after a week of its preparation.

1.3.3.2. Preparation of the gold nanospheres

For the nanospheres preparation, 196 mL of a 0.05 M CTAB (Aldrich 855820) solution was prepared. We added 2 mL of the 2.5×10^{-2} M solution of $HAuCl_4$. 1 mL water containing 50 mg ascorbic acid was then added. The color changed from yellow to colorless due to the reduction of the Au^{3+} ions into Au^{+}. 1 mL of the seed solution was then added. The final solution was then kept at a temperature 60°C for 2 hours and also kept under agitation. The final solution was red in color and the diameter of the particles was about 18 nm. The particles were dispersed in water and stabilised with CTAB. Figure 1.9 presents the experimental and the theoretical absorption versus wavelength for the gold spherical nanoparticles of diameter equal 18 nm stabilized with CTAB. We noticed that the experimental absorption was almost coincident with the theoretical one. This indicates that the size distribution is rather narrow for this synthesis. In order for the particles to reside at the interface, they should be capped with a hydrophobic surfactant, thiolalkanes were chosen. The capping procedure is though presented after the synthesis of the nanorods since it is similar in both cases.

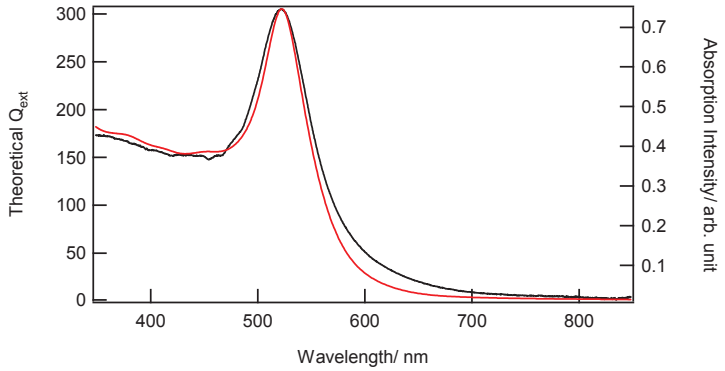

Figure 1.9: Theoretical (red) and experimental (black) absorption spectra versus wavelength of gold nanoparticles stabilised with CTAB 18nm.

1.4. Synthesis and characterisation of nanorods

Synthesis of nanostructures via simple wet chemical methods is one of the favored routes toward the effective large-scale production of nano-building blocks. Nanorods synthesis is challenging because the surface energy favors the formation of spherical particles rather than nanorods. However, surface capping agents such as CTAB [34] have been successfully used for the creation of rod shaped nanoparticles. Short aspect ratio gold nanorods are especially

interesting because of their optical properties. They exhibit the transverse as well as intense longitudinal plasmon bands in the visible region of the spectrum, making them promising candidates for sensing and imaging applications. Several synthesis methods were tested aiming to ameliorate the yield, the shape and the size of the nanorods. Nikoobakht and El-Sayed obtained gold nanorods of varied aspect ratio in solution by varying the amount of silver nitrate for a given amount of gold [25]. Furthermore, Sau and Murphy [26] observed that a change in the amount of the silver nitrate added could lead to the formation of non rod shaped particles. Therefore, the growth step played a critical role in the formation of the rods with a high yield. These authors also studied the effects of chemicals involved in the synthesis affecting the yield and the aspect ratio of the nanorods. A later study reported that using the same recipe but changing the supplier of the CTAB didn't yield nanorods particles. They concluded that a very dilute impurity in the CTAB surfactant could greatly affect the nanorods formation. Using the same recipe, CTAB from Acros, Sigma, and Aldrich didn't yield nanorods whereas CTAB from Fluka and MP Biomedicals did. For the synthesis of the nanorods in this work, CTAB from Fluka company (Fluka 52370) was purchased [27].

1.4.1. Preparation of the gold nanorods

1.6 mL of the 2.5×10^{-2} M solution of $HAuCl_4.3H_2O$ was added to 0.25 mL of a 2.5×10^{-2} M $AgNO_3$. 100 mL of 0.10 M CTAB solution was added to the previous solution. The solution appeared bright brown-yellow in color. We then added 0.64 mL of a 0.01 M ascorbic acid to the bright brown-yellow solution, followed by gentle mixing. The solution became colorless once the ascorbic acid was added and mixed. After that, 83µL of the seed solution prepared before and presented in paragraph 1.3.3.1 was added rapidly to the colorless solution. It is important to note that the only difference in the seed preparation is the CTAB source due to the impurity effect mentioned before. Hence, CTAB solution from Fluka (52370) was used. The final solution was gently mixed for 3 seconds and left undisturbed for at least 3 hours. In fact, when the seed solution was added before the ascorbic acid, the reaction became so slow, for that the seed solution was always added after the ascorbic acid addition [26]. The concentration of the final solution was calculated to be 1×10^{11} particles/mL. These chosen concentrations of chemical materials gave nanorods of 64 (±12) × 24 (±6) × 24 (±6) nm dimensions. Many other dimensions can be synthesised by changing the quantities of the several chemicals used but were not tested here [26].

Trials to determine if the CTAB in the seed solution or the growth solution was most important to nanorod growth were performed. CTAB supplied from Acros, Sigma or Aldrich to form the seeds and CTAB from Fluka (52370) or MP Biomedicals to perform the growth led to nanorods with a small yield and short dimensions. This indicated that CTAB is primarily important for the nanorods formation but is also important in the production of the seed particles as well. In Figure 1.10 are the experimental and the theoretical absorption spectra of the synthesized solution. The TEM image for this solution is given in Figure 1.11.

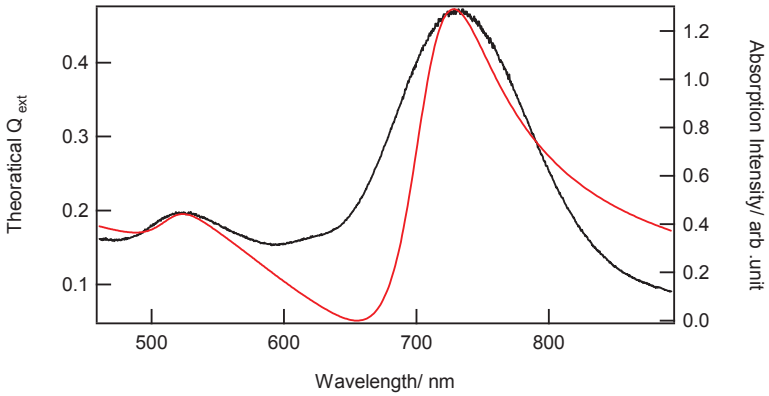

Figure 1.10 : Theoretical (red) and experimental (black) absorption spectra versus wavelength of gold nanorods of dimension 64×24 nm stabilised with CTAB.

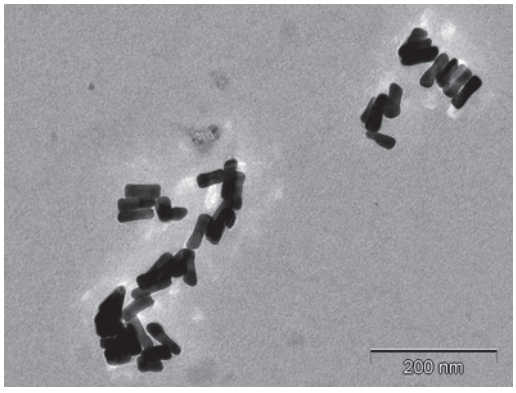

Figure 1.11 : TEM microscopy for the gold nanorods of dimension 64×24 nm.

1.4.2.Passageway to the organic phase

The final solutions obtained were aqueous solutions. In fact, and as will be seen later, both nanospheres and nanorods particles have been used to form nanoparticles films at the air/water interface. In order for the nanoparticles to be placed at the surface of water, they should be hydrophobic. Hence, the transfer to the organic solution was essential. For a 20 mL

nanorods solution already prepared in CTAB/water environment, the same volume of chloroform containing 20 mg of octadecanethiol chains ($C_{18}SH$) was mixed. The solution was agitated for 15 minutes, an emulsion taking place. Ethanol was added drop by drop while the solution was still under agitation until becoming a limpid solution. After that step the organic phase containing the nanoparticles was separated from the aqueous phase. At this stage, the organic phase was colored and the aqueous phase was colorless. The organic phase was collected, centrifuged for 20 minutes with a rate of centrifugation of 6000 revolutions per minute (rpm). The reaction mixture was washed with 20 mL ethanol and then re centrifuged in order to remove the phase transfer catalyst, excess thiol and reaction by-products. Then ethanol was evaporated and the particles were dispersed in chloroform. The concentration of the final solution for the octadecanethiol gold nanorods was 8.88×10^{10} particles/mL.

In order to cap the nanorods with dodecanethiol chains, the same procedure was used. The only difference is that we add 100 µL dodecanethiol chains to the 20 mL solution of the nanorods stabilized with CTAB in water. We then had gold nanorods stabilized with dodecanethiol chains of concentration 1×10^{11} particles/mL. The theoretical and experimental absorption spectra for these gold nanorods stabilised with dodecanethiol and octadecanethiol are present in Figure 1.12 (a) and (b) respectively. We notice that the theoretical spectra are narrower than the experimental ones for the nanorods stabilised with CTAB and alkanethiol. This is due to the size and the shape distributions and probably due also to aggregation. An important remark is the shift in the first and second SPR for the three types of nanorods. It is well known that the environment surrounding the particles affects the position of the SPR peak. For the nanorods stabilised with CTAB, the first SP resonance was located at 530 nm and the second one at 730 nm. For the nanorods stabilised with dodecanethiol, the first SP resonance was located at 544 nm and the second one at 765 nm, wavelengths slightly red shifted as compared to the CTAB capped rods. This may be attributed to a change towards a more compact capping layer although the surface bond may well play a non negligible role in this change. In addition, the spectrum recorded for the dodecanethiol capped nanorods exhibited a much broader SP resonance. This feature may arise from aggregation. The SPRs of the nanorods capped with octadecanethiol were located at 540 nm and 784 nm respectively. The changes in terms of wavelength shifts between the different SPR of the dodecanethiol capped and octadecanethiol capped nanorods were minimal for the first peak and red shifted for the second SPR peak. This shift possibly arises because of the increase of the surrounding

dielectric constant due to the longer chain length. In addition, the narrower band for the octadecanethiol indicates that the aggregation may be less present than in the case of dodecanethiol, something not totally unexpected since the chain length is longer and prevent better aggregation.

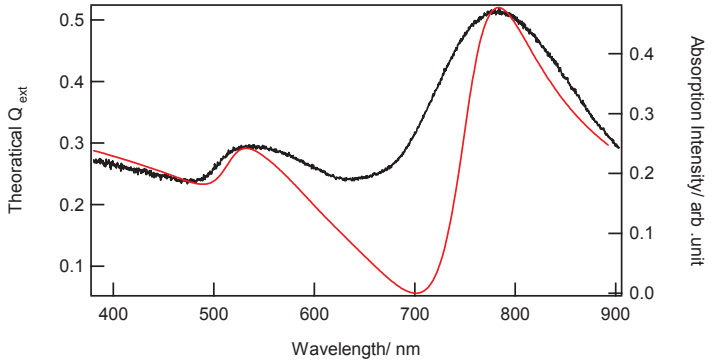

(a)

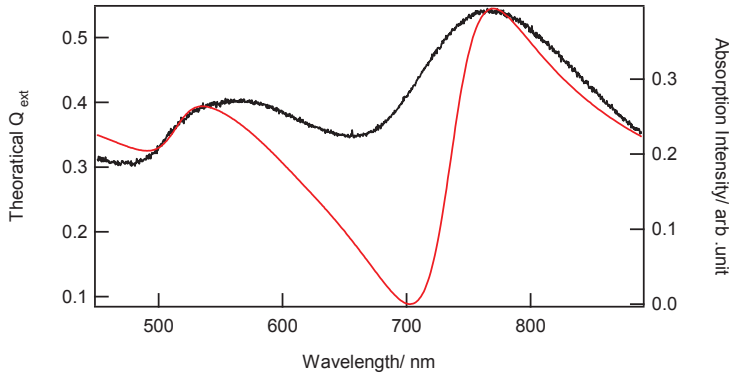

(b)

Figure 1.12 : (a) Theoretical (red) and experimental (black) absorption spectra versus wavelength of gold nanorods of dimension 64×24 nm capped with dodecanethiol, (b) Theoretical (red) and experimental (black) absorption spectra versus wavelength of gold nanorods of dimension 64×24 nm capped with octadecanethiol.

For the spherical particles the same transfer procedure was followed for the stabilisation of the nanoparticles with alkanethiol. The final concentration for the dodecanethiol gold solution was 4.3×10^{11} particles/mL and was 5.34×10^{11} particles/mL for the octadecanethiol gold solution.

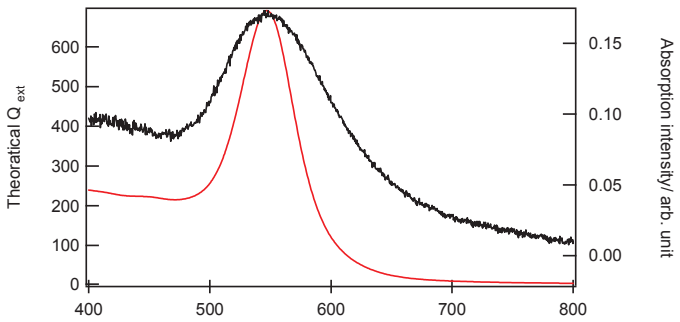

(a)

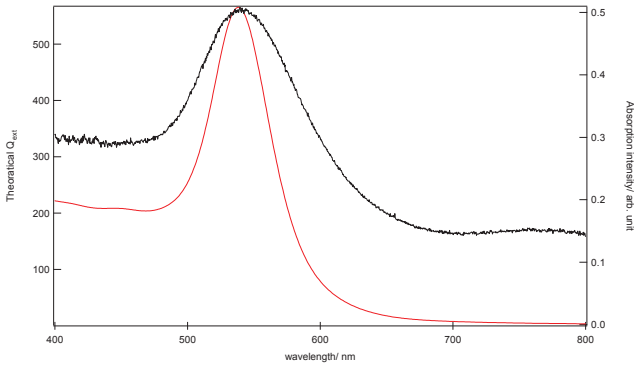

(b)

Figure 1.13: Absorption versus wavelength of: (a) theoretical (red) and experimental (black) spherical nanoparticles of 18 nm diameter capped with dodecanethiol, (b) theoretical (red) and experimental (black) spherical nanoparticles of 18 nm diameter capped with octadecanethiol.

Figure 1.9 indicates that the SPR is at 522 nm and the theoretical and experimental fits are in a very good agreement indicating the small size distribution of the solution. Once the nanorods were capped with dodecanethiol or octadecanethiol, see Figure 1.13 for the UV-visible absorption spectra, the SP resonance was shifted to 546 and 543 nm respectively. This difference in the peak position is surprising since an increase of the surrounding dielectric constant usually induces a red shift of the SPR band. However, this 3 nm shift is not a very significant shift.

1.5. Conclusion

A variety of chemical synthesis methods have been used for the preparation of metallic nanoparticle solutions of both spheres and nanorods. The properties of the synthesised

solutions were characterised through UV-visible absorption spectroscopy along with comparison to theoretical absorption spectra obtained from Mie theory. The TEM microscopy was used to deduce the shape and the size distributions of the synthesised particles. The particles were characterised by the HRS technique where the hyperpolarisability of each type of particles was deduced. Spherical nanoparticles and nanorods were used subsequently to form a two dimensional film at the air/water interface studied by linear reflectance and transmittance and SHG. Silver nanoparticles stabilised with citrate and dispersed in water were used to form a metallic film at the liquid/liquid interface.

.

References:

[1] D. L. Feldheim, *Metal Nanoparticles: Synthesis Characterization & Applications*: CRC, 2001.

[2] D. Burshtain, L. Zeiri, and S. Efrima, "Control of Colloid Growth and Size Distribution by AdsorptionSilver Nanoparticles and Adsorbed Anisate," *Langmuir,* vol. 15, pp. 3050-3055, 1999.

[3] P. C. Lee and D. Meisel, "Adsorption and surface-enhanced Raman of dyes on silver and gold sols," *J. Phys. Chem.,* vol. 86, pp. 3391-3395, 1982.

[4] L. M. Liz-Marzan and I. Lado-Tourino, "Reduction and Stabilization of Silver Nanoparticles in Ethanol by Nonionic Surfactants," *Langmuir,* vol. 12, pp. 3585-3589, 1996.

[5] H. Remita, J. Khatouri, M. Tréguer, J. Amblard, and J. Belloni, "Silver-palladium alloyed clusters synthesized by radiolysis," *J. Phys. D Atoms, Molecules and Clusters,* vol. 40, pp. 127-130, 1997.

[6] M. Brust, J. Fink, D. Bethell, D. J. Schiffrin, and C. Kiely, "Synthesis and reactions of functionalised gold nanoparticles," *J. Chem. Soc., Chem. Commun.,* pp. 1655-1656, 1995.

[7] M. J. Hostetler, J. E. Wingate, C.-J. Zhong, J. E. Harris, R. W. Vachet, M. R. Clark, J. D. Londono, S. J. Green, J. J. Stokes, G. D. Wignall, G. L. Glish, M. D. Porter, N. D. Evans, and R. W. Murray, "Alkanethiolate Gold Cluster Molecules with Core Diameters from 1.5 to 5.2 nm: Core and Monolayer Properties as a Function of Core Size," *Langmuir,* vol. 14, pp. 17-30, 1998.

[8] N. R. Jana, L. Gearheart, and C. J. Murphy, "Wet Chemical Synthesis of High Aspect Ratio Cylindrical Gold Nanorods," *J. Phys. Chem. B,* vol. 105, pp. 4065-4067, 2001.

[9] N. R. Jana, L. Gearheart, and C. J. Murphy, "Seeding Growth for Size Control of 5−40 nm Diameter Gold Nanoparticles," *Langmuir,* vol. 17, pp. 6782-6786, 2001.

[10] T. Yonezawa, K. Yasui, and N. Kimizuka, "Controlled Formation of Smaller Gold Nanoparticles by the Use of Four-Chained Disulfide Stabilizer," *Langmuir,* vol. 17, pp. 271-273, 2001.

[11] M. Brust and C. J. Kiely, "Some recent advances in nanostructure preparation from gold and silver particles: a short topical review," *Coll. and Surf. A: Physicochem and Engineer. Asp.,* vol. 202, pp. 175-186, 2002.

[12] J. Turkevich, P. C. Stevenson, and J. Hillier, "A study of the nucleation and growth processes in the synthesis of colloidal gold," *Disc. Farad. Soc.,* vol. 11, pp. 55-75, 1951.

[13] B. A. Korgel, S. Fullam, S. Connolly, and D. Fitzmaurice, "Assembly and Self-Organization of Silver Nanocrystal Superlattices: Ordered “Soft Spheres”,"*J. Phys. Chem. B,* vol. 102, pp. 8379-8388, 1998.

[14] U. Kreibig and M. Vollmer, *Optical properties of metal clusters*: Springer, 1995.

[15] B. Palpant, B. Pravel, J. Lerme, E. Cottancin, M. Pellarin, M. Treilleux, A. Perez, J. L. Vialle, and M. Broyer, "Optical properties of gold clusters in the size range 2–4 nm," *Phys. Rev. B,* vol. 57, pp. 1963-1963, 1998.

[16] C. F. Bohren and D. R. Huffman, *Absorption and scattering of light by small particles*, 1983.

[17] A. M. Michaels, M. Nirmal, and L. E. Brus, "Surface Enhanced Raman Spectroscopy of Individual Rhodamine 6G Molecules on Large Ag Nanocrystals," *J. Amer. Chem. Soc.,* vol. 121, pp. 9932-9939, 1999.

[18] K. L. Kelly, E. Coronado, L. L. Zhao, and G. C. Schatz, "The Optical Properties of Metal Nanoparticles: The Influence of Size, Shape, and Dielectric Environment," *The J. Phys. Chem. B,* vol. 107, pp. 668-677, 2003.

[19] J. J. Shiang, J. R. Heath, C. P. Collier, and R. J. Saykally, "Cooperative Phenomena in Artificial Solids Made from Silver Quantum Dots: The Importance of Classical Coupling,"*J. Phys. Chem. B,* vol. 102, pp. 3425-3430, 1998.

[20] R. G. Freeman, M. B. Hommer, K. C. Grabar, M. A. Jackson, and M. J. Natan, "Ag-Clad Au Nanoparticles: Novel Aggregation, Optical, and Surface-Enhanced Raman Scattering Properties," *J. Phys. Chem.,* vol. 100, pp. 718-724, 1996.

[21] P. Mulvaney, "Surface Plasmon Spectroscopy of Nanosized Metal Particles," *Langmuir,* vol. 12, pp. 788-800, 1996.

[22] J. Perez-Juste, I. Pastoriza-Santos, L. M. Liz-Marzan, and P. Mulvaney, "Gold nanorods: Synthesis, characterization and applications," *Coord. Chem. Rev.,* vol. 249, pp. 1870-1901, 2005.

[23] L. A. Bauer, N. S. Birenbaum, and G. J. Meyer, "Biological applications of high aspect ratio nanoparticles," *J. Mater. Chem.,* vol. 14, pp. 517-526, 2004.

[24] A. Haes, D. Stuart, S. Nie, and R. Van Duyne, "Using Solution-Phase Nanoparticles, Surface-Confined Nanoparticle Arrays and Single Nanoparticles as Biological Sensing Platforms," *J. Fluo.,* vol. 14, pp. 355-367, 2004.

[25] B. Nikoobakht and M. A. El-Sayed, "Preparation and Growth Mechanism of Gold Nanorods (NRs) Using Seed-Mediated Growth Method," *Chem. of Mater.,* vol. 15, pp. 1957-1962, 2003.

[26] T. K. Sau and C. J. Murphy, "Seeded High Yield Synthesis of Short Au Nanorods in Aqueous Solution," *Langmuir,* vol. 20, pp. 6414-6420, 2004.

[27] D. K. Smith and B. A. Korgel, "The Importance of the CTAB Surfactant on the Colloidal Seed-Mediated Synthesis of Gold Nanorods," *Langmuir,* vol. 24, pp. 644-649, 2008.

[28] P. Yang and F. Kim, "Langmuir-Blodgett Assembly of One-Dimensional Nanostructures," *Chem. Phys. Chem.,* vol. 3, pp. 503-506, 2002.

[29] D. V. Leff, P. C. Ohara, J. R. Heath, and W. M. Gelbart, "Thermodynamic Control of Gold Nanocrystal Size: Experiment and Theory," *The J. of Phys. Chem.,* vol. 99, pp. 7036-7041, 1995.

[30] R. L. Whetten and W. M. Gelbart, "Nanocrystal Microemulsions: Surfactant-Stabilized Size and Shape," *J. of Phys. Chem.,* vol. 98, pp. 3544-3549, 1994.

[31] M. Brust, M. Walker, D. Bethell, D. J. Schiffrin, and R. Whyman, "Synthesis of thiol-derivatised gold nanoparticles in a two-phase Liquid-Liquid system," *J. Chem. Soc., Chem.Commu.,* pp. 801-802, 1994.

[32] C. P. Collier, R. J. Saykally, J. J. Shiang, S. E. Henrichs, and J. R. Heath, "Reversible Tuning of Silver Quantum Dot Monolayers Through the Metal-Insulator Transition," *Science,* vol. 277, pp. 1978-1981, 1997.

[33] M. A. Hayat, *Colloidal gold: principles, methods and applications*. New Jersey: Academic press, , 1989.

[34] G. Mie, "Contributions to the optics of turbid media, particularly of colloidal metal solutions " *Ann. Phys.,* vol. 25, pp. 377-445, 1908.

[35] C. J. Murphy and N. R. Jana, "Controlling the Aspect Ratio of Inorganic Nanorods and Nanowires," *Advan. Mater.,* vol. 14, pp. 80-82, 2002

Chapter 2

Hyper Rayleigh Scattering of metallic nanoparticles

2.1. Introduction

Second Harmonic Generation (SHG) is a nonlinear optical process whereby two photons at the fundamental frequency ω are converted into one photon at the harmonic frequency 2ω. This process has been first observed in a quartz plate by Franken *et al.* [1]. It has since been widely used in laser science to convert one frequency into its second harmonic. Since this phenomenon is forbidden in centrosymmetric media within the electric dipole approximation, it has also been extended to the study of interfaces between two centrosymmetric media with great selectivity [2]. More recently it has also been used to investigate the nonlinear optical properties of metallic particles dispersed in a liquid solution. In this case, the method bears the name of Hyper Rayleigh Scattering (HRS) [3, 4], namely the scattering of harmonic light, because no coherent light at the harmonic frequency is generated. HRS is indeed an incoherent phenomenon where the total detected intensity is the incoherent superposition of the SHG intensities scattered by each nonlinear sources present in the sample. In this chapter, we have investigated the quadratic nonlinear optical properties of small metallic nanoparticles, more precisely silver and gold particles, by the HRS technique before investigating the two dimensional films made from them and supported at liquid interfaces. The choice of gold and silver metallic particles is based on the unique optical and electronic properties [5] of these particles which are dominated by the collective excitation of the electrons of the conduction band. This collective excitation is named Surface Plasmon Resonance (SPR). SPR enhancement of the quadratic nonlinear optical response of these particles is obtained when the second harmonic frequency is tuned to the SPR resonance of the particles, yielding large magnitudes for their hyperpolarizability tensor in particular [6-8]. The SPR frequency though depends on the particles' composition, morphology, shape, size or surrounding medium [9]. These unique properties have already been investigated extensively by optical techniques like

absorption spectroscopy, and by nonlinear optical ones which are now more and more developed [10, 11]. The use of nonlinear optical techniques with metallic particles in several fields such as catalysis [12], biological sensing [13], photonics and medicine [14], similarly to its use in molecular systems like self micelles [15], liposomes [16], and biomolecules [17] has been the focus of many studies over the past years.

Citrate-coated spherical silver or gold nanoparticles have principally been the centre of attention in the recent studies reported, in part by our own group. This is due to the synthesis of these systems which is rather simple and to the expected particle shape, close to that of perfect spheres. This has allowed our group in particular to investigate the origin of the HRS response and its different contributions as a function of the size of the nanoparticles. A dipolar contribution to the HRS intensity dominates at small metallic particle diameters and scales with the square of the surface area, finding its origin at the particle surface. Owing to the breaking of the centrosymmetry associated to the perfect spherical shape, this electric dipole contribution dominates at small diameters. This breaking is expected to arise from deviations from the perfect spherical shape. For larger particles diameters, a quadrupolar contribution associated with the retardation of the electromagnetic fields starts to take over the dipolar contribution. This quadrupolar contribution scales with the square of the particle volume [18]. These previous studies have all underlined the high sensitivity of the HRS technique to the shape and nature of the nanoparticle surface. In order to go a step beyond, this chapter is devoted to study thiol derivatization of silver and gold nanoparticles in order to investigate the role of surfactants adsorbed at the particle surface in the breaking of the centrosymmetry of the particles. These studies will also allow us to establish the sensitivity of the HRS technique to surface adsorption. Since sulfur has a strong affinity to transition metal surfaces because of the possibility to form multiple bonds with the surface metal [19], it is expected that alkanethiol molecules, beside their role in forming a protecting layer, will passivate the surface from the nonlinear optical point of view. Furthermore, as we shall see in later chapters, these thiol derivatized metallic particles will be used to form two-dimensional films at the interface. This first step will help us in characterizing these particles, and more precisely in addressing the role of these surfactants in the control of the growth and the shape of the particles as well as the extend of aggregation [20, 21]. Finally, it is worth noting that such alkanethiol derivatized particles have various applications, in biology [22] and film protection technology [19] to name a few.

In the first section of this chapter, a brief introduction to the HRS theory is given. In the second section, the experimental setup is described. The last section presents the experimental results. The HRS studies performed in our work are focused on the nonlinear optical response of two kinds of particles shapes: spherical particles and nanorods. For each shape, we have measured the quadratic hyperpolarisability and from the polarisation analysis of the HRS intensity we have been able to discuss the weight of the dipolar and the quadrupolar contributions to the response. Then, to address the problem of the surface modifications introduced by the thiolated compound adsorption, a comparison with other surfactants, especially citrate, has been done. The last part of this chapter concerns the HRS measurements of metallic nanorods stabilised with various surfactants. There exists very few nonlinear optical studies on such particles [23] despite their unique optical properties due to the presence of two SPR : a longitudinal one associated with the long axis of the nanorod and a transverse one associated with the short axis. Nanorods have also a greater sensitivity to their environment compared to spherical particles [24, 25] and are able to form two-dimensional assemblies [26, 27], an important point regarding this work.

2.2. Hyper Rayleigh Scattering theory

2.2.1. Principle

In nonlinear optics, the optical response of media is described by expressing the nonlinear polarization *P* as a power series of the electric field as:

$$\vec{P}_{NL} = \varepsilon_0(\chi^{(1)}\vec{E} + \vec{\chi}^{(2)} : \vec{E}\vec{E} + \vec{\chi}^{(3)} : \vec{E}\vec{E}\vec{E} + ...) \quad (2.1)$$

where $\vec{\chi}^{(1)}$ is the linear susceptibility and $\vec{\chi}^{(2)}$, $\vec{\chi}^{(3)}$ are respectively the second and third order susceptibilities. If we focus the discussion on the Second Harmonic Generation (SHG) process only, the first nonlinear order is defined by:

$$\vec{P}_{NL}^{(2)} = \varepsilon_0 \vec{\chi}^{(2)} : \vec{E}\vec{E} \quad (2.2)$$

One of the fundamental properties of the polarization is that it must remain invariant by the same transformations that leave unchanged the medium described. Hence, the nonlinear polarization critically depends on the symmetry of the medium. In the case of microscopic objects like nanoparticles much smaller than the wavelength of light, the electric dipole approximation can be assumed. In this case, the electric fields can be considered as constant over the dimensions of the order of the size of the particles. Hence, in order for the second order nonlinear processes to be observed, the medium must lack a centre of symmetry. Indeed, if we consider an inversion transformation with respect to the origin of the reference frame, the point *M* of coordinates *(x, y, z)* is transformed into the point *M'* of coordinates *(-x, -y, -z),* see Figure 2.1.

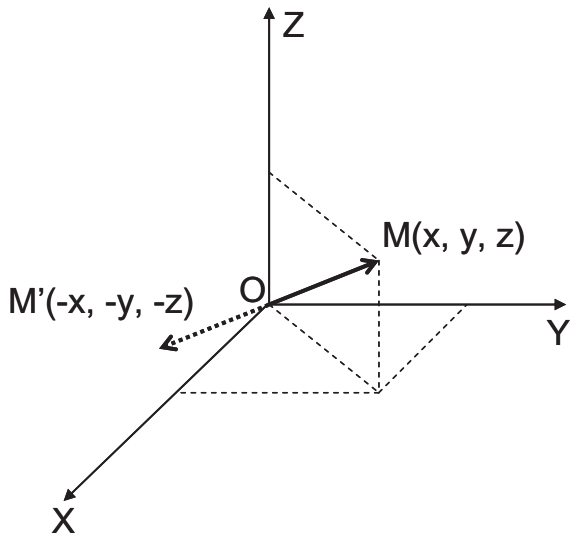

Figure 2.1 : Inversion transformation through the origin of the reference frame of point M(x, y, z) into point M' (-x, -y, -z)

Applying this transformation to the nonlinear polarisation $\vec{P}_{NL}^{(2)}$ leads to:

$$-\vec{P}_{NL}^{(2)} = \varepsilon_0 \vec{\vec{\chi}}^{(2)}(-\vec{E})(-\vec{E}) = \varepsilon_0 \vec{\vec{\chi}}^{(2)}\vec{E}\vec{E} = \vec{P}_{NL}^{(2)} \tag{2.3}$$

assuming that $\vec{\vec{\chi}}^{(2)}$ remains invariant. Therefore the only solution for this equation is $\vec{\vec{\chi}}^{(2)} = 0$ and for this reason SHG is forbidden in such media like liquids or gas. Because SHG is forbidden in centrosymmetric media, SHG is allowed where the inversion symmetry is broken like surfaces between centrosymmetric media. Therefore, SHG has been a method of choice

to study air-liquid or liquid-liquid interfaces. Through these studies, molecular adsorption and orientation have been at the focus of an extensive literature. In order to obtain such microscopic information from this macroscopic approach, the quadratic hyperpolarizability tensor β must be introduced. In this microscopic point of view, the nonlinear polarization given by the equation (2.2) is replaced by that of the induced dipole at the position $\vec{r}'$:

$$\vec{p}(\vec{r}',2\omega) = \vec{\vec{\beta}} : \vec{E}(\vec{r}',\omega)\vec{E}(\vec{r}',\omega) \tag{2.4}$$

where the electric field must be taken as the local electric field. Taking the plane wave approximation, the incident electromagnetic field $\vec{E}(\vec{r}',\omega)$ at position $\vec{r}'$ is given in the laboratory frame by :

$$\vec{E}(\vec{r}',\omega) = E_{\omega}(\hat{X}\cos\gamma + \hat{Y}\sin\gamma\, e^{i\delta})e^{i(\vec{k}.\vec{r}'-\omega t)} \tag{2.5}$$

where γ is the incident polarisation angle and δ is the relative phase between the field components along $\hat{X}$ and $\hat{Y}$. The propagation direction of the wave is along $\overrightarrow{OZ}$ and the vertical direction of the laboratory is taken along $\overrightarrow{OX}$. We have also chosen the detection direction to be along the $\overrightarrow{OY}$ direction with a 90° angle from the excitation direction. This angle allows us to avoid the direct transmission of the incident beam to the detection arm. The alignment of the detection arm is also easier.

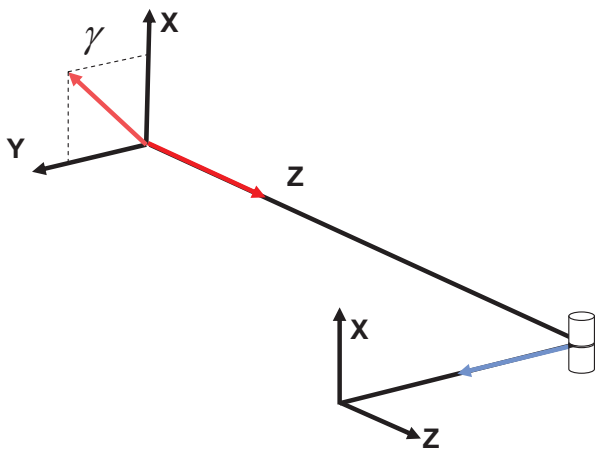

Figure 2.2: Scheme of the propagation and detection directions

Using equations (2.4) and (2.5), we obtain the expression of the harmonic dipole:

$$\vec{p}(\vec{r}',2\omega) = E_{\omega}^{2}\vec{\vec{\beta}}_{L}(\hat{X}\hat{X}\cos^{2}\gamma + (\hat{X}\hat{Y}+\hat{Y}\hat{X})e^{i\delta}\sin\gamma\cos\gamma + \hat{Y}\hat{Y}\sin^{2}\gamma e^{2i\delta})e^{2i(\vec{k}.\vec{r}'-\omega t)} \quad (2.6)$$

where $\vec{\vec{\beta}}_{L}$ is the quadratic hyperpolarisability tensor in the laboratory reference frame (*L* stands for Laboratory). This tensor is obtained from the corresponding microscopic tensor $\vec{\vec{\beta}}_{m}$, the quadratic hyperpolarisability tensor given in the microscopic reference frame (*m* stands for microscopic). This tensor contains all the information about the symmetry of the molecule or the particle. The transformation from one reference frame to the other is performed using the Euler angles, see Figure 2.3.

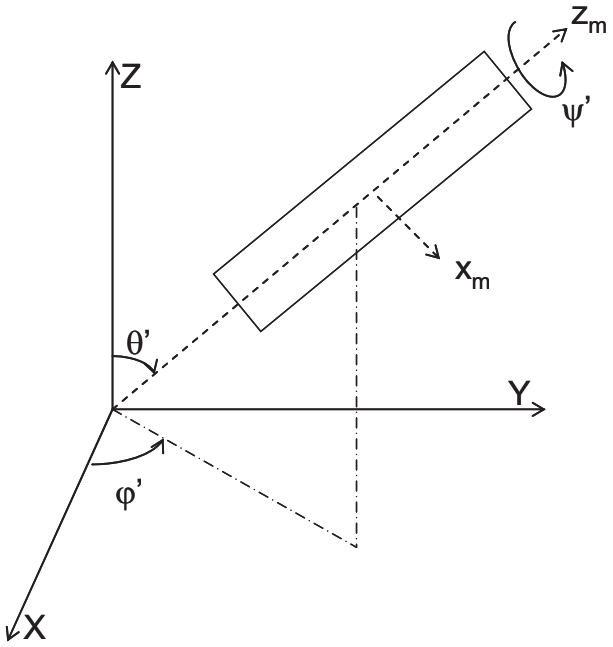

Figure 2.3 : Euler Angles to perform the change from the microscopic to the laboratory frame.

We can then use the transformation matrix $T(\theta',\phi',\psi')$ given in equation (2.7) into equations (2.8) and (2.9) where *θ', ϕ', ψ',* are the three Euler angles defining the transformation :

$$T(\theta',\phi',\psi') = \begin{pmatrix} -\sin\psi'\cos\theta'\sin\varphi' + \cos\psi'\cos\varphi' & \cos\psi'\cos\theta'\sin\varphi' + \sin\psi'\cos\varphi' & \sin\theta'\sin\varphi' \\ -\sin\psi'\cos\theta'\cos\varphi' - \cos\psi'\sin\varphi' & \cos\psi'\cos\theta'\cos\varphi' - \sin\psi'\sin\phi' & \sin\theta'\cos\varphi' \\ \sin\psi'\sin\theta' & -\cos\psi'\sin\varphi' & \cos\theta' \end{pmatrix} \quad (2.7)$$

$$\vec{\vec{\beta}}_L = T(\theta', \varphi', \psi')\vec{\vec{\beta}}_m \tag{2.8}$$

$$\beta_{L,IJK} = \sum_{ijk} T_I^i T_J^j T_K^k \beta_{m,ijk} \tag{2.9}$$

The emitted electromagnetic field of frequency 2ω is simply the field emitted by the dipole $\vec{p}(\vec{r}',2\omega)$ where the field's expression are well-known [28]. Considering the experimental configuration, the far-field radiation zone is considered where the dipole characteristic length is very small compared to the wavelength and the latter is very small compared to the distance to the detection. The electric field is therefore written as:

$$\vec{E}(\vec{r},\vec{r}',2\omega) = K^2\left(\hat{h}\times\vec{p}(\vec{r}',2\omega)\right)\times\hat{h}\frac{e^{iK|\vec{r}-\vec{r}'|}}{|\vec{r}-\vec{r}'|} \tag{2.10}$$

where $K=2\omega n^{2\omega}/c$ is the norm of the second harmonic wave vector and $\hat{h}=\vec{r}/r$ is the direction of propagation of the second harmonic field. This equation is valid when no multiple scattering occurs and when interactions between the fundamental and the harmonic scattering fields are neglected. Using equations (2.6) and (2.10), we obtain the detected scattered field from a nonlinear dipole, in our experimental configuration, and since the detection is at right angle from the propagation direction, therefore $\hat{h}=\hat{Y}$:

$$\vec{E}(\vec{r},\vec{r}',2\omega) = \begin{pmatrix} \beta_{L,XXX}\cos^2\gamma + 2e^{i\delta}\beta_{L,XXY}\cos\gamma\sin\gamma + e^{2i\delta}\beta_{L,XYY}\sin^2\gamma \\ 0 \\ \beta_{L,ZXX}\cos^2\gamma + 2e^{i\delta}\beta_{L,ZXY}\cos\gamma\sin\gamma + e^{2i\delta}\beta_{L,ZYY}\sin^2\gamma \end{pmatrix} E_\omega^2 K^2 \frac{e^{iK|\vec{r}-\vec{r}'|}}{|\vec{r}-\vec{r}'|} e^{2i\vec{k}.\vec{r}'} \tag{2.11}$$

Using the limit $r' << r$ because of the far field approximation, equation (2.11) yields:

$$\vec{E}(\vec{r},\vec{r}',2\omega) = \begin{pmatrix} \beta_{L,XXX}\cos^2\gamma + 2e^{i\delta}\beta_{L,XXY}\cos\gamma\sin\gamma + e^{2i\delta}\beta_{L,XYY}\sin^2\gamma \\ 0 \\ \beta_{L,ZXX}\cos^2\gamma + 2e^{i\delta}\beta_{L,ZXY}\cos\gamma\sin\gamma + e^{2i\delta}\beta_{L,ZYY}\sin^2\gamma \end{pmatrix} E_\omega^2 K^2 \frac{e^{iK|\vec{r}|}}{r} e^{i(2\vec{k}-\vec{K}).\vec{r}'} \tag{2.12}$$

For the hyperpolarizability tensor $\vec{\vec{\beta}}$, the first index corresponds to the direction of the detected electric field while the two other indices correspond to the direction of the exciting

electric field. Since we cannot distinguish between the two exciting fields since they arise from the same laser, we can permute the last two indices. Equation (2.12) allows us to write the second harmonic intensity for a source positioned at $\vec{r}'$ and measured in the $\vec{r}$ direction along the $\hat{Y}$ axis as follows:

$$I(\vec{r},\vec{r}',2\omega) = \frac{\varepsilon_0 c}{n^{2\omega}} \vec{E}(\vec{r},\vec{r}',2\omega)\vec{E}^*(\vec{r},\vec{r}',2\omega) \tag{2.13}$$

Equation (2.13) gives the intensity collected from a single microscopic source described through a radiating dipole at the harmonic intensity. Now that we have the second harmonic intensity, we will derive the HRS intensity from an ensemble of radiating dipoles and discuss the principle of the method.

2.2.2. HRS principles

As discussed above, the non linear polarisation possesses intrinsic symmetry properties leading in particular to $\vec{\vec{\chi}}^{(2)} = \vec{\vec{0}}$ in a centrosymmetric medium. This limit states that no coherent signal may be recovered from a centrosymmetrical medium like a liquid suspension of randomly oriented dipoles radiating at the harmonic frequency. However, it appears that an incoherent signal may still be detected. For *N* objects without interaction, which is the case of a diluted liquid suspension of molecules or particles for example, we apply the ergodicity principle stating the equivalence between the average over all possible orientations taken by a single molecule or particle over time with the average over all the molecules or particles at a single time *t*. This is true for large enough ensembles of molecules. This will lead to the incoherent addition of the second harmonic fields emitted by each molecule or particle [29]. The HRS intensity is finally given by the following equation:

$$I_{HRS}(\vec{r},2\omega) = \frac{\varepsilon_0 c}{n^{2\omega}} N\left\langle \vec{E}(\vec{r},\vec{r}',2\omega)\vec{E}^*(\vec{r},\vec{r}',2\omega)\right\rangle \tag{2.14}$$

where the symbol $\langle\ \rangle$ stands for the average over all the orientations taken by the molecule or particle. Experimentally, this HRS intensity rewrites as follows:

$$I_{HRS}(\vec{r},2\omega) = G^{'} N \left\langle \beta_L^2 \right\rangle I_\omega^2 \quad (2.151)$$

where

$$G^{'} = \frac{4\pi^2 c\left(n^{(2\omega)}\right)^3}{r^2 \lambda^4 \varepsilon_0} \quad (2.16)$$

and I_ω^2 is the intensity of the fundamental wave, N is the number of particles involved in the process and $\left\langle \beta_L \right\rangle$ is the absolute value of the hyperpolarisability tensor magnitude of the molecules or particles averaged over all possible orientations. The elements of the hyperpolarisability tensor are assumed within the laboratory frame. Also, λ is the fundamental wavelength, ε_0 is the electric vacuum permittivity, $n_{2\omega}$ is the refractive index at the harmonic frequency and c is the speed of light in vacuum. Experimentally, optical losses due to the absorption of the liquid solution at the fundamental and the harmonic frequencies can be incorporated using Beer-Lambert law. This gives:

$$I_{HRS}^0 = I_{HRS} e^{-[2A_\omega + A_{2\omega}]} \quad (2.17)$$

where A_ω and $A_{2\omega}$ are the absorbance at the fundamental and harmonic frequencies respectively. To have more information than the magnitude of the hyperpolarisability tensor, polarisation resolved studies are essential as we shall see now.

2.2.3. Polarised HRS

The measurement of the HRS intensity can be performed according to different polarisation configurations, allowing the measurement of different hyperpolarizability tensor elements [30, 31]. In particular, the vertically and horizontally polarised HRS intensities as a function of the polarisation angle γ of the incident electromagnetic field are given by:

$$I_{HRS}^{V} = GNI_{\omega}^{2}\left(\left\langle \beta_{L,XXX}\beta_{L,XXX}^{*} \right\rangle \cos^{4}\gamma + \left\langle 4\beta_{L,XXY}\beta_{L,XXY}^{*} + 2\beta_{L,XXX}\beta_{L,XYY}^{*}\cos 2\delta \right\rangle \cos^{2}\gamma \sin^{2}\gamma + \left\langle \beta_{L,XYY}\beta_{L,XYY}^{*} \right\rangle \sin^{4}\gamma \right) \quad (2.18)$$

$$I_{HRS}^{H} = GNI_{\omega}^{2}\left(\left\langle \beta_{L,ZXX}\beta_{L,ZXX}^{*} \right\rangle \cos^{4}\gamma + \left\langle 4\beta_{L,ZXY}\beta_{L,ZXY}^{*} + 2\beta_{L,ZXX}\beta_{L,ZYY}^{*}\cos 2\delta \right\rangle \cos^{2}\gamma \sin^{2}\gamma + \left\langle \beta_{L,ZYY}\beta_{L,ZYY}^{*} \right\rangle \sin^{4}\gamma \right) \quad (2.19)$$

In our experiment, the incident polarisation is linear and the factor $\cos 2\delta$ is equal to unity. We can thus rewrite the HRS intensity as follows:

$$I_{HRS}^{\Gamma} = a^{\Gamma}\cos^{4}\gamma + b^{\Gamma}\cos^{2}\gamma\sin^{2}\gamma + c^{\Gamma}\sin^{4}\gamma \quad (2.20)$$

where Γ is the polarisation angle of the scattered field at the harmonic frequency *2ω*. The vertical polarisation ($\Gamma = 0°$) is along the $\overrightarrow{OX}$ direction and the horizontal polarisation ($\Gamma = 90°$) is along the $\overrightarrow{OZ}$ direction. The three real coefficients are given by:

$$a^{V} = GNI_{\omega}^{2}\left\langle \beta_{L,XXX}\beta_{L,XXX}^{*} \right\rangle \quad (2.21)$$

$$b^{V} = GNI_{\omega}^{2}\left\langle 4\beta_{L,XXY}\beta_{L,XXY}^{*} + 2\beta_{L,XXX}\beta_{L,XYY}^{*} \right\rangle \quad (2.22)$$

$$c^{V} = GNI_{\omega}^{2}\left\langle \beta_{L,XYY}\beta_{L,XYY}^{*} \right\rangle \quad (2.23)$$

$$a^{H} = GNI_{\omega}^{2}\left\langle \beta_{L,ZXX}\beta_{L,ZXX}^{*} \right\rangle \quad (2.24)$$

$$b^{H} = GNI_{\omega}^{2}\left\langle 4\beta_{L,ZXY}\beta_{L,ZXY}^{*} + 2\beta_{L,ZXX}\beta_{L,ZYY}^{*} \right\rangle \quad (2.25)$$

$$c^{H} = GNI_{\omega}^{2}\left\langle \beta_{L,ZYY}\beta_{L,ZYY}^{*} \right\rangle \quad (2.26)$$

These parameters have particular relationships arising from the intrinsic symmetry of the experimental set-up, irrespective of the symmetry of the molecules or particles studied. In the case of a totally incoherent emission, the second harmonic intensity follows the relations:

$$\left(I_{HRS}^{0}(E=E_{\hat{X}})\right)^{V}+\left(I_{HRS}^{0}(E=E_{\hat{Y}})\right)^{V}=2\left(I_{HRS}^{0}(E=E_{45^{\circ}})\right)^{V} \tag{2.27}$$

in the case of the vertical polarisation (Γ=0°). Also, all configurations whereby the incident polarization is at 45° from the detected polarisation are equivalent yielding:

$$P_{45}=\frac{1}{\sqrt{2}}P_{X}+\frac{1}{\sqrt{2}}P_{Y} \tag{2.28}$$

Since we are concerned with an incoherent process, we can write for the intensity:

$$P_{45}^{2}=\frac{1}{2}P_{X}^{2}+\frac{1}{2}P_{Y}^{2} \tag{2.29}$$

thus giving

$$\frac{1}{2}a^{V}+\frac{1}{2}c^{V}=\frac{1}{4}(a^{V}+b^{V}+c^{V})$$

or

$$a^{V}+c^{V}=b^{V} \tag{2.30}$$

Projection of the fields along the horizontal direction leads to:

$$(I_{HRS}^{0^{\circ}})^{H}=(I_{HRS}^{45^{\circ}})^{H}=(I_{HRS}^{90^{\circ}})^{H} \tag{2.31}$$

giving

$$2a^{H}=2c^{H}=b^{H} \tag{2.32}$$

Finally, we obtain:

$$I_{HRS}^{V} = a^{V} \cos^2 \gamma + c^{V} \sin^2 \gamma \tag{2.33}$$

$$I_{HRS}^{H} = c^{V} \tag{2.34}$$

It is interesting to note that the HRS intensity depends but on two independent parameters a^V and c^V only for the vertical component and is independent of the angle γ for the horizontal component. It is therefore common to introduce the depolarization ratio D of c^V over a^V as:

$$D = \frac{c^{V}}{a^{V}} \tag{2.35}$$

The factor D allows to get characteristic information at the microscopic level on the molecules or particles, an interesting point when the molecules or particles have just a few number of accessible hyperpolarisability tensor elements.

In the case of perfectly spherical particles, theoretical calculations have shown that a four lobe polarisation resolved curve for the vertically polarised intensity was obtained. In this case, contributions associated with the centrosymmetrical components of the response must be taken into account requiring a model going beyond the electric dipole approximation described above, see Figure 2.4a. However, when the deformations of the spherical particles are too important, the contribution associated to the non centrosymmetric component dominates and a two lobe curve is obtained, in agreement with the electric dipole model given above. From a rather general point of view, and without discussing in detail the problem beyond the electric dipole approximation, incorporation of the retardation of the electromagnetic fields takes place once the size of the particles is no longer negligible compared to the wavelength of the incident light [32, 33].

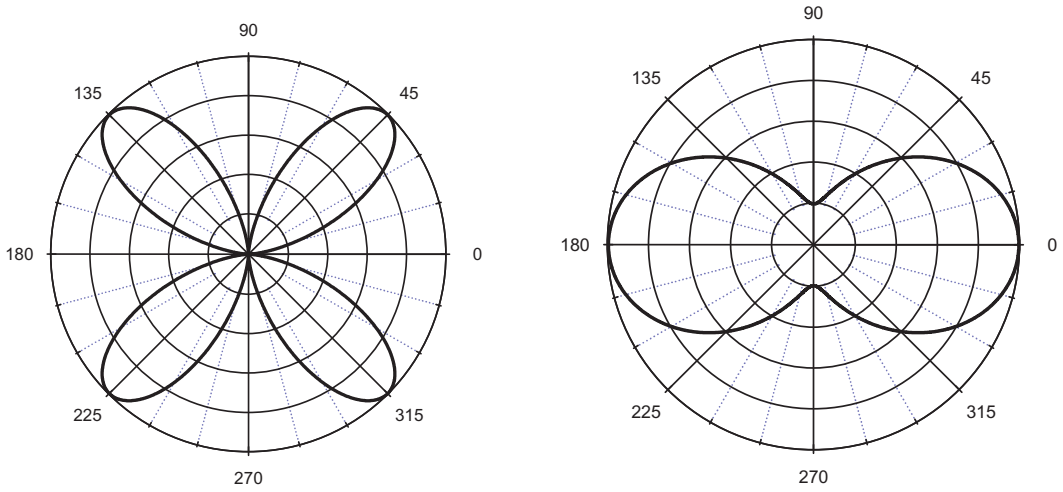

(a) (b)

Figure 2.4 : (a) Theoretical polar plot of a pure quadrupolar response. (b) Theoretical polar plot of a pure dipolar response

It is then useful to introduce the parameter ζ^V which quantifies the degree of deviation from the pure dipolar pattern, in other words to estimate the relative weight of the dipolar and quadrupolar contributions. This ζ^V parameter is given by:

$$\zeta^V = \left| \frac{b^V - (a^V + c^V)}{b^V} \right| \tag{2.36}$$

In the case of a pure dipolar response, see Figure 2.4b, the relation between the hyperpolarisability parameters is given by equation (2.30) and the ζ^V parameter is equal to zero. However in the case of the pure quadrupolar response of a perfect sphere, $a^V = c^V = 0$ and the parameter ζ^V is equal to unity. Any other value yields the relative weight of the two contributions and hence that of the retardation effects.

2.3. Experimental setup

The light source for the hyper Rayleigh scattering experiment was a mode-locked femtosecond Ti: Saphirre (Coherent, Mira 900) laser delivering at 800 nm pulses with 180 femtoseconds duration and a repetition rate of 76 MHz. The laser was pumped with a CW

diode pumped laser delivering 5 W at 532 nm. This femtosecond laser source provided two spectral domains: the first one extends from 750 to 900 nm with an optimum output around 800 nm and the second one extending from 950 to 1050 nm with an optimum at 970 nm. A computer controlled half wave plate at 800 nm was placed along the beam to set the polarisation of the fundamental input beam. After passing through a low-pass filter to remove any unwanted harmonic light generated before the cell, mostly that of the half wave plate which is made from a crystalline quartz plate, the fundamental light was focused by a microscopic objective (Melles Griot, NA = 0.3 and magnification x16) into a spectrometric cell containing the solution of the metallic particles.

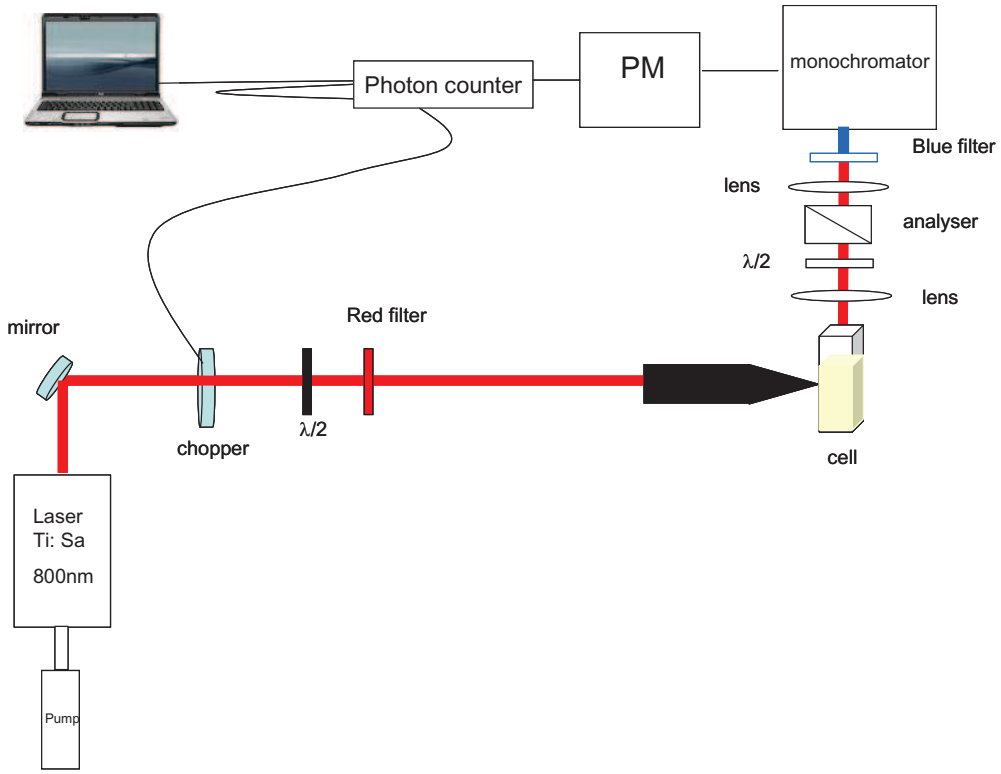

Figure 2.5 : Hyper Rayleigh Scattering (HRS) experimental setup

A mechanic chopper, set at a frequency of 130 Hz (Stanford Research systems, SR 540) was used to enable a gated photon counting allowing automatic subtraction of the noise level. For a minimum re-absorption at the harmonic frequency, the focal point was placed close to the walls of the cell. The HRS intensity was collected at right angle from the incident direction through a 2.5 cm focal length lens, then passed through a half wave plate at 400 nm set to Vertical or Horizontal position and then into a polarising cube set to vertical position. Both the half wave plate at 400 nm and the polarising cube were used as an analyser to collect light

vertically polarised. The second harmonic light was separated from the fundamental light by a high-pass filter and focused by another focal lens with a 2.5 cm focal length to the entrance slit of a monochromator (Acton, SP150) which allowed for a spectral selection of the HRS light. The HRS photons were detected with a cooled photomultiplier (Hamamatsu, R943-02) and counted with a photon counter (Stanford Research Systems, SR400). The photon counter received two signals, the first one as the overall signal and the second one as the noise, see Figure 2.5. The net signal was calculated from the subtraction of the overall signal from the noise one.

2.4. Results

The experiments were focused on the study of gold and silver metallic nanoparticles stabilized with different surfactants. Two shapes were investigated: nanospheres and nanorods. Neutral surfactants like alkanethiol [34] and charged surfactants like cetylammonium bromide (CTAB) [35] were used as stabilizers during the synthesis of the nanoparticles. Their binding to the particle's surface decreases the surface energy and allows the control of the growth, and subsequently of the shape of the particles [20, 21]. Besides, these surfactants act as stabilizers against aggregation. Techniques such as Raman [36] and X-ray photon spectroscopy [37] have been used in the past to study the structure and the organisation of different capping materials at the surface of nanoparticles. Applications in catalysis [38], chemical sensing or optoelectronics [39] are indeed heavily dependent on the surface properties of these nanostructures. In this section, we focus on the consequences of the presence of these strong surfactants on the quadratic nonlinear response. There exists many surface active organosulfur compounds that form a monolayer on gold surfaces. However, the most studied and probably the most well understood of these layers is that formed by alkanethiols on Au(111) surfaces [19]. We wish to see how their properties may be reflected in the hyperpolarisability tensor values. Before going into the description of these results, a first part is devoted to the nonlinear optical properties of the bare solvents.

2.4.1. Solvents

The nanoparticles used in the HRS measurements were dispersed in water, chloroform or hexane depending on the capping agent. Water and chloroform have already been studied by HRS. We have complemented these data for hexane using an external normalization

procedure of the HRS intensity collected for hexane with that obtained for water. Numerically, the hyperpolarisability value of water is [40] :

$$\beta_{water} = 0.56 \times 10^{-30} esu \tag{2.37}$$

Ultrapure Millipore water with resistivity 18.2 Ω.cm was used. The HRS intensities recorded for water, chloroform and hexane are shown in Figure 2.6 as a function of the harmonic wavelength. This experimental procedure, where the fundamental wavelength is fixed and the wavelength of detection tuned around the harmonic wavelength, is necessary to ensure that the process observed is indeed the conversion of two photons at the fundamental frequency into one photon at the harmonic frequency. This procedure allows the subtraction of any underlying broadband spectrum indicating the presence of fluorescence. The HRS signal was adjusted with a Gaussian function and a linear background, see equation (2.38). In the case of chloroform, we noticed the presence of a background confirming the necessity for the use of this procedure. This background was attributed to a fluorescence background, possibly arising from small impurities [41]. The Gaussian fit yielded the HRS intensity while the width was determined by the spectral width of the laser. The line fit gave the contribution of the fluorescence background. The fluorescence background was recalculated at the harmonic wavelength and subtracted since these two processes are incoherent. The fitted equation was therefore of the form:

$$y = (ax + b) + I_{HRS}\ e^{-([x-p]/w)^2} \tag{2.38}$$

where a and b yield the fluorescence background at the wavelength x, I_{HRS} the HRS intensity at the peak position p and w the width of the Gaussian line. Using the external reference method, where the HRS intensity is normalised against a cell with known HRS intensity, the hyperpolarisability magnitude of hexane and chloroform were deduced. In this work, we used water as the reference and hence used:

$$\frac{I_{HRS}^{reference}}{I_{HRS}^{solvent}} = \frac{N_{reference}\left\langle \beta_{reference}^2 \right\rangle}{N_{Solvent}\left\langle \beta_{Solvent}^2 \right\rangle} \tag{2.39}$$

No correction for the solvent absorption at both the fundamental and the harmonic wavelengths was necessary. In equation (2.39), $N_{reference}$ *and* $N_{Solvent}$ are the number densities in moles per liter of the reference and solvents. The values of 55.5 mol/L for water, 7.6 mol/L for hexane and 12.4 mol/L for chloroform were used. We obtained:

$$\beta_{hexane} = (0.68 \pm 0.01) \times 10^{-30}\, esu \tag{2.40}$$

and

$$\beta_{chloroform} = (1.03 \pm 0.02) \times 10^{-30}\, esu \tag{2.41}$$

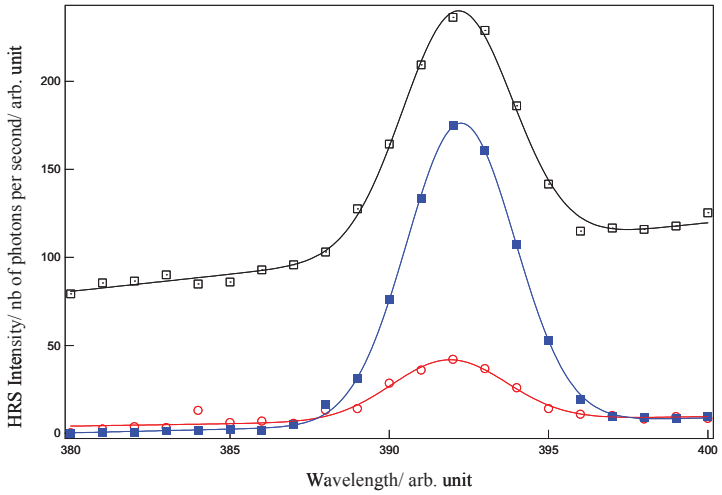

Figure 2.6 : HRS intensity versus wavelength for bare water (empty circles), bare hexane (filled cubes) and bare chloroform (empty cubes) adjusted with the fitting function given in equation (2.38).

These hyperpolarisability values are very similar to that reported in the past in our group by G. Revillod [42]. However, both in this earlier work and in this present work, the necessary corrections for the account of the changes due to the refractive indices between the three samples were not performed. Interestingly though, the hyperpolarisability of chloroform has also been reported in the literature [43]. A value of:

$$\beta_{CHCl_3} = 0.26 \times 10^{-30}\, esu \tag{2.42}$$

was given. The agreement between literature and our work can only be reconciled if a weaker value is used for water as shows a recent reference [44], in line with the main conclusion produced by G. Revillod. To obtain more information about the nature of the HRS intensities produced by these solvents, polarisation resolved measurements were performed. Polar plots of the HRS intensity as a function of the input polarisation angle γ of the linearly polarized fundamental beam for both chloroform and hexane are reported in Figure 2.7.

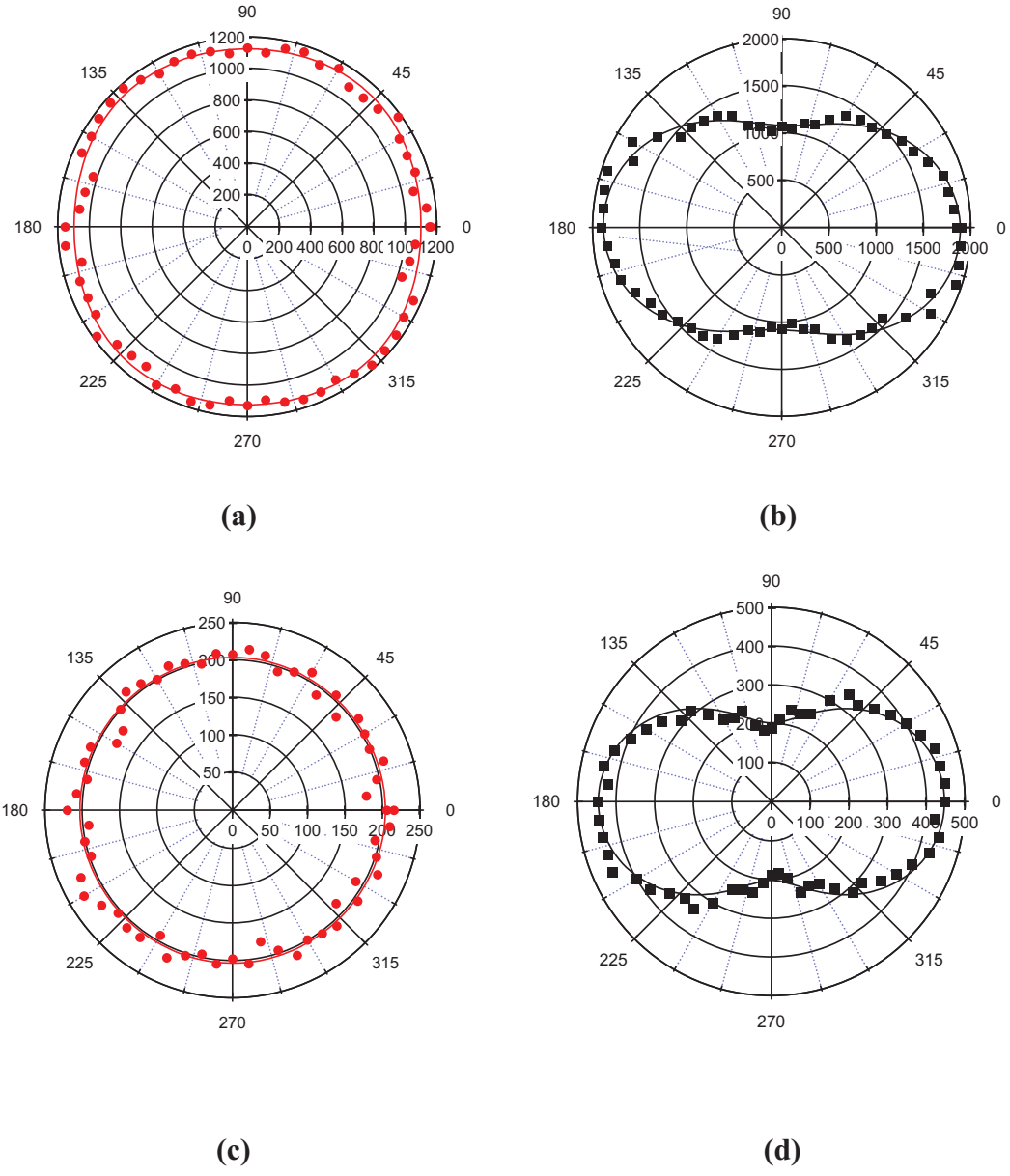

Figure 2.7 : Polar Plot of the HRS intensity as a function of the incoming fundamental beam polarisation angle: (a) and (b) Horizontal(along Z) and vertical (along X) polarisation experimental data (dots and squares) fitted with equation (2.20) for chloroform solution, (c) and (d) H and V polarisation for hexane respectively.

For both solvents, the plot of the vertically polarized HRS intensity presents a two lobe patterns whereas the plot of the horizontally polarized HRS intensity is independent of the angle γ. Nothing may be discussed from the latter plots of the horizontally polarized HRS intensity. However, from the plots of the vertically polarized HRS intensity, a depolarisation factor *D* as in equation (2.35) can be determined. It is found to be equal to 0.44 for hexane and 0.57 for chloroform. This latter value is greater than that reported by G. Revillod who reported a value of 0.3. The value of the depolarisation parameter *D* gives information about the symmetry of the compounds of interest. However, a reduced number of hyperpolarizability elements is required in this case. Using equation (2.36), we also evaluated the value of the ζ^V parameter for hexane and chloroform. A value of $\zeta^V = 0.03$ was found for hexane and $\zeta^V = 8.7 \times 10^{-3}$ for chloroform, confirming the dipolar character of the response. Nevertheless, some questions remain open. For instance, it is surprising to obtain a response from a hexane solution since hexane itself is a centrosymmetrical molecule.

2.4.2. Spherical capped nanoparticles

2.4.2.1. Dodecanethiol Silver nanoparticles

Dodecanethiol capped silver metallic nanoparticles were purchased from Sigma Aldrich (reference 667838-25 ML-08724BE) and used as received, dispersed in hexane, hence the preliminary experiments above on bare hexane. The diameter of these spherical alkanethiol capped silver nanoparticles was determined using Transmission Electron Microscopy (TEM). An average value of about 10 nm was found. The corresponding UV-visible absorption spectrum of a 5.05×10^{16} particles/L concentration of such a nanoparticles solution is also given in Figure 2.8. The absorption spectrum presents at about 400 nm a clear SP resonance. This resonance is expected to yield a large enhancement of the HRS intensity since the harmonic wavelength is in the vicinity of this resonance.

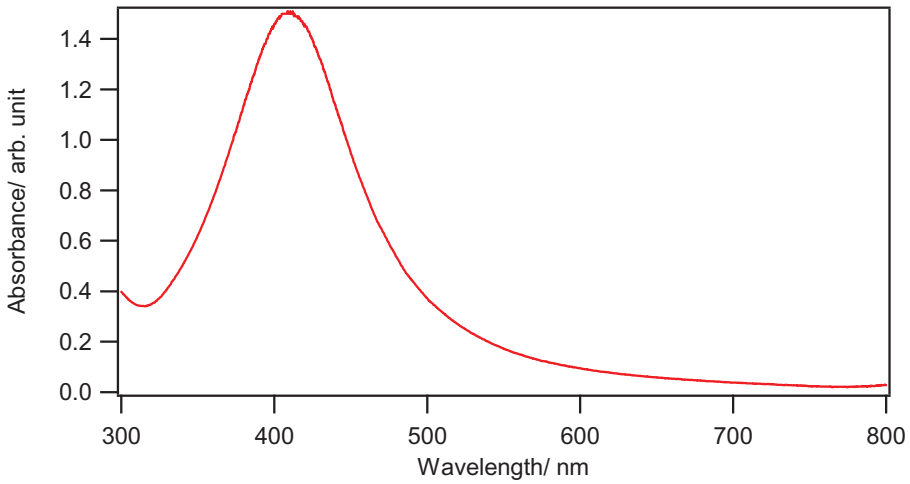

Figure 2.8 : The UV-visible absorption spectrum versus wavelength for dodecanethiol silver spherical nanoparticles of concentration 0.84×10^{-7} mol/L.

The nonlinear optical response of silver metallic nanoparticles has already been investigated by our group in aqueous solution. The hyperpolarisability β of these nanoparticles has been reported for different particle sizes [7]. However, the hyperpolarizability of thiols capped nanoparticles has never been measured although it has been found in these studies that the response originates from the surface of the particles for the smallest diameters. Here, our aim is therefore to investigate in greater details the effect of the Sulfur-Gold or Sulfur-Silver bond and its influence of the hyperpolarizability as compared to citrate-coated particles for instance. To determine the hyperpolarizability of the particles, the internal reference method was used whereby the HRS intensity for different values of the particle concentration is normalized against that of the bare solvent, see Figure 2.9. The HRS intensity obtained for bare hexane was in turn normalized to that of bare water through the external reference method. The experimental data given in Figure 2.9 were adjusted using the following equation:

$$\frac{I_{HRS}^{np}}{I_{HRS}^{solvant}} = \frac{\left\langle N_S\beta_S^2 + N_{np}\beta_{np}^2 \right\rangle}{\left\langle N_S\beta_S^2 \right\rangle} = 1 + b'N_{np}\left\langle \beta_{np}^2 \right\rangle \tag{2.43}$$

where

$$b' = \frac{1}{\left\langle N_S \beta_S^2 \right\rangle} \tag{2.44}$$

where the subscripts *np* and *S* stand for the nanoparticles and the reference solvent respectively. However, losses due to absorbance at the fundamental and the harmonic frequency were determined in a separate linear optical measurement.

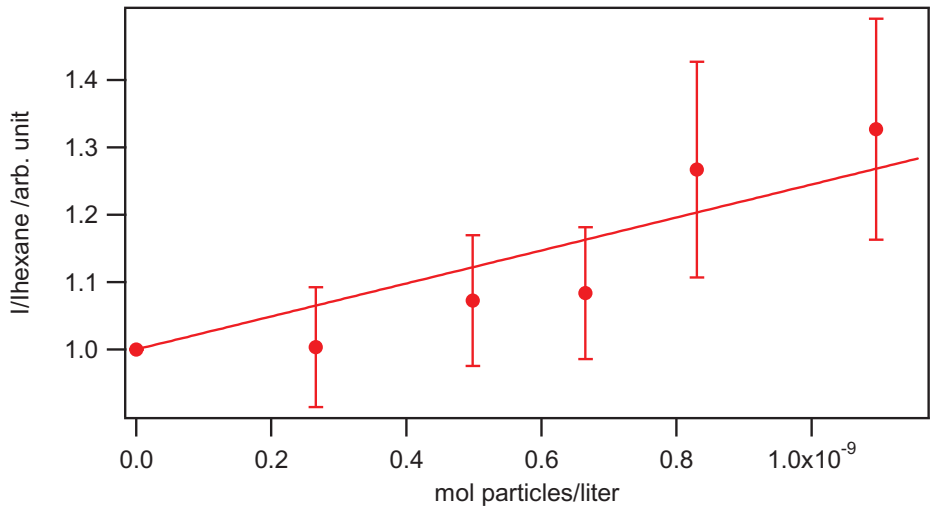

Figure 2.9 : Plot of the HRS intensity of the spherical AgC12 nanoparticles normalised to the hexane HRS intensity versus nanoparticles concentration adjusted with equation (2.43)

In these experiments, diluted concentrations of the nanoparticles solutions were used in order to avoid the formation of aggregates. A sufficient concentration was preserved though to measure with an adequate sensitivity the HRS intensity. Preliminary experiments performed with concentrations five times greater than that presented in Figure 2.9 indeed led to aggregation. The latter was clearly observed through the deviation from the straight line of the plots similar to those of Figure 2.9. The HRS intensity versus concentration plots were adjusted with a straight line based on equation (2.43) where the quadratic hyperpolarisability magnitude of hexane was taken as $\beta_h = (0.68 \pm 0.01) \times 10^{-30}\, esu$ and its concentration as 7.6 mol/L. A value of $\beta_{AgC12-10nm} = (2.99 \pm 0.23) \times 10^{-26}\, esu$ was measured for the hyperpolarisability of these dodecanethiol capped silver spherical nanoparticles. This hyperpolarizability magnitude is given as:

$$\beta_i = \sqrt{\left\langle \beta_{L,XXX}^2 \right\rangle + \left\langle \beta_{L,ZXX}^2 \right\rangle} \tag{2.45}$$

owing to the experimental configuration used for these measurements where the harmonic light is unpolarized and the fundamental light vertically polarized. The error bar is given as the standard deviation extracted from the fitting procedure. It is immediately clear that this value of hyperpolarisability is much smaller than that of citrate capped silver nanoparticles with an average diameter of about 20 nm. A value of $\beta_{Ag-20nm} = 4 \times 10^{-25} esu$ was reported for these particles [33]. Comparison of these hyperpolarisabilities must however be performed after correction for the particle size. As stated above, depending on the nature of the HRS response, the size correction differs. For an electric dipole response, the hyperpolarizability is a function of the particle's surface area whereas for an electric quadrupolar one, the hyperpolarizability is a function of the particle's volume. However, previous studies have shown that for citrate capped particles with diameters below 50 nm, the nature of the response was essentially electric dipole. Hence, for the alkanethiol capped silver particles with a diameter of 10 nm a surface correction leaded to a surface hyperpolarisability of $\beta_{0Surf} = 9.5 \times 10^{-29}$ esu/nm^2. Using the hyperpolarizability of the 20 nm diameter citrate capped silver nanoparticles, the corresponding value is $\beta_{0Surf} = 0.31 \times 10^{-27}$ esu/nm^2. The corrected hyperpolarizability values for the thiol capped particles is weaker than that obtained for the citrate capped ones. This is attributed to the surface bond between the adsorbate and the metal which is dramatically different in the two cases. Referring to reference [33] one can't affirm the behaviour of silver nanoparticles of such diameter whether it is of surface or a volume origin. For this reason, correction with respect to volume has also been performed; however the obtained value is also weaker than that obtained for the citrate capped ones.

To complement these measurements, polarisation resolved plots of the HRS intensity as a function of the fundamental angle of polarization were obtained for different concentrations of the silver nanoparticles. Plots for the *H*- and *V*- polarized HRS intensity are given in Figure 2.10 for a 0.3×10^{-9} mol/L concentration. However, a strong luminescence was clearly observed from the sample cell, see Figure 2.11.

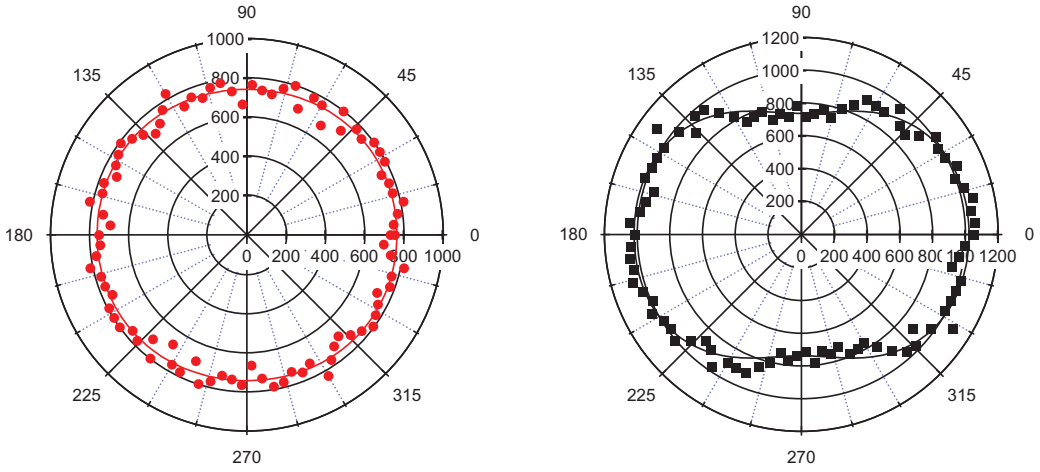

Figure 2.10 : Polar Plot of the HRS intensity as a function of the incoming fundamental beam polarisation angle: (left, circles) Horizontal (along Z) and (right, square) Vertical (along X) polarisation plots for a 0.3×10^{-9} mol/L concentration of D~10 nm AgC12 spherical nanoparticles and (solid) fit to equation (2.20)

On this Figure 2.11, the HRS line resides on a strong background. This multiphoton excited luminescence was assigned to the radiative recombination of electron-hole pairs. In this process, it is possible that trapping states at the surface of the particles, the presence of which can be due to the alkanethiol capping layer, could play a non negligible role [45,46]. As expected, the intensity of this luminescence signal increased almost linearly with the concentration. In order to subtract this luminescence from the polar plots given in Figure 2.10, a polarisation analysis was also performed with the detection fixed at the wavelength of 402 nm away from the HRS signal wavelength. The luminescence presented no polarisation dependence indicating a random orientation of the radiating dipoles. Several explanations have been proposed in the literature for the origin of these electron-hole pair radiative recombinations [47,48] but further investigations were not performed in this direction to fully identify this origin. Yet, it is finally interesting to note that differences in the photoluminescence polarisation were however observed between citrate and thiol capped metallic particles clearly pointing towards a major role played by the capping agent [45].

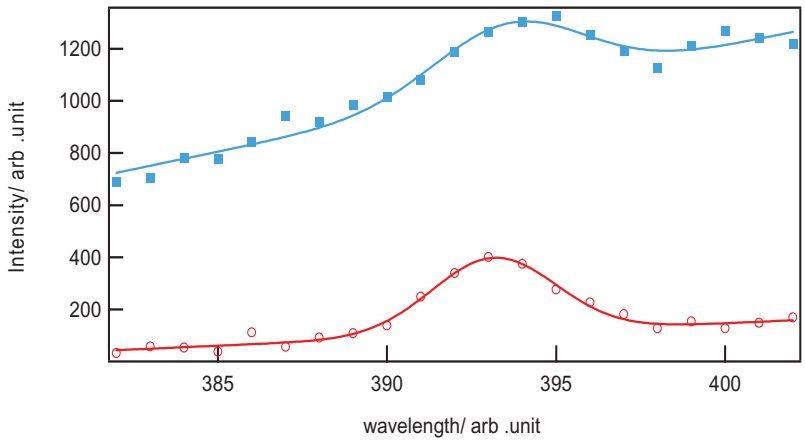

Figure 2.11: HRS Intensity versus wavelength for (circles) a pure hexane solution and (squares) a 0.3×10^{-9} mol/L concentration of spherical AgC12 nanoparticles. The solid line is a fit with equation (2.38).

The polarisation resolved plots of the HRS intensity recorded at 392 nm were then corrected for the luminescence observed at 402 nm using the luminescence wavelength dependence observed on Figure 2.11. Figure 2.12 shows the corrected polar plots for the 0.3×10^{-9} mol/L concentration.

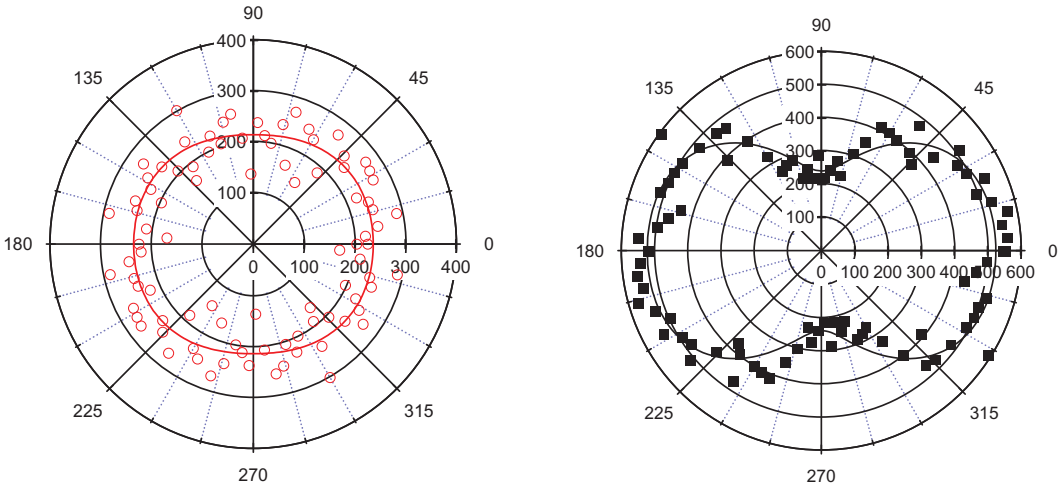

Figure 2.12 : Corrected polar plots of the HRS intensity as a function of the incoming fundamental beam polarisation angle: (left, circles) Horizontal (along Z) and (right, square) Vertical (along X) polarisation plots for a 0.3×10^{-9} mol/L concentration of D~10 nm AgC12 spherical nanoparticles and (solid) fit to equation (2.20)

As expected from the theoretical point of view given above, the H polarized HRS intensity is constant as a function of the polarisation angle of the fundamental beam. This behaviour was observed for all H polarized polar plots recorded for metallic spherical particles in this work and therefore will not be discussed nor plotted any more. However, for the *V* polarized plots, changes were observed and quantified through an adjustment procedure yielding the a^V, b^V and c^V parameters using equation (2.20). The adjustment procedure led to a parameter ζ^V with a value varying from 0.11 up to 0.19 depending on concentration, see Table 2.1. Such an increase of the parameter ζ^V is not expected for ideally dispersed solutions of particles. Hence, it is suspected that aggregation is taking place with possible effect on the hyperpolarizabilities. Despite this aggregation phenomenon, the HRS response from the particles remains dominantly dipolar, as expected for silver nanoparticles with such a small diameter. The ζ^V parameter value is however twice as large as that obtained for the 20 nm diameter citrate capped silver nanoparticles, the value of which is only 0.06. It is therefore impossible to asses the role of the capping layer on the ζ^V parameter. Its larger value as compared to that obtained for the citrate capped particles may arise from aggregation.

AgC12 spheres	0.84×10^{14} *p/l*	1.01×10^{14} *p/l*	2.019×10^{14} *p/l*
ζ^V	0.11	0.13	0.19

Table 2.1 : ζ^V parameter for different concentration of the dodecanethiol capped silver nanoparticles with a diameter of 10 nm.

2.4.2.2. Dodecanethiol gold nanoparticles

Before investigating the role of the alkyl chain of the capping layer, discussed in the next paragraph, we first studied the role of the metal instead, and subsequently the role of the bond strength. Indeed, gold nanoparticles have been extensively used in chemistry and the sulfur-gold bond is believed to be very strong [49]. Besides, because the experiments can only be performed at a fixed fundamental wavelength, the resonance conditions were also changed because the SPR will be now away from the harmonic wavelength. In the literature, previous studies of alkanethiol adsorption onto Au(111) surfaces have shown that at relatively dilute thiols concentrations, about 10^{-3} M, two distinct adsorption kinetics can be observed : a first one, rather fast corresponding to the diffusion controlled Langmuir adsorption depending on

the thiols concentration and a second step corresponding to a surface crystallization process where the alkyl chains get out of the disordered state towards forming a two dimensional crystal. The kinetics of the first step is governed in particular by the surface-head group reaction and its activation energy depends possibly on the density of the adsorbing sulfurs. On the other hand, the kinetics of the second step is related to the chain disorder, e.g. gauche defects, the different components of the chain-chain interactions (Van der Waals, dipole-dipole, etc…) and the surface mobility of the chains [50].

The average diameter of the nanoparticles used in this study was about 18 nm allowing a direct comparison with the citrate capped gold nanoparticles of similar diameter [32]. The UV visible absorption spectrum is given in Figure 2.13. The SPR for these particles is observed at 546 nm. The SPR width is rather large, indicating the probable aggregation of the particles besides the inhomogeneous broadening due to the size and shape distributions.

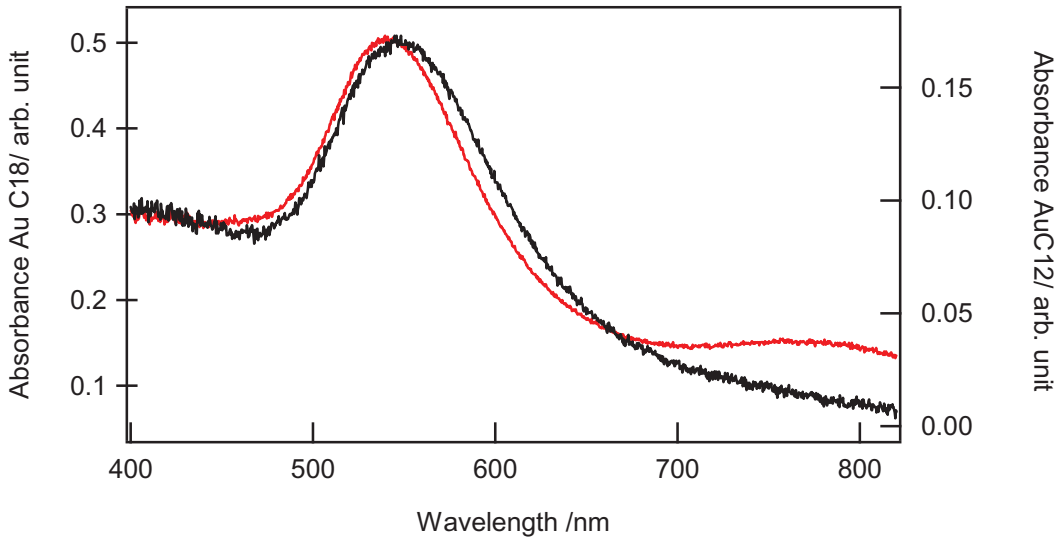

Figure 2.13 : UV-visible absorption spectra for dodecanethiol (black) and octadecanethiol (red) capped gold spherical nanoparticles of 2.3×10^{-10} mol/L concentration and 8.8×10^{-10} mol/L concentration respectively.

Figure 2.13 also gives the UV-visible absorption spectrum for the octadecanethiol nanoparticles. The latter one presents a shoulder starting at 700 nm as compared to the dodecanethiol nanoparticles. This indicates the presence of aggregation even upon passivating the particle with such long chain length. It is therefore clear that aggregation is heavily dependent on the capping layer of the particles. The HRS Intensity recorded for these dodecanethiol capped nanoparticles normalized to the HRS intensity of pure chloroform as a function of the nanoparticles concentration is shown in Figure 2.14. No UV-visible

absorbance was necessary at the concentrations used at both the fundamental and the harmonic wavelengths. The concentrations used in the HRS intensity measurements were indeed much less than that used for the UV-visible spectra presented in Figure 2.13. In the inset of Figure 2.14, the first 6 points are reported in an enlarged part to underline the small increase and the saturation of the HRS intensity versus concentration. Lower concentrations could not be tested for lack of sensitivity. The observed behaviour here is very similar to that observed for the dodecanethiol capped silver nanoparticles at higher concentrations. However, for the silver particles, linear slopes were recorded at lower concentrations whereas for the gold one, sensitivity prevented us from diluting further the particles solutions. Luminescence intensity was still observed though and a linear behaviour versus concentration was recorded, see Figure 2.15. However, luminescence depends on the number of particles whereas the HRS intensity dependence with the number of particles can be more complicated in the presence of aggregation owing to possible coherent contribution within the aggregates. Hence, no hyperpolarisability were obtained for these particles.

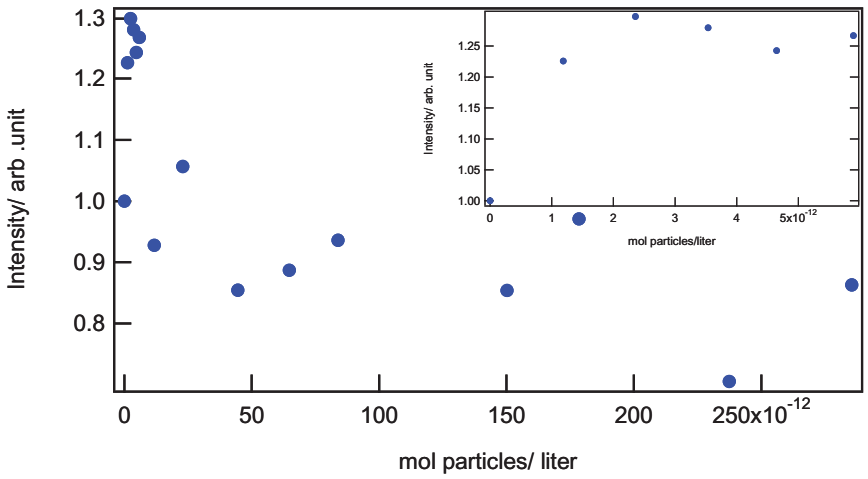

Figure 2.14 : The HRS intensity of the spherical AuC12 nanoparticles as a function of the nanoparticles concentration. (Inset) Close up view of the first points of the main graph.

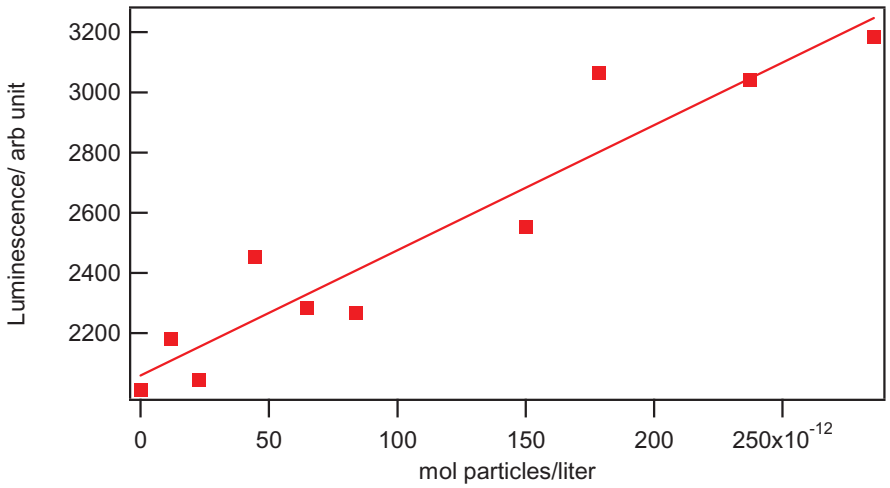

Figure 2.15 : Luminescence at the harmonic wavelength versus concentration of spherical AuC12 nanoparticles.

Considering the linear behaviour of the luminescence plot with the nanoparticles concentration, it therefore appears that HRS is a sensitive method to study aggregation. The polar plots of the HRS intensity as a function of the fundamental angle of polarization were however recorded, despite the presence of aggregation. Figure 2.16 shows the vertically polarized HRS intensity polar plots for a concentration of 1.48×10^{-10} mol/L. The plot was corrected for the luminescence polarization curve. The measured value of the ζ^V parameter was found to be $\zeta^V = 0.104$. This value is of the same order of magnitude as that reported for the corresponding silver particles although aggregation this time is clearly present. The corresponding value of the ζ^V parameter for citrate capped gold nanoparticles with a diameter of about 20 nm has been found in the past to be 0.06 [33]. Hence, for these dodecanethiol capped gold particles, the larger value found for the ζ^V parameter may not arise from intrinsic effects due to the capping layer but rather, from aggregation. The larger effective size of a small aggregate as compared to that of a single particle therefore favours the quadrupolar response.

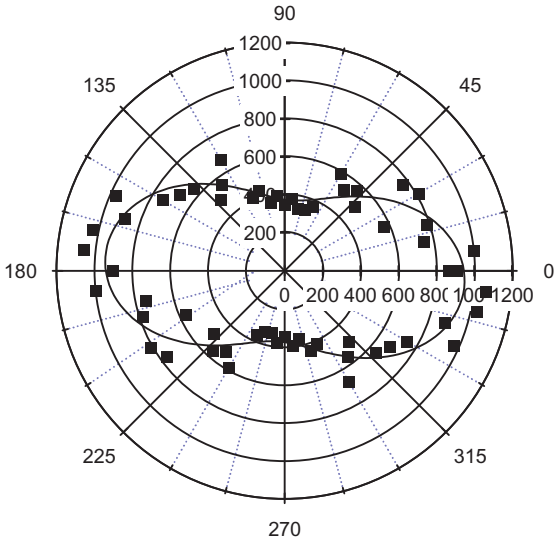

Figure 2.16 : Polar Plot of the HRS intensity as a function of the incoming fundamental beam polarisation angle: Vertical (along X) polarisation for a 1.5×10^{-10} mol. particles/L concentration of dodecanethiol capped nanoparticles of about 18 nm in diameter and (solid) fit to the experimental data using equation (2.20)

2.4.2.3. Octadecanethiol gold nanoparticles

The role of the capping layer was next investigated by changing the length of the alkyl chain. Elongation of the alkanethiol chain was thus obtained by replacing the dodecanethiol (AuC12) chain by the longer octadecanethiol (AuC18) one. However, the gold core was left unchanged. As seen on Figure 2.13, the SPR resonance observed on the UV-visible absorption spectrum was slightly shifted towards the blue side. This difference in the peak position is surprising since an increase of the surrounding dielectric constant usually induces a red shift of the SPR band. It is indeed expected that the longer alkyl chains lead to a thicker shell of organic material around the particle. This observed SPR shift position is therefore possibly due to more refined changes within the layer. For instance, disorder could yield a layer with a lower dielectric constant as opposed to a dense compact layer. Such a long chain is though important for the subsequent studies where preventing interactions between nanoparticles will be critical in the properties of the films [51]. The HRS intensity normalized to the HRS intensity of pure chloroform is then reported versus concentration in Figure 2.17. This time, the expected linear behaviour of the HRS intensity versus concentration is indeed present. Using the hyperpolarisability value of pure chloroform $\beta_{CHCl_3} = 0.26\times10^{-30} esu$ [43], the

hyperpolarisability value was measured to be $\beta_{AuC18-18nm} = (3.37 \pm 0.08) \times 10^{-26} esu$. Again, the HRS signal was corrected for luminescence by subtracting the background luminescence. The luminescence given in Figure 2.18 shows the linear behaviour expected versus concentration. The hyperpolarizability value of these octadecanethiol capped gold nanoparticles is also much smaller than that of a citrate capped gold nanoparticles with a diameter of about 20 nm [7] which is 2.7×10^{-25} *esu*. Similar conclusions on the role of the capping layer can therefore be drawn, the sulfur-gold bond decreasing by a factor of about 10 the nonlinearity. Note that here no correction for the size were performed since the diameters are similar, 18 nm for the octadecanethiols capped particles and 20 nm for the citrate capped ones. Polarisation-resolved HRS intensity plots were also performed. The vertically polarized HRS intensity polar plot is shown in Figure 2.19. The experimental data were fitted using equation (2.20) and the parameters a^V, b^V and c^V were determined. The parameter ζ^V was also evaluated. A value of $\zeta^V = 0.065$ is found. This value of the parameter ζ^V is very similar to the values obtained for citrate capped particles and smaller by a factor of about two as compared to the previous thiols capped particles. The HRS response is therefore dominantly dipolar. Although defects in the capping layer could reinforce the breaking of the spherical symmetry, retardation effects are known to be present at smaller diameters for silver particles as compared to gold ones.

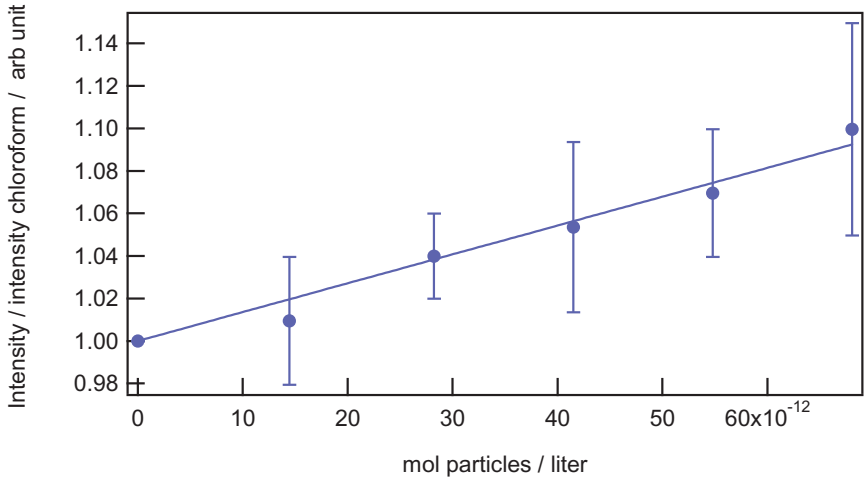

Figure 2.17 : HRS intensity of the spherical AuC18 nanoparticles normalized to pure chloroform HRS intensity as a function of the nanoparticles concentration fitted with equation (2.43).

This is due to the fact that retardation scales as a function of the product a/λ where a is the radius of the particle and λ is the wavelength in the particle medium [33]. We therefore conclude that the thiolated capping layer has a destructive effect on the hyperpolarizability value β in all cases, irrespective of the metal, gold or silver. In this respect, the sulfur-gold and sulfur-silver bonds are very similar.

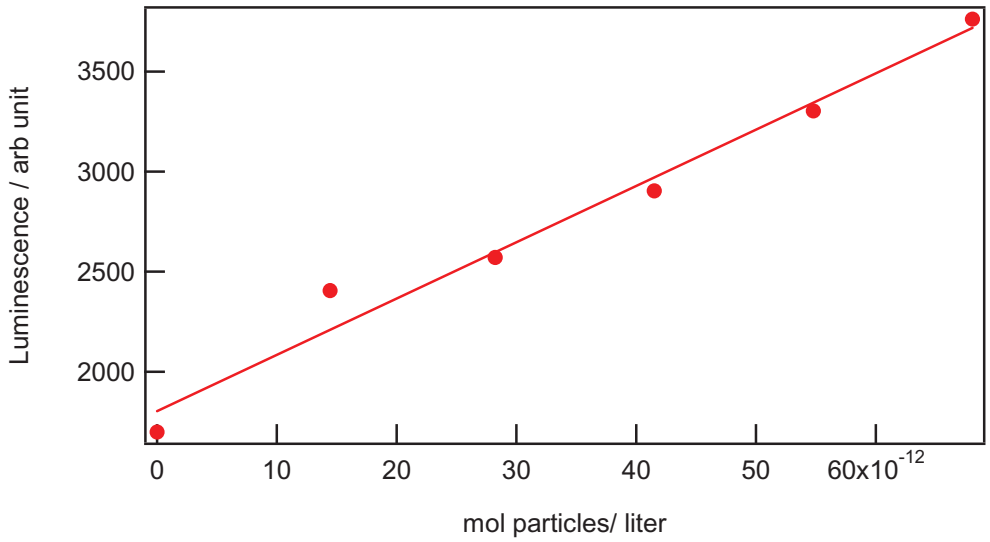

Figure 2.18 : Luminescence at the harmonic wavelength versus concentration of spherical AuC18 nanoparticles and line fit.

Finally, for the octadecanethiols capped gold particles, no sign of aggregation was noticed. This indicates that the long alkylthiol chains surrounding the nanoparticles prevent aggregation and probably interactions too.

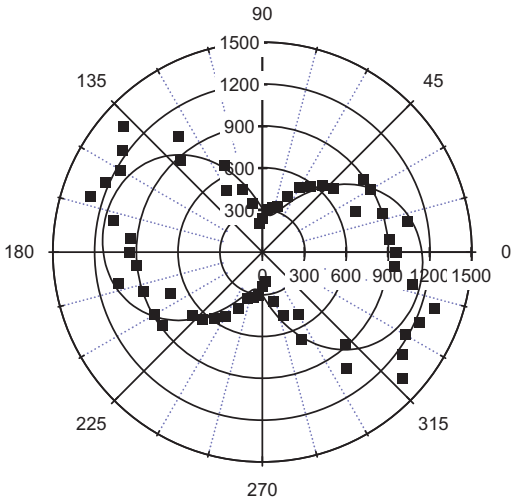

Figure 2.19 : V polarisation experimental points for 5.43×10^{-11}mol. particles/L concentration of D~18 nm octadecanethiol nanoparticles and (solid) fit to the experimental data points using equation (2.20)

2.4.2.1. Conclusions for alkylthiols capped nanoparticles

Comparison of the different hyperpolarizabilities measured must be corrected first for the different sizes and then for the resonance conditions if one compares gold and silver particles. Regarding the size correction, we have introduced the correction with respect to the surface area. In the case of very small particles, the dipolar contribution dominates and the ζ^V parameter is small. Table 2.2 presents a summary of the data for the particles studied: diameter, SPR wavelength, hyperpolarizability and ζ^V parameter. A direct comparison between gold and silver particles is though difficult since corrections for the field factors should be made in order to take into account the field enhancements.

In all cases though, the hyperpolarizability of the alkylthiol capped particles is much smaller that that of the citrate capped particles [33]. In the literature, theoretical studies comparing bare and thiol passivated Au_{38} gold nanocrystals using density functional calculations have shown that the passivation layer on the gold crystallite yielded a new compound, namely $Au_{38}(SCH_3)_{24}$, and was accompanied by a charge transfer from the outermost gold atoms to the surrounding adsorbed sulfur atoms. The integrated charge deficit of the gold core was found to be about 2*e*. Figure 2.20 shows two optimized structures of the bare and the

passivated cluster. In Figure 2.20, the sulfur atoms are presented as darker spheres and only one CH_3 group is shown. This figure clearly presents the modifications of the nanoparticle surface once passivated [52]. Another study has similarly shown that in the thiols capped particle, a strong metal-capping molecule interaction changes the local environment of the gold atoms and a charge transfer takes place, compensating for the lattice contractions [53]. This contraction effect has been studied in details [54] and arises from the Au-S bond. This charge transfer appears to reduce the hyperpolarizability of the particles. Regarding the values taken by the ζ^V parameter, it is observed that the quadrupolar contribution never dominates in the size range investigated, in line with previously reported data. This parameter ζ^V is also an interesting tool to investigate the appearance of aggregates in the sample solutions when other means like luminescence and even HRS dilution experiments are unable to clearly evidence the phenomenon.

Nanoparticles	Dimension	λmax	*β*/esu	ζ^V
AgC12	D=10nm	410	$2.99\pm0.23\times10^{-26}$	0.11
AgCitrate[33]	D=20nm	390	4×10^{-25}	0.06
AuC12sphere	D=18nm	546		0.10
AuC18sphere	D=18nm	543	$3.37\pm0.07\times10^{-26}$	0.065
Au citrate[33]	D=20nm	520	2.7×10^{-25}	0.06

Table 2.2: Nanoparticles data summary: diameter, SPR wavelength, hyperpolarisability and ζ^V parameter.

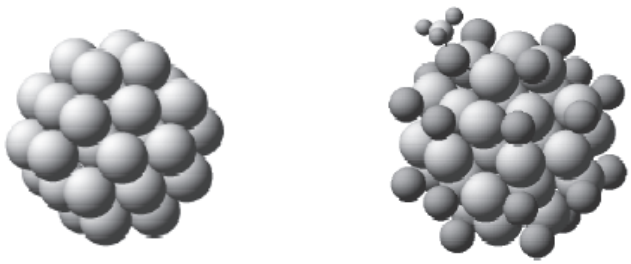

Figure 2.20 : Optimized structures of bare and thiol passivated gold cluster. The sulfur atoms are presented as darker spheres and only one CH_3 group is shown

2.4.3. Nanorods

Gold or silver metallic nanorods exhibit two surface plasmon resonances associated with their long and short axes. They yield therefore more complex absorption spectra. For gold nanorods, the first SPR associated with the excitation of the conduction band along the short axis is located around 520 nm in aqueous solutions whereas the second SPR associated with the excitation along the long axis is shifted towards the red side, away from 520 nm, of the spectrum. By increasing the aspect ratio of the nanorods, namely the ratio between the long and the short axes, the SPR wavelength is shifted to longer wavelengths and the absorption maximum increases. This aspect ratio can be controlled during the synthesis methods [55]. Furthermore, the longitudinal SPR mode of these nanorods is extremely sensitive to changes in the surrounding medium and its dielectric properties in particular. It is therefore expected that changes in the capping layer will lead to large changes in the optical properties of these nanorods. Few studies have been performed on nanorods using SHG to date [23 , 47] and no study of the influence of this capping layer on the hyperpolarizability of the nanorods has been performed yet. Hence, gold nanorods were synthesised in our laboratory and different capping layers were introduced in order to investigate the effect of this layer of surfactants on the quadratic hyperpolarisability. Following the synthesis method proposed in the literature [56], nanorods with dimensions of 64 nm × 24× 24 nm were obtained and dispersed in an aqueous solution with a cetyltrimethylammonium bromide (CTAB) capping layer. Phase transfer into chloroform of these nanorods was subsequently achieved to get either dodecanethiol or octadecanethiol capped nanorods. This principle of operation ensures in particular that the metallic nanorod core is identical for the different capping layers.

2.4.3.1. CTAB capped gold nanorods

Considering the principle of operation, we first discuss the case of the CTAB capped gold nanorods. The details of the synthesis method have been presented in chapter 1. The UV visible absorption spectrum is given in Figure 2.21.

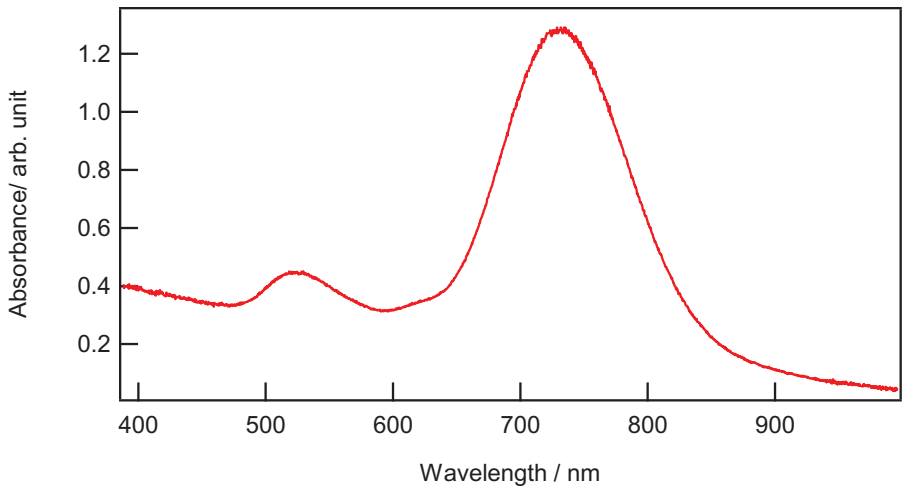

Figure 2.21: UV-visible absorption spectrum of an aqueous solution of 64×24× 24 nm gold nanorods stabilised with CTAB at a concentration of 8.3×10^{-11}mol/L.

The two SPR for these nanorods are located at 530 nm and 730 nm. The width of the resonance is expected to be inhomogeneous, arising from the broad size and shape distributions. From the TEM images, the average size of the nanorods is found to be indeed 64(±12)×24(±6)×24(±6) nm dimension. The HRS intensity measurements as a function of the concentration of the nanorods are shown in Figure 2.22.

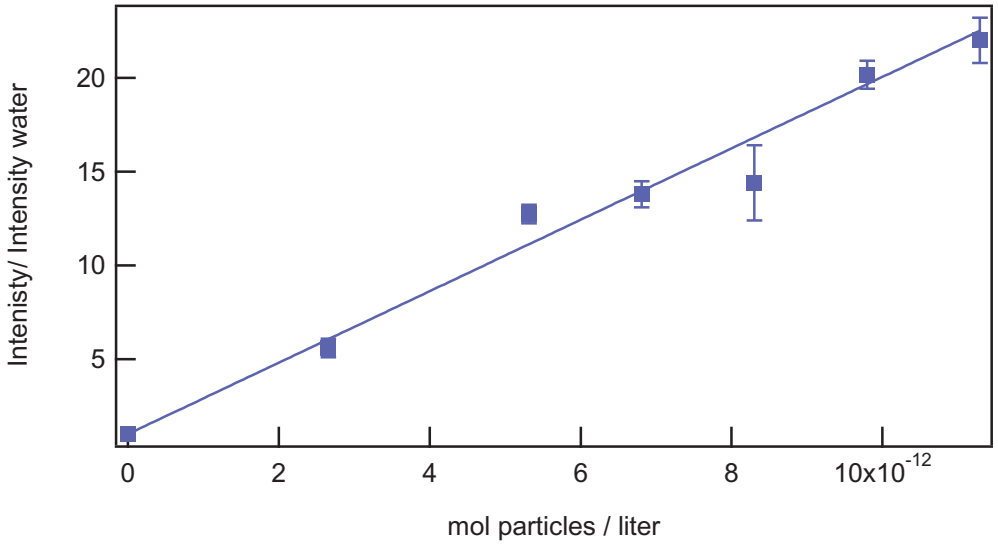

Figure 2.22: HRS intensity of 64×24×24nm gold nanorods with CTAB normalised to chloroform HRS intensity as a function of the nanorods concentration.

All HRS intensities have been normalized to the pure solvent intensity. Again, each point reported on Figure 2.22 entails the measurement of the HRS signal in a small domain of wavelengths around the HRS wavelength to subtract the luminescence. This luminescence is linear with the nanorods concentration as expected. The HRS intensities were also corrected for the absorbance of the solution at the fundamental and the harmonic frequencies using the absorbance determined from UV-Visible absorption measurement, according to equation (2.17). From the slope of the line fit, we measured a quadratic hyperpolarizability β for these CTAB capped nanorods using the hyperpolarizability of water $\beta_w = 0.56 \times 10^{-30} esu$ as the reference. The hyperpolarizability value for the nanorods was found to be $\beta_{AuCTAB-64\times24nm} = (5.67 \pm 0.09) \times 10^{-24} esu$, probably one of the largest hyperpolarizability reported so far. This hyperpolarizability value is also greater by a factor of about 15 times than that of the dodecanethiol capped silver spherical nanoparticles and octadecanethiol capped gold spherical nanoparticles, although the latters are smaller in terms of their volumes. The large hyperpolarizabilities reported here can though be explained by the partially resonant character of the HRS intensity owing to the proximity of the longitudinal SPR with the fundamental wavelength and the interband transitions with the harmonic wavelength. To complement these results, polarisation curves of the harmonic light were obtained, see Figure 2.23. These polarisation curves were adjusted with equation (2.20) after subtracting the luminescence to deduce the parameters a^V, b^V and c^V and thus the parameter ζ^V . In the present case, the luminescence was polarized. Similarly to the case of the spherical particles, the luminescence is expected to arise from electron-hole pair radiative combination but the capping layer may play an important role as a trapping region. The horizontally polarised HRS intensity plot for these nanorods also exhibited a circle, similarly to the case of the spheres. The parameter ζ^V was found to be 0.028. This value shows that the dipole contribution dominates over the quadrupolar one despite the size of the rods.

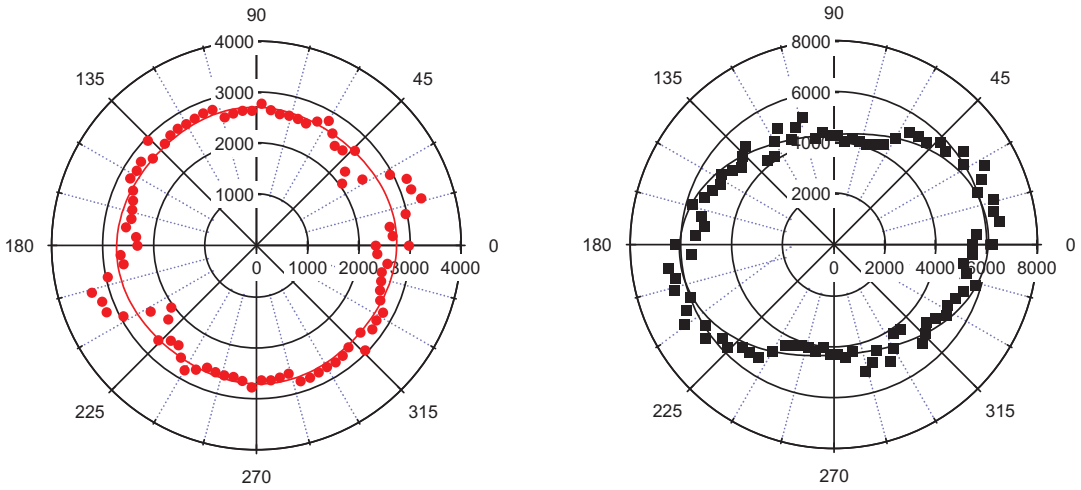

Figure 2.23: Horizontally and vertically polarized HRS intensity plots (circles and squares respectively) for a 6.81×10^{-10} mol/L concentration of 64×24×24nm CTAB capped nanorods and (solid) fit to the experimental data using equation (2.20).

2.4.3.2. Gold nanorods capped with dodecanethiol

The CTAB capped nanorods where then transferred into an organic phase to substitute the CTAB capping layer by an alkanethiol capping layer. Since the only change is the capping layer, we ensure that the gold core remain unmodified. We first investigate dodecanethiol capped gold nanorods dispersed in chloroform. The UV-visible absorption spectrum for both the dodecanethiol and the CTAB capped nanorods is given in Figure 2.24. The two SPR for the dodecanethiol capped nanorods are located at 544 nm and 765 nm, at wavelengths slightly red shifted as compared to the CTAB capped rods. This may be attributed to a change towards a more compact capping layer although the surface bond may well play a non negligible role in this change. In addition, the spectrum recorded for the dodecanethiol capped nanorods exhibits much broader SPR resonance. This feature may arise from aggregation, similarly to the case of the spherical particles.

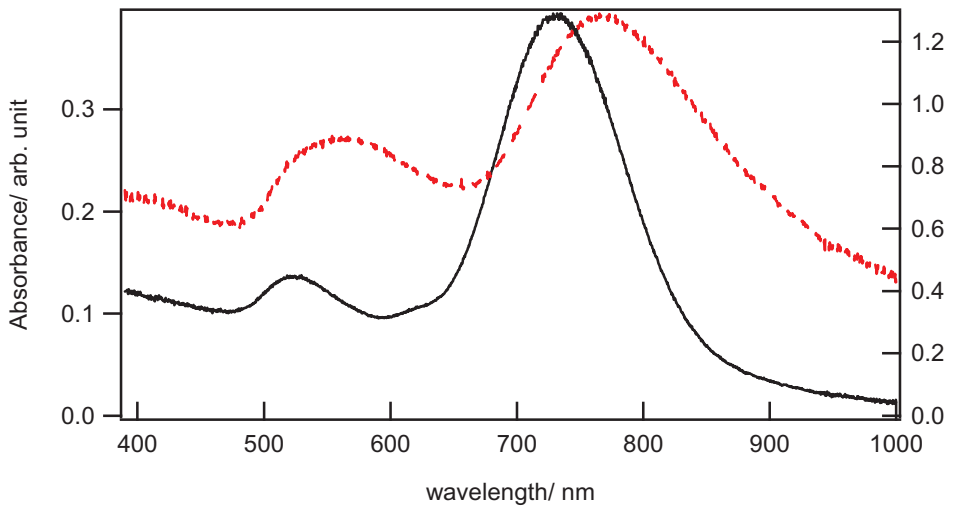

Figure 2.24 : UV-visible absorption spectrum of 64×24×24nm dodecanethiol capped gold (dotted line) nanorods for a concentration of 5×10^{-11}mol/L and CTAB (black line) capped gold nanorods for a concentration of 8.3×10^{-11}mol/L.

The HRS Intensity for these nanorods is shown in Figure 2.25 as a function of the nanoparticles concentration. The HRS intensity was corrected for the absorption at the harmonic and fundamental wavelengths using the UV-visible absorption spectrum and equation (2.17). The experimental data were fitted using equation (2.43). The slope of the line fit gave the hyperpolarisability β of these dodecanethiol capped nanorods using as reference the chloroform hyperpolarisability $\beta_{CHCl_3} = 0.26\times10^{-30}\,esu$ [43]. The hyperpolarisability β value was measured to be $\beta_{AuC12-64\times24nm} = (2.73\pm0.08)\times10^{-25}\,esu$, a value clearly weaker than that reported for the CTAB capped nanorods.

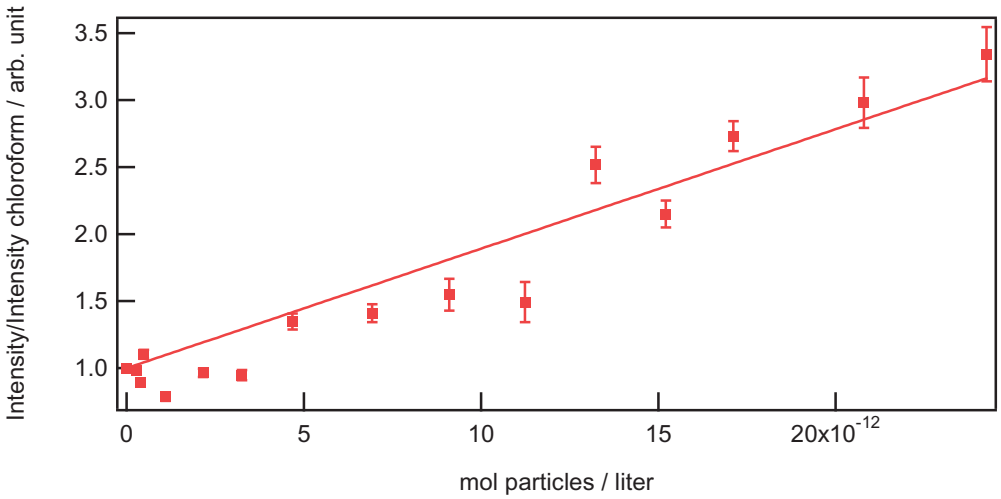

Figure 2.25 : HRS intensity of 64×24×24nm dodecanethiol capped gold nanorods normalized to chloroform as a function of the nanorods concentration.

The polarisation resolved study of the HRS intensity was also performed, see Figure 2.27, before which polarisation at 402 nm were performed to subtract the luminescence (Fig 2.26). As expected, the horizontally polarized plot is a circle in agreement with the electric dipole model given above.

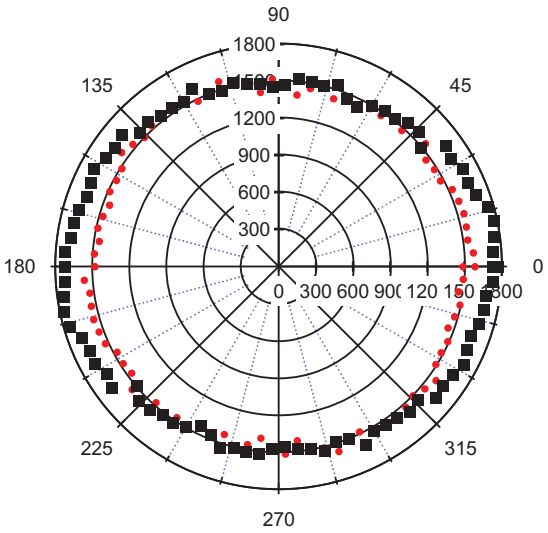

Figure 2.26: H (circles) and V (cubes) polarisation plot for the luminescence of dodecanethiol 64×24×24nm nanorods at 402 nm.

The vertically polarized HRS intensity is however not a circle, see Figure 2.27, and the three parameters a^V, b^V and c^V can be extracted. A value of 0.3 is obtained for the ζ^V parameter for the concentration of 9.63×10^{-12} mol/L whereas a value of 0.56 is found for the concentration of 1.94×10^{-11} mol/L. This rather large value for the ζ^V parameter indicates a similar weight of the dipolar and quadrupolar contributions. A much smaller value was obtained for the CTAB capped nanorods. It is however difficult to conclude unambiguously because the capping layer may well play a non negligible role in passivating the nanorods surface from defects. These defects, either morphological or electronic defects like surface or trapping states, can indeed favour a dipolar response through a non homogeneous distribution over the rods surface. It is though interesting to note that Figure 2.25 exhibits a rather disturbed linear plot indicating that aggregation may also play a non negligible role, similarly to the case of alkanethiols capped spherical particles.

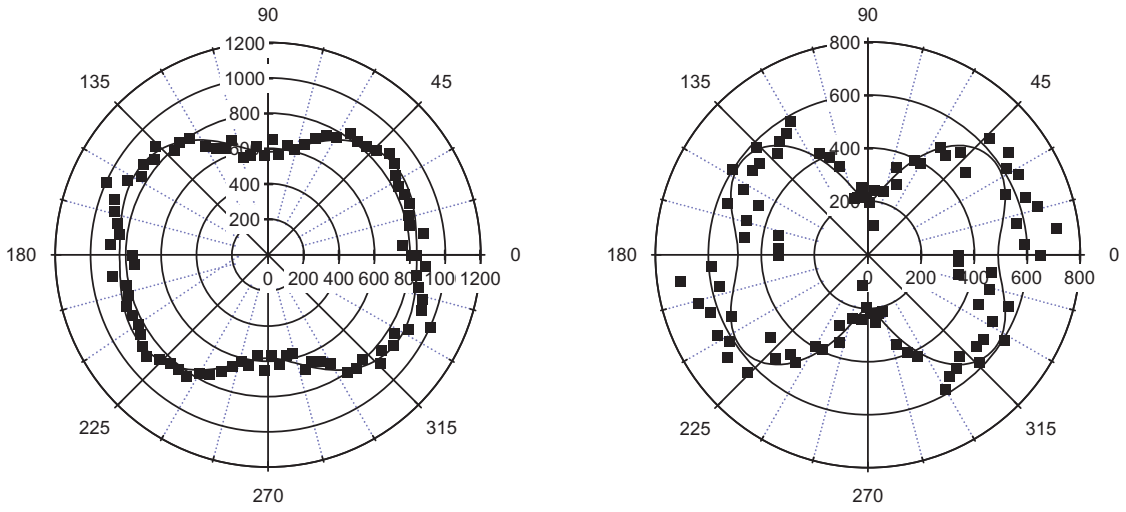

(a) (b)

Figure 2.27 : Polar Plot of the HRS intensity as a function of the incoming fundamental beam polarisation angle: (a) Vertical (along X) polarisation for 9.63×10^{-12} mol/L concentration (b) Vertical (along X) polarisation for 1.94×10^{-11} mol/L of 64×24×24nm dodecanethiol capped gold nanorods and (solid) fit to the experimental data using equation (2.20)

In order to minimize the aggregation, alkanethiols with longer alkyl chains were used to cap the nanorods.

2.4.3.3. Gold nanorods capped with octadecanethiol

The UV-visible absorption spectrum of octadecanethiols capped gold nanorods is given in Figure 2.28.

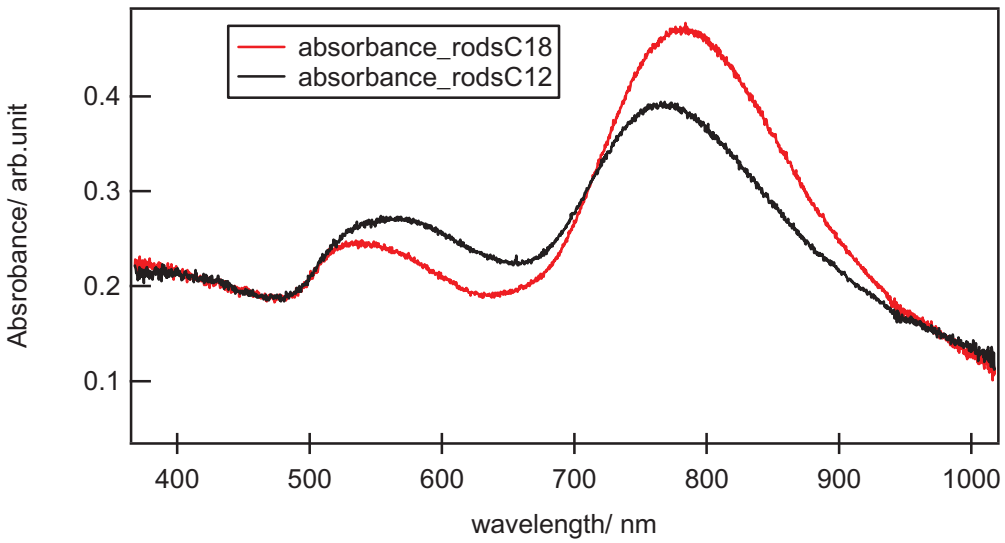

Figure 2.28 : The UV-visible absorption spectrum for 64×24×24nm dodecanethiol capped gold nanorods of concentration 5×10^{-11}mol/L and 5.5×10^{-11} mol/L concentration for the octadecanethiol capped gold nanorods.

The two SPR are located at 540 nm and 784 nm respectively. The changes in terms of wavelength shifts between the different SPR of the dodecanethiol capped and octadecanethiol capped nanorods are minimal. Furthermore, the intensity of the long wavelength SPR is increased whereas the intensity of the short wavelength one is decreased. In principle, no changes in the aspect ratio of the rods should occur during the phase transfer process. However, the spectra may indicate a slight decrease of the aspect ratio for the dodecanethiol capped rods. Besides, the long wavelength SPR appears more symmetrical and this may indicate that aggregation is less present in the case of the octadecanethiol capped nanorods. The HRS intensity after correction for absorption at both wavelengths was then plotted as a function of the nanorods concentration and a value of $\beta_{AuC18-64\times24nm} = (2.78 \pm 0.05)\times10^{-25}\,esu$ was found for the hyperpolarisability. This value is identical to that obtained for the dodecanethiol capped rods. This result clearly indicates that the change in the alkyl chain length does not affect the HRS response of the rods. The change seems too minimal to be noticed. The polarisation curves are given in Figure 2.30 and a value of 0.13 is found for the ζ^{V} parameter. This value shows that the dipolar contribution now dominates over the quadrupolar one. If the changes between the alkyl chain length is minimal as seen for the hyperpolarizability value and that all other morphological parameters are identical, in particular the sulfur-gold bond and the gold nanorod core size, then this value may indicate that aggregation is indeed limited with the longer alkyl chains. Nevertheless, the

hyperpolarizabilities measured for alkylthiols capped gold nanorods remain about 20 times smaller than that obtained for the CTAB capped gold nanorods.

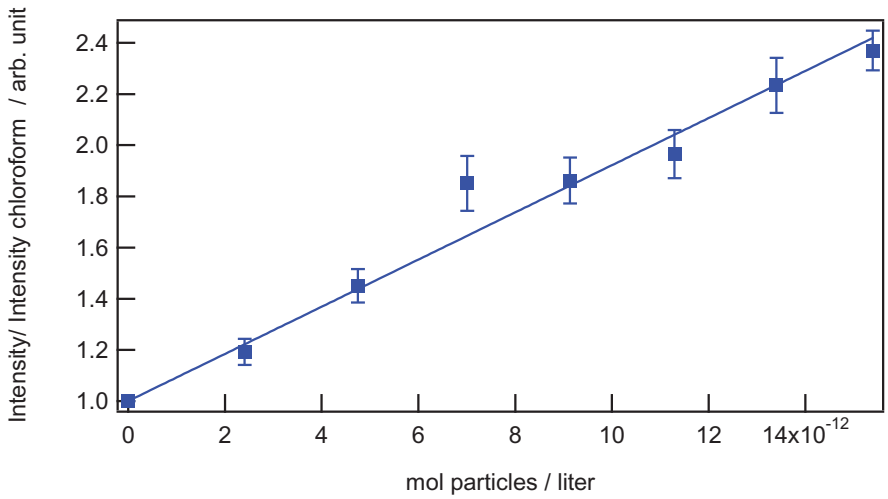

Figure 2.29: Normalised HRS intensity of 64×24×24nm octadecanethiol capped gold nanorods as a function of the nanorods concentration.

We finally add that the linear plot observed on Figure 2.29 is clearly more regular than the one previously found for the dodecanethiol capped nanorods. This is further supporting the decrease of aggregation as the alkyl chain is lengthened.

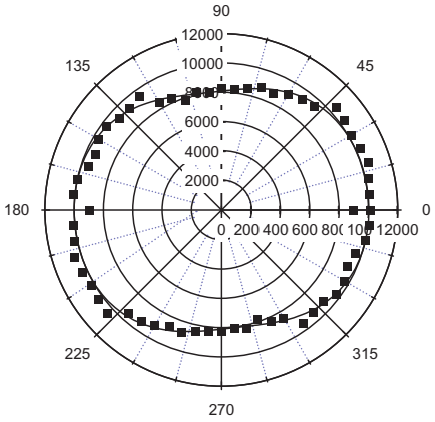

Figure 2.30: Vertically polarized HRS intensity plot (squares) for a 1.58×10^{-11} mol/L concentration of 64×24×24nm octadecanethiol capped gold nanorods and (solid) fit to the experimental data using equation (2.20)

2.4.3.4. Comparison for gold nanorods

Contrary to what is expected for regular nanorods which possess a centrosymmetric shape in the absence of defects, namely a quadrupolar response with clear four lobes, the observed patterns of the polarisation resolved HRS intensity plots are dominated by the dipolar contribution with two lobes only. A quantitative view is given by the ζ^V parameter which indicates that for CTAB and octadecanethiol capped rods the dipolar response clearly dominates whereas for the dodecanethiol capped rods the dipolar and the quadrupolar contributions have similar weights. The identification of a single origin for this difference is not possible. Indeed, between CTAB and alkylthiol capped rods, the surface layer where the chemical bond between gold metal and the adsorbate occurs is not the same. In view of the results obtained for the spherical particles though, these results tend to support the point of a strong aggregation for the dodecanethiol capped rods.

Considering the hyperpolarizability values, it appears again, similarly to the spherical particles; that the presence of the sulfur-gold bond tends to dramatically decrease the hyperpolarizability. The strong value observed for the CTAB capped nanorods can be compared to that obtained for spherical particles. However, one has to take into account the shape of the particles. Considering the much smaller value of the hyperpolarizability obtained for the citrate coated spheres, both a volume and a surface corrections are unable to account for the large discrepancy. It is therefore strongly suggested that the CTAB capping layer favors large hyperpolarizabilities. It is however difficult to state if this is a chemical origin due to the surface bonding or if the CTAB layer induces a strong breaking of the centrosymmetry of the shape of the particle that would in turn yield a strongly allowed pure dipole response of large amplitude. On the opposite, all the results produced here tend to indicate that the sulfur-gold bond decreases the hyperpolarizability. For the same reasons, it is difficult to state if the origin is of chemical nature or if this is a passivation of the defects.

Nanoparticles	Dimension	λmax	β/esu	$\beta_{atom}/10^{-30}$esu	ζ^V
Au sphere citrate [33]	D=20nm	520	2.7×10^{-25}	1.14	0.06
AuRodsCTAB	64×24×24nm	530,730	$5.67\pm0.09\times10^{-24}$	1.21	0.028
AuRodsC12	64×24×24nm	544,765	$2.73\pm0.08\times10^{-25}$	0.058	*0.56*
AuRodsC18	64×24×24nm	540,784	$2.78\pm0.05\times10^{-25}$	0.059	*0.13*

Table 2. 3 : Diameter, SPR wavelength, hyperpolarisability and ζ^V parameter for the gold nanorods and a citrate capped gold sphere for comparison.

2.5. Conclusions

HRS has been used to characterize the nonlinear optical response of second order of the samples prepared. Besides the hyperpolarisability values, the ζ^V parameter has also been determined through polarisation resolved HRS measurements. From these results, we have been able to compare the role of the capping layer in the enhancement or quenching of the hyperpolarizabilities. It appears that CTAB capping layer seems to enhance the hyperpolarizability whereas alkylthiol capping layers on the opposite tend to quench the response. Furthermore, it appears that the length of the alkyl chain does not provide any effect on the hyperpolarizability. However, the role of the alkyl chain appears critical in preventing aggregation. Indeed, it clearly appears that short alkyl chains are not able to prevent aggregation, although the aggregation seems rather weak anyhow as seen from the linearity of the HRS dilution plots. On the opposite, the longer octadecanethiol capping layers are suitable to prevent aggregation.

References:

[1] A. E. H. P. A. Franken, C. W. Peters, and G. Weinreich, "Generation of Optical Harmonics," *Phys. Rev. Lett.,* vol. 7, p. 118, 1961.

[2] F. Brown, R. E. Parks, and A. M. Sleeper, "Nonlinear Optical Reflection from a Metallic Boundary," *Phys. Rev. Lett.,* vol. 14, p. 1029, 1965.

[3] K. Clays and A. Persoons, "Hyper-Rayleigh scattering in solution," *Phys. Rev. Lett.,* vol. 66, pp. 2980-2980, 1991.

[4] K. Clays and A. Persoons, "Hyper-Rayleigh scattering in solution," *Rev. Scien. Instrum.,* vol. 63, pp. 3285-3289, 1992.

[5] U. Kreibig and M. Vollmer, "Optical properties of metal clusters, Vol. 25," *Springer (Springer, Berlin),* 1993.

[6] R. C. Johnson, J. Li, J. T. Hupp, and G. C. Schatz, "Hyper-Rayleigh scattering studies of silver, copper, and platinum nanoparticle suspensions," *Chem. Phys. Lett.,* vol. 356, pp. 534-540, 2002.

[7] J. Nappa, G. Revillod, I. Russier-Antoine, E. Benichou, C. Jonin, and P. F. Brevet, "Electric dipole origin of the second harmonic generation of small metallic particles," *Phys. Rev. B,* vol. 71, pp. 165407-165407, 2005.

[8] I. Russier-Antoine, G. Bachelier, V. Sabloniere, J. Duboisset, E. Benichou, C. Jonin, F. Bertorelle, and P.-F. Brevet, "Surface heterogeneity in Au-Ag nanoparticles probed by hyper-Rayleigh scattering," *Phys. Rev. B,* vol. 78, pp. 035436-8, 2008.

[9] C. F. Bohren and D. R. Huffman, *Absorption and scattering of light by small particles*, 1983.Wiley Science,1998.

[10] T. Ung, L. M. Liz-Marzan, and P. Mulvaney, "Optical Properties of Thin Films of Au@SiO2 Particles," *J. Phys. Chem. B,* vol. 105, pp. 3441-3452, 2001.

[11] C. P. Collier, R. J. Saykally, J. J. Shiang, S. E. Henrichs, and J. R. Heath, "Reversible Tuning of Silver Quantum Dot Monolayers Through the Metal-Insulator Transition," *Science,* vol. 277, pp. 1978-1981, 1997.

[12] G. n. Schmid and L. F. Chi, "Metal Clusters and Colloids," *Advan. Mater.,* vol. 10, pp. 515-526, 1998.

[13] R. Elghanian, J. J. Storhoff, R. C. Mucic, R. L. Letsinger, and C. A. Mirkin, "Selective Colorimetric Detection of Polynucleotides Based on the Distance-Dependent Optical Properties of Gold Nanoparticles," *Science,* vol. 277, pp. 1078-1081, 1997.

[14] G. K. Darbha, U. S. Rai, A. K. Singh, and P. C. Ray, "Gold-Nanorod-Based Sensing of Sequence Specific HIV-1 Virus DNA by Using Hyper-Rayleigh Scattering Spectroscopy," *Chem. A Europ. J.,* vol. 14, pp. 3896-3903, 2008.

[15] G. Revillod, I. Russier-Antoine, E. Benichou, C. Jonin, and P.-F. Brevet, "Investigating the Interaction of Crystal Violet Probe Molecules on Sodium Dodecyl Sulfate Micelles with Hyper-Rayleigh Scattering," *J. Phys. Chem. B,* vol. 109, pp. 5383-5387, 2005.

[16] X. Shang, Y. Liu, E. Yan, and K. B. Eisenthal, "Effects of Counterions on Molecular Transport Across Liposome Bilayer: Probed by Second Harmonic Generation," *J. Phys. Chem. B,* vol. 105, pp. 12816-12822, 2001.

[17] P. K. Schmidt and G. W. Rayfield, "Hyper-Rayleigh light scattering from an aqueous suspension of purple membrane," *App. Opt.,* vol. 33, pp. 4286-4292, 1994.

[18] G. Bachelier, I. Russier-Antoine, E. Benichou, C. Jonin, and P.-F. o. Brevet, "Multipolar second-harmonic generation in noble metal nanoparticles," *J. Opt. Soc. Amer. B,* vol. 25, pp. 955-960, 2008.

[19] A. Ulman, "Formation and Structure of Self-Assembled Monolayers," *Chem. Rev.,* vol. 96, pp. 1533-1554, 1996.
[20] R. L. Whetten and W. M. Gelbart, "Nanocrystal Microemulsions: Surfactant-Stabilized Size and Shape," *J. Phys. Chem.,* vol. 98, pp. 3544-3549, 1994.
[21] D. V. Leff, P. C. Ohara, J. R. Heath, and W. M. Gelbart, "Thermodynamic Control of Gold Nanocrystal Size: Experiment and Theory," *The Journal of Physical Chemistry,* vol. 99, pp. 7036-7041, 1995.
[22] P. J. Debouttiere, S. Roux, F. Vocanson, C. Billotey, O. Beuf, A. Favre-R□guillon, Y. Lin, S. Pellet-Rostaing, R. Lamartine, P. Perriat, and O. Tillement, "Design of Gold Nanoparticles for Magnetic Resonance Imaging," *Advan. Funct. Mater.,* vol. 16, pp. 2330-2339, 2006.
[23] C. Hubert, L. Billot, P. M. Adam, R. Bachelot, P. Royer, J. Grand, D. Gindre, K. D. Dorkenoo, and A. Fort, "Role of surface plasmon in second harmonic generation from gold nanorods," *App. Phys. Lett.,* vol. 90, pp. 181105-3, 2007.
[24] Yu, S.-S. Chang, C.-L. Lee, and C. R. C. Wang, "Gold Nanorods: Electrochemical Synthesis and Optical Properties," *J. Phys. Chem. B,* vol. 101, pp. 6661-6664, 1997.
[25] M. B. Mohamed, K. Z. Ismail, S. Link, and M. A. El-Sayed, "Thermal Reshaping of Gold Nanorods in Micelles," *J. Phys. Chem. B,* vol. 102, pp. 9370-9374, 1998.
[26] B. Nikoobakht, Z. L. Wang, and M. A. El-Sayed, "Self-Assembly of Gold Nanorods," *J. Phys. Chem. B,* vol. 104, pp. 8635-8640, 2000.
[27] F. Kim, S. Kwan, J. Akana, and P. Yang, "Langmuir−Blodgett Nanorod Assembly," *J. Amer. Chem. Soc.,* vol. 123, pp. 4360-4361, 2001.
[28] J. D. Jackson, "Classical Electrodynamics John Wiley & Sons," *Inc., New York,* 1975.
[29] P. D. Maker, "Spectral Broadening of Elastic Second-Harmonic Light Scattering in Liquids," *Phys. Rev. A,* vol. 1, pp. 923-923, 1970.
[30] J. L. Oudar, "Optical nonlinearities of conjugated molecules. Stilbene derivatives and highly polar aromatic compounds," *J. Chem. Phys.,* vol. 67, pp. 446-457, 1977.
[31] J. L. Oudar and J. Zyss, "Structural dependence of nonlinear-optical properties of methyl-(2,4-dinitrophenyl)-aminopropanoate crystals," *Phys. Rev. A,* vol. 26, pp. 2016-2016, 1982.
[32] J. Nappa, I. Russier-Antoine, E. Benichou, C. Jonin, and P. F. Brevet, "Second harmonic generation from small gold metallic particles: From the dipolar to the quadrupolar response," *J. Chem. Phys.,* vol. 125, pp. 184712-6, 2006.
[33] I. Russier-Antoine, E. Benichou, G. Bachelier, C. Jonin, and P. F. Brevet, "Multipolar Contributions of the Second Harmonic Generation from Silver and Gold Nanoparticles," *J. Phys. Chem. C,* vol. 111, pp. 9044-9048, 2007.
[34] M. Brust, M. Walker, D. Bethell, D. J. Schiffrin, and R. Whyman, "Synthesis of thiol-derivatised gold nanoparticles in a two-phase Liquid-Liquid system," *J. Chem. Soc., Chem. Commun.,* pp. 801-802, 1994.
[35] J. Tanori and M. P. Pileni, "Control of the Shape of Copper Metallic Particles by Using a Colloidal System as Template," *Langmuir,* vol. 13, pp. 639-646, 1997.
[36] K. Kamogawa, K. Tajima, K. Hayakawa, and T. Kitagawa, "Raman spectroscopic studies of submillimolar surfactant solutions. Concentration dependence of the carbon-hydrogen stretching Raman lines," *J. Phys. Chem.,* vol. 88, pp. 2494-2497, 1984.
[37] J. E. B. Katari, V. L. Colvin, and A. P. Alivisatos, "X-ray Photoelectron Spectroscopy of CdSe Nanocrystals with Applications to Studies of the Nanocrystal Surface," *J. Phys. Chem.,* vol. 98, pp. 4109-4117, 1994.
[38] G. Seifert, "G. Schmid (ed.). Clusters and colloids. From Theory to Applications. VCH Verlagsgesellschaft, Weinheim 1994, 546 p., 232 figs., 37 tabs., hard cover, ISBN 3-527-29043-5," *Crystal Research and Technology,* vol. 29, pp. 956-956, 1994.

[39] C. A. Mirkin, R. L. Letsinger, R. C. Mucic, and J. J. Storhoff, "A DNA-based method for rationally assembling nanoparticles into macroscopic materials," *Nature,* vol. 382, pp. 607-609, 1996.

[40] F. W. Vance, B. I. Lemon, and J. T. Hupp, "Enormous Hyper-Rayleigh Scattering from Nanocrystalline Gold Particle Suspensions," *J. Phys. Chem. B,* vol. 102, pp. 10091-10093, 1998.

[41] A. Cirpan, H. P. Rathnayake, P. M. Lahti, and F. E. Karasz, "Luminescence of fluorenes 2,7-conjugatively extended with pyrenylvinylene and pyrenylvinylene-phenylenevinylene," *J. Mater. Chem.,* vol. 17, pp. 3030-3036, 2007.

[42] G. Revillod, "Diffusion hyper Rayleigh des assemblages moléculaires," Université Claude Bernanrd Lyon1, Lyon, 2006.

[43] J. Zyss, T. C. Van, C. Dhenaut, and I. Ledoux, "Harmonic rayleigh scattering from nonlinear octupolar molecular media: the case of crystal violet," *Chem. Phys.,* vol. 177, pp. 281-296, 1993.

[44] J. Campo, F. Desmet, W. Wenseleers, and E. Goovaerts, "Highly sensitive setup for tunable wavelength hyper-Rayleigh scattering with parallel detection and calibration data for various solvents," *Optics Express,* vol. 17, pp. 4587-4604, 2009.

[45] J. P. Wilcoxon, J. E. Martin, F. Parsapour, B. Wiedenman, and D. F. Kelley, "Photoluminescence from nanosize gold clusters," *J. Chem. Phys.,* vol. 108, pp. 9137-9143, 1998.

[46] P. Apell, R. Monreal, and S. Lundqvist, "Photoluminescence of noble metals," *Physica Scripta,* vol. 38, pp. 174-179, 1988.

[47] J. Nappa, G. Revillod, J.-P. Abid, I. Russier-Antoine, C. Jonin, E. Benichou, H. H. Girault, and P. F. Brevet, "Hyper-Rayleigh scattering of gold nanorods and their relationship with linear assemblies of gold nanospheres," *Farad. Discuss.,* vol. 125, pp. 145-156, 2004.

[48] O. P. Varnavski, M. B. Mohamed, M. A. El-Sayed, and T. Goodson, "Relative Enhancement of Ultrafast Emission in Gold Nanorods," *J. Phys. Chem. B,* vol. 107, pp. 3101-3104, 2003.

[49] a. L H Dubois and R. G. Nuzzo, "Synthesis, Structure, and Properties of Model Organic Surfaces," Annu. Rev. Phys. Chem. vol. 43: pp437-463, 1992.

[50] C. D. Bain, E. B. Troughton, Y. T. Tao, J. Evall, G. M. Whitesides, and R. G. Nuzzo, "Formation of monolayer films by the spontaneous assembly of organic thiols from solution onto gold," *J. Amer. chem. Soc.,* vol. 111, pp. 321-335, 1989.

[51] C. A. F. Daniel L. Feldheim, Jr. , *Metal nanoparticles: Synthesis, Characterization and Applications, Editor: Marcel Dekker, New York,* , 2002.

[52] H. Hakkinen, R. N. Barnett, and U. Landman, "Electronic Structure of Passivated Au38(SCH3)24 Nanocrystal," *Phys. Rev. Lett.,* vol. 82, pp. 3264-3264, 1999.

[53] P. Zhang and T. K. Sham, "Tuning the electronic behavior of Au nanoparticles with capping molecules," *App. Phys. Lett.,* vol. 81, pp. 736-738, 2002.

[54] D. Zanchet, H. Tolentino, M. C. Martins Alves, O. L. Alves, and D. Ugarte, "Inter-atomic distance contraction in thiol-passivated gold nanoparticles," *Chem. Phys. Lett.,* vol. 323, pp. 167-172, 2000.

[55] F. Kim, J. H. Song, and P. Yang, "Photochemical Synthesis of Gold Nanorods," *J. Amer. chem. Soc.,* vol. 124, pp. 14316-14317, 2002.

[56] T. K. Sau and C. J. Murphy, "Seeded High Yield Synthesis of Short Au Nanorods in Aqueous Solution," *Langmuir,* vol. 20, pp. 6414-6420, 2004.

Chapter 3

Theory

3.1. Introduction

The SHG process has been first observed in a quartz plate by Franken *et al.* [1]. Theoretical models of surface SHG have been the interest of several authors over more than 45 years. Bloembergen and Pershan [2], for instance, focused on solving Maxwell's equations for the second harmonic field $E^{(2)}$ radiated by a nonlinear polarisation induced by an incident field. In 1965 Brown *et al.* introduced the term $\vec{E}\vec{\nabla}.\vec{E}$ to fit their experimental data of the SHG signal from the surface of a silver mirror [3]. Later the same year, S.S. Jha found that a correction term as a function of the electric and the magnetic field should be added to the field gradient term in order to obtain a better fit for the experimental data [4, 5]. Just after, Bloembergen and Shen reported the nonlinearity of a plasma [6]. Later the same year, the experimental results of Brown and Parks at a silver surface underlined the role of magnetic dipole contribution in the SHG signal [7]. Lee *et al.* presented the variation of the SH intensity upon the application of a dc electric field [8].. In 1968, Bloembergen *et al* [9] published a seminal article where they derived a model for a thick slab of nonlinear material lying at the interface between two linear optical media. Here, thick means that the thickness is of the order of the wavelength of light. In their work, they emphasized that the origin of the SH signal arises from the quadrupole electric nonlinear polarization. This origin should indeed dominate over purely surface effects for media with high refractive indices. However, subsequent experiments performed by Brown *et al.* [10] showed that the SH signal from silver evaporated surfaces could not be described with Bloembergen *et al.* model. In 1971, J. Rudnick and E.A. Stern [11] developed a theory for the SHG response from metal surfaces based on the breaking of the centrosymmetry at the metal interface. They divided the SH contributions into three different source terms, introducing three phenomenological parameters: *a*, *b* and *d*. The first parameter *a* is related to a surface current oscillating at the harmonic frequency perpendicular to the surface, the second one corresponds to a surface current at the harmonic frequency parallel to the surface and the third one is a bulk current oscillating at the harmonic frequency. The bulk

current was shown to extend into the metal over about a skin depth, typically several hundred angstroms while the surface currents are confined to the surface region over a few angstroms. However, there are limitations to this model. For example, the periodic lattice structure of the metal or the surface roughness were not taken into account. A first step in the development of a proper theory was made by Sipe *et al.* [12] and then by Corvi *et al.* [13, 14]. These groups introduced the hydrodynamic model for the free electron gas in a metal to get expressions for the three different nonlinear currents. The anisotropy in the second harmonic generation from metal surfaces was introduced by Tom *et al.*[15]. Sipe and co-workers [16, 17] proposed a phenomenological model describing real experimental geometries using a sheet of nonlinear polarisation of vanishing thickness representing the interface. Later, it was though pointed out by Guyot-Sionnest and Shen [18] that all previous derivations lacked a term in the nonlocal description of the nonlinear surface polarisation source, namely the gradient of the electric quadrupolar susceptibility tensor. A paper of Liebsch and Schaich presented the calculation of the frequency dependence of the $a(\omega)$ which characterises the perpendicular second harmonic surface polarisation[19]. More recent works [20] have developed a general framework for this phenomenological model where a complete account of all contributions is given.

In the recent years, advances have been made using the density functional theory to obtain an improvement in the description of the electronic density near the metal surface. This was first started by M. Weber and A. Liebsch [21] where the SH signal was shown to be very sensitive to surface electronic properties, capable to yield a detailed information about the electronic distribution near the surface. P.G. Dzhavakhidze *et al.* in 1992 [22] further developed this approach at the metal-electrolyte interface, giving an account of the SHG signal dependence on the charge on the metal as well as the effect of adsorption. W. Schmickler and M Urbakh in 1993 also employed the electronic density functional calculations to determine theoretically the variation of the SH signal with the electrode charge in the presence and absence of specifically adsorbed ions [23]. Furthermore, the influence of nanoscale roughness on the SHG signal at the metal-electrolyte interface has also been examined [24-26].

In the literature, two approaches have been used to describe the SH intensity from a metallic surface: a first one based on the use of the Rudnick and Stern parameters $a(\omega)$, $b(\omega)$ and $d(\omega)$ and a second one using the susceptibility tensor elements. Very few works [27, 28] have though presented the equations relating the Rudnick and Stern parameters with the

susceptibility tensor elements, especially in the international unit system. In this chapter, this connection between the susceptibility tensor elements and the *a(ω)*, *b(ω)* and *d(ω)* parameters will be made. Then, the hydrodynamic model will be used to get the expressions for the different nonlinear polarisation contributions. In a second part of this chapter, we will then establish the expression of the SH intensity as a function of the polarization states of the incident and the harmonic light, based on the forms available using the susceptibility elements. These expressions will be useful to adjust our experimental data presented in the following chapters.

3.2. The model of the free electron gas

In metals, the conduction band electrons are fully delocalized. These electrons are free to move, forming a gas of electrons. In this chapter, the hydrodynamic model is used to describe the nonlinear polarization for such a free electron gas under the excitation by an external electromagnetic field.

3.2.1. Free Electron Gas Theory in the bulk of a medium

We will take the simplest case presented in several hand books where the electron gas is considered as a fluid (either liquid or gas) in a medium, this fluid is characterised by its velocity $\vec{v}$ and density ρ , at each point *r*. The hydrodynamic model is based on Newton's second law for an electron of effective mass *m*, charge *–e*, and average velocity $\vec{v}$. Under the excitation by a fundamental oscillating electromagnetic wave, the equation of motion is written as follows [29]:

$$\frac{\partial \vec{v}}{\partial t} + \left(\vec{v}.\vec{\nabla}\right)\vec{v} = -\frac{\vec{\nabla}P}{m} - \frac{e}{m}\left(\vec{E} + \vec{v} \times \vec{B}\right) \tag{3.1}$$

This equation is called a Navier-Stokes equation and arises from applying Newton's second law to fluid motion, together with the assumption that the fluid stress is the sum of a diffusing

viscous term (proportional to the gradient of velocity), plus a pressure term. On the other hand the continuity equation is given by:

$$\frac{\partial \rho}{\partial t} + \nabla.(\rho v) = 0 \tag{3.2}$$

To simplify the problem, the pressure P is supposed uniform, then $\vec{\nabla} P = 0$. The incident field is chosen of the form $E = Ae^{i(k.r-\omega t)}$. We consider a series expansion:

$$\rho = \rho^{(0)} + \rho^{(1)} + \rho^{(2)} + .. \tag{3.3}$$

$$\vec{v} = \vec{v}^{(1)} + \vec{v}^{(2)} + .. \tag{3.4}$$

$$J = J^{(1)} + J^{(2)} + .. \tag{3.5}$$

where

$$J^{(1)} = \rho^{(0)} v^{(1)} \tag{3.6}$$

$$J^{(2)} = \rho^{(0)} v^{(2)} + \rho^{(1)} v^{(1)} \tag{3.7}$$

where we impose $\vec{v}^{(0)} = 0$ for order (0), since the zero order is obtained at equilibrium.

$$\frac{\partial \vec{v}^{(1)}}{\partial t} = \frac{-e}{m}\vec{E} = -i\omega \vec{v}^{(1)} \tag{3.8}$$

that gives

$$\vec{v}^{(1)} = \frac{e\vec{E}^{(1)}}{im\omega} \tag{3.9}$$

where the density at order (1) is determined using the continuity equation (3.2)

$$\frac{\partial \rho^{(1)}}{\partial t} + \nabla.\left(\rho^{(0)} v^{(1)}\right) = 0 \tag{3.10}$$

Substituting $\vec{v}^{(1)}$ by its value given in (3.9), equation (3.10) becomes

$$\rho^{(1)} = -\frac{e}{m\omega^2} \nabla.\left(\rho^{(0)} \vec{E}^{(1)}\right) \tag{3.11}$$

Equation (3.1) at order 2 gives:

$$\frac{d\vec{v}^{(2)}}{\partial t} + \left(\vec{v}^{(1)}.\vec{\nabla}\right)\vec{v}^{(1)} = \frac{-e}{m}\left[\vec{v}^{(1)} \times \vec{B}^{(1)}\right] \tag{3.12}$$

where no electric field at the harmonic frequency is present. Substitute $\vec{v}^{(1)}$ by its value given in (3.9), equation (3.12) becomes:

$$-2i\omega v^{(2)} = \frac{e^2}{m^2\omega^2}\left(\vec{E}^{(1)}.\vec{\nabla}\right)E^{(1)} - \frac{e^2}{im^2\omega}\vec{E}^{(1)} \times \vec{B}^{(1)} \tag{3.13}$$

for a monochromatic incident electromagnetic field of frequency ω. Using Maxwell Faraday equation from the Maxwell equations given as follows:

$$\nabla \times E = -\frac{\partial B}{\partial t} \tag{3.14}$$

which gives

$$B = \nabla \times \frac{E}{i\omega} \tag{3.15}$$

then equation (3.13) can be written as follows:

$$\begin{aligned} -2i\omega\vec{v}^{(2)} &= \frac{e^2}{m^2\omega^2}(E.\nabla)E + \frac{e^2}{m^2\omega^2}E\times(\nabla\times E) \\ &= \frac{e^2}{m^2\omega^2}\left[(E.\nabla)E + E\times(\nabla\times E)\right] \end{aligned} \tag{3.16}$$

where the second order velocity $\vec{v}^{(2)}$ is written as follows after substituting the first order velocity given in equation (3.9)

$$\vec{v}^{(2)} = -\frac{e^2}{2im^2\omega^3}\left(\vec{E}^{(1)}.\vec{\nabla}\right)\vec{E}^{(1)} - \frac{e^2}{2m^2\omega^2}\left(\vec{E}^{(1)}\times B^{(1)}\right) \tag{3.17}$$

Using the following vector equation:

$$\frac{1}{2}\vec{\nabla}\left[\vec{E}^{(1)}.\vec{E}^{(1)}\right] = \left(\vec{E}^{(1)}.\vec{\nabla}\right)\vec{E} + \vec{E}^{(1)}\times\left(\vec{\nabla}\times\vec{E}^{(1)}\right) \tag{3.18}$$

equation (3.16) yields:

$$-2i\omega v^{(2)} = \frac{e^2}{m^2\omega^2}\frac{1}{2}\nabla(E.E) \tag{3.19}$$

Thus the velocity of second order $\vec{v}^{(2)}$ is given by:

$$\vec{v}^{(2)} = \frac{ie^2}{4m^2\omega^3}\vec{\nabla}(E.E) \tag{3.20}$$

and the second order current density $J^{(2)}$ using equation(3.7):

$$J^{(2)}(2\omega) = \frac{i\rho^{(0)}e^2}{4m^2\omega^3}\vec{\nabla}(E.E) + \frac{ie^2}{m^2\omega^3}\left[\vec{\nabla}.\left(\rho^{(0)}E\right)\right]E \tag{3.21}$$

where the nonlinear polarisation is simply the time integral of the current density given as follows:

$$\vec{J} = \frac{\partial \vec{P}}{\partial t} \tag{3.22}$$

giving the nonlinear polarisation:

$$P^{(2)}(2\omega) = -\frac{\rho^{(0)} e^2}{8m^2\omega^4}\vec{\nabla}\left(\vec{E}^{(1)}.\vec{E}^{(1)}\right) - \frac{e^2}{2m^2\omega^4}\left[\vec{\nabla}.\left(\rho^{(0)}\vec{E}^{(1)}\right)\right]\vec{E}^{(1)} \tag{3.23}$$

This polarisation equation can be written also as

$$\vec{P}^{(2)} = \frac{e^3 n^{(0)}}{4m^2\omega^4}\left(\vec{E}^{(1)}.\vec{\nabla}\right)\vec{E}^{(1)} + \frac{e\varepsilon_0}{2m\omega^2}\left(\nabla.\vec{E}^{(1)}\right)\vec{E}^{(1)} - \frac{e^3 n^{(0)}}{4im^2\omega^3}\left(\vec{E}^{(1)} \times B^{(1)}\right) \tag{3.24}$$

using

$$\vec{J}^{(2)} = \frac{e^3 n^{(0)}}{2im^2\omega^3}\left(\vec{E}^{(1)}.\vec{\nabla}\right)\vec{E}^{(1)} + \frac{e\varepsilon_0}{im\omega}\left(\nabla.\vec{E}^{(1)}\right)\vec{E}^{(1)} + \frac{e^3 n^{(0)}}{2m^2\omega^2}\left(\vec{E}^{(1)} \times B^{(1)}\right) \tag{3.25}$$

This second order current density is proportional to $\exp[-2i\omega t]$ and is obtained using equation (3.7) and $\rho^{(0)} = -en^{(0)}$ as well as substituting both the first order and the second order velocities by their values given in equations (3.9) and (3.17). The polarisation equation in (3.24) is given as a function of both the electric and the magnetic field while that given in equation (3.23) is only dependent on the electric field. This is in the case where the medium is considered isotropic and the electron gas pressure and the ohmic damping are neglected. We notice here that in the absence of field oscillating at the harmonic frequency, the nonlinear current is driven by the incoming electromagnetic wave through the gardient of the electric field.

3.2.2. Free Electron Gas Theory at the surface.

In this section, we perform a similar development as that given in section 3.2.1. However, we now have to incorporate the electron density and thus its gradient which is no more considered zero as in the case of the bulk. In addition we will incorporate the free electron gas pressure in the equation of motion and the ohmic damping. The equation of motion is then written as follows [30]:

$$\frac{\partial \vec{v}}{\partial t} + \left(\vec{v}.\vec{\nabla}\right)\vec{v} = \frac{-e}{m}\left[\vec{E} + \vec{v} \times \vec{B}\right] - \frac{1}{mn}\vec{\nabla}p - \frac{1}{\tau}\vec{v} \tag{3.26}$$

where $\vec{E}$ and $\vec{B}$ are the electric and magnetic fields of the incident exciting wave respectively, n is the electron density, $\vec{v}$ the velocity and the pressure p of the free electron gas is not considered uniform inhere. Also, $-e$ is the electron charge, m is the electron mass and τ is the scattering rate constant which quantifies the extent of ohmic damping. In the following, this last term will be neglected for simplicity. All these quantities are functions of space and time but we have omitted this dependence for the equations to be written in a clear way. Besides, the motion of the electrons is also driven by the continuity equation given in (3.2). The gas pressure is written as a function of the Fermi energy as follows [31] :

$$p = \frac{2}{5} n E_F \tag{3.27}$$

where the Fermi energy is given in solid state physics by[32]

$$E_F = \frac{\hbar^2}{2m}\left(3\pi^2 n\right)^{2/3} \tag{3.28}$$

therefore substitute (3.28) in (3.27) we have the gas pressure variation with electron density given by:

$$p(\vec{r},t) = \zeta\left[n(\vec{r},t)\right]^{5/3} \tag{3.29}$$

where

$$\zeta = (3\pi^2)^{2/3}\hbar^2 / 5m \tag{3.30}$$

The resolution of Euler's equation for the electron gas is not a simple task. Hence, we will seek a solution for the electron density as a superposition of the different contributions oscillating at the fundamental and the harmonic frequencies of the incident electromagnetic wave. Consequently, we will develop all quantities as series expansions. If $A(\vec{r},t)$ is one of these functions, i.e. $\vec{v}(\vec{r},t)$, $n(\vec{r},t)$, $\rho(\vec{r},t)$, $\vec{E}(\vec{r},t)$ or $\vec{B}(\vec{r},t)$, we will write :

$$A(\vec{r},t) = \sum_{i=0}^{\infty} A^{(i)}(\vec{r},t) \tag{3.31}$$

where the term for $i = 0$ is the static term, the one for $i = 1$ is the term oscillating at the fundamental frequency of the exciting electromagnetic wave and so on. We will discuss the first three orders of the development.

3.2.2.1. Order (0)

At order 0, the quantities of the form $A^{(0)}(\vec{r},t)$ are static terms describing the free electron gas. We therefore impose $\vec{v}^{(0)}(\vec{r},t) = \vec{0}$ and $\vec{B}^{(0)}(\vec{r},t) = \vec{0}$ since the zero order is obtained at equilibrium in the absence of the incoming light, the fields of the latter oscillating at the harmonic frequency. The magnetic field in this case is zero since no electron motion occurs. The electric field is however not zero because inhomogeneities in the electron gas density give rise to a static electric field. Therefore, Eq.(3.26) at order zero is :

$$\frac{e}{m} n^{(0)} \vec{E}^{(0)} + \frac{5}{3m} \zeta \left(n^{(0)}\right)^{2/3} \vec{\nabla} n^{(0)} = 0 \tag{3.32}$$

where here all higher orders are neglected. The pressure p can be substituted by its value given in Eq.(3.29). Then, $\vec{\nabla}\left[n^{5/3}\right]$ at order zero is:

$$\vec{\nabla}\left[n^{(0)^{5/3}}\right]=\frac{5}{3}\left(n^{(0)}\right)^{2/3}\vec{\nabla}\left[n^{(0)}\right] \tag{3.33}$$

From Eq.(3.32), we recognize that the static term of the electric field arising from the density inhomogeneities is independent of the incoming electromagnetic wave. Eq.(3.29) yields :

$$\vec{E}^{(0)}=\frac{\beta_0^2}{\omega_0^2}\vec{\nabla}\rho^{(0)} \tag{3.34}$$

where we define

$$\omega_0^2=\frac{n^{(0)}e^2}{\varepsilon_0 m} \tag{3.35}$$

as the plasma frequency and

$$\beta_0^2=\frac{5}{3m\varepsilon_0}\zeta\left(n^{(0)}\right)^{2/3} \tag{3.36}$$

as the velocity parameter. The static charge density is $\rho^{(0)}=-en^{(0)}$.

3.2.2.2. Order (1)

At order one, we only keep the terms oscillating at the fundamental frequency. Eq.(3.26) is then written as :

$$n^{(0)}\left[\frac{\partial}{\partial t}+\frac{1}{\tau}\right]\vec{v}^{(1)}=-\frac{en^{(0)}}{m}\vec{E}^{(1)}-\frac{en^{(1)}}{m}\vec{E}^{(0)}-\frac{1}{m}\vec{\nabla}p \tag{3.37}$$

First of all we need to determine $\vec{\nabla}p$ at order one where p is given by Eq.(3.29).

$$\vec{\nabla}p = \vec{\nabla}\left(\zeta\left[n\right]^{5/3}\right) = \vec{\nabla}\left(\zeta\left[n^{(0)} + n^{(1)}\right]^{5/3}\right) = \vec{\nabla}\left(\zeta\left(n^{(0)}\right)^{5/3}\left[1+\frac{n^{(1)}}{n^{(0)}}\right]^{5/3}\right) \tag{3.38}$$

Using the following approximation:

$$(1+x)^m = 1 + mx + \frac{1}{2!}m(m-1)x^2 + \ldots \tag{3.39}$$

we get :

$$\vec{\nabla}p = \frac{5}{3}\zeta\left(n^{(0)}\right)^{2/3}\vec{\nabla}(n^{(0)}) + \frac{5}{3}\zeta\vec{\nabla}\left(n^{(1)}(n^{(0)})^{2/3}\right) \tag{3.40}$$

The first term is of order zero and will not be considered anymore. Eq.(3.37) now becomes :

$$n^{(0)}\left[\frac{\partial}{\partial t}+\frac{1}{\tau}\right]\vec{v}^{(1)} = -\frac{en^{(0)}}{m}\vec{E}^{(1)} - \frac{en^{(1)}}{m}\vec{E}^{(0)} - \frac{5}{3m}\zeta\vec{\nabla}\left[\left(n^{(0)}\right)^{2/3}n^{(1)}\right] \tag{3.41}$$

Multiplying Eq.(3.41) by *–e*, inserting Eqs.(3.34) and (3.35) and using the derivative of the product of two functions, it yields :

$$\left[\frac{\partial}{\partial t}+\frac{1}{\tau}\right]\vec{j}^{(1)} = \varepsilon_0\omega_0^2\vec{E}^{(1)} - \varepsilon_0 n^{(0)}\vec{\nabla}\left[\frac{\beta_0^2}{n^{(0)}}\rho^{(1)}\right] \tag{3.42}$$

with the introduction of the current density vector at order one given by $\vec{j}^{(1)} = -en^{(0)}\vec{v}^{(1)}$. This equation above defines the first order electron current density induced by the fundamental electromagnetic wave exciting the free electron gas. It therefore also describes the first order linear polarisation. We can rewrite this equation as:

$$\frac{\partial^2}{\partial t^2}\vec{P}^{(1)} - \vec{L}.\vec{P}^{(1)} = \frac{e^2n^{(0)}}{m}\vec{E}^{(1)} \tag{3.43}$$

with the operator $\vec{L}$ defined as :

$$\vec{L} = -\frac{5}{9m}\zeta\left(n^{(0)}\right)^{-1/3}\left(\vec{\nabla}n^{(0)}\right)\vec{\nabla} + \frac{5}{3}\zeta\left(n^{(0)}\right)^{2/3}\vec{\nabla}\vec{\nabla} \tag{3.44}$$

using the first order electron current :

$$\vec{j}^{(1)} = \frac{\partial}{\partial t}\vec{P}^{(1)} \tag{3.45}$$

and the first order charge density

$$-en^{(1)} = \rho^{(1)} = -\vec{\nabla}.\vec{P}^{(1)} \tag{3.46}$$

Substituting ω_0^2 and β_0^2 by their expressions and neglecting the ohmic damping, Eq.(3.43) gives the relationship between the exciting electric field and the induced linear polarisation. In the bulk of the metal where we may neglect the inhomogeneities in the free electron gas density introduced by the second term in Eq.(3.43), we find, assuming a harmonic oscillating time dependence for the polarisation of the form $\vec{P}^{(1)} \propto \exp[-i\omega t]$:

$$\vec{P}^{(1)} = \varepsilon_0 \chi \vec{E}^{(1)} \tag{3.47}$$

with

$$\chi^{(1)} = \frac{-e^2 n^{(0)}}{\varepsilon_0 \omega^2 m} = -\frac{\omega_0^2}{\omega^2} \tag{3.48}$$

where the bulk linear electronic susceptibility is introduced. We then reach the usual expression for the dielectric constant of the free electron gas as a function of the frequency:

$$\varepsilon^{\omega} = 1 + \chi^{(1)} = 1 - \frac{\omega_0^2}{\omega^2} \tag{3.49}$$

At the surface of the free electron gas, this solution is though no longer valid owing to the occurrence of charge density gradients. Hence the operator $\vec{L}$ has to be reinstated. However, simplifications may still arise if we assume that gradients occur along a direction normal to the interface. This direction is here taken as the *Oz* axis.

3.2.2.3. Order (2)

At order two, Eq.(3.26) becomes :

$$\begin{aligned} & n^{(0)}\left[\frac{\partial}{\partial t} + \frac{1}{\tau}\right]\vec{v}^{(2)} + n^{(1)}\left[\frac{\partial}{\partial t} + \frac{1}{\tau}\right]\vec{v}^{(1)} + n^{(0)}\left(\vec{v}^{(1)}.\vec{\nabla}\right)\vec{v}^{(1)} = -\frac{en^{(0)}}{m}\vec{E}^{(2)} - \frac{en^{(1)}}{m}\vec{E}^{(1)} \\ & -\frac{en^{(2)}}{m}\vec{E}^{(0)} - \frac{en^{(0)}}{m}\left(\vec{v}^{(1)} \times \vec{B}^{(1)}\right) - \frac{5}{3m}\zeta\vec{\nabla}\left[\left(n^{(0)}\right)^{2/3}\left(n^{(2)} + \frac{1}{3}\frac{\left(n^{(1)}\right)^2}{n^{(0)}}\right)\right] \end{aligned} \tag{3.50}$$

where $\vec{\nabla}\left[n^{5/3}\right]$ at order two is :

$$\frac{5}{3}\vec{\nabla}\left[\left(n^{(2)} + \frac{1}{3}\frac{\left(n^{(1)}\right)^{2/3}}{n^{(0)}}\right)\left(n^{(0)}\right)^{2/3}\right] \tag{3.51}$$

Eq.(3.50) can be rewritten as a time evolution equation of the nonlinear polarisation $\vec{P}^{(2)}$ with two excitation terms as follows :

$$\frac{\partial^2}{\partial t^2}\vec{P}^{(2)} - \vec{L}.\vec{P}^{(2)} = \frac{e^2 n^{(0)}}{m}\vec{E}^{(2)} + \vec{S}_f + \vec{S}_p \tag{3.52}$$

with the two source terms:

$$\vec{S}_f = en^{(0)}\left(\vec{v}^{(1)}.\vec{\nabla}\right)\vec{v}^{(1)} - e\vec{v}^{(1)}\frac{\partial n^{(1)}}{\partial t} + \frac{e^2 n^{(1)}}{m}\vec{E}^{(1)} + \frac{e^2 n^{(0)}}{m}\left(\vec{v}^{(1)} \times \vec{B}^{(1)}\right) \tag{3.53}$$

and

$$\vec{S}_p = \frac{5e}{9m}\zeta\vec{\nabla}\left[\left(n^{(1)}\right)^2\left(n^{(0)}\right)^{-1/3}\right] \tag{3.54}$$

The different source terms appearing in the time evolution equation are convective terms and coupling terms between the free electron gas and the electromagnetic excitation fields.

3.3. Nonlinear polarisation source

In the bulk of the medium, the inhomogeneities appearing in the operator $\vec{L}$ may be neglected in Eq.(3.52). With the same assumption, the source term $\vec{S}_p$, see Eq.(3.53), also vanishes in the bulk of the metal. Therefore, using $n^{(1)} = 0$ since only the static electronic distribution is non zero in the bulk volume, Eq.(3.52) becomes :

$$\vec{P}^{(2)} = \varepsilon_0\chi\vec{E}^{(2)} - \frac{e}{8m\omega^2}\varepsilon_0\left(\varepsilon^{\omega} - 1\right)\vec{\nabla}\left[\vec{E}^{(1)}.\vec{E}^{(1)}\right] \tag{3.55}$$

where the vector equality given in Eq.(3.18) has been used. In Eq.(3.55), we observe that the nonlinear polarisation is made up of two terms: The first term is the term arising from the linear process of wave propagation at the harmonic frequency whereas the second term is the nonlinear polarization arising from the nonlinear process of SHG. It is therefore a contribution proportional to the electric field itself with a factor equal to the electronic susceptibility of the bulk metal. Using Eq.(3.48) at the harmonic frequency gives :

$$\chi = \frac{1}{4}\chi^{(1)} = -\frac{e^2 n^{(0)}}{4\varepsilon_0 m\omega^2} \tag{3.56}$$

where $\chi = \chi^{(1)}(2\omega)$ has to be distinguished from the nonlinear susceptibility tensor $\chi^{(2)}$. The second term in Eq.(3.55) gives the nonlinear polarisation of the uniform free electron gas under excitation by incident electromagnetic wave. In the regions were sudden changes occurs, that is at the surface of the metal, the solution of the problem is given with the following two equations :

$$\begin{aligned} -\Omega^2 P_k^{(2)} &= S_k \\ L_0 P_z^{(2)} &= S_z \end{aligned} \tag{3.57}$$

where we assume that gradients only occur along the z coordinate. The coordinate k is here defined as the coordinate in the plane of the interface. The operator L_0 vanishes in this direction. Hence, this operator reduces to:

$$L_0 = \omega_0^2 - \omega^2 + \frac{5}{9m}\zeta\left(n^{(0)}\right)^{-1/3}\frac{\partial n^{(0)}}{\partial z}\frac{\partial}{\partial z} + \frac{5}{3}\zeta\left(n^{(0)}\right)^{2/3}\frac{\partial^2}{\partial z^2} \tag{3.58}$$

The electric field amplitude at the first order is then constituted of the sum of an electric field within the bulk of the metal due to electromagnetic incident excitation field and the induced linear current densities and an electric field in the surface region due to the induced linear current densities in the surface region. The total electric field at the first order can be then written as:

$$\vec{E}^{(1)} = \vec{E}_b^{(1)} + \vec{E}_s^{(1)} \tag{3.59}$$

where $\vec{E}_b^{(1)}$ and $\vec{E}_s^{(1)}$ are the bulk and the surface field contributions respectively. For the source term, this yields:

$$S_k = -ev_k^{(1)} \frac{\partial n^{(1)}}{\partial t} + \frac{e^2 n^{(1)}}{m} E_{kb}^{(1)} = \frac{2e}{m} E_{kb}^{(1)} \frac{\partial P_z^{(1)}}{\partial z} \tag{3.60}$$

and

$$S_z = \frac{e}{m} E_{zb}^{(1)} \frac{\partial P_z^{(1)}}{\partial z} + \frac{\partial V}{\partial z} \tag{3.61}$$

where V is given by :

$$V = \frac{5e}{9m} \zeta (n^{(1)})^2 (n^{(0)})^{-1/3} - \left(\frac{\omega^2}{en^{(0)}} + \frac{e}{2m} \right) \left(P_z^{(1)} \right)^2 \tag{3.62}$$

Eqs.(3.60) and (3.61) give the two components along the surface normal and perpendicular direction to the plane of the surface. In the source terms S_k and S_z, only the first term of the series expansion in powers of the ratio l/λ is kept, l being the characteristic distance for the electron density gradients and λ being the wavelength of the incoming light. The distance l corresponds approximately to the Fermi wavelength over which the gradient occurs in the free electron gas. This therefore provides an estimation of the thickness of the surface region. We thus have $l/\lambda << 1$ at optical wavelengths for the ratio l/λ. The quantities derived in Eqs.(3.57)-(3.62) are all z dependent quantities. Thus, the nonlinear polarization solution of the system given in Eq.(3.57) is valid in the plane of z coordinate. Since we are interested in the response from the complete surface region, we should integrate in the z direction over the strata of thickness l to find the total nonlinear polarisation of the interface region. The interface nonlinear polarisation, defined as the dipole moment density per unit area in the plane of the surface is then written:

$$Q^k = -\frac{2e}{m\Omega^2} \int_0^l E_{(kb)}^{(1)} \frac{\partial P_z^{(1)}}{\partial z} dz = -\frac{e}{2m\omega^2} E_{kb}^{(1)}(0) P_z^{(1)}(0) \tag{3.63}$$

which reduces to

$$Q^k = -\frac{e\varepsilon_0(\varepsilon^\omega - 1)}{2m\omega^2} E_{kb}^{(1)}(0) E_z^{(1)}(0) \tag{3.64}$$

with the help of Eqs.(3.47) and (3.49). Along the z coordinate, the problem is more complicated since we have to use Eqs.(3.43) and (3.57). It is important here to remark though that the operator L_0 introduces the structure of the metal surface and therefore the possibility of large amplitude fluctuations over short distances. This is related to the occurrence of resonances. With an effective plasma frequency ω_0 for the nonlinear current density in the surface region, we can write :

$$\int_0^l L_0 P_z^{(2)} dz = \left(\omega_0^2 - \Omega^2\right) Q^z \tag{3.65}$$

in order to avoid the integration over the z coordinate. Thus, this allows the determination of the Q^z component of the interface nonlinear polarization by calculating the integral in the surface region of the source term only:

$$Q_z = \frac{1}{\omega_0^2 - \Omega^2} \int_0^l S_z dz \tag{3.66}$$

Substituting S_z by its value given in Eq.(3.61) and V given in Eq.(3.62), it gives :

$$Q^z = \frac{e\varepsilon_0(\varepsilon^\omega - 1)}{m(\omega_0^2 - \Omega^2)} \frac{\varepsilon^\omega + 3}{2} \left[E_z^{(1)}(0)\right]^2 \tag{3.67}$$

Here it is explicitly stated that the electric field is taken to be within the metal. In the integration of Eq.(3.66), we have indeed taken into account the fact that the source term vanishes when approaching the limit $z = l$. In the literature [11, 12], it is common to use the two phenomenological parameters a and b , also called the surface Rudnick and Stern

parameters, to describe the nonlinear response of the metal surface. The possibility of resonances introduced above is obtained in a rather unrefined way. The nonlinear polarisation at the surface is thus often rewritten as:

$$Q^{k} = \frac{e\varepsilon_0 b\left(\varepsilon^{\omega} - 1\right)}{2m\omega^2} E_z^{(1)}(0) E_k^{(1)}(0) \tag{3.68}$$

$$Q^{z} = \frac{e\varepsilon_0 a\left(\varepsilon^{\omega} - 1\right)}{4m\omega^2} \left[E_z^{(1)}(0)\right]^{2} \tag{3.69}$$

In the end, we have obtained the overall nonlinear polarisation arising from both the surface and the bulk of the metal. The surface contributions are given by Eqs.(3.68) and (3.69) where the first is parallel to the surface and the second one is perpendicular to the surface whereas the bulk contribution is given by the second term in Eq.(3.55).

3.4. Three layer model

To calculate the SH intensity at the interface between a metal and a dielectric medium, we introduce a three layer geometry where a linear slab of vanishing thickness embeds the sheet of nonlinear polarisation. The three-layer model described in Figure 3.1 consists of two media 1 and 2 of optical relative permittivities ε_1^{ω}, ε_1^{Ω} and ε_2^{ω}, ε_2^{Ω} at the fundamental ω and harmonic Ω frequencies respectively and a thin slab lying between these two media named medium *m* with its relative permittivities $\varepsilon^{\omega}, \varepsilon^{\Omega}$ at the fundamental and harmonic frequencies [20]. This medium *m* is the true interfacial region localized between $z = t_1$ and $z = t_2$, $t_2 < 0$ and the sheet of nonlinear polarisation lies at $z = 0$. The thickness of the slab, or medium *m*, is small compared to the wavelength of light. Thus we have $t_1 + t_2 \leq \lambda$. The laboratory frame is oriented with the surface normal along the $\hat{z}$ axis pointing upwards and the $\hat{x}$ axis along the interface. The $\hat{y}$ direction is chosen to define a direct $(\hat{x}, \hat{y}, \hat{z})$ frame.

A fundamental wave is incident on the thee layer system from the upper side with an angle of incidence θ_1^{ω}. Due to the laws of reflection and refraction, the fundamental beam propagates

in the inner slab *m* with angle θ^{ω} and in medium 2 with the angle θ_2^{ω}. Total internal reflection (TIR) between medium *1* and medium *m* takes place when $\mathrm{Re}(\varepsilon_1^{\omega}) > \mathrm{Re}(\varepsilon^{\omega})$. The different harmonic beams propagate with angles θ_1^{Ω}, θ_2^{Ω} and θ^{Ω} in medium *1, 2* and *m* respectively.

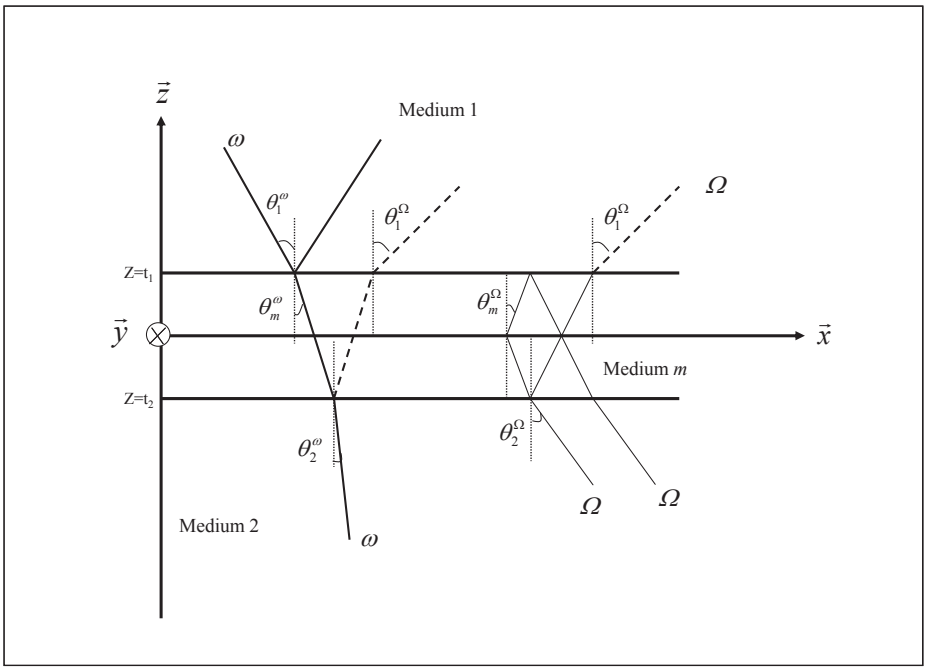

Figure 3.1: Schematics of the three layer model with the geometrical configuration

3.4.1. The non-linear polarization source

The general expression of the total nonlinear polarisation can be written as follows [33] :

$$\vec{P}_{tot}^{(2)}(\vec{r},t) = \vec{P}_S^{(2)}(\vec{r},t) - \vec{\nabla}.\vec{\vec{Q}}^{(2)}(\vec{r},t) + \frac{\mu_0}{i\omega}\vec{\nabla}\times\vec{M}^{(2)}(\vec{r},t) + \ldots \tag{3.70}$$

where $\vec{P}$, $\vec{\vec{Q}}$ and $\vec{M}$ denote the electric dipole and electric quadrupole polarization and magnetization respectively. This equation is valid when volume elements whose dimensions are small compared to the wavelength are used to average the microscopic quantities. The first term of Eq.(3.70) is the local contribution whose origin can be found in the sheet of non-linear polarization placed at the position z = 0 :

$$\vec{P}_S(\vec{r},t) = \vec{P}_S(2\omega)\exp\left(2i\vec{\kappa}.\vec{R}\right)\exp(-2i\omega t)\delta(z-0) \tag{3.71}$$

We have here assumed a monochromatic incident wave, only taking the component oscillating at the frequency 2ω :

$$\vec{P}_S(2\omega) = \frac{1}{2}\varepsilon_0\chi_S : \vec{E}_m(z=0)\vec{E}_m(z=0) \tag{3.72}$$

We have emphasized the *z*-dependence of the electric field vector for clarity, indicating only that the fields are taken within the inner slab. In Eq.(3.71), we have also used the vector $\vec{\kappa}$, the component in the plane of the interface of the fundamental wavevector $\vec{k}^{\omega}$, and the two-dimensional space vector $\vec{R}$ lying in the plane of the interface :

$$\vec{\kappa} = \kappa\,\vec{e}_x$$

$$\kappa = \frac{\omega}{c}\sqrt{\varepsilon_m^{\omega}}\sin_m^{\omega} \tag{3.73}$$

The second part of Eq.(3.70) gives the bulk terms, also called the nonlocal terms :

$$\vec{P}^{(2)}_{bulk}(\vec{r},t) = -\vec{\nabla}.\vec{\vec{Q}}^{(2)}(\vec{r},t) + \frac{\mu_0}{i\omega}\vec{\nabla}\times\vec{M}^{(2)}(\vec{r},t) + \ldots \tag{3.74}$$

The second term in this equation will be neglected hereafter since the magnetic contribution is negligible compared to the electric one in the present problem. In homogeneous, non magnetic, centrosymmetric media and for incident monochromatic plane waves, the divergence of the nonlinear electric quadrupole polarisation is written as follows:

$$\left[\vec{\nabla}.\vec{\vec{Q}}^{(2)}(\vec{r},t)\right]_i = \varepsilon_0\left[\gamma\nabla_i\left(\vec{E}.\vec{E}\right) + \beta\left(\vec{\nabla}.\vec{E}\right)E_i + \varsigma E_i\nabla_i E_i\right] + \varepsilon_0\left[\nabla_j\chi^{(2)}_{Q,ijkl}\right]E_k E_l \tag{3.75}$$

where

$$\beta = \chi^{(2)}_{Q,iijj} \tag{3.76}$$

$$\gamma = \frac{1}{2}\chi^{(2)}_{Q,ijij} \tag{3.77}$$

$$\varsigma = \chi^{(2)}_{Q,iiii} - \left(\chi^{(2)}_{Q,ijji} + \chi^{(2)}_{Q,iijj} + \chi^{(2)}_{Q,ijij} \right) \tag{3.78}$$

the parameters β and γ characterizing the harmonic response of an isotropic medium independent of the orientation of the medium [9]. The parameter ς is due to a possible anisotropy of the medium [33]. Since we assume an isotropic medium, the third term in Eq.(3.75) vanishes. In a homogeneous medium, the second term of Eq.(3.75) vanishes also, due to Maxwell equation :

$$\vec{\nabla}.\vec{E} = \frac{1}{\varepsilon_0 \varepsilon}\vec{\nabla}.\vec{D} = 0 \tag{3.79}$$

Under these conditions Eq.(3.75) is then written :

$$\left[\vec{\nabla}.\vec{Q}^{(2)}(\vec{r},t) \right]_i = \varepsilon_0 \left[\gamma \nabla_i \left(\vec{E}.\vec{E} \right) \right] + \varepsilon_0 \left[\nabla_j \chi^{(2)}_{Q,ijkl} \right] E_k E_l \tag{3.80}$$

This equation contains both the field gradient contribution and the susceptibility tensor gradient contribution. The field gradient contribution has in turn two terms corresponding to the two regions where it originates. Assuming different optical constants in the bulk of the media and within the inner slab, we have to consider two regions of graded optical index, as shown in Figure 3.2. In the three layer model used here, we describe three media, media 1 and 2 and the interfacial region containing the nonlinear polarisation sheet. The first region

expands from the bulk of medium 1 to the inner slab at the plane $z = t_1$ and the second one from the bulk of medium 2 to the inner slab at the plane $z = t_2$. These regions of optical index inhomogeneity give rise to field gradients and the corresponding nonlinear polarization can be written with the explicit dependence on the region where the fields are considered. Since media 1 and 2 are considered homogeneous, we can assume that the optical index only varies within the regions $[t_1, T_1]$ and $[t_2, T_2]$. However, the variation of the dielectric constant in these two regions is unknown. The polarisation equation is then given by:

$$P_{fg}^{(2)}(\gamma,t) = \frac{1}{2}\varepsilon_0\gamma_1\nabla\left[E_1(r,t).E_1(r,t)\right] + \frac{1}{2}\varepsilon_0\gamma_2\nabla\left[E_2(r,t).E_2(r,t)\right] \tag{3.81}$$

The subscript *fg* denotes "field gradient" and the field subscripts denotes the medium where they are taken. The parameter γ_i scales the nonlinear bulk response of the medium *i*. In a metallic medium, its value is obtained using the free electron gas model described above from Eq.(3.55) :

$$\gamma_b = -\frac{e\,d}{8m\omega^2}\varepsilon_0\left(\varepsilon^{\omega} - 1\right) \tag{3.82}$$

Eq.(3.82) therefore introduces the phenomenological parameter *d* that accounts for the bulk magnitude contribution. This parameter is expected to be equal to 1 for perfect metals. Finally, the susceptibility tensor gradient contribution is given as follows [33] :

$$P_{sg}^{(2)}(r,t) = \frac{1}{2}\varepsilon_0\nabla\left[\chi_Q^{(2)}(r,t)\right] : E(r,t)E(r,t) \tag{3.83}$$

where the susceptibility gradient can also be written according to the two interface regions on both sides of the nonlinear polarization sheet. In the model presented in this chapter, we will neglect this contribution.

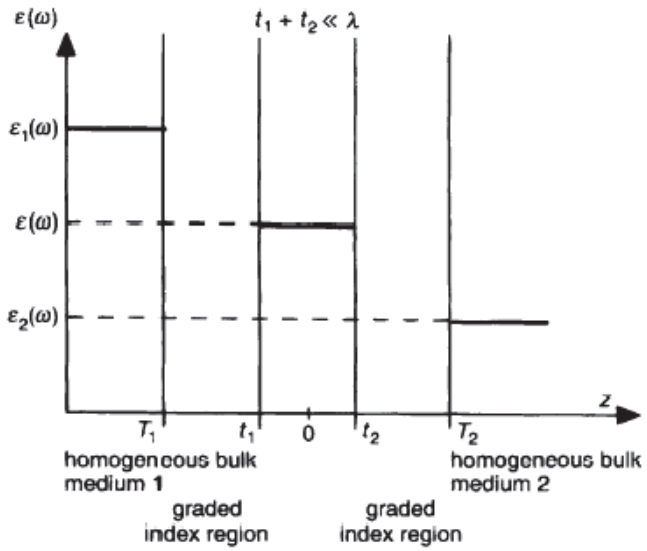

Figure 3.2 : schematics of the different regions in the vicinity of the interface (see.[20])

In conclusion to this paragraph, we will consider two contributions in the nonlinear polarization: a surface contribution, or local term, $\vec{P}_S(\vec{r},t)$ and a bulk contribution or nonlocal term, $P_{fg}^{(2)}(r,t)$.

3.4.2. Surface contributions

We assume that the interface belongs to the ∞m crystal group. The interface is therefore considered as isotropic and any rotation around the surface normal will leave the interface unchanged. The three unique non vanishing susceptibility tensor elements are then [34] :

$$\chi_{S,\perp\perp\perp} = \chi_{S,zzz} \tag{3.84}$$

$$\chi_{S,\perp///} = \chi_{S,zxx} = \chi_{S,zyy} \tag{3.85}$$

$$\chi_{S,///\perp} = \chi_{S,xxz} = \chi_{S,yyz} = \chi_{S,xzx} = \chi_{S,yzy} \tag{3.86}$$

The intensity arising from this surface contribution is given for the *S* and *P* polarisation configurations as follows:

$$I_S^{ED} = K\left|a_1\chi_{S,///\perp}\sin(2\gamma)\right|^2 I^2 \tag{3.87}$$

$$I_P^{ED} = K\left|(a_2\chi_{S,///\perp} + a_3\chi_{S,\perp///} + a_4\chi_{S,\perp\perp\perp})\cos^2\gamma + a_5\chi_{S,\perp///}\sin^2\gamma\right|^2 I^2 \tag{3.88}$$

where K is a constant depending on the experimental geometry and absolute constants, I is the fundamental intensity and γ is the input polarisation angle. The $\gamma = 0$ angle corresponds to the p-polarised incident field angle and the angle $\gamma = \pi / 2$ corresponds to the s-polarised field. All the a_i coefficients are given in Table 3.1. The details of the calculations are given in reference [20, 35].

Coefficients	Isotropic surface
Electric dipole approximation	$a_1 = \tilde{e}_Y^{\omega}\ \tilde{e}_Z^{\omega}\ \tilde{e}_Y^{\Omega}$ $a_2 = -2\tilde{e}_Z^{\omega}\ \tilde{e}_X^{\omega}\ \tilde{e}_X^{\Omega}$ $a_3 = \tilde{e}_X^{\omega}\ \tilde{e}_X^{\omega}\ \tilde{e}_Z^{\Omega}$ $a_4 = \tilde{e}_Z^{\omega}\ \tilde{e}_Z^{\omega}\ \tilde{e}_Z^{\Omega}$ $a_5 = \tilde{e}_Y^{\omega}\ \tilde{e}_Y^{\omega}\ \tilde{e}_Z^{\Omega}$
Fundamental $\vec{\tilde{e}}^{\omega}$ and	$\tilde{e}_X^{\omega} = t_{1m}^{p}\left(r_{m2}^{p} - 1\right)\cos\theta_m^{\omega}$ $\tilde{e}_Y^{\omega} = t_{1m}^{s}\left(r_{m2}^{s} + 1\right)$ $\tilde{e}_Z^{\omega} = t_{1m}^{p}\left(r_{m2}^{p} + 1\right)\sin\theta_m^{\omega}$
Harmonic vectors $\vec{\tilde{e}}^{\Omega}$	$\tilde{e}_X^{\Omega} = \left(R_{m2}^{p} - 1\right)T_{m1}^{P}\cos\theta_m^{\Omega}$ $\tilde{e}_Y^{\Omega} = \left(R_{m2}^{s} + 1\right)T_{m1}^{S}$ $\tilde{e}_Z^{\Omega} = \left(R_{m2}^{p} + 1\right)T_{m1}^{P}\sin\theta_m^{\Omega}$

Table3. 1: Isotropic a_i coefficients calculated in the electric dipole approximation. $r_{ij}^{s/p}$ and $t_{ij}^{s/p}$ are the Fresnel coefficients for reflection and transmission at the fundamental frequency ω across the interface from medium i to medium j in the case of a S- and a P-polarised wave respectively. $R_{ij}^{s/p}$ and $T_{ij}^{s/p}$ are the Fresnel coefficients at the harmonic frequencyΩ. θ_m^{ω} and θ_m^{Ω} are respectively the incidence and the reflection angles in the interfacial slab.

3.4.3. Bulk contribution from field gradients

It is possible to recast the bulk contribution into an effective tensor as [20] :

$$\chi_{eff,\perp//\!/} = \chi_{S,\perp//\!/} + \frac{b_1}{a_5}\left(\gamma_{b1}^{equiv.} + \gamma_{b2}^{equiv.}\right) \tag{3.89}$$

$$\chi_{eff,\perp\perp\perp} = \chi_{S,\perp\perp\perp} + \left(\frac{b_2}{a_4} - \frac{a_3 b_1}{a_4 a_5}\right)\left(\gamma_{b1}^{equiv.} + \gamma_{b2}^{equiv.}\right) \tag{3.90}$$

where

$$b_1 = (1 + r_{m2}^{s})(t_{1m}^{s})^2 \, \tilde{e}_z^{\Omega} \tag{3.91}$$

$$b_2 = \left[(1 + r_{m2}^{p})^2 + 2(\sin^2\theta_m^{\omega} - \cos\theta_m^{\omega}) r_{m2}^{p}\right](t_{1m}^{p})^2 \, \tilde{e}_z^{\Omega} \tag{3.92}$$

As seen previously, $r_{ij}^{s/p}$ and $t_{ij}^{s/p}$ are the Fresnel coefficients for reflection and transmission at the fundamental frequency ω across the interface from medium *i* to medium *j* in the case of a s- and a p-polarised wave respectively. The factors $\gamma_{b1}^{equiv.}$ and $\gamma_{b2}^{equiv.}$ are written as a function of the reflection and transmission Fresnel coefficients of the harmonic wave. Through Eqs.(3.89) and (3.90), we observe, as expected, that only the elements $\chi_{eff,\perp//\!/}$ and $\chi_{eff,\perp\perp\perp}$ have a bulk contribution due to field gradients. We can rewrite Eqs.(3.87) and (3.88) using these effective tensor elements :

$$I_S = K\left|a_1 \chi_{S,//\!/\perp} \sin(2\gamma)\right|^2 I^2 \tag{3.93}$$

$$I_P = K\left|(a_2 \chi_{S,//\!/\perp} + a_3 \chi_{eff,\perp//\!/} + a_4 \chi_{eff,\perp\perp\perp})\cos^2\gamma + a_5 \chi_{eff,\perp//\!/} \sin^2\gamma\right|^2 I^2 \tag{3.94}$$

3.4.4. Case of the dielectric - metallic interface

We have now the expressions of the SH intensity in the S-out and P-Out polarization configurations including the surface and the bulk contributions. Using a unique $\gamma_b^{equiv.}$

parameter for the bulk contribution since one of the bulk medium is air or liquid, we have three unique non vanishing susceptibility tensor elements given by:

$$\chi_{eff,\perp///} = \chi_{S,\perp///} + \frac{b_1}{a_5}\gamma^{equiv.} \tag{3.95}$$

$$\chi_{eff,\perp\perp\perp} = \chi_{S,\perp\perp\perp} + \left(\frac{b_2}{a_4} - \frac{a_3 b_1}{a_4 a_5}\right)\gamma^{equiv.} \tag{3.96}$$

$$\chi_{eff,///\perp} = \chi_{S,///\perp} \tag{3.97}$$

Besides, we also have $\chi_{S,\perp///} = 0$ [28], as shown in the literature. The final step of the derivation is thus to express the SH intensities given above as a function of the Rudnick and Stern parameters *a, b* and *d* appearing from the free electron gas model. Using the hydrodynamic model, we have defined three contributions in the nonlinear polarisation:

$$\chi_{s,\perp\perp\perp} = \frac{e\varepsilon_0 a\left(\varepsilon^{\omega} - 1\right)}{4m\omega^2} \tag{3.98}$$

$$\chi_{s,///\perp} = \frac{e\varepsilon_0 b\left(\varepsilon^{\omega} - 1\right)}{2m\omega^2} \tag{3.99}$$

$$\gamma_b^{equiv.} \propto \gamma_b = -\frac{e\,d}{8m\omega^2}\varepsilon_0\left(\varepsilon^{\omega} - 1\right) \tag{3.100}$$

Using these expressions, we get by identification:

$$I_S = K\left|a_1 \frac{e\varepsilon_0(\varepsilon - 1)b}{2m\omega^2}\sin(2\gamma)\right|^2 I^2 \tag{3.101}$$

and

$$I_P = K\left|(a_2 \frac{e\varepsilon_0(\varepsilon - 1)b}{2m\omega^2} + a_4 \frac{e\varepsilon_0(\varepsilon - 1)a}{4m\omega^2} + b_2\ \gamma_b^{equiv.})\cos^2\gamma + b_1\ \gamma_b^{equiv.}\sin^2\gamma\right|^2 I^2 \tag{3.102}$$

These equations constitutes the basic equations to develop the SH response from the interface studied in this work within the framework of the nonlinear currents.

3.5. Conclusion

The hydrodynamic model has been presented to get an expression for the nonlinear polarisation from both the interface and the bulk metal. The surface contribution parallel and perpendicular to the plane of the surface arises from the non centrosymmetry of the interface whereas the bulk contribution arises from the skin effect in the metal. An overview of the three layer model is also presented from which the effective tensor elements and the S and P polarisation equations are given. Then a relation between the $a(\omega)$, $b(\omega)$ and $d(\omega)$ parameters obtained in the hydrodynamic model and the effective susceptibility tensor elements is found. The overall SHG intensity equations will be used in the following chapters to adjust the experimental data for the *S* and *P* polarisation curves recorded from the interfaces in the presence of metallic nanoparticles.

References:

[1] A. E. H. P. A. Franken, C. W. Peters, and G. Weinreich, "Generation of Optical Harmonics," *Phys. Rev. Lett.,* vol. 7, p. 118, 1961.

[2] N. Bloembergen and P. S. Pershan, "Light Waves at the Boundary of Nonlinear Media," *Phys. Rev.,* vol. 128, pp. 606-606, 1962.

[3] F. Brown, R. E. Parks, and A. M. Sleeper, "Nonlinear Optical Reflection from a Metallic Boundary," *Phys. Rev. Lett.,* vol. 14, p. 1029, 1965.

[4] S. S. Jha, "Nonlinear Optical Reflection from a Metal Surface," *Phys. Rev. Lett.* vol. 15, p. 412, 1965.

[5] S. S. Jha, "Theory of Optical Harmonic Generation at a Metal Surface," *Phys. Rev.,* vol. 140, p. A2020, 1965.

[6] N. Bloembergen and Y. R. Shen, "Optical Nonlinearities of a Plasma," *Phys. Rev.,* vol. 141, p. 298, 1966.

[7] F. Brown and R. E. Parks, "Magnetic-Dipole Contribution to Optical Harmonics in Silver," *Phys. Rev. Lett.,* vol. 16, p. 507, 1966.

[8] C. H. Lee, R. K. Chang, and N. Bloembergen, "Nonlinear Electroreflectance in Silicon and Silver," *Phys. Rev. Lett.,* vol. 18, p. 167, 1967.

[9] N. Bloembergen, R. K. Chang, S. S. Jha, and C. H. Lee, "Optical Second-Harmonic Generation in Reflection from Media with Inversion Symmetry," *Phys. Rev.,* vol. 174, pp. 813-813, 1968.

[10] F. Brown and M. Matsuoka, "Effect of Adsorbed Surface Layers on Second-Harmonic Light from Silver," *Physical Review,* vol. 185, p. 985, 1969.

[11] J. Rudnick and E. A. Stern, "Second-Harmonic Radiation from Metal Surfaces," *Phys. Rev. B,* vol. 4, pp. 4274-4274, 1971.

[12] J. E. Sipe, V. C. Y. So, M. Fukui, and G. I. Stegeman, "Analysis of second-harmonic generation at metal surfaces," *Phys. Rev. B,* vol. 21, p. 4389, 1980.

[13] M. Corvi and W. L. Schaich, "Hydrodynamic-model calculation of second-harmonic generation at a metal surface," *Physical Review B,* vol. 33, p. 3688, 1986.

[14] W. L. Schaich and A. Liebsch, "Nonretarded hydrodynamic-model calculation of second-harmonic generation at a metal surface," *Phys. Rev. B,* vol. 37, p. 6187, 1988.

[15] H. W. K. Tom and G. D. Aumiller, "Observation of rotational anisotropy in the second-harmonic generation from a metal surface," *Phys. Rev. B,* vol. 33, p. 8818, 1986.

[16] V. Mizrahi and J. E. Sipe, "Phenomenological treatment of surface second-harmonic generation," *J. Opt. Soc. Ame. B,* vol. 5, pp. 660-667, 1988.

[17] J. E. Sipe, "New Green-function formalism for surface optics," *J. Opt. Soc. Ame. B,* vol. 4, pp. 481-489, 1987.

[18] P. Guyot-Sionnest and Y. R. Shen, "Local and nonlocal surface nonlinearities for surface optical second-harmonic generation," *Phys. Rev. B,* vol. 35, p. 4420, 1987.

[19] A. Liebsch and W. L. Schaich, "Second-harmonic generation at simple metal surfaces," *Phys. Rev. B,* vol. 40, p. 5401, 1989.

[20] P. F. Brevet, "Phenomenological three-layer model for surface second-harmonic generation at the interface between two centrosymmetric media," *J. Chem. Soc., Farad. Transc.,* vol. 92, pp. 4547-4554, 1996.

[21] M. G. Weber and A. Liebsch, "Theory of second-harmonic generation by metal overlayers," *Phys. Rev. B,* vol. 36, p. 6411, 1987.

[22] P. G. Dzhavakhidze, A. A. Kornyshev, A. Liebsch, and M. Urbakh, "Theory of second-harmonic generation at the metal-electrolyte interface," *Phys. Rev. B,* vol. 45, pp. 9339-9339, 1992.
[23] W. Schmickler and M. Urbakh, "Electronic distribution and second-harmonic generation at the metal-electrolyte interface," *Phys. Rev. B,* vol. 47, p. 6644, 1993.
[24] G. T. Boyd, T. Rasing, J. R. R. Leite, and Y. R. Shen, "Local-field enhancement on rough surfaces of metals, semimetals, and semiconductors with the use of optical second-harmonic generation," *Phys. Rev. B,* vol. 30, p. 519, 1984.
[25] P. Guyot-Sionnest, A. Tadjeddine, and A. Liebsch, "Electronic distribution and nonlinear optical response at the metal-electrolyte interface," *Phys. Rev. Lett.,* vol. 64, p. 1678, 1990.
[26] C. K. Chen, A. R. B. de Castro, and Y. R. Shen, "Surface-Enhanced Second-Harmonic Generation," *Phys. Rev. Lett.,* vol. 46, pp. 145-145, 1981.
[27] D. Krause, C. W. Teplin, and C. T. Rogers, "Optical surface second harmonic measurements of isotropic thin-film metals: Gold, silver, copper, aluminum, and tantalum," *J. Appl. Phys.,* vol. 96, pp. 3626-3634, 2004.
[28] K. A. O'Donnell and R. Torre, "Characterization of the second-harmonic response of a silver–air interface," *New Joural of Phys.,* vol. 7, pp. 154-154, 2005.
[29] F. SANCHEZ, *Optique non-lineaire Cours et problemes resolus*: ellipses, 1999.
[30] P.-F. Brevet, *Surface second harmonic generation*, 1997.
[31] P. Halevi, "Hydrodynamic model for the degenerate free-electron gas: Generalization to arbitrary frequencies," *Phys. Rev. B,* vol. 51, pp. 7497-7497, 1995.
[32] C. Kittel, *Physique de l'etat solide*: DUNOD, 1983.
[33] P. Guyot-Sionnest and Y. R. Shen, "Bulk contribution in surface second-harmonic generation," *Phys. Rev. B,* vol. 38, pp. 7985-7985, 1988.
[34] P. Guyot-Sionnest, W. Chen, and Y. R. Shen, "General considerations on optical second-harmonic generation from surfaces and interfaces," *Phys. Rev. B,* vol. 33, p. 8254, 1986.
[35] G. Gassin-Martin, "Etude statique et dynamique par réflectance linéaire et Génération de Second Harmonique de films de molécules et de nanoparticules métalliques à l'interface air/eau," 2007.

Chapter 4

Linear optical response of silver nanoparticles films at the air/liquid interface

4.1. Introduction

Assembly and self organisation of alkanethiol-capped silver nanoparticles has taken the attention of lots of groups around the world owing to the possibility to obtain compact two-dimensional films. This is principally due to the availability of particle sample solutions with excellent shape and size monodispersity [1, 2] [3]. The Langmuir technique has been one of the methods used to achieve the formation of those organised nanoparticles films at the air/water interface. It is a rather powerful approach with several unique characteristics. First, large area films can be formed which can be transferred onto solid substrates with the Langmuir-Blodgett technique. Second, the average interparticle distance can be tuned through control of the compression process. A wide range of physical properties of the films can be obtained, in particular the insulator-to-metal transition has been observed for silver nanocrystals [4, 5] by the group of Heath. This same group has performed theoretical calculations to investigate the modifications arising from disorder [6]. This disorder arises from the fact that the synthesized particles can never be exactly identical, even if the size distribution is as narrow as possible.

In a two dimensional assembly, the hexagonal assembly for example, the main variables are the nanocrystal diameter, the average interparticle separation, the nature of the surfactant molecules as well as the domain size. The interparticle distance plays an important role in controlling the nature of the interaction between neighbouring particles. A change from a classical coupling description to quantum coupling one must take place when the silver particle separation distance is less than 1 nm, for instance [7]. In fact, the distance between constituent atoms determines which type of coupling takes place. Quantum coupling is operative once the atoms are in close proximity (few Angstroms) and the electrons are shared

between sites, thus having what is called exchange interactions. This latter work was followed by subsequent studies using impedance spectroscopy as a function of the interparticle distance [8]. The same group also emphasized that upon the increase in the concentration of nanoparticles used to form the monolayer, spontaneous reorganisation of the self assembled domains from circular clusters to stripes takes place. These experimental results were verified by simulations. The reorganisation has been described as resulting from competition between attraction, causing the aggregation of the particles, and a long range repulsion limiting the aggregations to finite domains [9]. Phase diagrams of silver passivated nanoparticles were therefore investigated as a function of the particle size, the thickness of the surfactant layer, the nature and the size distribution of the metal core. An excess volume term related to the length of the ligand and the size of the metal core could thus be defined. Different ranges of this excess volume were studied, yielding phase diagrams differing owing to the value of this excess volume. Out of the TEM images, the distance separating the silver cores surrounded by a dodecanethiol surfactant layer was found equal to about 12-20 Angstroms [10]. Another study using scanning tunnel microscopy showed that the density of states calculation for interparticle distance larger than 1.28 nm was temperature dependent while it was temperature independent when the interparticle distance was only about 0.5 nm. This transition was in particular taken as a signature of the metal-insulator transition [11]. An early publication presented a calculation for the complex dielectric function $\varepsilon(\omega) = \varepsilon_1(\omega) + i\varepsilon_2(\omega)$ of a monolayer and a bilayer Langmuir film of silver alkanethiol nanoparticles. Upon the MI transition, the real part $\varepsilon_1(\omega)$ *was* acquiring a negative value [12]. This work was followed by a study of the effects of the size distribution of the particles on the insulator-to-metal transition. It was predicted that the transition was taking place for dodecanethiol-capped silver nanoparticles with an average diameter of about 7 nm when the width of the size distribution is less than 3% [13]. Recently, Wormeester et *al*. reported the ellipsometric identification of the collective optical properties of silver nanoarrays on a highly oriented pyrolytic graphite substrate. They showed that at an angle of incidence of 70°, the plasmon resonance excited by the electric field component perpendicular to the surface is observed while for lower angles of incidence only the plasmon resonance excited by the electric field component parallel to the surface was observed. In this case, identical behaviours for the *S*- and *P*- polarized reflectivity is observed [14].

In addition to silver nanoparticles films, gold nanoparticles films were prepared by the same Langmuir technique. The synthesis of gold nanoparticles stabilised by various surfactants has indeed been a field of interest over the last years [15-18]. Optical effects associated with the assembly of $Au@SiO_2$ particles into densely packed film have been studied. It has been shown that upon the increase of the shell thickness, transformation of the film from a transparent insulating glass into an opaque metallic gold film was taking place. The use of the Maxwell-Garnett (MG) model was then helpful to predict the shift in the reflectance peak as a function of the metal volume [19] and the layer numbers [20]. Pressure area isotherms and X-ray measurements were also performed on dodecanethiol-capped gold Langmuir monolayers. Reversibility in such a system was recorded for film containing excess thiols and this was explained in terms of the ligand repulsion overcoming the Van der Waals interparticle attraction [21]. Finally, metallic nanorods are gaining an interest in the recent years since the development in their synthesis is now becoming reproductive and highly controlled. Hence, size monodispersity is now reached. Nanorods assembly has also been pursued over the past ten years [22, 23] for metallic and non-metallic rods. We will present in this chapter the linear response of gold nanorods films at the air/water interface.

In this chapter, we have been interested in the study of the linear optical response of metallic nanoparticles films at the air/water interface. Through reflectance and transmittance measurements, we have investigated the interactions between the particles and finally observed a transition, probably an insulator to metal transition. The MI transition is indeed expected to be accompanied by strong modifications in the linear optical properties of the film. The linear optical properties will also be useful for the nonlinear studies on these metallic films and these studies will be presented in the next chapter. Several samples were used, silver and gold nanoparticles, both nanospheres and nanorods. Different chain lengths were used to investigate the role of the interparticle distance in modifying the properties of an insulating film upon compression. The first part of this chapter is devoted to the linear response of spherical nanoparticles. The second part presents the results regarding gold nanorods whereas the third one is concerned with a Maxwell Garnett approach to the problem.

4.2. Linear response of spherical silver nanoparticles film

4.2.1. Experimental setup

The principles of the linear optical set-up are given in Figure 4.1. The reflectance or absorbance of the metallic nanoparticles monolayer at the air/water interface was recorded during the compression of the film. The transmittance and reflectance measurements were realized at normal incidence using a microscope objective.

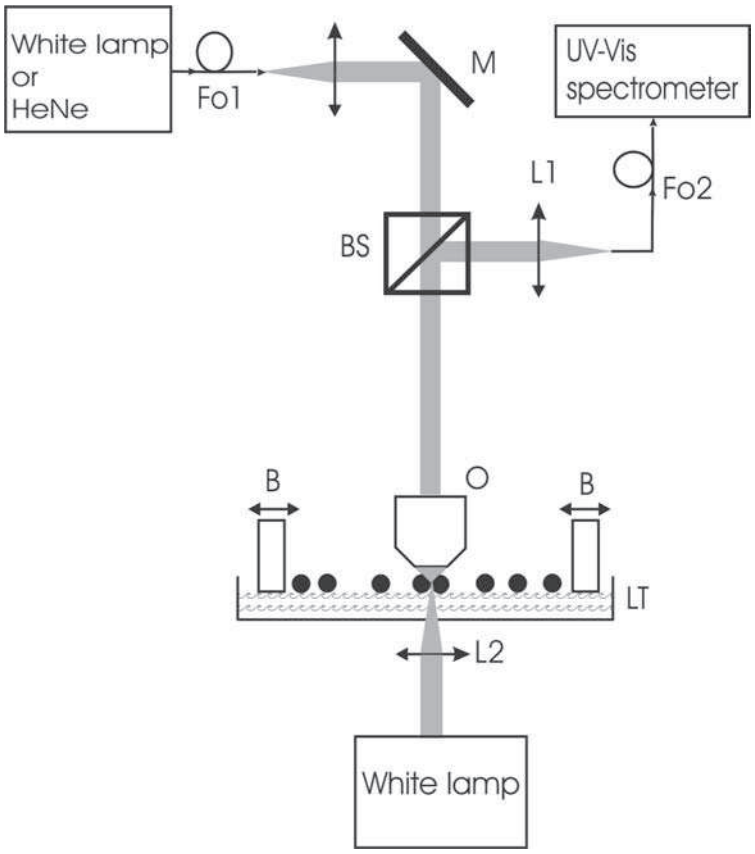

Figure 4.1 : Principle of the linear experimental set-up. LT: Langmuir trough, B: barriers, O: objective, L1, L2: lenses, BS: beam splitter, M: Mirror, FO1, FO2: optical fibers.

White light from a Deuterium-halogen lamp was coupled to the Langmuir trough through an optical fibre. The light exiting this fibre was sent to a metallic mirror (M) where it was reflected. The light then passed through a 50/50 beam splitter and was directed onto the film through a microscopic objective (X16, NA=0.32). The light reflected from the film was passed through the beam splitter a second time and collected through another fibre and sent to

a UV-visible spectrometer (Ocean optics). A diode array allowed the direct recording of the UV-visible absorption or reflectance spectra. Commercial software was used to control the spectrometer as well as the Langmuir trough to register the surface pressure/ area isotherms. For the absorbance of the film, a second white light lamp was placed under the trough to obtain the transmission spectra. The absorbance of the film was then obtained from the transmission spectra.

4.2.2. Reflectance of pure air/water interface

To obtain the reflectance of the film, it was necessary to first record a reference spectrum. We have taken the reflection spectrum of the white light from the pure water subphase as our reference spectrum. A typical reflection spectrum on the pure water surface is given in Figure 4.2.

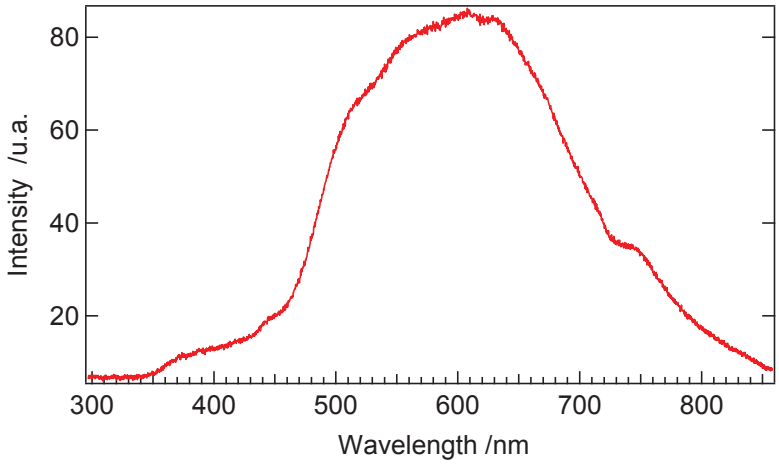

Figure 4.2 : Reflection spectrum on pure water surface.

The reflectance of the pure water surface is given in Figure 4.3 as a function of wavelength. The values have been obtained from the refractive index of water [24] and the Fresnel formula:

$$R = \left| \frac{n_w - n_1}{n_w + n_1} \right|^2 \tag{4.1}$$

with $n_1 = 1$ for the upper medium which is air .

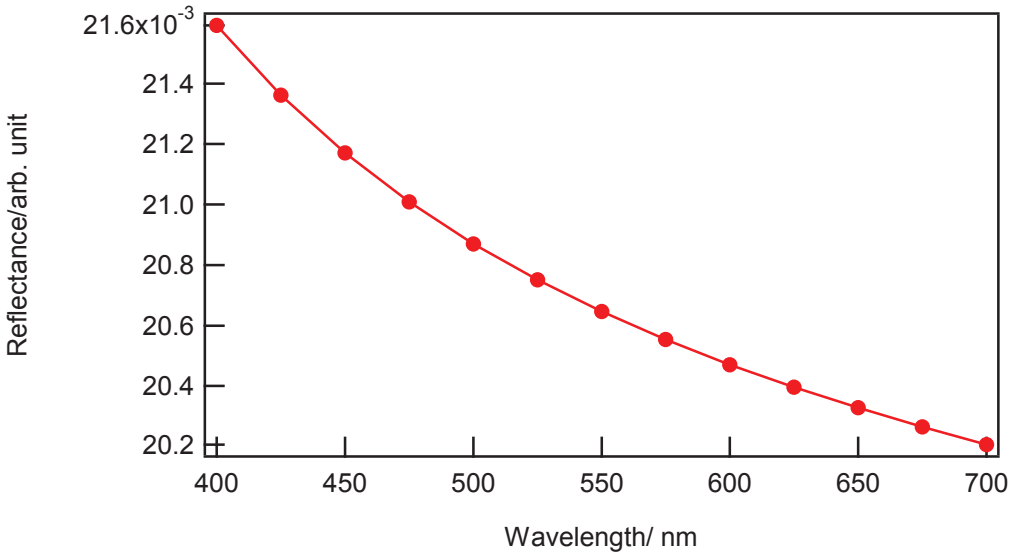

Figure 4.3: Reflectance of a pure water surface (calculation obtained from the values of the refractive index of neat water[24].

The variation of the reflectance in the UV-visible spectral domain 400 – 700 nm is relatively small, only 6%. For the calculation of the reflectance R_{film} of the film, we have used the mean value of R_w = 0.0207 for the neat water surface at all wavelengths using the refractive index n_w = 1.3356, hence neglecting dispersion [24]. Once the reference spectrum I_W was obtained, the reflectance of the film was obtained by measuring the reflection spectrum I_{film} and using the following formula:

$$R_{film} = R_w \frac{I_{film}}{I_W} \tag{4.2}$$

Furthermore, in order to record the absorbance of the film, a white light lamp was placed under the trough. The transmission spectrum of the white light through the pure water subphase was taken as our reference. The absorbance was calculated using Beer-Lambert law as:

$$A = \log_{10}\left(\frac{I_0}{I}\right) \tag{4.3}$$

where I_0 is the reference spectrum, namely that of the transmission through the pure water phase, and I the transmission spectrum of the nanoparticles film.

4.2.3. Silver spherical nanoparticles film

The reflectance of dodecanethiol-capped spherical silver nanoparticles films was first studied. In fact, and as mentioned before, the alkanethiol chains length could be varied from 3 to 18 carbons thereby varying the minimum interparticle distance. Films formed with particles coated with long chain thiols were stable against attractive interactions whereas films made from particles coated with short chain thiols were less stable. Two kinds of silver particles were eventually investigated in details: particles passivated with dodecanethiols (C_{12}) and particles passivated with hexanethiols (C_6).

C_{12} chains are considered as intermediate chains, yielding edge-edge distances between particles approximately equal to the length of a single chain [25]. A silver spherical nanoparticles film was therefore formed using synthesised dodecanethiol-capped spherical silver nanoparticles with an average diameter of about 8 ± 1 nm. Commercial particles with an average diameter of 10 nm (Sigma-Aldrich) and a similar capping layer were also used. For the particles synthesized in our laboratory, the number of particles needed to form a monolayer for the 15 cm² area of the closed trough was estimated to be about ~2.13×10^{13} particles for a close-packed hexagonal lattice. Several amounts of particles corresponding to average surface densities below and above this critical value were deposited on the water surface. For the hexanethiol-capped silver nanoparticles, the number of particles needed to form a close-packed hexagonal lattice for the 15 cm² area of the closed trough was estimated to be the same as that capped with dodecanethiol. In fact, the length of a dodecanethiol chain is about 1 nm, and that of hexanethiol is about 0.5nm. This chain should be taken into consideration upon calculating the number of particles needed for the full coverage, but since the size distribution of the synthesised particles was large, and the variation of the diameter was 8±1 nm, this chain length contribution was ignored and the calculations were performed assuming a diameter of 9 nm. The calculation of the volume needed to have a full coverage at 15 cm² is detailed below. The main problem arising with the particles synthesized in our laboratory was the exact determination of the particles concentration. For this reason, commercial nanoparticles were also used. In that case, the number of particles needed to form

a monolayer for a closed trough area of 15 cm^2 was calculated to be 1.7×10^{13} particles. The concentration of this initial solution was 3.03×10^{17} particles/L. Figure 4.4 presents a scheme for a closed packed hexagonal lattice.

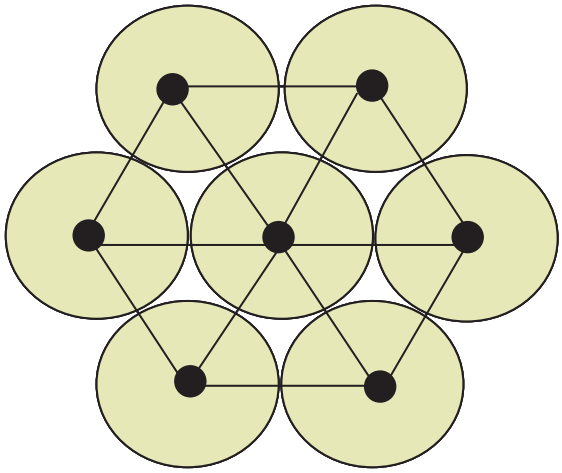

Figure 4.4: Scheme for a closed packed hexagonal lattice.

Here is present the detailed calculation for the home made dodecanethiol nanoparticles of diameter 8±1 nm. The diameter is set to 9 nm in order to take into consideration the chain length. The number of particles per unit cell for a hexagonal lattice is equal to 3 and the number of particles is calculated for a monolayer at an area of 15 cm².

$$N_{Hexagonal} = \frac{S_{trough}}{S_{unit}^{hcp}} \times n_0^{hcp} = \frac{15\times10^{-4}}{\frac{3\sqrt{3}}{2}d^2} \times 3 = \frac{15\times10^{-4}}{\frac{3\sqrt{3}}{2}(9\times10^{-9})^2} \times 3 = 2.13\times10^{13}\ particles \quad (4.4)$$

4.2.3.1. Synthesised dodecanethiol silver particles

4.2.3.1.1. Isotherm of the Langmuir film

The Langmuir trough is fabricated from polytetrafluroethylene (PTFE), a very hard and hydrophobic polymer. The trough had an area of 100 cm^2 with two motorized barriers. The trough was filled with the liquid phase, usually neat water ((Millipore water, 18MΩcm, pH 7). The particles solution was spread with a syringe drop by drop over the entire surface of the subphase. Then, with the closing of the barriers, the particles were allowed to come closer and to eventually form a compact monolayer. The surface pressure was recorded during the compression. It was measured by the method of the Wilhelmy plate, a strip of chromatography paper suspended at the air-water interface. The piece of paper is pulled down into the bulk of the sub-phase upon the increase of the surface tension. Since the number of

particles deposited on the surface was known, the surface pressure was therefore reported as a function of the area occupied by a single particle. Those plots of the surface pressure versus the area occupied per particle are known as pressure-area isotherms. These isotherms were registered at constant temperature using the thermostat system circulation connected to the trough. The thermostat was held at 12°C. Figure 4.5 presents an isotherm for a solution of silver dodecanethiol nanoparticles. The rate of the barrier motion was set to 5 cm^2/min. Since the optical measurements were taken at specific areas of the trough, the isotherm presents a sequence of pressure drops, see Figure 4.5. These pressure drops arise from the film rearrangements. The surface pressure recorded for this isotherm increases up to a value of 35 mN/m. These interactions were simultaneously monitored through the recording of the linear reflectance during the compression as presented in the following paragraph.

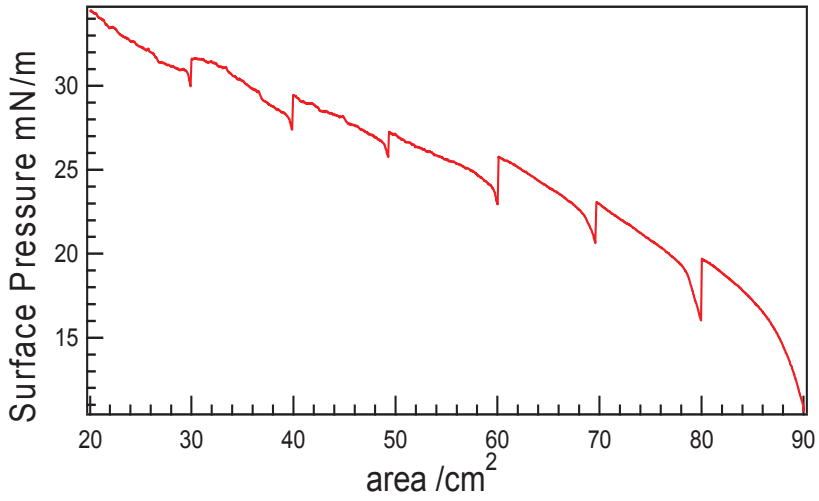

Figure 4.5: Isotherm taken after injecting 1.13×10^{11} *particles/cm². Each drop of surface pressure corresponds to an optical measurement.*

4.2.3.1.2. Reflectance versus compression

First of all, a reflectance spectrum of the clean water surface was taken as the reference spectrum. A defined initial amount of the synthesized silver nanoparticles was then injected into the trough at an open area of 100 cm² area. The barrier velocity was set to 5 cm²/min. Reflectance spectra were then taken at various trough areas, namely 90, 80…, 20 cm². The isotherm registered while performing these optical measurements given below in Figure 4.6 is given in Figure 4.5. The linear reflectance versus wavelength shown in Figure 4.6 corresponds to an initial surface density of 1.13×10^{11} particles/cm^2.

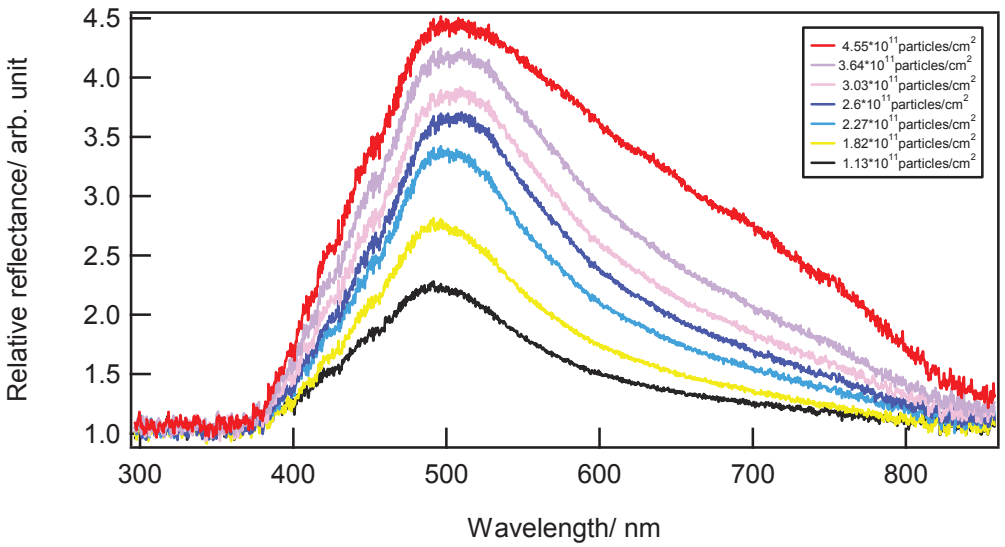

Figure 4.6: Linear reflectance versus wavelength at different trough areas for an initial density of 1.13×10^{11} *particles/cm².*

The optical signal fluctuated strongly, particularly at low average particle densities, *i.e.* at large trough areas. These fluctuations are clearly exhibited on Figure 4.7 where two spectra recorded at the same trough area of 80 cm² within 2 minutes time interval are presented. Averaging procedures were therefore used in the recording of these spectra. For small trough areas corresponding to higher average particle densities, the fluctuations almost vanished, yielding better optical data. Theses fluctuations arise from the inhomogeneity of the film in the laser spot and the Brownian diffusion and convection processes occurring in the film. A detailed study of these fluctuations has been discussed in reference [26] where correlation reflectance spectroscopy has been performed, revealing the inhomogeneous nature of the film and its dynamics. In particular a uniform translational flow along with the Brownian diffusion motion were observed.

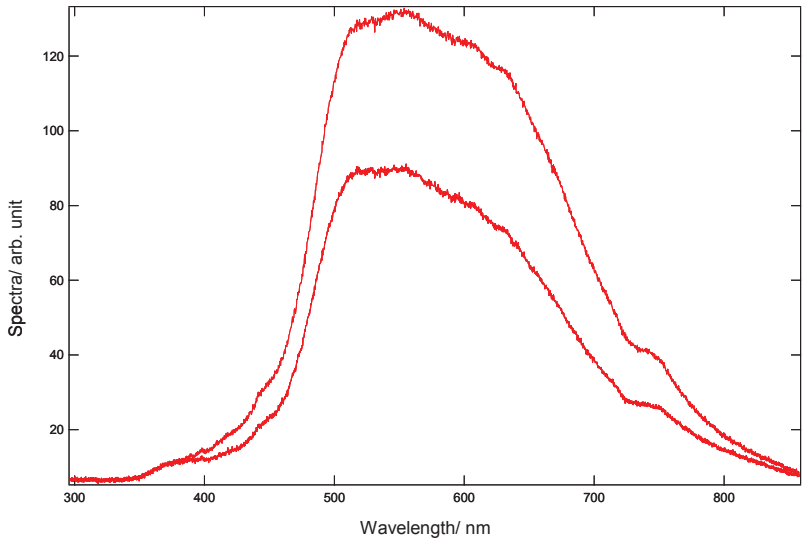

Figure 4.7: Fluctuation of the transmission spectrum at a trough area of 80cm^2. The spectra are recorded at 2 minutes interval

From the reflectance spectra given in Figure 4.6, we notice a small red shift of the maximum of the reflectance and the appearance of a shoulder at longer wavelengths. This behaviour is easily observed after the normalization of the reflectance spectra, as shown in Figure 4.8.

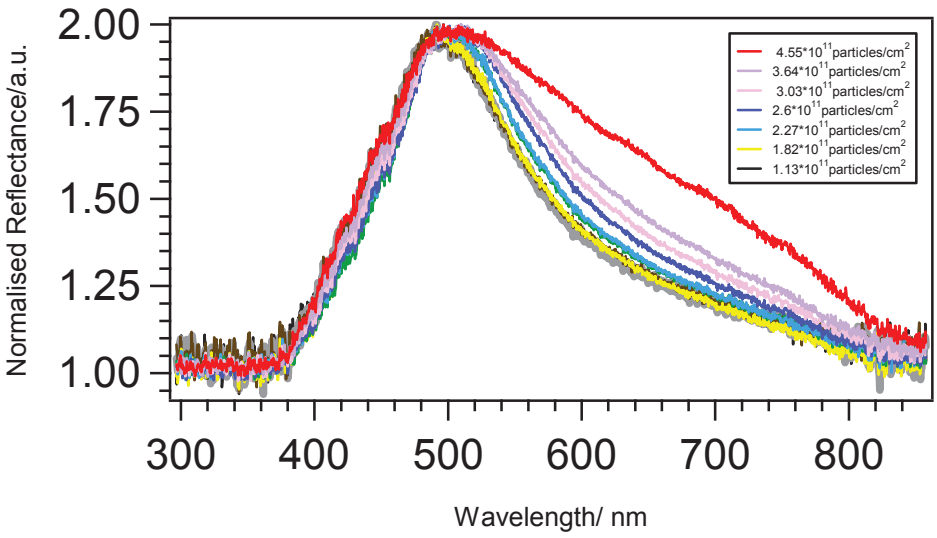

Figure 4.8: Normalized Reflectance versus wavelength at different areas.

Not all experiments presented such a signature of the particle interactions, probably because of the fluctuations due to the film inhomogeneities. Furthermore, it was observed that for low surface concentrations of the particles, the interactions between particles could be barely seen; see the initial low concentration reflectance spectra given in Figure 4.8. From the average

normalized reflectance spectra, the reflectance at 700 nm can be reported as a function of the average particle density. This wavelength corresponds to the centre position of the shoulder in the spectra of Figure 4.8. The reflectance increase at 700 nm with the average particle density is almost linear, see Figure 4.9. Similarly, the red shift of the wavelength of the maximum of the reflectance spectra is also linear with the average particle density of the film.

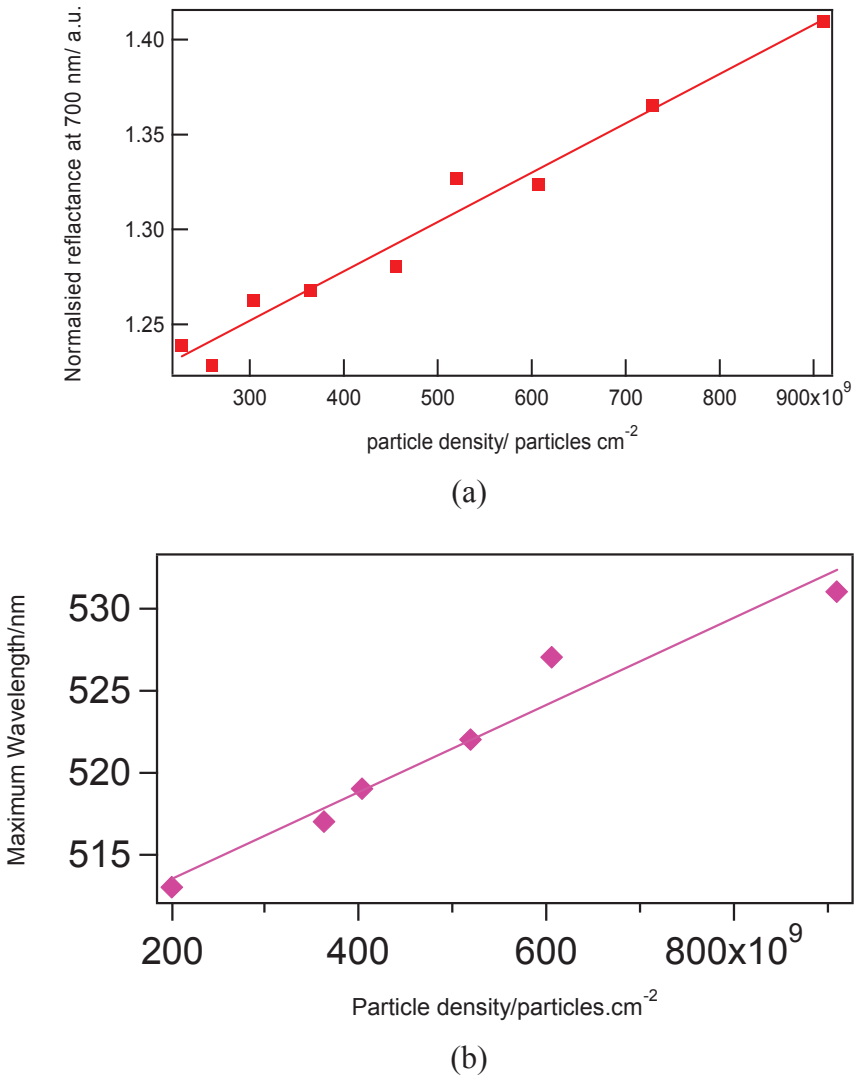

Figure 4.9: (a) Average normalized reflectance versus particle density at 700 nm, (b) Wavelength of the maximum reflectance versus particle density.

The presence of this shoulder at 650-700 nm and the red-shift of the wavelength of the maximum reflectance of the film are two indicators of the presence of interactions between particles in the film. Besides these initial additions, additions providing higher average surface densities were also performed. As mentioned above, the number of particles needed to

form a monolayer is ~2.13×10^{13} particles for the closed trough. Several additions below and above this critical value were added. We noticed then first an increase of the reflectance followed by a decrease, see Figure 4.10 where the reflectance versus wavelength is reported for an initial density of 2×10^{11} particles/cm² a density double that presented before.

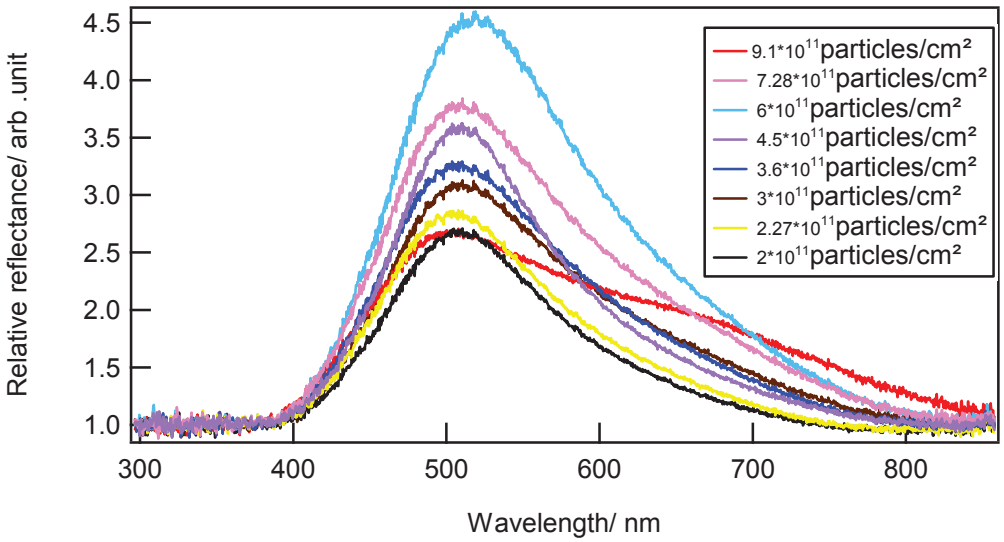

Figure 4.10: Relative reflectance versus wavelength for an initial density of 2×10^{11} particles/cm²

We notice that the decrease of the reflectance started at a concentration of ~0.73×10^{12}particles/cm². Several experiments were therefore performed at various initial densities and the average reflectance at 500 nm of all these experiments versus density is given in Figure 4.11. The average density at which the reflectance starts to decrease is about 0.8×10^{12} particles/cm². The reflectance saturates and starts to decrease before the critical value of the average surface density, an indication that defects like void areas can be present in the film. The decrease of the reflectance indicates also changes in the properties of the film.

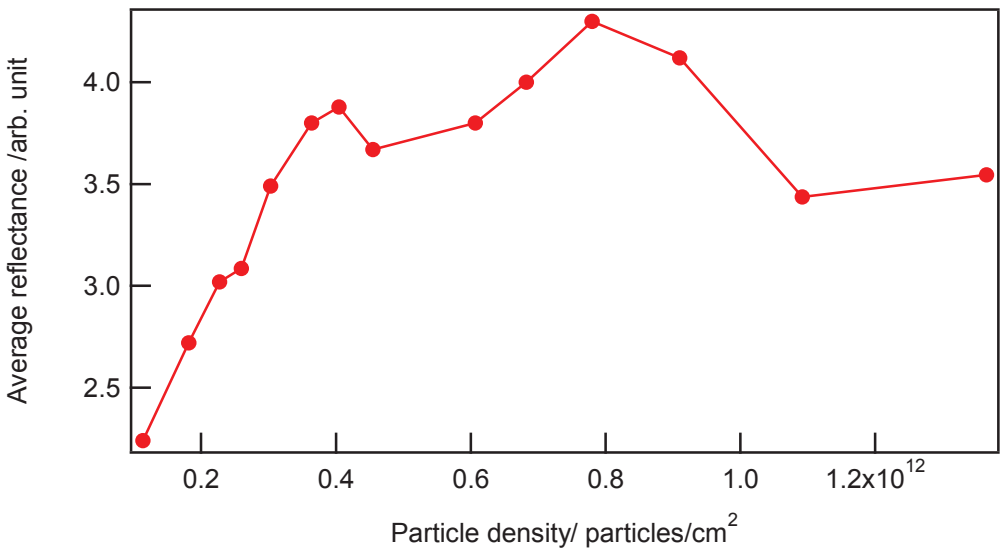

Figure 4.11: Average reflectance versus particle density at 500 nm.

The critical value observed for this film is ~ 85% of the full coverage, based on the assumption of a perfectly compact hexagonal-packed film at full coverage. Considering the occurrence of defects in the film over the large areas probed by the optical beam, the value is close to the monolayer film formation.

4.2.3.1.3. Transmission versus compression

Transmission spectra were also taken for the pure water surface, after which specific amounts of nanoparticles was injected on the surface when the barriers were totally opened, the trough area being set to 90 cm². The barrier rate was similar to the previous experiments, set to 5 cm²/min. The transmittance spectra were taken at various trough areas, namely 90, 80, 70, 60,…20 cm². The plot of the absorbance versus wavelength upon compression is given in Figure 4.12. In this experiment, the initial average surface density was 1.13×10^{11} particle/cm^2, the same density as that used for the first reflectance spectra experiment. We notice the presence of a clear red shift of the wavelength of the maximum absorbance, similarly to the case of the reflectance spectra, see Figure 4.12 and arrow.

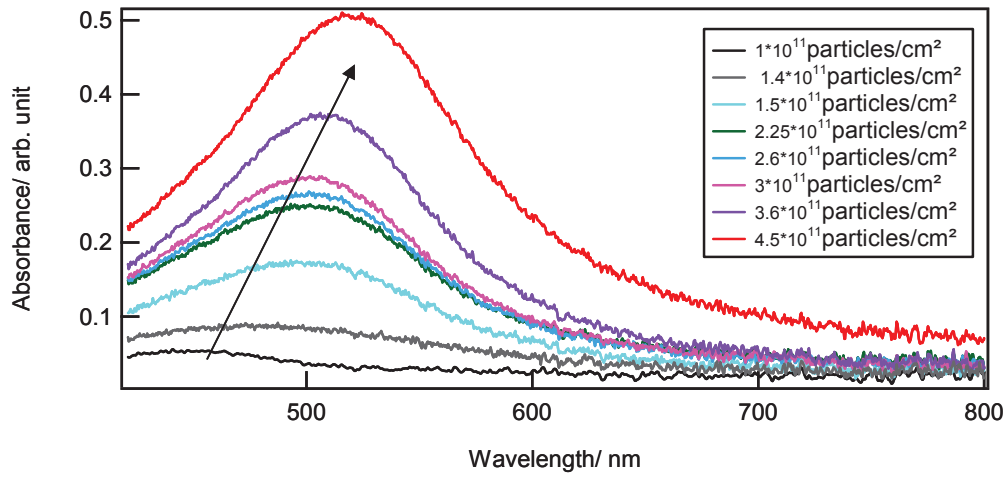

Figure 4.12: Absorbance versus wavelength at different densities starting from the initial concentration of 1.13×10[11] particles/cm².

This red shift starts from below 500 nm, close to 450 nm at an area of 90 cm², and reaches 530 nm at an area of 20 cm². This red shift in the transmission spectra seems therefore stronger than that reported for the reflectance spectra where the shift in wavelength starts from a value about 500 nm and reaches 530 nm only. However, the initial transmission spectra are rather flat and the wavelength of maximum absorbance is difficult to determine. It is interesting to note that the absorbance spectra do not present a strong shoulder as opposed to the reflectance spectra, see figure 4.13.

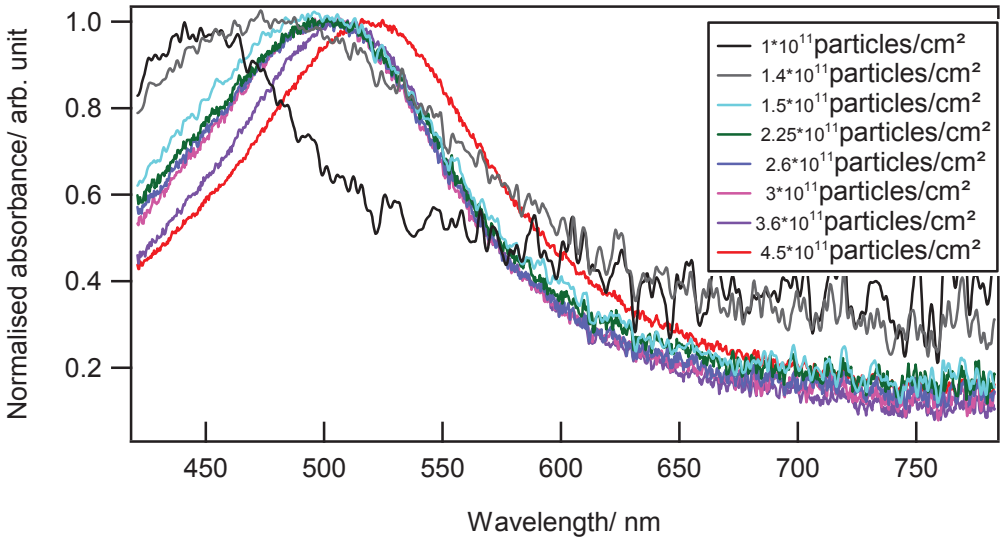

Figure 4.13: Normalised transmission spectra of Figure 4.12.

The two behaviour reported for the reflectance and transmission spectra and the shoulder at 650-700 nm in the reflectance spectra are the signature of the presence of interactions between particles.

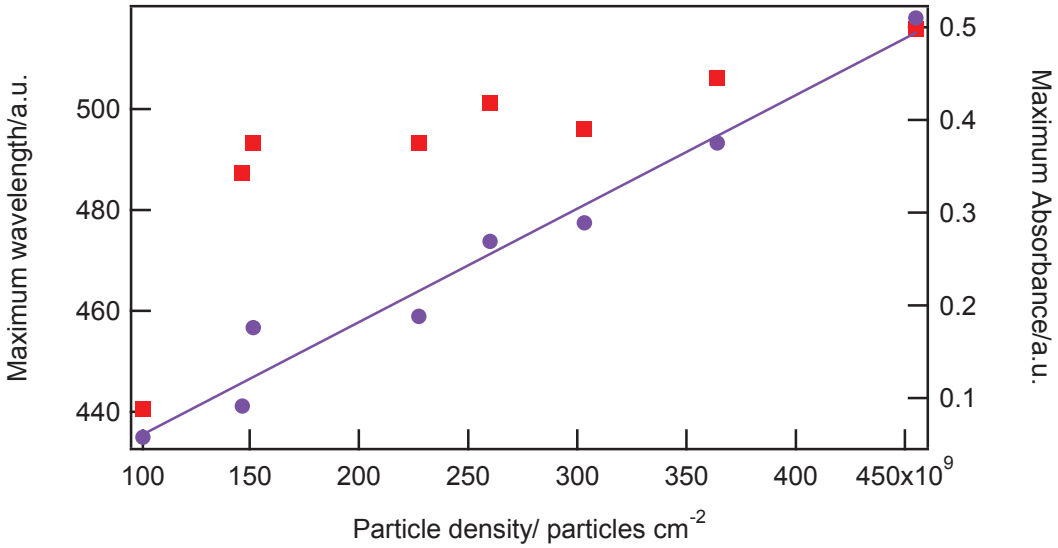

Figure 4.14: Maximum wavelength (■) shift and maximum absorbance (●) change as a function of the average particle density.

4.2.3.1.4. Conclusions for these measurements

We have observed modifications of the reflectance and the transmittance of the nanoparticle film during its compression. These modifications are attributed to the particle interactions, most probably the particle aggregation into large domains. These spectra can be described with a simple model based on a Maxwell-Garnett approach detailed at the end of the chapter. In order to favour these interactions, we repeated this work with hexanethiol-capped silver particles. These particles had the same diameter of about 8 ± 1 nm as the dodecanethiol-capped ones. They were synthesised following the same method as that used for the dodecanethiol-capped ones but replacing dodecanethiol with hexanethiol.

4.2.3.2. Synthesised hexanethiol silver spherical nanoparticles

4.2.3.2.1. Isotherm of the Langmuir film

Changing the chain length of the surfactant allows the control of the interactions between the nanoparticles. Figure 4.15 presents the surface pressure versus trough area isotherm for an initial density of 1.08×10^{11} particles/cm² hexanethiol-capped silver nanoparticles with an average diameter of 9 nm. The maximum surface pressure reached about 30 mN/m. We notice that the surface pressure never reached a plateau although a change of slope is observed.

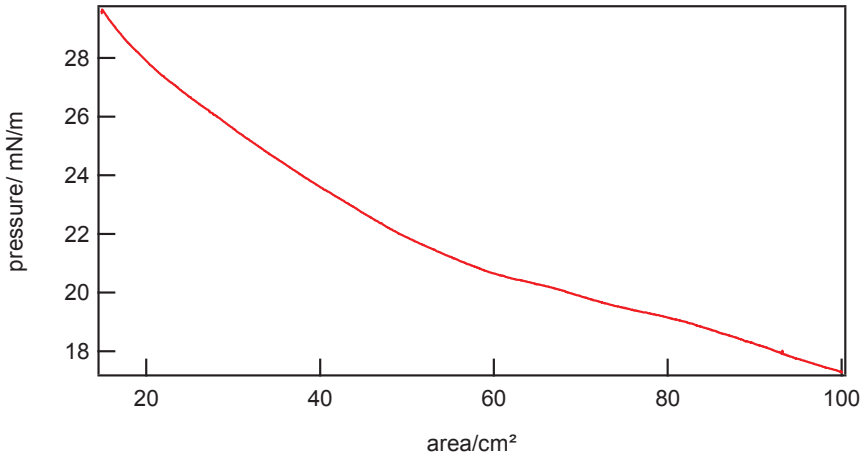

Figure 4.15: Pressure versus trough area isotherm for an initial density of 1.08×10^{11} *particles/cm².*

4.2.3.2.2. Reflectance versus compression

Reflectance spectra were taken for various initial amounts. The red shift of the wavelength of maximum reflectance and the appearance of a shoulder at longer wavelengths are clearly observed.

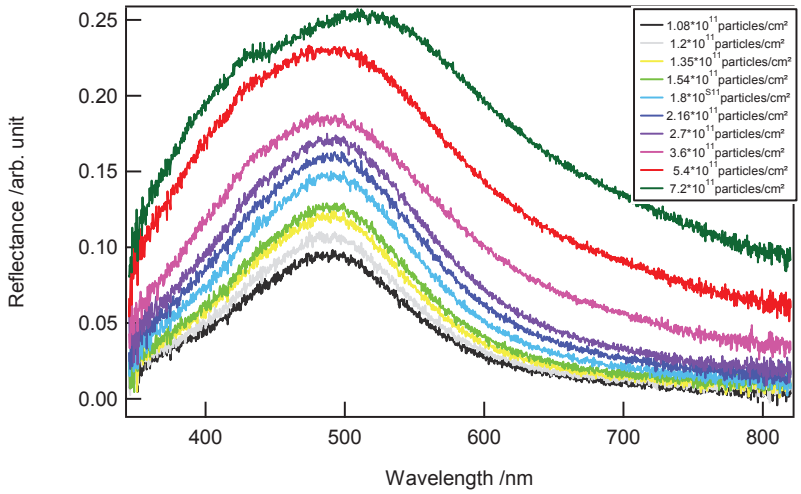

Figure 4.16: Experimental reflectance spectra upon compression for an initial density of 1.08×10^{11} *particles*/cm²

Normalised reflectance spectra are presented in Figure 4.17. The shoulder at long wavelengths and the red shift of maximum reflectance are clearly visible. However, the profile of the reflectance spectra is considerably modified as compared to the previous case of the dodecanethiol-capped silver particles. These changes underline that indeed the short chain length of the hexanethiol-capping layer cannot prevent the strong interactions between the particles.

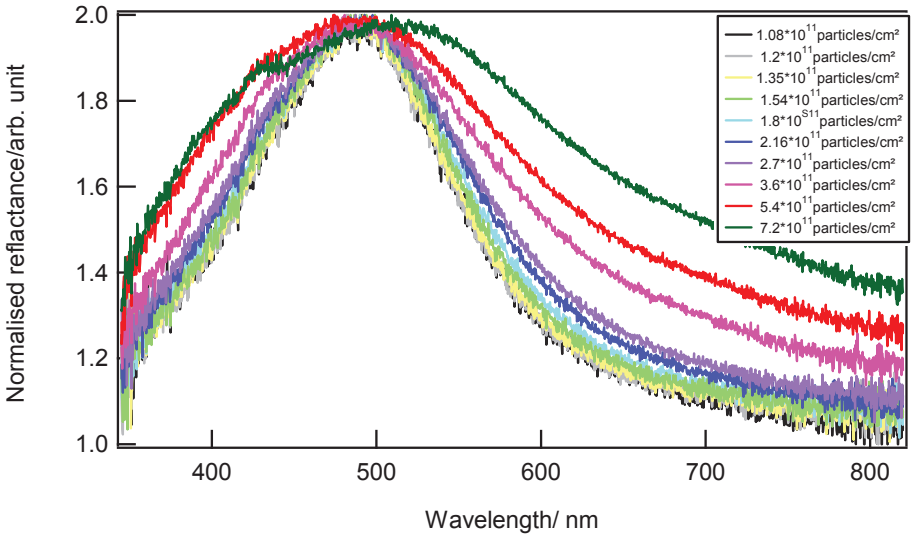

Figure 4.17: Normalized reflectance spectra upon compression for an initial density of 1.08×10^{11} *particles/cm².*

Regardless the signature of the interaction, no drop in the signal was noticed. This might be attributed to the fact that the initial density isn't high enough to form a compact film. Another

probable cause of the absence of the drop is the high size distribution of this synthesis solution. A previous work by the group of Heath showed in the past that the width of the size distribution is a significant source of disorder within the system. Disorder tends to introduce defects preventing the observation of strong interactions between the particles. A critical width of 3% for the size distribution was even determined [13]. For this reason, commercial dodecanethiol-capped spherical silver nanoparticles were purchased and used, assuming that the particles synthesized in our laboratory did not possess an enough narrow size distribution.

4.2.3.3. Commercial dodecanethiol silver spherical particles

4.2.3.3.1. Isotherm of the Langmuir film

Figure 4.18 presents the pressure/area isotherm of a commercially available dodecanethiol-capped silver spherical nanoparticles solution with a diameter of about 10 nm. This isotherm exhibits the characteristics of a classical isotherm for a Langmuir film with a final plateau at high concentration. This plateau appears after the breaking point, the point at which a compact film is formed. The surface pressure is now much larger indicating the formation of a much more compact film, possibly with less defects than previously possible.

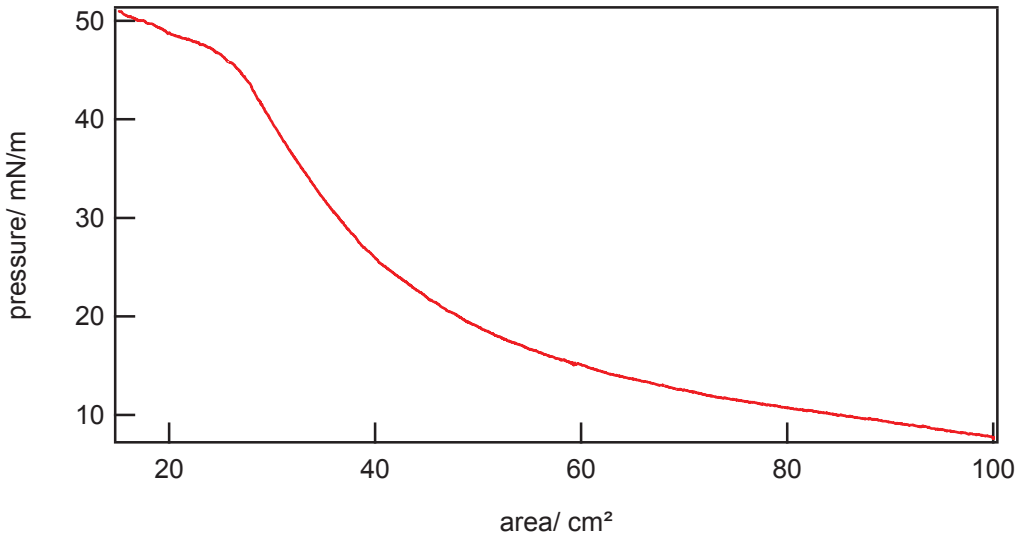

Figure 4.18: Pressure versus area isotherm for commercial dodecanethiol-capped silver nanoparticles for an initial amount of 3.5×10^{11} particles/cm².

The surface pressure isotherm was also reported versus the number density along with another initial density, see Figure 4.19. For the initial density of 3.5×10^{11} particles/cm², a plateau

appears in the isotherm at a surface pressure of 45 mN/m. In terms of average particle density, this plateau appears at 1.6×10^{12} particles/cm². This experiment was repeated for an initial density of 7.1×10^{11} particles/cm². In that case, the shoulder appears at 43 mN/m, corresponding to an average number density also of 1.6×10^{12} particles/cm². We repeated these pressure/area isotherms for many different initial amounts. At the highest initial amount of 8.08×10^{13}particles, a small decrease in the pressure at a trough area of 18 cm² was observed, signalling the onset of the collapse of the film. This collapse is due to the formation of multilayers in the film.

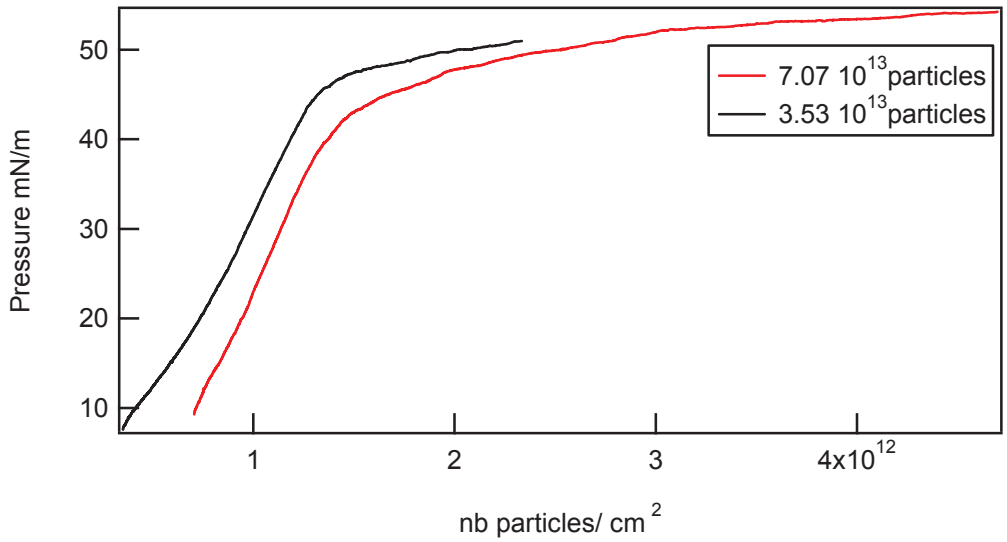

Figure 4.19: Pressure versus concentration of commercial silver dodecanethiol nanoparticles for 3.5×10^{11}particles/cm² and 7.1×10^{11}particles/cm² initial densities.

The particle average surface density needed to form a monolayer film was calculated to be 1.15×10^{12} particles/cm² assuming a hexagonally-packed compact film. Such a density is within our reach considering the possibility to increase the volume of the solution deposited at the water surface. In order to analyse this isotherm behaviour a simple comparison is performed with a similar isotherm of dodecanethiol gold nanoparticles already reported [21]. The isotherm registered on that occasion is similar to the one obtained here. The isotherm was furthermore divided into three stages. The first stage where the increase in pressure is slow is attributed to the gathering of the islands of particles together. The second stage corresponds to a rather compact film where voids between the particles still exist. This explanation is supported by a TEM images at each compression stage. At the end of the second stage, where the shoulder appears, microscopic liquid droplets are reported. The third stage is reached upon

further compression where wrinkles appear as dark lines parallel to the barriers. The presence of the droplets cannot be discussed in our case owing to the unavailability of TEM images. However, the presence of wrinkles was noticed at the highest amounts of particles corresponding to 4.04×10^{12} particles/cm². The wrinkles were appearing as brown lines parallel to the barrier.

4.2.3.3.2. Reflectance versus compression

The same procedure for the optical measurements was repeated for the commercial dodecanethiol-capped silver spherical nanoparticles. The reflectance at the clean water surface was taken as the reference spectrum. A defined initial concentration of the commercial silver nanoparticles was injected into the trough opened to area 100 cm². The particles were deposited and a waiting time of about 10 minutes was taken before starting the recording of the reflection spectra. This time interval allows the hexane solution to fully evaporate and allows the homogeneous distribution of the particles at the water surface. The reflectance of the film was then obtained by dividing the reflection spectra by the reference spectrum on the neat water interface. The barrier velocity was set to 2 cm²/min and reflectance spectra were taken at various trough areas, namely 100, 90, 80…, 15 cm². The isotherm was registered simultaneously with the reflectance spectra. The experimental reflectance spectra at different trough areas is given in Figure 4.20 for an initial density of 5.1×10^{11} particles/cm². This value is about 3 times the density required to form a monolayer at 15 cm².

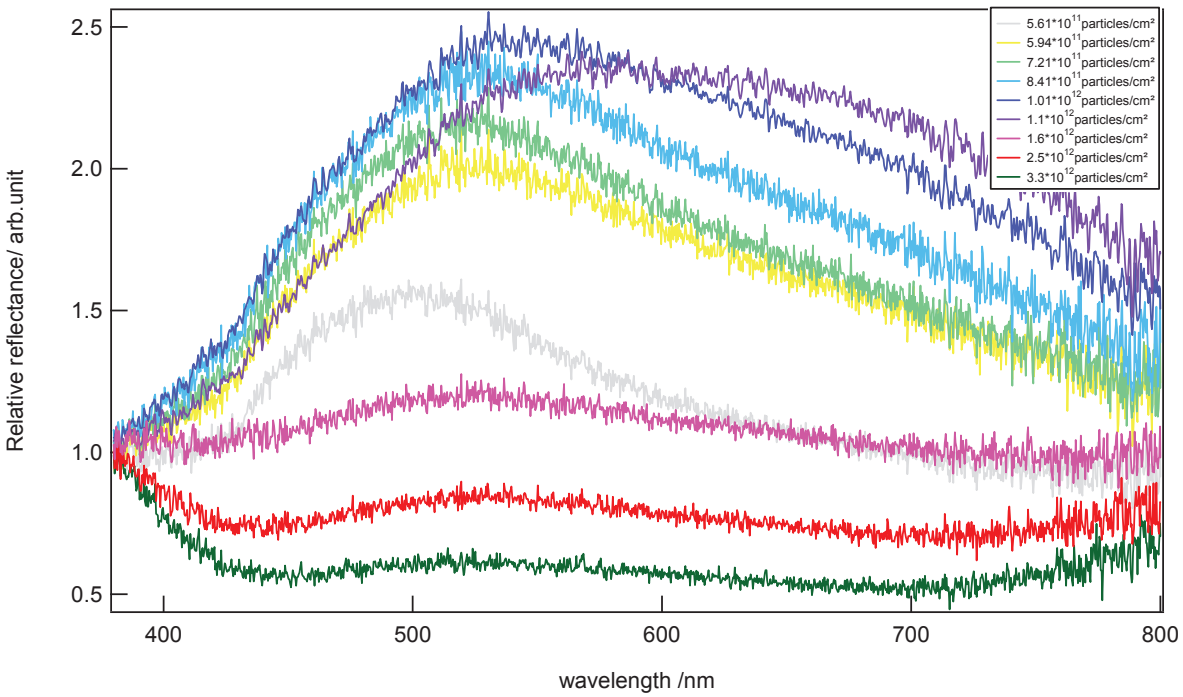

Figure 4.20: Experimental reflectance spectra at different trough areas for an initial density of 5.1×10^{11} particles/cm² deposited.

Upon compression, we notice first an increase of the reflectance of the film along with the appearance of a shoulder at longer wavelength. With the compression, the film becomes more reflective. However, at a trough area of 45 cm², a decrease of the reflectance is observed till the closed trough area of 15cm². Similarly to the case of the synthesized dodecanethiol-capped silver nanoparticles, the reflectance of the film presents both a red shift of the wavelength of maximum reflectance and a shoulder between 550 and 700 nm upon compression up to the trough area of 45 cm^2. To underline better these features, normalisation of the reflectance spectra is given in Figure 4.21.

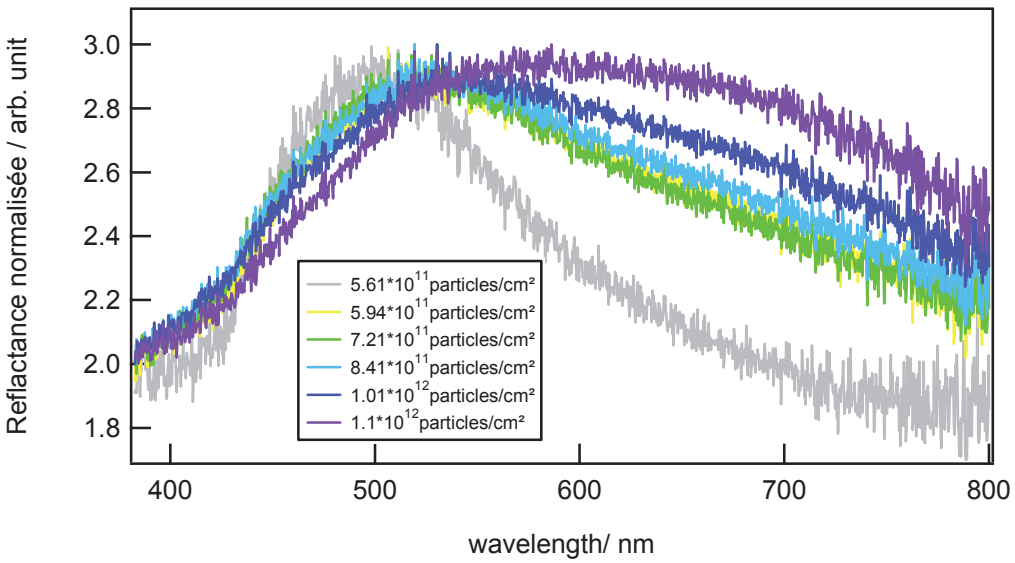

Figure 4.21: Normalised reflectance spectra for an initial density of 5×10^{11} particles/cm².

Normalisation of the reflectance spectra is not performed for the trough areas of 30, 20 and 15 cm² since the reflectance has dropped in those cases. The appearance of the shoulder and the red shift from 490 nm at area of 90 cm² to 570 nm at area of 45 cm² are clearly evidenced of interactions. Both the red shift and the shoulder are more prominent than those registered for the synthesized dodecanethiol-capped and the hexanethiol-capped silver nanoparticles. These two features indicate the occurrence of strong interactions between the particles as a result of the decrease of the trough area. The interparticle separation distance is often defined through the two parameters *D* and *2r*, respectively the centre-to-centre distance between two particles and the core diameter. As reported by Heath et al., an insulator-to-metal transition is expected for the condition $D/2r < 1.2$ [7]. In our case, this condition is close to be fulfilled for the smallest trough area. In Figure 4.22 is presented the reflectance value at the wavelength of 500 nm obtained for an initial density deposited of 5×10^{11} particles/cm². We notice that the critical density at which the reflectance starts to decrease is about 1×10^{12} particles/cm²along with its isotherm. This average surface density is smaller than that required to form a monolayer which is calculated to be 1.15×10^{12} particles/cm². However, a perfect film is not expected over the whole trough area, defects being highly likely present. Furthermore, this reflectance decrease is initiated before the appearance of the shoulder in the isotherm which is observed at about 1.6×10^{12} particles/cm² as the result of the formation of a compact film. These results therefore indicate that the metal-to-insulator transition may have been reached.

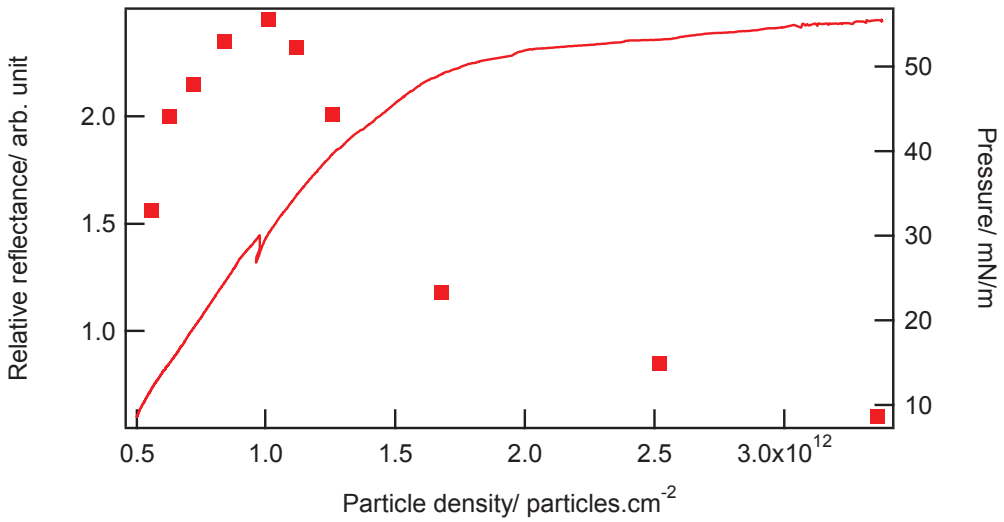

Figure 4.22: Reflectance at 500 nm (left axis) and surface pressure (right axis) versus the average particle density for an initial density of 5×10^{11} particles/cm².

In order to determine with more precision the exact average surface density required for the reflectance to fall, the experiments were repeated with initial amounts of particles increasing from 2×10^{11} particles/cm² up to 8.1×10^{11} particles/cm² for an open trough area of 100 cm^2. Figure 4.23 therefore presents the experimental reflectance registered at 500 nm for an increasing value of the average surface density.

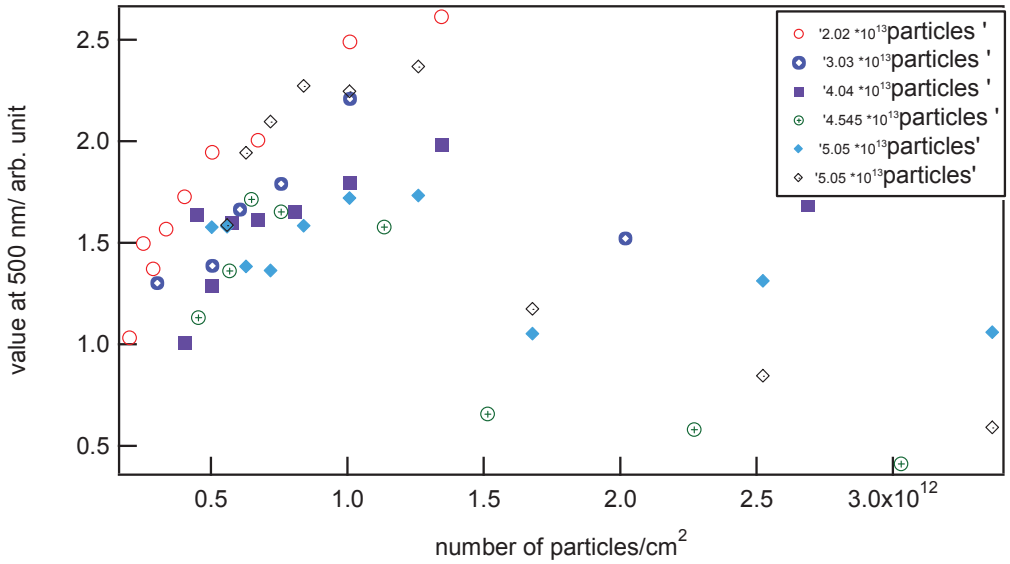

Figure 4.23: Reflectance at 500 nm versus particle density. Each color corresponds to an initial amount of particles.

We notice first a rather linear increase of the reflectance as a function of the average surface density until a maximum is reached at a limiting density of about 1.1×10^{12} particles/cm^2. This

average surface density is actually close to the density required to form a compact hexagonally-packed monolayer film equal to 1.15 $\times 10^{12}$ particles/cm^2. This limiting density varied from one experiment to another due to the inhomogeneity of the film and the presence of defects. In addition, uncontrollable losses of particles upon injection by sticking to the barriers and the wall boundaries can participate in this inhomogeneity. It hence appears that the critical density occurs between the two limiting densities of 1.1×10^{12} and 1.4×10^{12} particles/cm².

Once the average interparticle distance gets very small, the linear reflectance drops. This is what is expected from a thin metallic silver film [28], further supporting the fact that we have observed the metal-to-insulator transition. In the previous experiments with the synthesized dodecanethiol and hexanethiol-capped nanoparticles, no such drop in reflectance was observed despite the possibility of the occurrence of multilayers in the film. This is attributed to the quality of the particle preparation and more precisely to the width of the size distribution. However, previous works by Heath group showed that the insulator-to-metal transition takes place in a bilayer film [12]. Comparing the reflectance behaviour with compression in our film as compared to that of Collier et *al.*[5] where a continuous metallic film was formed with particles capped with different thiol chains ranging from C_3 to C_{10}, we notice the same general behaviour of reflectance, see Figure 4.24, with a clear drop. However, in their experiment, the reflectance does not show any sign of interactions between the particles.

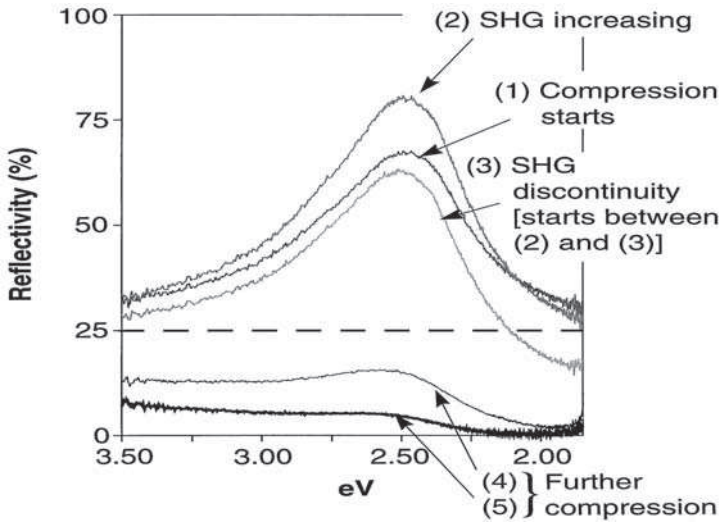

Figure 4.24: Reflectance spectra from a Langmuir monolayer of 4 nm particles passivated with n-propanethiol collected as the film was compressed (see .[5])

4.2.3.4. The Metal-to-Insulator transition

The experimental results obtained for the various samples presented indicate that an insulator-to-metal transition has been observed for the commercially available dodecanethiol-capped nanoparticles. One of the critical parameters is expected to be the width of the size distribution. The signature of the transition is the drop of the reflectance observed at the highest compression explored in this work. At this stage though, no proof of the absence of multilayers has been provided although the formation of multilayers found in the synthesized dodecanethiol- and hexanethiol-capped particles did not lead to such a reflectance drop. Finally, it is added, that it is possible that at much higher average densities, well beyond the collapse of the monolayer film, the transition can be observed in dodecanethiol- and hexanethiol-capped particles films. No evidence has been found supporting this possibility.

In order to further support the hypothesis of the metal-to-insulator transition, conductivity measurements were performed to determine the resistivity of the film upon compression, thereby determining the conductivity. The measurements were performed in a static way and cannot be considered therefore as impedance measurements although such measurements would be highly desirable. Two electrodes were placed at the interface, just touching the surface of the water phase. The resistance was measured using a circuit consisting of a rheostat and the electrodes immersed in water. A LabView program was used to perform the experiment. The resistance was then deduced from the rheostat intensity and the voltage across the electrodes. No noticeable variation of the conductance upon the compression was noticed. These experiments should be repeated with greater sensitivity.

4.3. Linear response of spherical gold particles film

The same experiments as those reported above were undertaken for thiols-capped gold spherical nanoparticles since no insulator-to-metal transition have been reported for this system. The surface pressure/area isotherm, linear reflectance and the conductivity measurements were performed for several thiol-capped gold nanoparticles capped differing through the length of the chain. Changing the chain length of the surfactant allows the control

of the interactions between the nanoparticles. It was previously demonstrated that the interaction between the particles increases with the decrease of the separation between the particles controlled by the length of the alkane chain [18]. The concentrations of the nanoparticles were deduced using UV-visible absorption spectra since it was impossible to obtain an initial concentration for the nanoparticles solution. Losses at the different stages of the synthesis were indeed observed as deposits on the glassware, for instance. The surface pressure/area isotherm for the gold particles films did not differ much from those obtained for the silver nanoparticles films. In the reflectance spectra versus compression recorded, an increase of the reflectance with the concentration was observed. A weak red shift of the wavelength of the maximum reflectance was noticed but no shoulder at longer wavelengths and no reflectance drop at high compression was observed. This behaviour shows that the interparticle interactions remain rather weak for all chain lengths. It is possible that the morphological properties of the solutions available were not suitable to induce the transition.

4.4. Linear response of gold nanorods film

The previous studies were devoted to spherical silver and gold nanoparticles. The role of the size distribution was underlined as a major parameter controlling the appearance of the transition. To further complement these studies, nanorods particles were also used to form a metallic film at the Langmuir trough subphase. Octadecanethiol gold nanorods of dimension 64×24×24 nm the synthesis of which is given in chapter one were used to form a film at the air/water interface. The reflectance spectra upon compression were registered at various trough areas and initial amounts. The relative reflectance spectra at different trough areas is shown in Figure 4.25 for an initial surface density of 9.5×10^6 particles/cm². The particles were deposited and a waiting time of about 5 minutes was left before starting recording the reflection spectra. This time interval allows the evaporation of the chloroform solution as well as the homogeneous distribution of the particles at the water surface. The reflectance spectra of the film were then obtained by dividing the reflection spectra by the reference spectrum on the neat water interface. The barrier velocity was set to 5 cm²/min and reflectance spectra were taken at various trough areas: 100, 90, 80…, 20 cm².

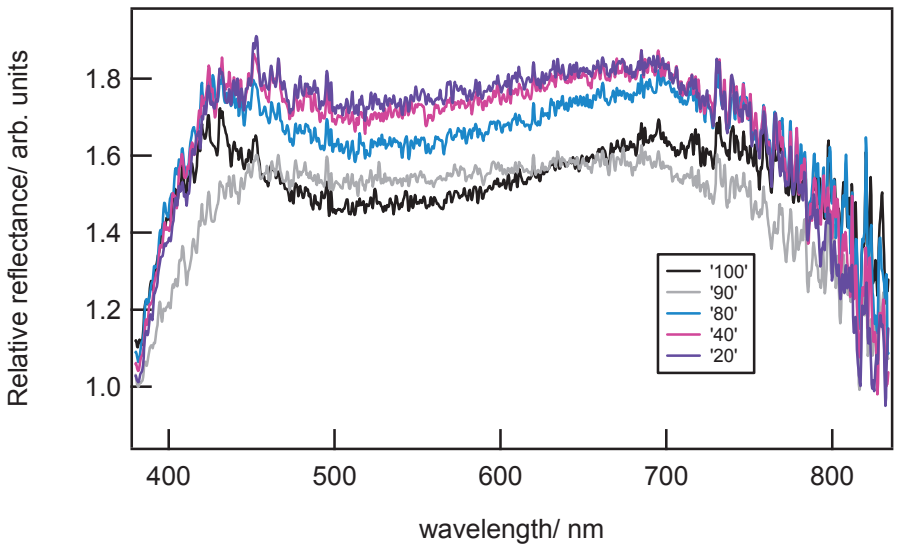

Figure 4.25: Relative reflectance versus wavelength for an initial density of 9.5 ×10^6 particles/cm² (black), 1.05×10^{7}particles/cm² (grey), 1.18×10^{7}particles/cm² (blue), 2.37×10^{7}particles/cm² (purple), 4.75×10^{7}particles/cm² (violet)

The reflectance spectra present two broadband resonances associated with the two surface plasmon resonances (SPR) of the nanorods. The reflectance increased upon compression accompanied with a slight deformation in the spectra indicative of the aggregation process in the film. The deformation of the spectra is clear upon the increase of the initial concentration added to the subphase. Figure 4.26 presents three relative reflectance spectra for three different initial additions. The relative density of the black curve corresponds to 9.55×10^6 particles/cm², the red one to 9.5×10^8 particles/cm² and the blue one to 3.3 ×10^9 particles/cm².

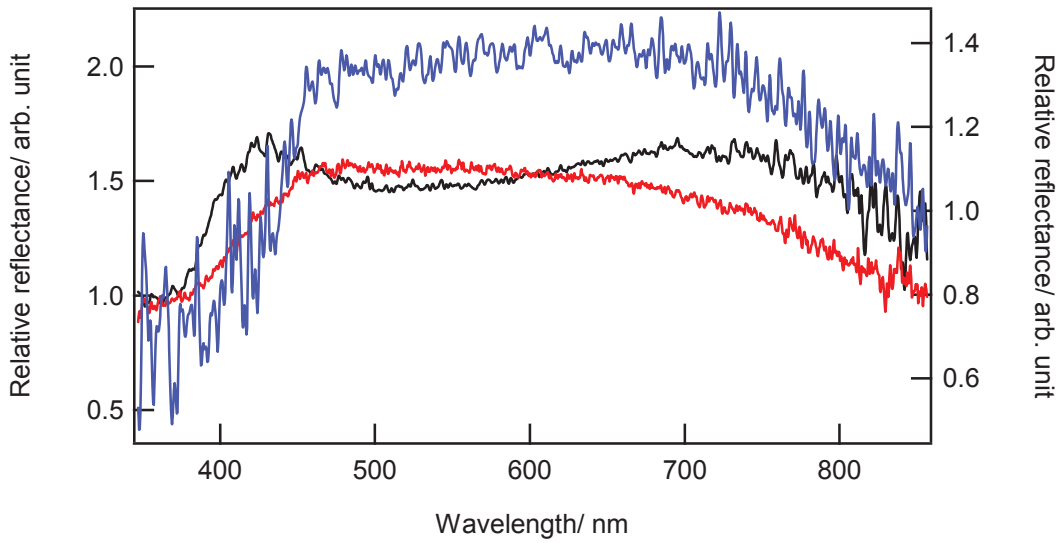

Figure 4.26: Relative reflectance spectra for the surface concentrations of 9.55 $\times 10^6$ particles/cm² (black), 9.5 $\times 10^8$ particles/cm² (red), and 3.3 $\times 10^9$ particles/cm² (blue).

We notice that at low average surface concentration, the reflectance exhibit a shallow dip around 500 nm. Upon increase of the density, the reflectance spectrum flattens and increases. The changes of the profile of the spectra are a sign of the interactions between the particles occurring in the film. Upon compression, the inter-particle distance decreases and thus favouring the interactions between the particles. To simulate these experimental data, a Maxwell-Garnett model was used [29].

4.5. Theory of the reflectance of a nanoparticles film

The aim of this part is to gain insight and simulate the experimental results obtained in reflection and transmission with white light from and through a metallic nanoparticles monolayer. The principle is to calculate the reflectance and the transmittance of a thin slab as illustrated in the following Figure 4.27.

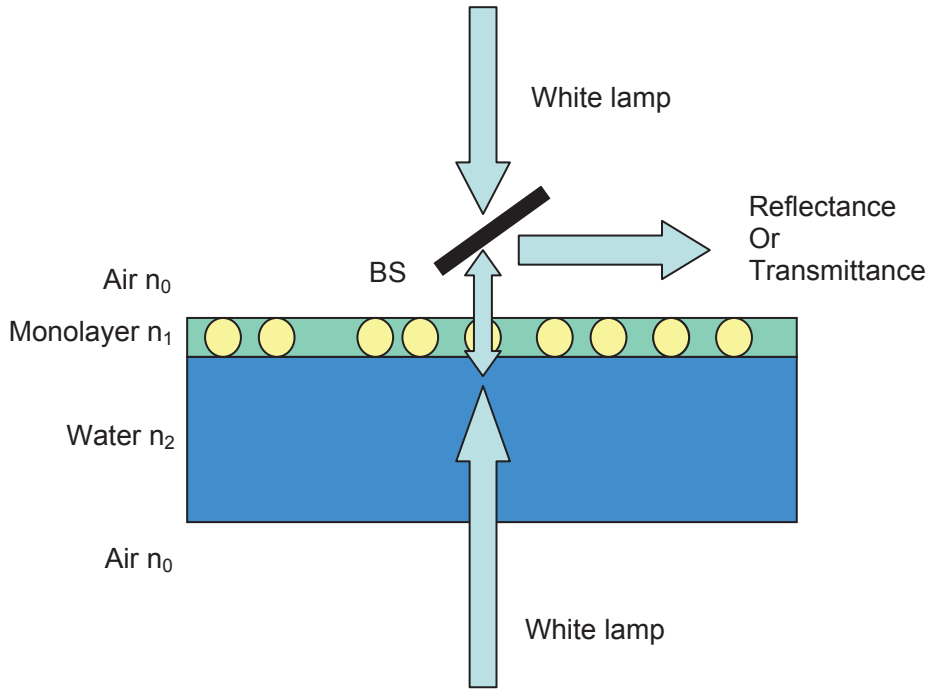

Figure 4.27: Schematics of the experimental system consisting of a thin film of metallic particles at the surface of water.

4.5.1. Fresnel coefficients:

We start by calculating the complex coefficients of reflection and transmission for a thin film located between two transparent media, namely air with refractive index $n_0 = 1$ and water with refractive index $n_2 = 1.34$. The thickness of the water medium is much greater than the wavelength and therefore we do not take into consideration the multiple reflections in this phase.

4.5.1.1. Reflectance R

We consider the reflections at the two interfaces of the film, namely the air/film and film/water interfaces. Letting r_{ij} and t_{ij} be the reflection and transmission coefficients of the light propagating from medium i to medium j [30], the reflection coefficient in amplitude is given by:

$$r_c = r_{01} + t_{01}e^{i\delta}r_{12}e^{i\delta}t_{10} + \ldots = r_{01} + \frac{t_{01}t_{10}r_{12}e^{2i\delta}}{1 - r_{12}r_{10}e^{2i\delta}} \tag{4.5}$$

with

$$\delta = \frac{2\pi}{\lambda} n_f d \cos(\varphi) \tag{4.6}$$

where λ is the wavelength of the incident light. φ is the angle of incidence set to zero in our case, n_1 is the refractive index of the thin film, d is the film thickness which is taken equal to the diameter of the particle. r_{01}, r_{12}, t_{01} and t_{10} are the Fresnel coefficients given by:

$$r_{01} = \frac{n_0 - n_1}{n_0 + n_1} = r_0 \qquad r_{12} = \frac{n_1 - n_2}{n_1 + n_2} = r_1 \tag{4.7}$$

$$r_{10} = -r_0 \tag{4.8}$$

$$t_{01} = \frac{2n_0}{n_0 + n_1} = 1 + r_0 \tag{4.9}$$

$$t_{10} = 1 - r_0 \tag{4.10}$$

After simplifications of Eq.(4.5), we get the following formula :

$$r_c = \frac{r_0 + r_1 e^{2i\delta}}{1 + r_0 r_1 e^{2i\delta}} \tag{4.11}$$

The reflectance R, the ratio of reflected to input power, is then given by

$$R = \left| r_c \right|^2 \tag{4.12}$$

4.5.1.2. Transmittance T

The transmitted light impinges on the film through the sub-phase (water under the film). The first step is to calculate the transmittance T_w through the air/water interface:

$$T_w = 1 - R_w \tag{4.13}$$

where

$$R_w = \left|r_{20}\right|^2 = \left|\frac{n_2 - n_0}{n_2 + n_0}\right|^2 \tag{4.14}$$

Then, we calculate the transmission from water to air, the film being located between the two media :

$$t_c = t_{21}e^{i\delta}t_{10} + t_{21}(e^{i\delta}r_{10}e^{i\delta}r_{12}e^{i\delta})t_{10} + \ldots = \frac{t_{21}t_{10}e^{i\delta}}{1 - r_{12}r_{10}e^{2i\delta}} \tag{4.15}$$

where δ , r_{10},t_{10}, r_{12} are defined above and t_{21} is defined by $t_{21} = 1 - r_1$. We have then:

$$t_c = \frac{(1 - r_0)(1 - r_1)e^{i\delta}}{1 + r_0 r_1 e^{2i\delta}} \tag{4.16}$$

and the transmittance is given by

$$T_c = \frac{n_0}{n_2}\left|t_c\right|^2 \tag{4.17}$$

The total transmittance is given by :

$$T = T_c\, T_w \tag{4.18}$$

To be able to calculate the reflectance and transmittance, we have now to determine the refractive index n_1 of the thin film embedding the silver nanoparticles.

4.5.2.Dielectric function of spherical silver nanoparticles

The experimental values of the bulk silver dielectric functions were taken from Johnson and Christy [31]. Modifications of these experimental values are essential because of the nanometre size of the nanoparticles. To implement these modifications, we introduce the Drude Model [7] giving the dielectric function of the free electrons in the bulk metal through :

$$\varepsilon_{D,b} = \left(1 - \frac{\omega_p^2}{\omega_{ci}^2 + \omega^2}\right) + \frac{i\omega_p \omega_{ci}}{\omega(\omega_{ci}^2 + \omega^2)} \tag{4.19}$$

where $\upsilon_f = 1.4 \times 10^8 \, cm\, s^{-1}$ is the Fermi velocity in bulk silver and $l = 57 \times 10^{-7} \, cm$ is the mean free path of an electron in bulk silver. ω_p is the free electron bulk plasma frequency and $\omega_{ci} = \upsilon_f / l$ is the collision rate of the electrons in the bulk, equal to the bulk plasma line width. The line width due to finite size is

$$\omega_c(r) = \left(\frac{1}{l} + \frac{1}{r}\right)\upsilon_f \tag{4.20}$$

Combining Eqs.(4.19)-(4.20), we get the following expression for finite sizes :

$$\varepsilon_{D,f}(\omega, r) = \left(1 - \frac{\omega_p^2}{\omega_c^2(r) + \omega^2}\right) + \frac{i\omega_p \omega_c(r)}{\omega(\omega_c^2(r) + \omega^2)} \tag{4.21}$$

Thus, the dielectric constant of the metal particle is :

$$\varepsilon = \varepsilon_{\exp} - \varepsilon_{D,b} + \varepsilon_{D,f}(\omega, r) \tag{4.22}$$

allowing us to calculate the polarizability β of a sphere of radius r through :

$$\beta = \frac{\varepsilon - \varepsilon_m}{\varepsilon + 2\varepsilon_m} \tag{4.23}$$

where ε_m is the dielectric constant of the medium.

4.5.3.Dielectric function of the film – Maxwell Garnett model

From the experimental results, it is clear that the film is built up by closing the barriers and this takes place progressively, *i.e.* the nanoparticles are not in contact with each other at the beginning of the experiment. We introduce the effective dielectric constant related to the volume fraction *f* of the film, ratio of the volume occupied by the silver nanoparticles in a unit volume of the film. For *f = 1*, we have a compact pure metallic film. We can relate *f* to the quantity *D/2r* where *D* is the distance between the centres of adjacent particles and *2r* is the diameter of the silver particle by the following relation :

$$\frac{D}{2r} = \left(\frac{\pi}{2\sqrt{3} f} \right)^{1/2} \tag{4.24}$$

As an effective medium approximation, the Maxwell-Garnett model assumes that there is no aggregation taking place. After calculating the polarizability β in Eq.(4.23) and having the volume fraction f and the dielectric constant of the medium ε_m , we can calculate the effective dielectric constant for the spheres [29] :

$$\varepsilon_{eff} = \varepsilon_m \left[1 + \frac{3f \dfrac{\varepsilon - \varepsilon_m}{\varepsilon + 2\varepsilon_m}}{1 - f \dfrac{\varepsilon - \varepsilon_m}{\varepsilon + 2\varepsilon_m}} \right] \tag{4.25}$$

The effective dielectric constant for the ellipsoidal form is given as follows :

$$\varepsilon_{eff} = \frac{(1-f)\varepsilon_m + f\beta\varepsilon}{1-f+f\beta} \tag{4.26}$$

where β for an ellipsoid is given by the following equation:

$$\beta = \int\int P(L_1, L_2)\frac{\lambda_1+\lambda_2+\lambda_3}{3} dL_1 dL_2 \tag{4.27}$$

$P(L_1, L_2)$ is the shape probability distribution function and

$$\lambda_i = \frac{\varepsilon_m}{\varepsilon_m + L_i(\varepsilon-\varepsilon_m)} \qquad \text{(j=1, 2, 3)} \tag{4.28}$$

and

$$L_1 = \frac{abc}{2}\int_0^\infty \frac{dq}{(a^2+q)f(q)} \tag{4.29}$$

$$L_2 = \frac{abc}{2}\int_0^\infty \frac{dq}{(b^2+q)f(q)} \tag{4.30}$$

We then deduce the refractive index where

$$n_1 = \sqrt{\varepsilon_{eff}} \tag{4.31}$$

We have to keep in mind that the Maxwell-Garnett model has a range of validity. The particles embedded in the medium should be ellipsoidal, much smaller than the wavelength of light, randomly and uniformly distributed and should not form any continuous network within the medium [19, 20]. Furthermore *f* should be restricted to values below 0.1 to avoid particle interactions. In our simulation, we have applied the model up to values around 0.9 and therefore the results should be analyzed carefully. The fundamental question that needs to be addressed is to what extent can macroscopic objects still retain the optical properties of the isolated nanoparticles when the volume fraction is increased and interaction starts. It has been shown by Heath *et al.* that the classical model is limited to a given interparticle distance. Below the distance *D/2r=1.2,* the classical model fails to reproduce the drop at small

interparticle distance [7]. In Figure 4.28 is given the experimental and theoretical reflectance for the synthesized and the commercial spherical silver nanoparticles as well as for the gold nanorods. In Figure 4.28(a), the experimental and theoretical reflectance spectra are given for a density of 2.25×10^{11} particles/cm². The volume fraction f was used as an adjustment parameter. The theoretical curve presented in Figure 4.28-(a) was obtained for a value of f = 0.64. In Figure 4.28(b), the experimental reflectance is given for the commercial nanoparticles with a diameter of about 10 nm capped with dodecanethiol at density 6.31×10^{11} particles/cm². The theoretical curve was obtained for a value of f = 0.7. In Figure 4.28(c), the experimental reflectance is given for the gold nanorods of dimensions 64×24×24 nm at an average surface density of 3.3×10^{9} particles/cm². Since aggregation is believed to take place in the case of the nanorods, we have chosen to adjust the experimental data by changing the a/b ratio, thereby modeling aggregation through this change. The first adjustment is obtained for a ratio of a/b = 0.87 and the second for a ratio of a/b = 0.79. We tend here to increase the b axis length to shift the reflectance into longer wavelengths. It should be underlined that this model is a crude model yielding a schematic idea of the evolution of the reflectance with the volume fraction. In the case of the nanorods, the adjustment was performed by shifting the reflectance towards larger wavelength by modifying the a/b ratio. This is a considerable approximation of the real problem.

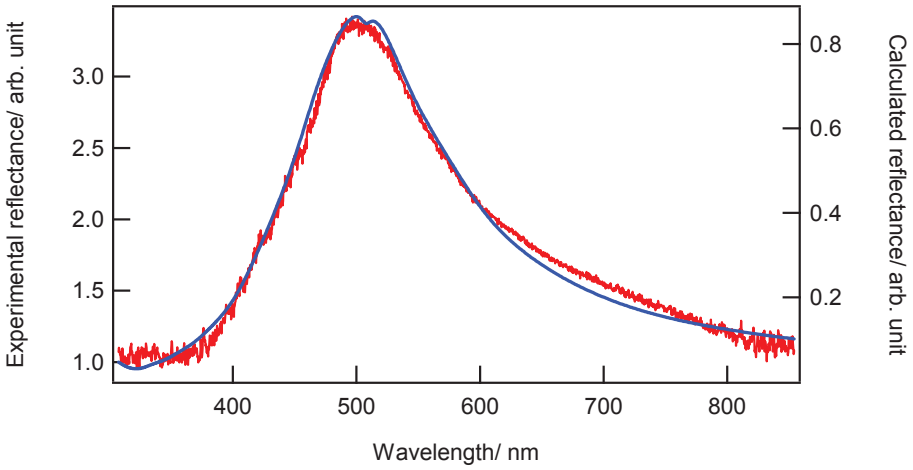

(a)

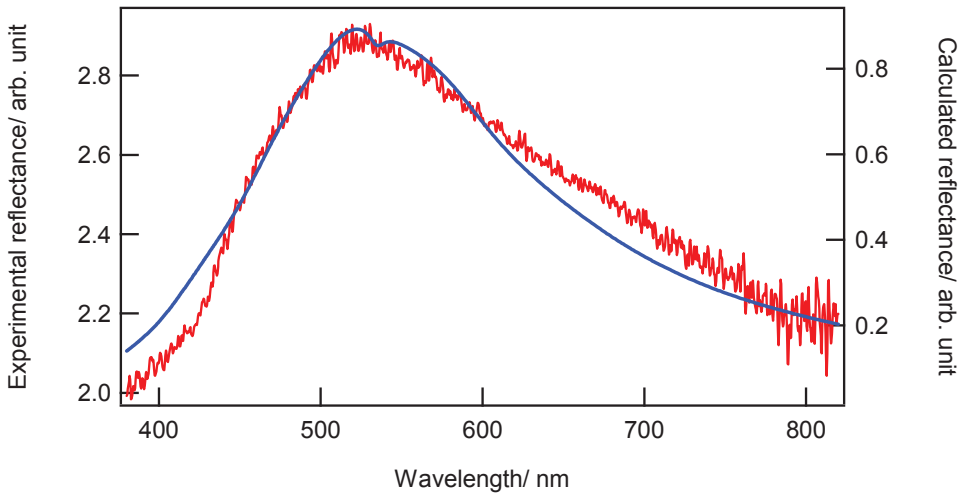

(b)

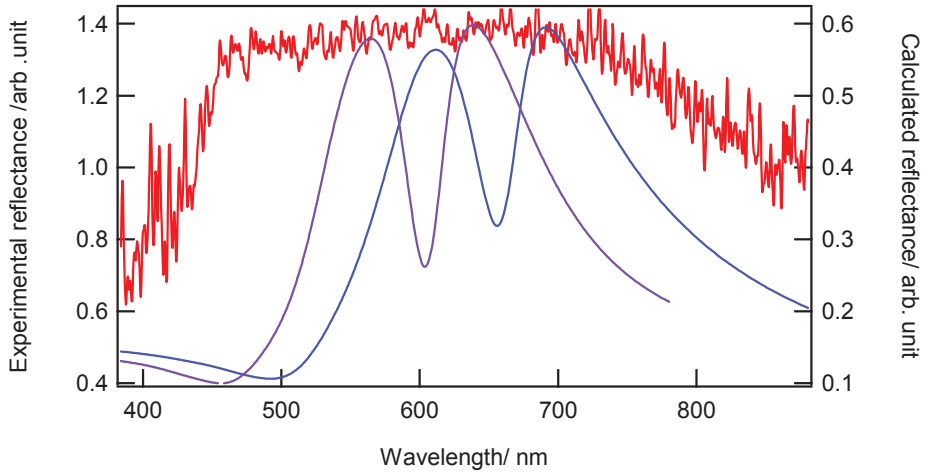

(c)

Figure 4.28: (a) Reflectance spectra of synthesized silver dodecanethiol nanoparticles of diameter ~8 nm at density 2.25×10^{11} particles/cm², f= 0.64, (b) Reflectance spectra of commercial silver dodecanethiol nanoparticles of diameter ~10 nm at density 6.31×10^{11} particles/cm², f= 0.7, (c) reflectance spectra of gold octadecanethiol nanorods of dimension 64×24×24 nm at density 3.3 ×10^{9} particles/cm². The violet color was obtained for a ratio of a/b=0.8 and the blue was for a ratio a/b=0.72.

In fact, the orientation of the nanorods at the interface should have been taken into consideration [32], however in the presented simulation this orientation was not considered for simplification.

4.6. Conclusion

Silver and gold nanoparticles were used to form films at the air/water interface in a Langmuir trough. The surface pressure/area isotherm, the reflectance, transmittance and conductivity of each sample studied were recorded. A drop in the reflectance spectra for commercial dodecanethiol silver nanoparticles was registered, a possible signature of the insulator to metal transition. The reflectance spectra obtained once the metal-insulator transition had taken place resembled that of a thin metallic silver film. This transition provides evidence of the strong coupling between adjacent particles leading to metallic properties of the film. In the formation of the films, it also appears that the size distribution appears to play an essential role. The MI transition requires a narrow size distribution in order to favor the compact organization of the film.

References:

[1] S. H. Kim, G. Medeiros-Ribeiro, D. A. A. Ohlberg, R. S. Williams, and J. R. Heath, "Individual and Collective Electronic Properties of Ag Nanocrystals,"*J. Phys. Chem. B,* vol. 103, pp. 10341-10347, 1999.

[2] G. Markovich, D. V. Leff, S.-W. Chung, H. M. Soyez, B. Dunn, and J. R. Heath, "Parallel fabrication and single-electron charging of devices based on ordered, two-dimensional phases of organically functionalized metal nanocrystals," *App. Phys. Lett.,* vol. 70, pp. 3107-3109, 1997.

[3] B. A. Korgel, S. Fullam, S. Connolly, and D. Fitzmaurice, "Assembly and Self-Organization of Silver Nanocrystal Superlattices: Ordered “Soft Spheres”,"*J. Phys. Chem. B,* vol. 102, pp. 8379-8388, 1998.

[4] S. W. Chung, G. Markovich, and J. R. Heath, "Fabrication and Alignment of Wires in Two Dimensions," *J. Phys. Chem. B,* vol. 102, pp. 6685-6687, 1998.

[5] C. P. Collier, R. J. Saykally, J. J. Shiang, S. E. Henrichs, and J. R. Heath, "Reversible Tuning of Silver Quantum Dot Monolayers Through the Metal-Insulator Transition," *Science,* vol. 277, pp. 1978-1981, 1997.

[6] F. Remacle, C. P. Collier, G. Markovich, J. R. Heath, U. Banin, and R. D. Levine, "Networks of Quantum Nanodots: The Role of Disorder in Modifying Electronic and Optical Properties,"*J. Phys. Chem. B,* vol. 102, pp. 7727-7734, 1998.

[7] J. J. Shiang, J. R. Heath, C. P. Collier, and R. J. Saykally, "Cooperative Phenomena in Artificial Solids Made from Silver Quantum Dots: The Importance of Classical Coupling," *J. Phys. Chem. B,* vol. 102, pp. 3425-3430, 1998.

[8] G. Markovich, C. P. Collier, and J. R. Heath, "Reversible Metal-Insulator Transition in Ordered Metal Nanocrystal Monolayers Observed by Impedance Spectroscopy," *Phys. Rev. Lett.,* vol. 80, pp. 3807-3807, 1998.

[9] R. P. Sear, S.-W. Chung, G. Markovich, W. M. Gelbart, and J. R. Heath, "Spontaneous patterning of quantum dots at the air-water interface," *Phys. Rev. E,* vol. 59, pp. R6255-R6255, 1999.

[10] J. R. Heath, C. M. Knobler, and D. V. Leff, "Pressure/Temperature Phase Diagrams and Superlattices of Organically Functionalized Metal Nanocrystal Monolayers: The Influence of Particle Size, Size Distribution, and Surface Passivant,"*J. Phys. Chem. B,* vol. 101, pp. 189-197, 1997.

[11] G. Medeiros-Ribeiro, D. A. A. Ohlberg, R. S. Williams, and J. R. Heath, "Rehybridization of electronic structure in compressed two-dimensional quantum dot superlattices," *Phys. Rev. B,* vol. 59, pp. 1633-1633, 1999.

[12] S. Henrichs, C. P. Collier, R. J. Saykally, Y. R. Shen, and J. R. Heath, "The Dielectric Function of Silver Nanoparticle Langmuir Monolayers Compressed through the Metal Insulator Transition," *J. Ame. Chem. Soci.,* vol. 122, pp. 4077-4083, 2000.

[13] K. C. Beverly, J. F. Sampaio, and J. R. Heath, "Effects of Size Dispersion Disorder on the Charge Transport in Self-Assembled 2-D Ag Nanoparticle Arrays," *J. Phys. Chem. B,* vol. 106, pp. 2131-2135, 2002.

[14] H. Wormeester, A.-I. Henry, E. S. Kooij, B. Poelsema, and M.-P. Pileni, "Ellipsometric identification of collective optical properties of silver nanocrystal arrays," *J. Chem. Phys.,* vol. 124, pp. 204713-9, 2006.

[15] M. Brust, M. Walker, D. Bethell, D. J. Schiffrin, and R. Whyman, "Synthesis of thiol-derivatised gold nanoparticles in a two-phase Liquid-Liquid system," *J. Chem. Society, Chem. Commun.,* pp. 801-802, 1994.

[16] D. V. Leff, L. Brandt, and J. R. Heath, "Synthesis and Characterization of Hydrophobic, Organically-Soluble Gold Nanocrystals Functionalized with Primary Amines," *Langmuir,* vol. 12, pp. 4723-4730, 1996.

[17] M. Brust and C. J. Kiely, "Some recent advances in nanostructure preparation from gold and silver particles: a short topical review," *Coll. and Surf. A: Physicochem. Engi. Aspe.,* vol. 202, pp. 175-186, 2002.

[18] V. V. Agrawal, N. Varghese, G. U. Kulkarni, and C. N. R. Rao, "Effects of Changes in the Interparticle Separation Induced by Alkanethiols on the Surface Plasmon Band and Other Properties of Nanocrystalline Gold Films," *Langmuir,* vol. 24, pp. 2494-2500, 2008.

[19] T. Ung, L. M. Liz-Marzán, and P. Mulvaney, "Gold nanoparticle thin films," *Coll. and Surf. A: Physicochem. Engi. Aspe.,* vol. 202, pp. 119-126, 2002.

[20] T. Ung, L. M. Liz-Marzan, and P. Mulvaney, "Optical Properties of Thin Films of Au@SiO2 Particles," *J Phys. Chem. B,* vol. 105, pp. 3441-3452, 2001.

[21] D. G. Schultz, X.-M. Lin, D. Li, J. Gebhardt, M. Meron, J. Viccaro, and B. Lin, "Structure, Wrinkling, and Reversibility of Langmuir Monolayers of Gold Nanoparticles," *J Phys. Chem. B,* vol. 110, pp. 24522-24529, 2006.

[22] F. Kim, S. Kwan, J. Akana, and P. Yang, "Langmuir−Blodgett Nanorod Assembly," *J Ame. Chem. Soc.,* vol. 123, pp. 4360-4361, 2001.

[23] P. Yang and F. Kim, "Langmuir-Blodgett Assembly of One-Dimensional Nanostructures," *Chem. Phys. Chem,* vol. 3, pp. 503-506, 2002.

[24] D. R. Lide, *CRC Handbook of chemistry and physics*, 80th edition ed., 2000.

[25] D. L. Feldheim and C. A. Foss, *Metal nanoparticles: Synthesis, Characterization and Applications*, 2002.

[26] G. Martin-Gassin, Y. E. Harfouch, E. Benichou, G. Bachelier, I. Russier-Antoine, C. Jonin, S. Roux, O. Tillement, and P.-F. Brevet, "Correlation reflectance spectroscopy of heterogeneous silver nanoparticle films upon compression at the air/water interface," *J. Phys.: Cond. Matter.,* vol. 20, pp. 055228-055228, 2008.

[27] G. Markovich, C. P. Collier, S. E. Henrichs, F. Remacle, R. D. Levine, and J. R. Heath, "Architectonic Quantum Dot Solids," *Acco. of Chem. Research,* vol. 32, pp. 415-423, 1999.

[28] C. A. Davis, D. R. McKenzie, and R. C. McPhedran, "Optical properties and microstructure of thin silver films," *Opt. Commun.,* vol. 85, pp. 70-82, 1991.

[29] D. R. H. Craig F. Bohren, *Absorption and Scattering of Light by Small Particles*. New York: Wiley Science Paperback Series 1983.

[30] B. Palpant, "Effet de taille dans la réponse optique 'agrégat de métaux noble en matrice: Etude expérimentale et interprétation théorique," Univ-lyon1, 1998.

[31] P. B. Johnson and R. W. Christy, "Optical Constants of the Noble Metals," *Phys. Rev. B,* vol. 6, p. 4370, 1972.

[32] B.G. McMillan, L.E.A. Berlouis, F.R. Cruickshank, P.F. Brevet, "*Reflectance and SERS from an ordered array of gold nanorods*." *Electrochimica Acta,* vol. 53, p1157-1163, 2007.

Chapter 5

Second Harmonic Generation of metallic nanoparticles at the air/liquid Interface

5.1. Introduction

We have seen in Chapter 4 using linear reflectance spectroscopy, that strong interactions can take place at high compression in a film formed by hydrophobic dodecanethiol-capped metallic silver nanoparticles, the diameter of which is about 10 nm. This was observed through the sudden change of the reflectance of the interface. One possibility for the origin of this sudden change is the insulator-to-metal transition (IM) in the film. The drop in reflectance upon compression at above a fixed surface concentration was taken as the signature of a transition which could be attributed to the IM transition. In order to monitor this transition in greater details, SHG has been employed because this technique is very sensitive to electron delocalization. Furthermore, SHG being inherently surface sensitive, it will provide information about the nature and properties of the film formed at this interface. Indeed, as explained before, SHG is a surface specific technique and is hence a perfect tool to study the properties of films formed at the air/water interface[1-2]. Such systems of the form air/film/water will therefore present indeed two interfaces, namely the air/film and the film/water interfaces. Besides, SHG is an interesting technique since it is applicable to all interfaces accessible by light. The harmonic output signal is usually easily separated from the fundamental input by spectral filtering and the use of monochromatic or pulsed lasers will provide high spectral and temporal resolution [3].

In this work, we are interested to observe the IM transition using SHG and analyze the data in terms of the second order susceptibility tensor elements. The latter elements are in particular sensitive to the local symmetry of the film, whether in-plane or out-of-plane, something that the linear optical techniques do not provide since they lack surface sensitivity.

The variation of the second order tensor element upon compression should reveal information in particular about the strength of the interparticle coupling. In the past, Heath et *al.* have studied these linear and nonlinear optical response in Langmuir monolayers of silver nanoparticles with diameters ranging between 2 and 5 nm capped with C_3-, C_6- and C_{10}-thiol chains as a function of the average interparticle distance [4]. These studies were followed by a theoretical calculation using a one-electron Hamiltonian within the context of a tight binding model to derive the change in the second order susceptibility tensor elements with the interparticle distance. A model including a single hexagonal superlattice domain containing about 500 particles was used [5]. Another theoretical model devoted to the study of the main modifications due to disorder in such a quantum dot lattice has been presented too where the second harmonic response was used as a convenient probe of the changes in the electronic structure [6]. Low frequency impedance spectroscopy on such Langmuir monolayer of alkylthiol passivated silver nanoparticles was also performed as a function of the interparticle distance [7]. The authors found that at a very small interparticle distances, namely when $D/2r = 1.2$ where D is the distance between particles and $2r$ the diameter of the particle, the transition was observed through a change from an equivalent *RC* circuit to an inductive circuit. The same group has published several reports to understand the behaviour of both the linear and nonlinear response in this system. Classical models using an effective medium approach have been used to determine the linear and the nonlinear optical properties of the films upon compression. These models worked for large interparticle distance but failed close to the IM transition in the linear case. For the nonlinear one, the model failed [8]. They also calculated the contributions of the local fields to the SHG intensity based on their experimental results previously published [4]. They showed that their measurements were dominated by the second order susceptibility tensor elements and not by the linear optical properties of the films. Therefore, the quadratic susceptibility $\chi^{(2)}$ is an excellent indicator of the interparticle coupling changes and is sensitive to the disorder of the system [9]. They finally showed using a normalized density of states that the IM transition takes place at very small interparticle distances, namely $D/2r < 1.2$ [10].

The SHG studies performed in this chapter are focused on the nonlinear optical response of two types of films of metallic nanoparticles. The first part of this chapter is dedicated to the SHG response of metallic films made from spherical dodecanethiol-capped nanoparticles at the air/water interface. Polarisation studies at the neat interface have been

performed first to deduce the susceptibility tensor elements of the bare air/water interface, similarly to the work performed by Heath et *al*.. The nanoparticles were then subsequently added at the interface and a polarisation study was performed to observe the modifications occurring in the nonlinear response as a function of the average surface concentration of particles at the interface. A polarisation study of the film formed at the end of the experiment, at the highest compression, was also performed to deduce the dominant contributions of the nonlinear response in such a film. The second part of the chapter is devoted to the study of the SH response of a film made from metallic nanorods at the interface. In fact and since the form and the size of the particle may play an important role in modifying the appearance of the transition that can be observed for instance through the nonlinear optical response, we were interested in considering nanoparticles films formed using nanorods. Nanorods of dimensions 64 × 24 × 24 nm for their three axes were passivated with dodecanethiol and octadecanethiol chains and used to form films at the air/water interface. A detailed polarisation study at various compression areas corresponding to various average interparticle distances was performed.

5.2. Spherical silver nanoparticles

The studies were first focused on spherical dodecanethiol-capped silver nanoparticles. The linear optical response of the films made from these particles has been described in the previous Chapter. A sudden change in the reflectance was observed indicating the presence of strong interactions between the nanoparticles. We are interested to study this type of interaction and monitor any transition that might take place in the film using the SHG technique. Moreover, silver nanoparticles are well suited for a study at the harmonic wavelength of 400 nm since the SPR for an individual silver particle is located around 400 nm. This proximity yields an enhancement of the SHG response. For gold nanoparticles, the SPR is located around 530 nm and the enhancement is not prominent.

5.2.1.Experimental setup and film preparation

In Figure 5.1, the SHG experimental set-up is described. The nonlinear light source used was a femtosecond Ti: sapphire laser (Tsunami) with a fundamental wavelength set at 800 nm.

The repetition rate was 80 MHz and the pulse duration was about 70 femtoseconds. A motorized half wave plate at 800 nm was placed along the beam to define the linear polarisation angle γ of the fundamental input beam. A long-wavelength pass filter was placed to remove any second harmonic light generated prior to the interface. The two mirrors placed after this filter had a dielectric coating to ensure that no second harmonic light was generated before the Langmuir trough. The incident angle of the fundamental beam on the interface was set to 70°. This fundamental beam was focused to the interface by a 10 cm focal length lens. The average power at the interface level was about 0.5 W. The SHG light at 400 nm generated from the interface was collected with a second lens with a 10 cm focal length. Two short-wavelength pass filters were placed to separate the second harmonic light from fundamental one and the background. The second harmonic light was then passed through a half wave plate and a polarizer cube allowing only vertically polarized light. The half wave plate was used to define the detected polarization of the harmonic light. The harmonic beam was then focused by a third lens onto the entrance slit of the spectrometer and then collected by a cooled CCD camera. The experiment was controlled by a custom-written LabVIEW software.

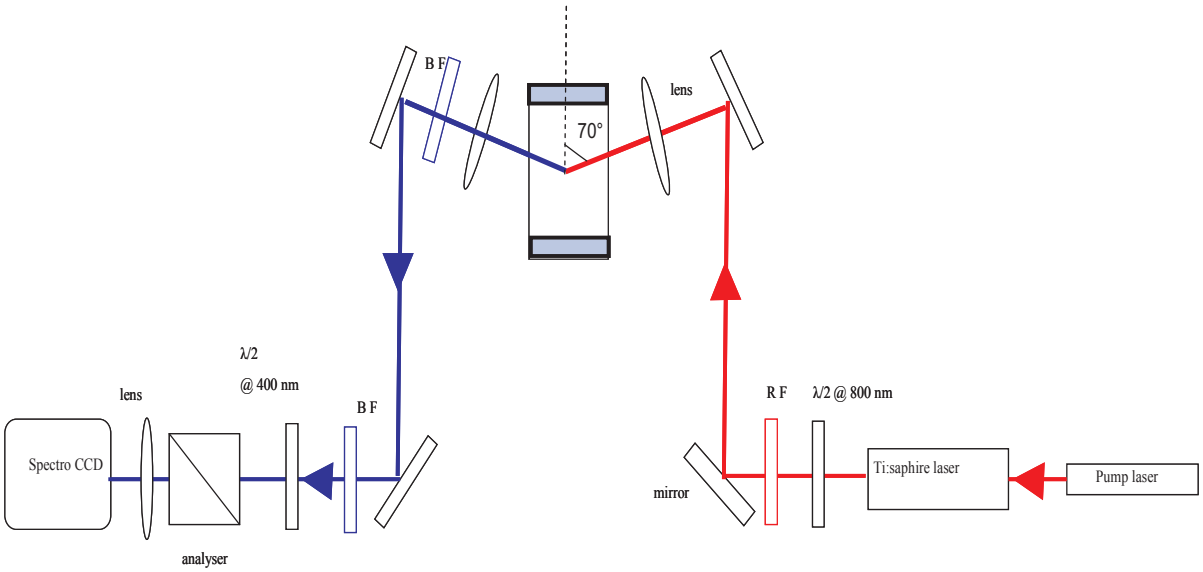

Figure 5.1: SHG experimental setup

The first experiment consisted in detecting a SHG signal from the bare air/water interface. The fundamental laser beam was set at 792 nm. The exact value of this wavelength is not critical although it is important that it is close to 800 nm in order to get later an enhancement at 400 nm with the SP resonance of the silver particles. Figure 5.2 gives a narrow spectrum of

the SH signal intensity for the pure air/water interface using an acquisition time of 60 seconds. The experimental data are fitted with a Gaussian function. The maximum of the Gaussian function is found at 396 nm, confirming that a SHG process is taking place. However, we notice the presence of a background due to noise and multiphoton excited luminescence. This background is removed from the SHG signal using an adjusted background with the Gaussian fit, see Figure 5.2. The SH intensity is obtained from the amplitude of the Gaussian function. In addition, the control of the laser power was essential to ensure that the nanoparticles were not damaged due to high fundamental intensities. Therefore, the average laser power never exceeded 0.5 W.

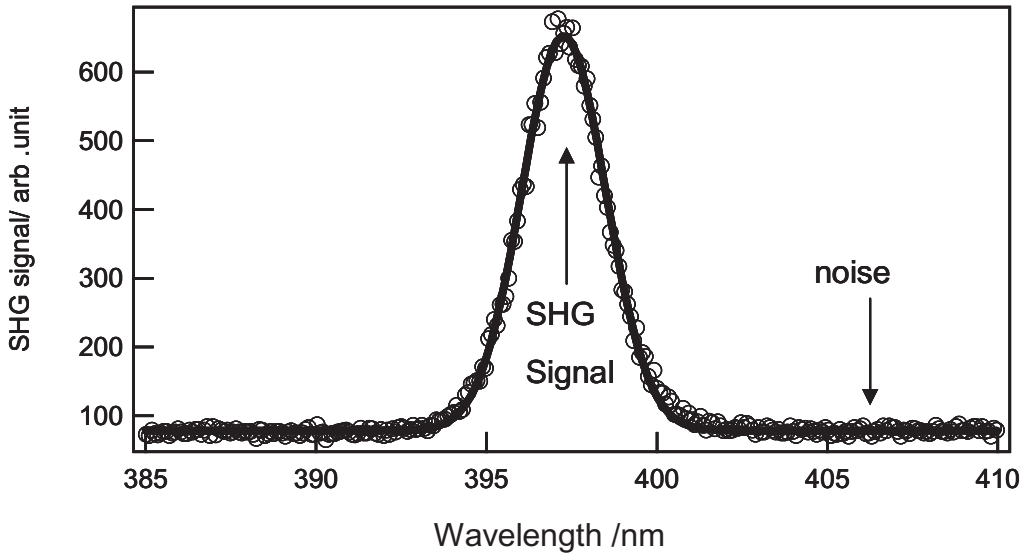

Figure 5.2: Monochromaticity of the SHG light generated at the air/water interface (○). The solid line is a Gaussian fit to remove the noise signal.

For the film preparation in the Langmuir trough, the same procedure as that explained in Chapter 4 was used. First, the trough was cleaned and then filled with ultra pure water (Millipore water, 18 MΩcm, pH 7). A pressure-area isotherm was then recorded to ensure that the water surface was clean. The thermostat of the trough was fixed at 12°C to prevent as much as possible the evaporation of water. The number of particles needed to form a monolayer film was then calculated to be 1.15×10^{12} particles/cm², considering a close packed film of 10 nm diameter particles capped with dodecanethiol. Particle numbers corresponding to concentrations less than, equal to and larger than this critical concentration were then added to the interface in order to study the film in different regimes, namely below and above the

monolayer regime. In the case of above monolayer regimes, multilayer films can be formed. It is also important to note too that the injected number of particles was not necessarily corresponding to the actual surface concentration measured. Indeed, losses of particles at the walls of the trough and on the two barriers were taking place although it was difficult to quantify this observation. These losses were easily noticed upon the injection of the particles at the interface because some of the particles had a tendency to stick to the barriers. This observation is however important because it prevented us from getting exact values of the average surface particles concentration forming the film. After injection, the system was left idle for about 5 minutes for the particles to disperse almost homogeneously at the interface and for the organic solvent to evaporate completely. In our case, hexane was used as the solvent.

5.2.2. Polarisation study of the air/water interface

We started our measurements with the recording of the SHG signal intensity from the neat air/water interface in order to have a reference signal. This proved later to be important to monitor all changes in the SH signal once the particles were deposited at the interface. Moreover, it was interesting to study the neat air/water interface and deduce the susceptibility tensor elements of this interface to compare the results with the literature. Assuming that the water surface is isotropic with its surface normal taken as the $\hat{z}$ direction, we are left with only three independent and non vanishing tensor elements, namely $\chi^{(2)}_{eff,XXZ}$, $\chi^{(2)}_{eff,ZXX}$ and $\chi^{(2)}_{eff,ZZZ}$, out of the initial 27 elements of the general case. These three tensor elements characterize the nonlinear response of the interface. The S-Out and P-Out SHG output intensities were therefore recorded as a function of the input polarization angle γ to extract these elements. However, and because we measure intensities rather than amplitudes, we only have access to the magnitude and the relative phase of these tensor components. Thus, the absolute phase of these elements remained unknown. Phase experiments with a quartz plate would be required to get such information [11]. This neat air/water interface has been studied previously by several authors, Goh et *al.* [12] in particular. The latter authors found a positive phase for the three components of the effective susceptibility tensor. We will assume similarly a positive phase for the three elements in our case too. The experimental data are presented in Figure 5.3. These experimental data were normalized with respect to the $\gamma = 0°$ angle value of

the P-Out intensity curve, a point also named the *pP* value. An adjustment procedure with Eqs.(3.93)-(3.94) of Chapter 3 for the S-Out and P-Out polarization plots was then performed. The two equations used to adjust the experimental data were therefore:

$$I_s \propto \left| a_1 \chi_{eff,xxz} \sin(2\gamma) \right|^2 \tag{5.1}$$

$$I_p \propto \left| (a_2 \chi_{eff,xxz} + a_3 \chi_{eff,zxx} + a_4 \chi_{eff,zzz}) \cos^2\gamma + a_5 \chi_{eff,zxx} \sin^2\gamma \right|^2 \tag{5.2}$$

Coefficient	Value
a_1	0.346
a_2	-0.390
a_3	0.193
a_4	0.327
a_5	0.347

Table 5.1: Value of the a_i coefficients presented in equations (5.1) and (5.2) at a neat air/water interface. The refractive index of water is considered dispersive

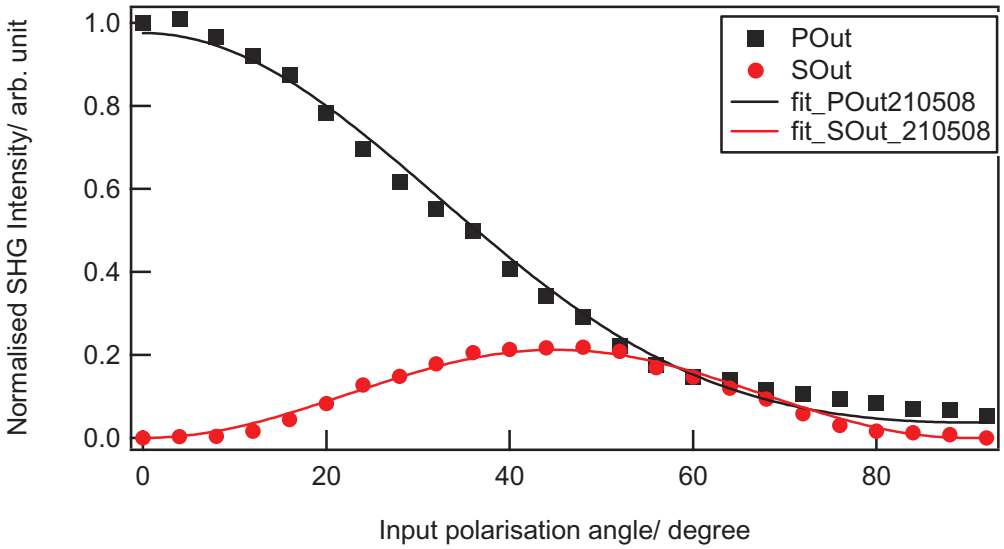

Figure 5.3: SHG as a function of the input polarisation angle for the air/water interface. S-out($\Gamma = 90°$)(●) , and P-out($\Gamma = 0°$)(■)fitted with equations 5.1, and 5.2 respectively. The experimental data were normalized to the value at 0° of the P polarisation curve.

From the S-Out polarization curve, the element $\chi^{(2)}_{eff,XXZ}$ was deduced. The S-Out polarization curve has a bell-shape curve. This value was then introduced in the *P*-Out polarization expression to deduce the elements $\chi^{(2)}_{eff,ZXX}$ and $\chi^{(2)}_{eff,ZZZ}$. Since only relative intensities were recorded, normalization with respect to the $\chi^{(2)}_{eff,ZZZ}$ element was used because the breaking of centrosymmetry occurs mainly along the OZ axis. We therefore set $\chi^{(2)}_{eff,ZZZ} = 1$, yielding $\chi^{(2)}_{eff,ZXX} = 0.17$ and $\chi^{(2)}_{eff,XXZ} = 0.41$. These results are very similar to those found by Goh et *al.* where the element $\chi^{(2)}_{eff,XXZ}$ is about 2.3 times larger than the element $\chi^{(2)}_{eff,ZXX}$ at 20°C. In our case, a ratio of 2.4 is found. For neat air/solvent interfaces, it is difficult to separate the dipolar and the quadrupolar contributions of the tensor elements. Goh *et al.* used a temperature dependent experiment to perform this distinction since the dipolar contribution is strongly dependent on the absolute orientation of the molecules at the interface whereas the quadrupolar one is weakly dependent on it. Upon increasing the temperature, randomisation of the molecular orientation is indeed expected to reduce the dipolar contribution to zero since two molecules having opposite orientation would mutually cancel their contribution to the dipolar susceptibility. For transparent solvents, the Kleinmann rule stating that far away from any resonance the tensor elements χ_{XXZ} and χ_{ZXX} are equal should be obeyed [13]. This can however only be true if the dipolar contribution largely dominates over the quadrupolar one. Kleinmann rule is not obeyed in the case of their results and neither in the case of ours. A detailed study performed by A.A.Tamburello. Luca et *al*. [14] on air/liquid and liquid/liquid interfaces showed that the air/liquid interface possess a strong quadrupolar response arising from the bulk volume. Several air/liquid interfaces where tested such as air/water, air/hexane and air/DCE and compared to liquid/liquid ones such as water/DCE and hexane/water. The experimental results showed that the susceptibility tensor elements of the air/liquid interfaces are larger in magnitude than those of the liquid/liquid one and that they do not obey the Kleinmann rule. The large quadrupolar contribution present of the air/liquid interfaces was explained as arising from the large mismatch between the optical dielectric constant of the liquid and that of air. The large ratio of 2.3-2.4 measured in our case and the experiments of Goh *et al.* is therefore explained by the large quadrupolar contribution present for air/liquid interfaces. We finally note that our results for the air/water interface are in a very good agreement with those obtained by Luca *et al.*.

5.2.3.Polarisation study of monodispersed nanoparticles

After determining the tensor elements for the pure air/water interface, a polarisation study was done for a density of 7.1×10^9 particles/cm^2, an average surface density corresponding to a surface coverage of about 0.5% in terms of the density corresponding to close packed full coverage. The aim of this measurement was to investigate the tensor elements of the interface for diluted particle concentration where interactions between particles are expected to be minimal. It is also important to control whether the surface contribution dominate or not over the bulk one in the presence of particles at the interface [15]. In Figure 5.4, the S-Out, and P-Out polarizations are reported for such a low coverage. The tensor element $\chi^{(2)}_{eff,ZZZ}$ is still the dominant one and all the tensor element values were normalized with respect to it. Hence, we obtained $\chi^{(2)}_{eff,ZZZ} = 1$ with $\chi^{(2)}_{eff,ZXX} = 0.29$ and $\chi^{(2)}_{eff,XXZ} = 0.43$. We notice a clear increase of the tensor element $\chi^{(2)}_{eff,ZXX}$ from 0.17 to 0.29, almost a factor of 2, with the addition of a very small amount of nanoparticles. The tensor element $\chi^{(2)}_{eff,XXZ}$ does not increase significantly. In fact such measurement is delicate since the signal fluctuated and for that we needed to increase the acquisition time.

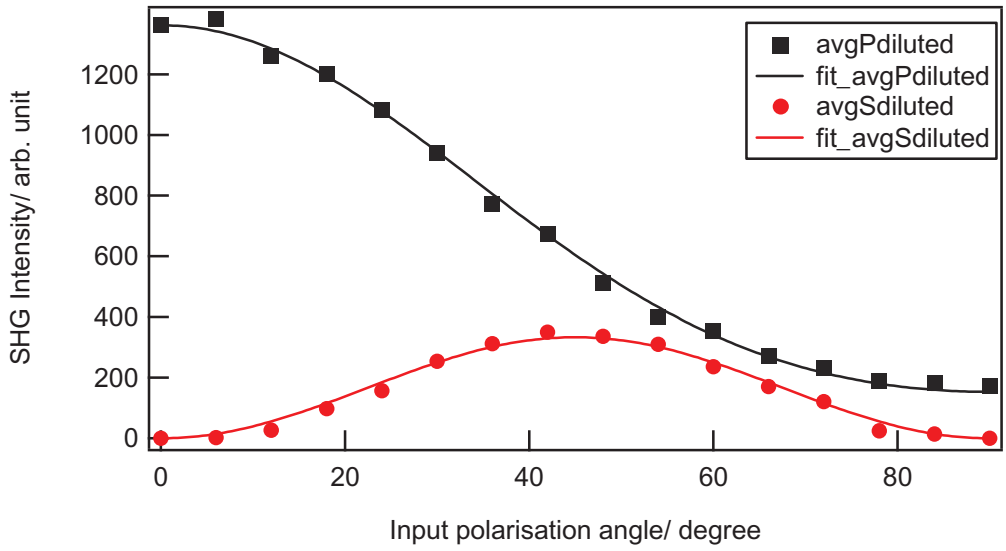

Figure 5.4: The P (■), and S- (●) polarized SH Intensity as a function of the input polarisation angle of the fundamental incoming beam of a 7.12×10^9 particles /cm^2 concentration fitted with their respective equations.

Out of these measurements we can conclude that the surface current parallel to the interface given by the tensor element $\chi^{(2)}_{eff,ZXX}$ is doubled upon the addition of very low concentration

of particles. Also, the element $\chi^{(2)}_{eff,XXZ}$, which is related to the Rudnick and Stern parameter d increases slightly and this is expected for such low concentration. However, the surface current perpendicular to the surface remains the dominating contribution

5.2.4. SHG signal versus compression

Figure 5.5 presents the pressure (right) and the SHG intensity (left) versus concentration for an initial density of 7.07×10^{11} particles/cm². We notice that the SHG intensity started to drop at a density about 1.1×10^{12} particles/cm². Following the procedure performed in the linear optical case, and in order to determine an average value for the critical density after which the signal drops, several experiments were performed where different initial additions of particles were deposited at the interface and studied by SHG using the nonlinear experimental setup presented in Figure 5.1. The rate of compression was 5 cm²/min. Both the SHG signal and the surface pressure were registered versus compression for each initial addition.

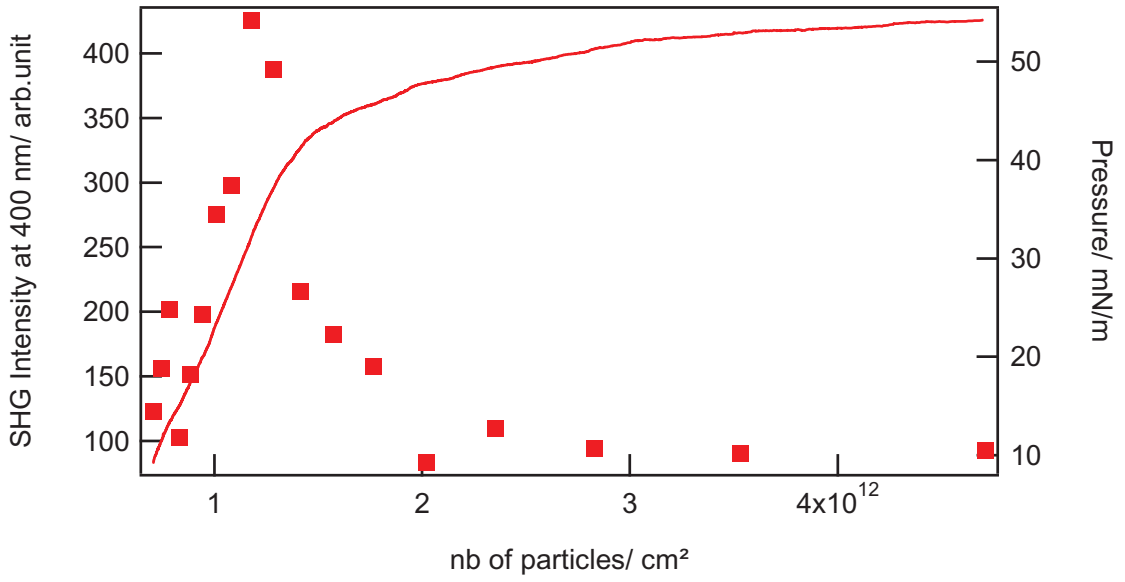

Figure 5.5: SHG intensity and pressure versus concentration for an initial density of 7.07×10^{11} particles/cm²

The general behaviour of the SH signal is similar to that of the linear signal. We notice a sharp increase of the SHG intensity followed by a sharp decrease. The maximum in the SHG signal corresponds to an enhancement by a factor of about 20 as shown on Figure 5.6. A factor of about 3 for the linear reflectance was observed. Because of the large fluctuations in the SH signal intensity though, this enhancement factor varied dramatically from one

experiment to another as well as the corresponding average surface concentration. Hence, the experiments were repeated several times for many different average surface concentrations, see Figure 5.6, in order to ensure the reproducibility of the phenomenon observed.

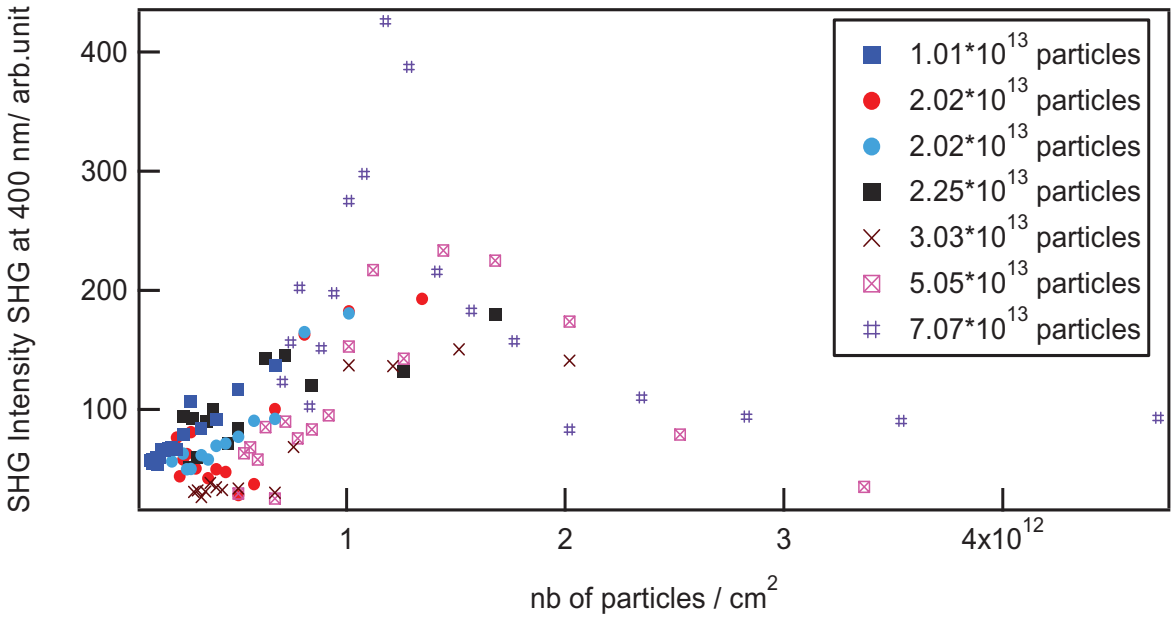

Figure 5.6: SHG Intensity versus average surface particle density for dodecanethiol-capped silver nanoparticles with a diameter of D ~ 10 nm. Various initial additions were used.

The SH signal initially increases upon compression. In a regime where interparticle interactions are neglected, the SHG intensity is proportional to the square of the number of particles illuminated. Hence, the initial increase should scale quadratically with the concentration. Such a behaviour is not clear, partly because of the intensity fluctuations. Another origin for the absence of such a clear dependence may be that the interactions cannot be fully neglected. Hence, the response from the particles also depends on the average density. The complete behaviour of the SHG intensity with the average surface concentration is therefore difficult to extract. Once a critical average surface concentration is reached, the SH signal intensity drops. This decrease in the SH signal is difficult to unambiguously attribute although it may be associated to the IM transition [16].

In the work of C.P. Collier et *al.,* silver nanoparticles the diameter of which was ranging between 2 and 5 nm were used to form a metallic nanoparticles film at the surface of a Langmuir trough. The comparison in the linear optical measurements between their

experiment and ours is provided in Chapter 4. Here we restrict the comparison to the SH behaviour only. The nanoparticles used by Collier et *al*. were of diameter 2 to 5 nm and capped with different thiol chains, starting from C_3 to C_{10}. C_{12} chains were not tested and therefore cannot be compared directly to our work. In our case, short alkyl chains led to unstable particles. These authors observed a similar drop in the SH intensity for particles capped with C_3 and C_6 alkanethiol chains but not with C_{10} chains. The absence of the drop in the latter chains was attributed to the relatively large inter-particle distances obtained in this film owing to the chain length. The IM transition is indeed expected to take place when the particle separation distance gets very small, below about 0.5 nm. Their experimental results for the SHG signal versus area per particle as well as the surface pressure of the Langmuir film are given in Figure 5.7. The SHG intensity increases with the average surface concentration, indicated as area per particle, before a drop occurs of the SH intensity down to a constant value. The pressure versus area isotherm indicates that the drop in the SHG intensity appears well before the film collapse, the latter appearing at about 800 - 850 Angstrom². The isotherm reported on Figure 5.7 is though unusual because the surface pressure increases further, beyond the onset of collapse. The increase is non negligible, of the order of 10 mN/m. This behaviour is unusual in the sense that beyond the collapse, the film pressure is not expected to increase further. Rather, multilayers are formed for instance or drops in the surface pressure are observed owing to the breaking of the film [17-19].

The pressure versus concentration curve for our dodecanethiol silver nanoparticles present a discontinuity at a concentration of 1.6×10^{12} particles/cm² as shows Figure 5.5. This concentration is actually about the same as the critical concentration found for the SH signal intensity drops. However, owing to the signal fluctuations and the film inhomogeneity, the critical concentration value was observed to range from 1.1 to 1.6 $\times10^{12}$ particles/cm². This value can be compared to the concentration of particles required to form a monolayer film with close packing for the 10 nm diameter particles. A value of 1.15×10^{12} particles/cm² was found. This concentration is within the range of the critical concentrations observed, especially if we take into consideration the losses taking place upon injection. Comparing our results to those of Collier *et al.*, we also note that beyond the SHG intensity drop, the SH intensity value is rather weak, in any case much weaker than the one recorded by these authors.

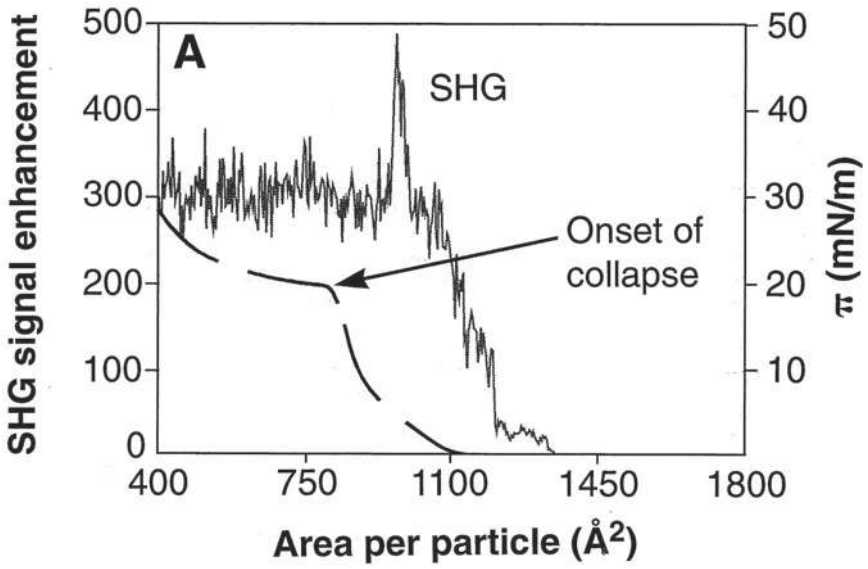

Figure 5.7: SHG signal (left) and surface pressure (right) of the Langmuir film as a function of the area per particle for hexanethiol capped silver nanoparticles [4].

It is interesting to add also that the drop in SHG intensity appears at about the same surface concentration as that obtained for the linear optical reflectance. Assuming that the interparticle interactions remain of similar amplitude throughout the compression, no drop should be seen in the linear reflectance spectrum since the latter should follow the thickness of the film beyond the onset of collapse. However, in the nonlinear regime, multilayer films could lead to a decrease in the SHG intensity owing to a random orientation of the particles in the thicker film. The behaviour is however not supported by the linear optical reflectance measurements. The observation of an IM transition is finally also supported by the final appearance of the film which possesses a shiny reflecting looking at the end of the experiment.

5.2.5.Polarisation study and comparison with a silver metallic film

Polarisation studies were also performed to complement the above results. Figure 5.8 presents the S-Out and P-Out polarisation curves plotted versus the input polarisation angle for the film of initial density 7.07×10^{11} particles/cm² at an area of 100 cm², a density well below the SHG intensity drop.

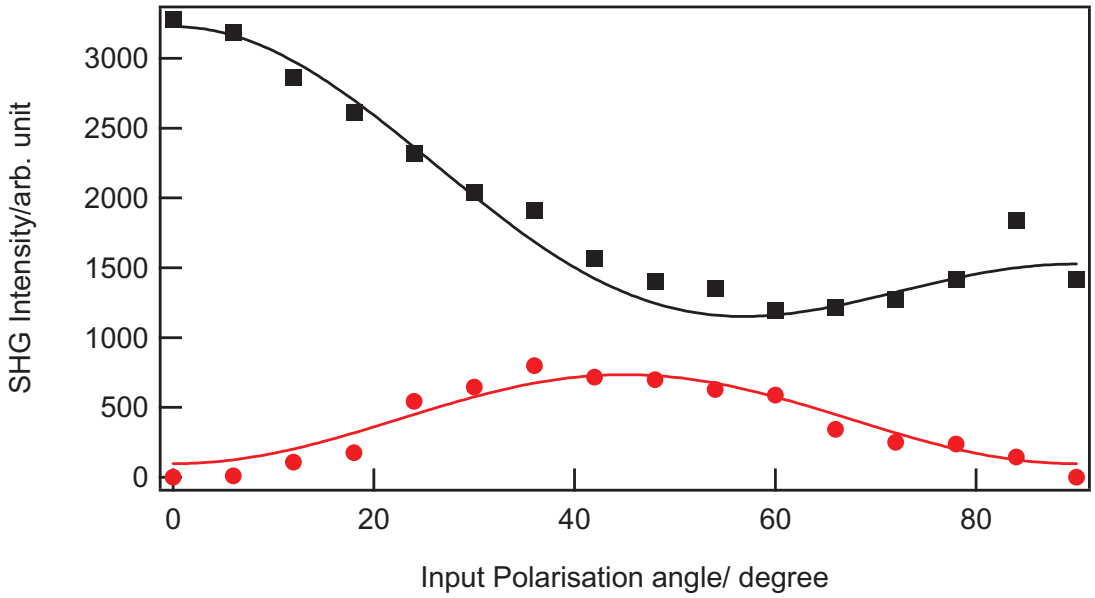

Figure 5.8: The P (■), and S- (●) polarized SH Intensity as a function of the input polarisation angle of the fundamental incoming beam of a 7.07×10^{11} particles /cm^2 concentration fitted with their respective equations.

The SHG signal for this density fluctuated a lot confirming the presence of domains with different densities. By increasing the acquisition time at each angle of polarization, an averaging of the signal over a longer period of time was performed allowing the recording of a polarization curve at 100 cm². The tensor elements were measured to be $\chi^{(2)}_{eff,ZXX} = 0.44$, $\chi^{(2)}_{eff,XXZ} = 0.49$ using the normalization procedure with $\chi^{(2)}_{eff,ZZZ} = 1$. We notice the gradual increase of the $\chi^{(2)}_{eff,ZXX}$ element over the course of the different experiments, from 0.17 for the neat air/water interface water, to 0.29 for a 0.5% coverage of the surface. Its value reaches 0.44 for a coverage of about 70%. A similar increase for the element $\chi^{(2)}_{eff,XXZ}$ from 0.41 for the neat air/water interface, to 0.43 for a coverage of 0.5% to a 0.49 for a coverage of 70% is also observed. The dominant element is always $\chi^{(2)}_{eff,ZZZ}$, indicating that the SH surface contribution perpendicular to the surface remains the dominant contribution at all coverage. The relative increase of the two other elements indicates however that in-plane contribution starts to play a non negligible role in the process.

We have also tried to register the S, and P polarization plots at a concentration of about 1.6×10^{12} particles/cm² which is the critical concentration where we had the maximum of the

SH signal. We did not succeed because of the fluctuations, even with large increases of the acquisition time. S, and P polarization curves beyond the transition were however obtained and are plotted versus the input polarisation angle in Figure 5.9. The average surface concentration is 3.5×10^{12} particles/cm². The coverage is about 4 times that needed to form a single monolayer. In this regime, we likely have multilayers but no clear signature was observed on the isotherms.

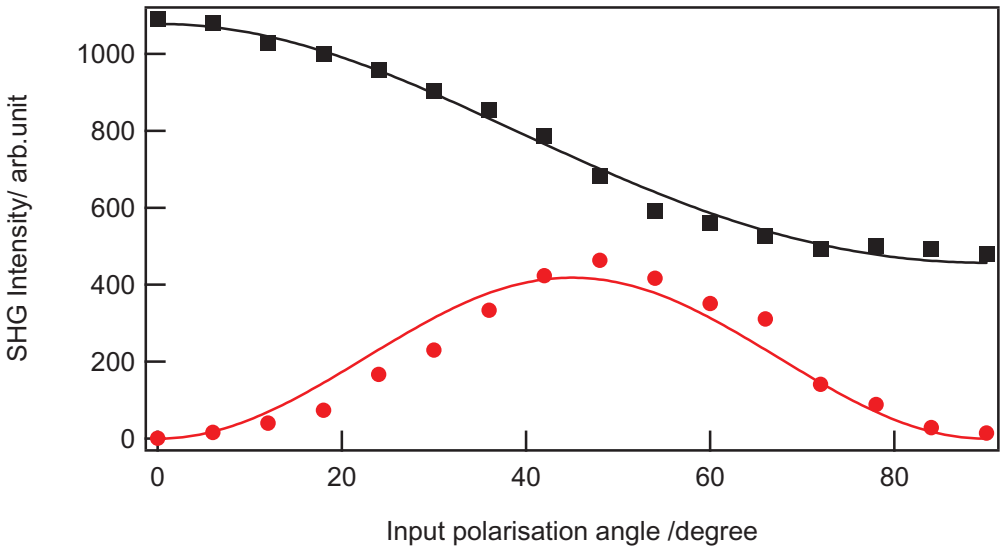

Figure 5.9: The P (■) and S- (●) polarized SH Intensity as a function of the input polarisation angle of the fundamental incoming beam of a 3.5×10^{12} particles /cm^2 density fitted with their respective equations.

It should be stressed though that the transition is observed at much weaker surface concentration. The S, and P polarization curves were adjusted and the tensor elements deduced. We notice the usual domination of the $\chi^{(2)}_{eff,ZZZ}$ element similarly to the previous cases. With the tensor element $\chi^{(2)}_{eff,ZZZ}$ normalized unity, we get $\chi^{(2)}_{eff,ZXX}$ = 0.57 and $\chi^{(2)}_{eff,XXZ}$ = 0.54. The tensor elements $\chi^{(2)}_{eff,ZXX}$ and $\chi^{(2)}_{eff,XXZ}$ continue to increase. These elements have now almost equal values. The values taken by the different elements are reported below.

Tensor elements	XXZ	ZXX	ZZZ
Neat air/water	0.41	0.17	1
~0.5% AgC12	0.43	0.29	1
~70% AgC12	0.49	0.44	1
~400% AgC12	0.54	0.57	1

Table 5.2: Tensor elements as a function of percentage coverage

We conclude from theses experimental results that the tensor elements $\chi^{(2)}_{eff,XXZ}$ and $\chi^{(2)}_{eff,ZXX}$ increase upon the film formation. The increase of the $\chi^{(2)}_{eff,ZXX}$ element is greater than that of the $\chi^{(2)}_{eff,XXZ}$ one. Upon normalization of the tensor element $\chi^{(2)}_{eff,ZZZ}$ to unity, we notice that the element $\chi^{(2)}_{eff,ZXX}$ which is related to the Rudnick and Stern *b* parameter through Eq.(3.99) of Chapter 3 increases. This underlines that the surface current parallel to the interface increases. This supports the idea that surface currents may develop at higher compressions. Also, the element $\chi^{(2)}_{eff,XXZ}$, which is related to the Rudnick and Stern *d,* may indicate that in thick films the electromagnetic field drops are non negligible, possibly because of the film thickness arising from multilayer formation. However, the surface current perpendicular to the surface remains the dominating contribution. Moreover, it appears that the film properties are still very different from that of a perfect metallic silver film [20].

5.3. Nonlinear response of gold nanorods

Previously, problems in the yield and monodispersity have been limiting researchers to use nanorods in various fields of study. Since the synthesis of gold nanorods in decent yield and monodispersity has been developed comparatively recently, works using nanorods have been published, developing an interest in various applications of such a special shape of particles [21]. Meyer and co-workers have recently reviewed the biological applications of high aspect ratio nanoparticles, mainly discussing those related to gold nanorods and nanotubes [22]. Other applications are directly related to the optical properties of the nanorods. For example, the sensitivity of the plasmon resonance frequency toward the refractive index of the surroundings makes them suitable candidates for biological sensing applications [23]. A further refinement of this type of applications is related to the thermal sensitivity of the

nanorods. Upon irradiation with a single pulse of a nanosecond laser, reshaping of the nanorods takes place leading into spheres [24, 25]. Self assembly of nanorods has been an important direction besides the synthesis. The design and preparation of organised and aligned particles have been an important aspect of study. The self-assembly of gold nanorods in aqueous CTAB solution was initially studied by El-Sayed and co-workers who monitored the influence of nanoparticle concentration, solvent evaporation, ionic strength and surfactant concentration for gold nanorods with an aspect ratio of ~4.6 prepared by the electrochemical method [26]. Depending on the conditions, the gold nanorods were observed to assemble in one, two- or three-dimensional structures. A similar study was carried out by Murphy and co-workers for longer nanorods (aspect ratio of about 13–18) prepared by the seed-mediated method [27]. They then extended the study of nanoparticle self-assembly to other shapes, concluding that the nature of the self-assembly and its driving force depend on nanoparticle shape and also on the extent of the shape anisotropy [27]. Works investigating the formation of one-dimensional nanostructures of rod-like shape using the Langmuir–Blodgett technique has also been applied to thiol-capped gold nanorods [28-30]. The different structures observed were attributed to the different interactions between the structures as the surface pressure was varied. TEM images from LB assembly of thiol capped gold nanorods showed that these nanorods have tendency to form nanorod ribbons spontaneously and to align side by side upon compression [30].

In the present work, dodecanethiol and octadecanethiol capped gold nanorods with of dimension 64 × 24 × 24 nm were used to form the nanorods metallic film at the interface. These two chain length were used to controlling somehow the inter-particle distance between the nanorods. The inter-particle distance between nanorods capped with octadecanethiol is expected to be larger than that between nanorods capped with dodecanethiol. Silver nanorods synthesis wasn’t an easy task. For that reason, our choice was oriented towards the gold nanorods. In the field of optics, a special interest is given to this shape of nanoparticles, owing to the two plasmon surface resonances. To our knowledge, the publications studying the nonlinear response of nanorods are scarce [31, 32]. No nonlinear optical study of nanorods film at the air/water interface using the SHG technique has been published. We therefore wish to compare our results with those obtained for the spherical nanoparticles upon compression at the air/water interface.

5.3.1.Isotherm

Pressure versus area isotherms were performed simultaneously with the recording of the SH signal intensity upon compression. The isotherm curves for both nanorods capped with C_{12} and C_{18} are presented in Figure 5.10. We notice that for these concentrations of gold nanorods capped with C_{12} thiols, the behaviour of the pressure versus area isotherm is significantly different compared to that formed by spherical nanoparticles capped with C_{12} thiols presented in Figure 5.5. Both isotherms present an increase in the pressure upon compression but the rate of increase and the change of slope are clearly different. The most remarkable difference appears at large areas. We notice a fast increase in the pressure between 100 and 85 cm² followed by a decrease of the rate of increase before a second change in slope occurs. In the end, the surface pressure reaches a value of 20 mN/m at 20 cm². We do not notice further changes of slope because the concentration of particles added to the interface is very low. In order to form a monolayer, the number of particles needed is calculated to be 1.3×10^{12} for a closed packed film where the nanorods are considered lying within the surface. Therefore, the coverage reached a value of about 0.005% at 15 cm² for the initial density of 4.38×10^{7}particles/cm². For gold nanorods capped with octadecanethiol the general behaviour is almost the same. The change of slope is clearer, starting at an area of 85 cm² till an area of 60 cm². Since the concentration added to perform the isotherm for both types of particles is almost the same, this allows us to compare the difference in behaviour due to the chain length. The main difference is the longer plateau present in the case of the octadecanethiol-capped rods. This could be due to the fact that the longer chains prevent the aggregation of the particles at the first stages of the film and also during the injection stage. This long ligand will thus preserve the nanorods from aggregating. With the C_{12} thiols, the plateau is shorter possibly indicating more disorder in the film. No indication of the onset of collapse is observed in these films. One reason is the low concentration added. Another reason could be that disorder is more important as compared to the case of spherical nanoparticles films and therefore the transition is not clear. For higher concentration, starting with an addition of 600 µL corresponding to 5.32×10^{10} particles, the transition is observed for the octadecanethiol-capped nanorods. This concentration corresponds to only 5.4 % of a full coverage at an area of 15 cm². This concentration is therefore still very far away from that of the 100% coverage. In addition, defects can play an important role. Out of the isotherm curves, it is clear that there exist differences in the films formed from spheres or rods.

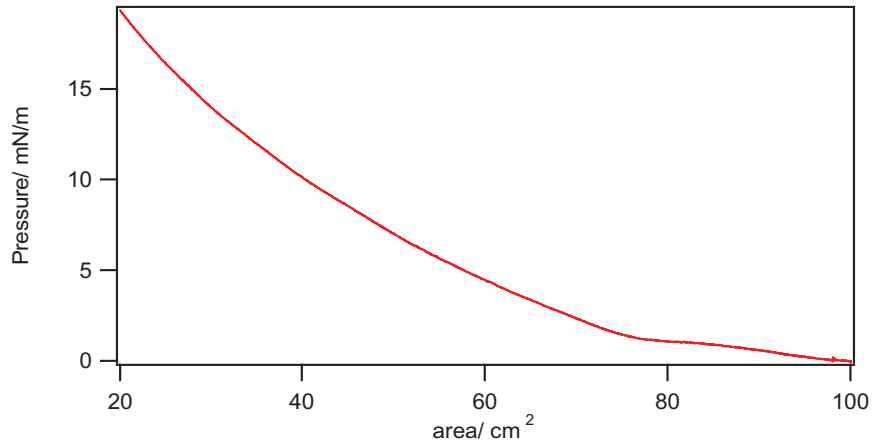

(a)

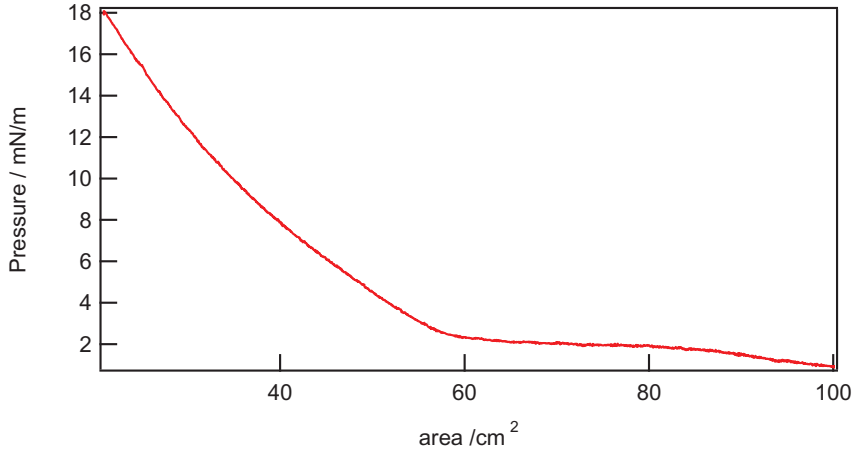

(b)

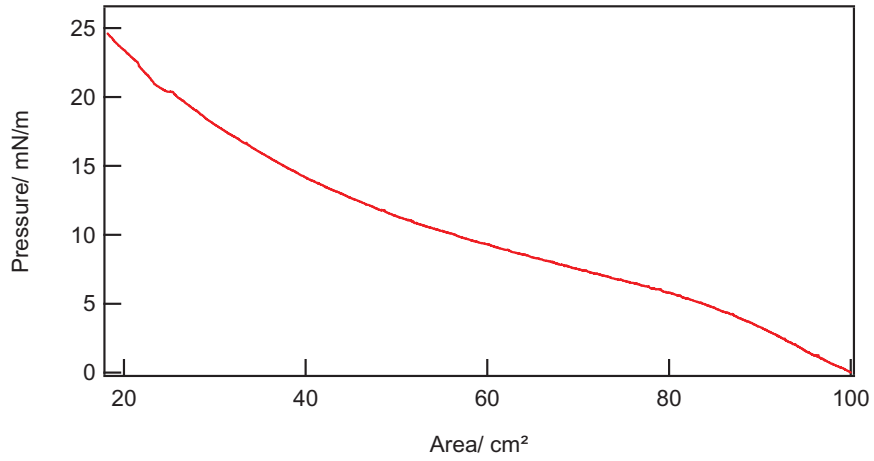

(c)

Figure 5.10: Pressure versus area isotherm for the initial density of: (a) 4.38 ×10^7 particles/cm² of gold nanorods capped with dodecanethiol, (b) 4.75×10^7 particles/cm² of gold nanorods capped with octadecanethiol, (c) 1.77×10^8 particles/cm² of gold nanorods capped with octadecanethiol

5.3.2.SHG signal evolution upon compression

Several initial additions corresponding to different initial surface concentrations were performed at the neat air/water interface and the compression was done for each addition at a speed rate of 2 cm²/min. or 5 cm²/min. These slow rates of compression allow the simultaneous slow organisation of the particles. The compression was started at an area of 100 cm² and stopped at an area of 15 cm². Figure 5.11 presents the SHG signal recorded at 400 nm as a function of the average surface concentration of the gold nanorods capped with dodecanethiol for various initial additions.

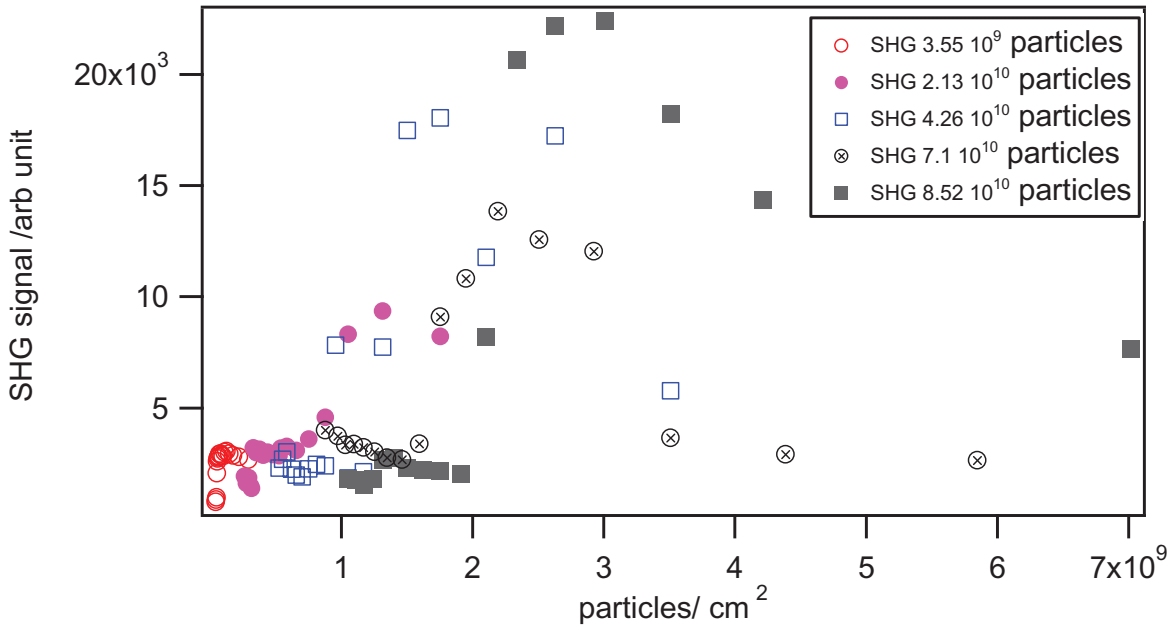

Figure 5.11: SHG signal enhancement as a function of particle density for dodecanethiol gold nanorods of dimension 64×24×24nm

An increase of the SHG intensity is first observed, followed by a plateau after which a further increase occurs before a drop of the SHG signal takes place. Figure 5.12 presents the SHG versus compression for the highest initial density added to the subphase of octadecanethiol nanorods. We notice that a small plateau is present at high density, a density much greater than that where the SHG signal dropped. This assures that indeed we are far away from a drop due to the collapse of the film.

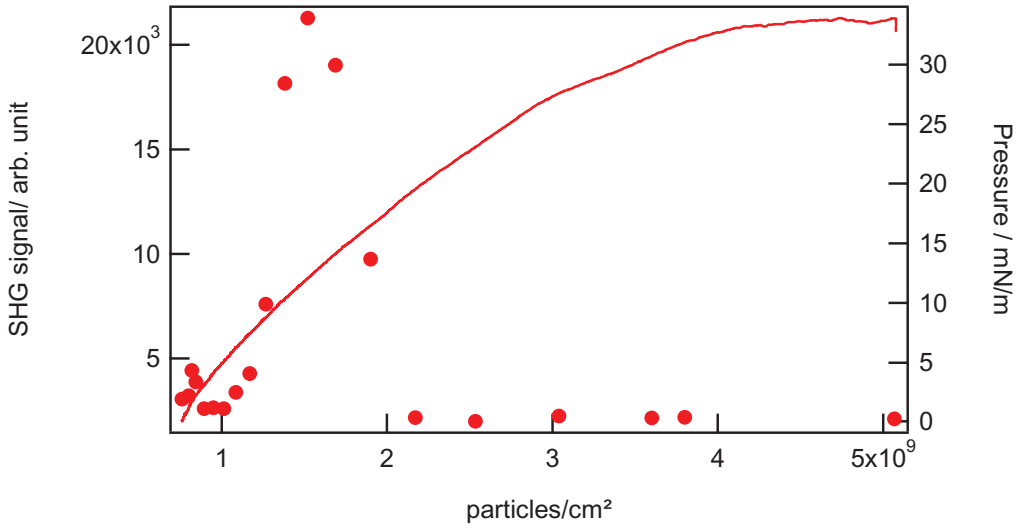

Figure 5.12: SHG intensity and pressure versus concentration for an initial density of 7.6×10^{10} particles/cm² for octadecanethiol nanorods.

Figure 5.13 presents the SHG signal as a function of the average surface concentration of the gold nanorods capped with octadecanethiol for several initial densities. This figure again presents the SHG signal recorded at 400 nm for several initial additions of the nanorods concentration. The overall evolution of the SHG signal in both cases is significantly different from that of the spherical nanoparticles. We first notice an initial rapid increase of the signal followed by a drop in the case of spheres. For the nanorods instead, we notice a first initial increase of the SHG signal followed by a plateau before a sharp increase and then drop. The main difference with the spheres therefore lies in the plateau recorded before the sharp increase that might be attributed to the IM transition.

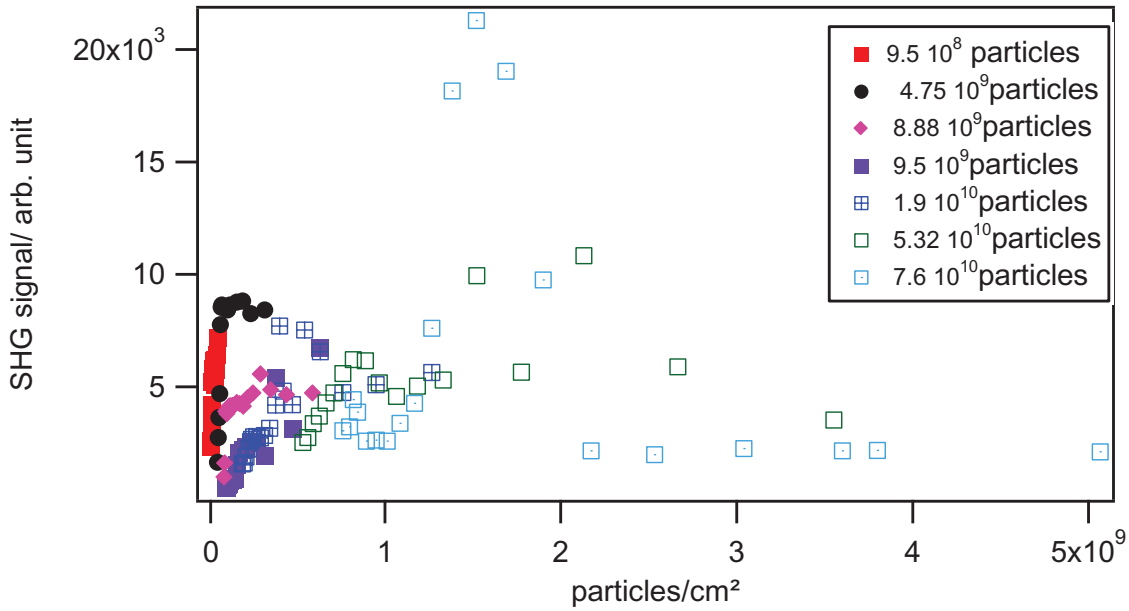

Figure 5.13: SHG signal enhancement as a function of particle density for octadecanethiol gold nanorods of dimension 64×24nm

A close-up view of the initial SHG signal increase is given in Figure 5.14. This figure presents the SHG signal as a function of the nanorods concentration for two additions corresponding to 9.5×10^{8} particles and 4.75×10^{9} particles of gold nanorods capped with octadecanethiol. The initial surface area again is 100 cm². The inset of Figure 5.14 presents the SHG signal versus concentration of an initial addition of 9.5×10^{8} particles.

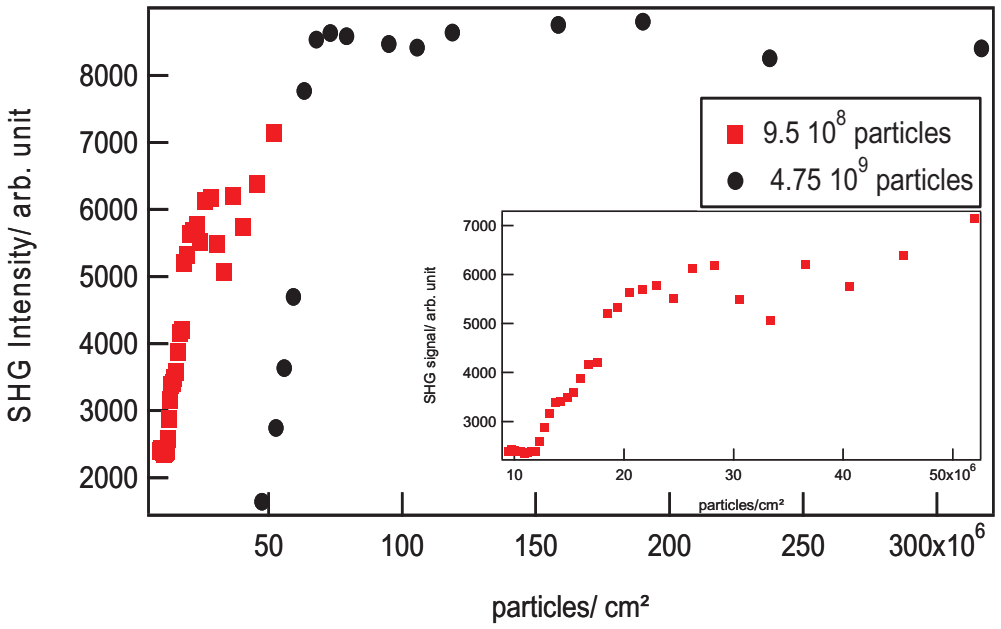

Figure 5.14: Expand of the first part of figure 5.13. SHG signal as a function of particle density for octadecanethiol gold nanorods of dimension 64×24×24nm for 9.5×10^{8} particles and 4.75×10^{9} particles.

The main difference in the SHG plots between C_{12} and C_{18} capped nanorods is in the occurrence of a plateau at low concentrations. In the case of the dodecanethiol-capped nanorods, this plateau is not well defined. The origin of this plateau is not clear. Similarly to the case of the spherical particles, the SHG intensity scales with the square of the surface concentration of particles. Upon compression, this concentration increases and the SHG intensity increases. However, as the compression increases, interactions between particles will take place as identified with linear optical reflectance. Hence, the response will scale differently, depending on the details of the interactions. However, the observation of a plateau indicates that the increase in the number of particles is compensated by a decrease of the effective hyperpolarizability per particle. Another possibility is that within this range, re-organisation takes place within the film, leaving the average surface concentration of particles almost constant.

On the reverse, the critical concentration measured is about the same for both nanorods. The critical concentration at which the SHG signal is the largest for the dodecanethiol-capped nanorods is within the range between 2×10^{9} and 3×10^{9} particles/cm^2 while for octadecanethiol nanoparticles the range is between 1×10^{9} and 2×10^{9} particles/cm^2. Since the

nanorods are similar and only differ by the length of the alkyl chains, these two similar values is not surprising. In fact and since the chain length of octadecanethiol is longer than that of dodecanethiol (1.5 nm and 1 nm respectively), such a difference in the density is expected. In both cases, the maximum of the SHG signal corresponds to an enhancement factor of ~200 compared to that of the neat interface and a factor about ~35 as compared to that of the uncompressed monolayer in the case of dodecanethiol nanorods. For the octadecanethiol nanoparticles, the enhancement factor is ~70 compared to the uncompressed monolayer. The enhancement factor is about 2 times greater for the dodecanethiol-capped nanorods as compared to the spherical dodecanethiol-capped nanoparticles. The SHG enhancement thus probably depends on both the interparticle distance and the morphology of the film. From the experimental results, the SHG enhancement in case of nanorods is greater than that of spherical ones. It is difficult to relate this enhancement to the defects in the film.

The number of particles needed to form a monolayer film of nanorods is calculated to be 1.3×10^{12} particles at the area 15 cm². This number of particles corresponding to a hexagonal filling is never obtained and this is the main difference between these set of experiments and that of the spherical nanoparticles. The maximum number of octadecanethiol-capped nanorods corresponded to only 12% of the concentration required for the full coverage. Besides, and as in the case of spherical nanoparticles, losses of particles do occur also for nanorods. Since in the case of nanorods the concentration is not a high one, losses are however expected to be limited. As a result, Figures 5.11 and 5.13 show that beyond a given density value around 1×10^{9}-3×10^{9} particles/cm^2, fast decrease and in some cases a drop in the SH signal is noticed. Considering the corresponding surface coverage, it is not sure that this decrease takes place because of the formation of a metallic film. A surface coverage of only 12% is obtained although it is possible that the film is semi-continuous with a high number of defects. The possibility of the formation of multilayer films is however severely reduced. In addition, the size and shape distribution, of the order of 10%, can also increase the defects in the film.

5.3.3.Polarisation study

In order to go further in the investigation of these films, polarization curves at the different stages of the compression were performed. The acquisition time was 60 seconds at each polarization angle because of the fluctuations. The polarization curves were done at different

stages of the compression: low coverage, plateau, end of plateau and drop. Considering the different curves, the interest was focused on the ratio 45S/pP of SHG intensities. This ratio increases with the compression. Table 5.3 presents the value of this ratio for all the polar curves of the octadecanethiol nanorods. Figure 5.15 gives the curves recorded at different densities, namely 6.3×10^{7} particles/cm² and 3.16×10^{9} particles/cm² at an area of 20 cm^2. The acquisition time was set to 60 seconds for the S, and P and polarization curves because of the fluctuations. We notice that the value at γ = 45° for the S-Out polar curve at higher concentration increases dramatically as compared to the lower concentration. This increase directly indicates that the tensor element χ_{XXZ} normalized to the element χ_{ZZZ} increases too. In addition, polar curve of a film of 10% full coverage percentage of dodecanethiol rods acquired such an increase in the 45S/pP value confirming this increase presence for both types of passivations.

Concentration p/cm²	6.33×10^{7} (first increase)	3.1×10^{8} (plateau)	6.3×10^{8} (second increase)	2.5×10^{9} (drop)	3.1×10^{9} (drop)
Coverage%	7.4×10^{-2}	0.36	0.73	3%	4%
45S/pP	0.146	0.25	0.12	0.51	0.4

Table 5.3: Concentration, percentage coverage and 45S normalized to pP at different stages of the SHG evolution octadecanethiol nanorods.

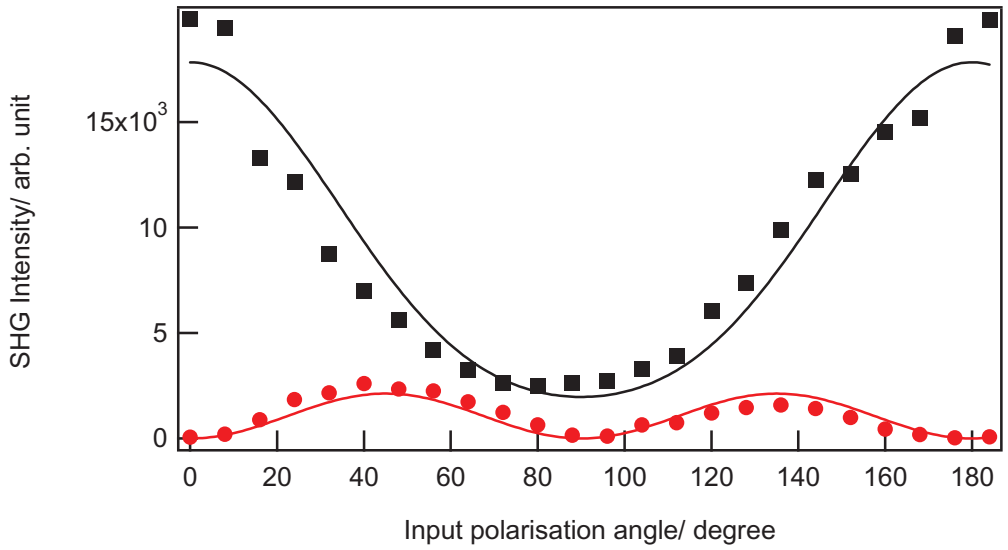

(a)

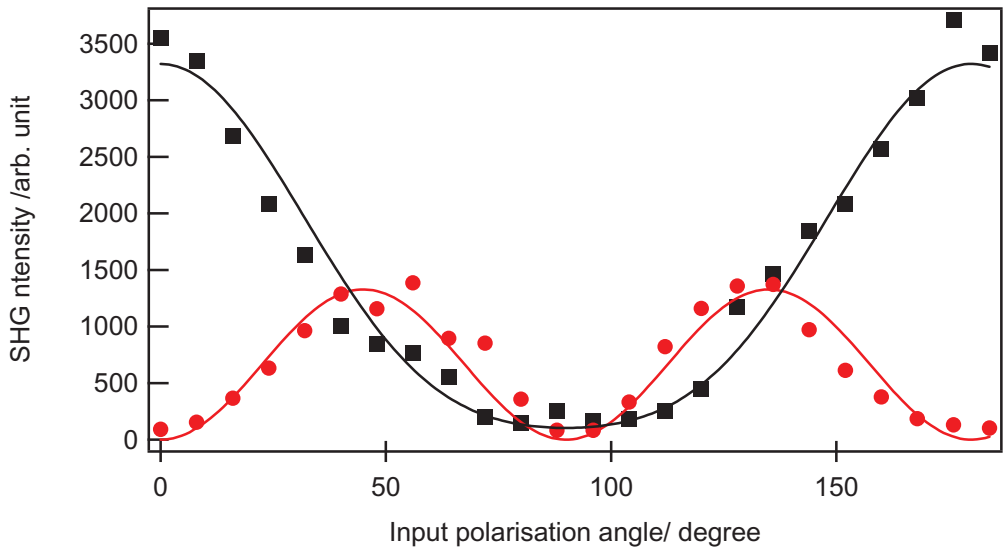

(b)

Figure 5.15: S (●), and P (■) Polarisation curve at particle density: (a) 6.3×10^{7}particles/cm² and (b) 3.16×10^{9}particles/cm² for octadecanethiol nanorods film at 20 cm².

These results again emphasize that the in-plane contribution gets larger as the film is formed. This suggests that in-plane interparticle interactions gets larger, as expected.

5.4. Conclusion

The nonlinear response of nanoparticles films was studied using a femtosecond laser at the air/water interface using the SHG technique. Films formed from dodecanethiol-capped silver spherical nanoparticles the diameter of which was about 10 nm and dodecanethiol- or octadecanethiol-capped gold nanorods with dimensions 64 × 24 × 24 nm were studied in details. The SHG signal evolution upon compression of the film allowed us to underline the change in the properties of the nanoparticles film. A drop in the SH signal for some samples at the highest concentrations was observed, attributed to a possible insulator to metal transition for the spherical particles and possibly to the nanorods despite the low coverage. The evolution of the SHG signal for the gold nanorods was partially different from that of the spherical particles. An increase in the SHG intensity for the silver spherical particles with the nanoparticles concentration was observed but the exact dependence is not clear, possibly because of the interactions between particles in the film. For the nanorods, the SHG signal dependence with the nanorods concentration also possesses a plateau value, attributed to a phase transition the origin of which remains to clarify. The maximum in the SHG signal corresponded to an enhancement by a factor of ~200 in the case of dodecanethiol nanorods and almost the same factor in the case of octadecanethiol nanorods. The maximum in the SHG signal corresponded to enhancement by a factor of ~20 in the case of silver nanoparticles only. SP resonance enhancement, particle shape and even film morphology may be responsible for such an observation. Polarization curves were also performed in order to investigate the dominant source to the nonlinear response. In all cases, the dominant contribution remains the breaking of the inversion symmetry along the normal direction perpendicular to the interface. However, in all cases, the increase of the in-plane contributions is clearly demonstrated indicating that in-plane contributions like particle interactions play a growing role as the compression increases.

References:

[1] N. Bloembergen, R. K. Chang, S. S. Jha, and C. H. Lee, "Optical Second-Harmonic Generation in Reflection from Media with Inversion Symmetry," *Phys. Rev.,* vol. 174, pp. 813-813, 1968.

[2] P. F. Brevet, "Phenomenological three-layer model for surface second-harmonic generation at the interface between two centrosymmetric media," *J. Chem. Soc., Farad. Trans.,* vol. 92, pp. 4547-4554, 1996.

[3] Y. R. Shen, "Optical Second Harmonic Generation at Interfaces," *Ann. Rev. Phys. Chem.,* vol. 40, pp. 327-350, 1989.

[4] C. P. Collier, R. J. Saykally, J. J. Shiang, S. E. Henrichs, and J. R. Heath, "Reversible Tuning of Silver Quantum Dot Monolayers Through the Metal-Insulator Transition," *Science,* vol. 277, pp. 1978-1981, 1997.

[5] F. Remacle, C. P. Collier, J. R. Heath, and R. D. Levine, "The transition from localized to collective electronic states in a silver quantum dots monolayer examined by nonlinear optical response," *Chem. Phys. Lett.,* vol. 291, pp. 453-458, 1998.

[6] F. Remacle, C. P. Collier, G. Markovich, J. R. Heath, U. Banin, and R. D. Levine, "Networks of Quantum Nanodots: The Role of Disorder in Modifying Electronic and Optical Properties," *J. Phys. Chem. B,* vol. 102, pp. 7727-7734, 1998.

[7] G. Markovich, C. P. Collier, and J. R. Heath, "Reversible Metal-Insulator Transition in Ordered Metal Nanocrystal Monolayers Observed by Impedance Spectroscopy," *Phys. Rev. Lett.,* vol. 80, pp. 3807-3807, 1998.

[8] J. J. Shiang, J. R. Heath, C. P. Collier, and R. J. Saykally, "Cooperative Phenomena in Artificial Solids Made from Silver Quantum Dots: The Importance of Classical Coupling," *J. Phys. Chem. B,* vol. 102, pp. 3425-3430, 1998.

[9] C. P. Collie, S. Henrich, and n. J. R. Heath, "Direct measurement of local field factors for second-harmonic generation from quantum dot Langmuir monolayers compressed through the metal-insulator transition," *Philo. Magaz. Part B,* vol. 79, pp. 1299-1299, 1999.

[10] G. Markovich, C. P. Collier, S. E. Henrichs, F. Remacle, R. D. Levine, and J. R. Heath, "Architectonic Quantum Dot Solids," *Acco. Chem. Rese.,* vol. 32, pp. 415-423, 1999.

[11] K. Kemnitz, K. Bhattacharyya, J. M. Hicks, G. R. Pinto, B. Eisenthal, and T. F. Heinz, "The phase of second-harmonic light generated at an interface and its relation to absolute molecular orientation," *Chem. Phys. Lett.,* vol. 131, pp. 285-290, 1986.

[12] M. C. Goh, J. M. Hicks, K. Kemnitz, G. R. Pinto, T. F. Heinz, K. B. Eisenthal, and K. Bhattacharyya, "Absolute orientation of water molecules at the neat water surface," *J. Phys. Chem.,* vol. 92, pp. 5074-5075, 1988.

[13] D. A. Kleinman, "Nonlinear Dielectric Polarization in Optical Media," *Phys. Rev.,* vol. 126, p. 1977, 1962.

[14] A. A. T. Luca, P. Hebert, P. F. Brevet, and H. H. Girault, "Surface second-harmonic generation at air/solvent and solvent/solvent interfaces," *J. Chem. Soc., Farad. Trans.,* vol. 91, pp. 1763-1768, 1995.

[15] J. M. Hicks, K. Kemnitz, K. B. Eisenthal, and T. F. Heinz, "Studies of liquid surfaces by second harmonic generation," *J. Phys. Chem.,* vol. 90, pp. 560-562, 1986.

[16] P. P. Edwards and M. J. Sienko, "The transition to the metallic state," *Accou. Chem. Rese.,* vol. 15, pp. 87-93, 1982.

[17] M. C. Petty, *Langmuir-Blodgett Films: An Introduction*: Cambridge University Press, 1996.

[18] J. R. Heath, C. M. Knobler, and D. V. Leff, "Pressure/Temperature Phase Diagrams and Superlattices of Organically Functionalized Metal Nanocrystal Monolayers: The Influence of Particle Size, Size Distribution, and Surface Passivant," *J. Phys. Chem. B,* vol. 101, pp. 189-197, 1997.

[19] N. Innocente, C. Blecker, C. Deroanne, and M. Paquot, "Langmuir Film Balance Study of the Surface Properties of a Soluble Fraction of Milk Fat-Globule Membrane," *J. Agricu. Food Chem.,* vol. 45, pp. 1559-1563, 1997.

[20] H. B. Jiang, L. Li, W. C. Wang, J. B. Zheng, Z. M. Zhang, and Z. Chen, "Reflected second-harmonic generation at a silver surface," *Phys. Rev. B,* vol. 44, pp. 1220-1220, 1991.

[21] J. Perez-Juste, I. Pastoriza-Santos, L. M. Liz-Marzan, and P. Mulvaney, "Gold nanorods: Synthesis, characterization and applications," *Coord. Chem. Rev.,* vol. 249, pp. 1870-1901, 2005.

[22] L. A. Bauer, N. S. Birenbaum, and G. J. Meyer, "Biological applications of high aspect ratio nanoparticles," *J. Mate. Chem.,* vol. 14, pp. 517-526, 2004.

[23] A. Haes, D. Stuart, S. Nie, and R. Van Duyne, "Using Solution-Phase Nanoparticles, Surface-Confined Nanoparticle Arrays and Single Nanoparticles as Biological Sensing Platforms," *J. Fluo.,* vol. 14, pp. 355-367, 2004.

[24] S.-S. Chang, C.-W. Shih, C.-D. Chen, W.-C. Lai, and C. R. C. Wang, "The Shape Transition of Gold Nanorods," *Langmuir,* vol. 15, pp. 701-709, 1999.

[25] S. Link, C. Burda, B. Nikoobakht, and M. A. El-Sayed, "How long does it take to melt a gold nanorod: A femtosecond pump-probe absorption spectroscopic study," *Chemi. Phys. Lett.,* vol. 315, pp. 12-18, 1999.

[26] B. Nikoobakht, Z. L. Wang, and M. A. El-Sayed, "Self-Assembly of Gold Nanorods," *J. Phys. Chem. B,* vol. 104, pp. 8635-8640, 2000.

[27] N. R. Jana, L. A. Gearheart, S. O. Obare, C. J. Johnson, K. J. Edler, S. Mann, and C. J. Murphy, "Liquid crystalline assemblies of ordered gold nanorods," *J. Mater. Chem.,* vol. 12, pp. 2909-2912, 2002.

[28] S. Kwan, F. Kim, J. Akana, and P. Yang, "Synthesis and assembly of BaWO4 nanorods," *Chem. Commun.,* pp. 447-448, 2001.

[29] F. Kim, S. Kwan, J. Akana, and P. Yang, "Langmuir−Blodgett Nanorod Assembly," *J. Amer. Chem. Soc.,* vol. 123, pp. 4360-4361, 2001.

[30] P. Yang and F. Kim, "Langmuir-Blodgett Assembly of One-Dimensional Nanostructures," *Chem. Phys. Chem.,* vol. 3, pp. 503-506, 2002.

[31] J. Nappa, G. Revillod, J.-P. Abid, I. Russier-Antoine, C. Jonin, E. Benichou, H. H. Girault, and P. F. Brevet, "Hyper-Rayleigh scattering of gold nanorods and their relationship with linear assemblies of gold nanospheres," *Farad. Disc.,* vol. 125, pp. 145-156, 2004.

[32] R. Zong, J. Zhou, Q. Li, L. Li, W. Wang, and Z. Chen, "Linear and nonlinear optical properties of Ag nanorods/AAM composite films," *Chem. Phys. Lett.,* vol. 398, pp. 224-227, 2004

Chapter 6

Linear and Nonlinear response of silver nanoparticles at the liquid/ liquid interface: From particles to continuous film

6.1. Introduction

As already discussed, SHG is a powerful technique to study surfaces and interfaces since in the dipole approximation it is forbidden in the bulk of a medium having inversion symmetry, while at the interface inversion symmetry is broken and SHG is allowed. These SHG studies can be used to determine surface symmetry properties or to characterize the nature of the adsorbates at the interface [1, 2], for example giving information about the surface coverage and the orientation at the surface [3, 4]. These reasons have led us to use SHG to investigate the detailed nature of liquid interfaces, in particular in the presence of metallic particles [5]. Silver nanoparticles were therefore dispersed at the water/organic interface to study the linear and nonlinear properties of the film thus formed. The neat water/1-2 dichloroethane (DCE) interface used in our experiment has already been studied by D.S. Walker *et al* [6] by similar methods. This interface is indeed extensively used as an electrochemical interface between two immiscible electrolyte solutions (ITIES). Indeed, this interface can be externally polarized yielding a control of its electrical properties, with interest for the investigation of ion or electron transfer for instance. Using vibrational sum-frequency spectroscopy (VSFS) as a probe of its structure, D.S. Walker *et al* have focused their work on the molecular orientation and distribution to determine whether the interfacial region is molecularly sharp or diffuse. Their results support a picture where the interface is molecularly disordered with properties similar to a mixed phase interfacial region. SHG studies on the neat water/1-2 dichloroethane [7] showed also that the main source of the non linearity arises from the surface itself rather than from the two adjacent bulk solutions. Besides, the polarity of the interface as well as that of other interfaces like the air/water interface has been investigated

using a polarity indicator molecule, N,N'-diethyl-*p*-nitroaniline (DEPNA). The energy shifts of the π–π* transition of this compound observed at the interface by SHG owing to the polarity environments allows indeed to place on a general polarity scale all these interfaces [8].

Metal liquid-like films (MELLF) [9] have also been investigated in the past. These films have unique properties because they retain a colloidal character film, even if they are spread on a liquid surface like that between two immiscible liquids, water and an organic solvent. These films have properties that resemble those of a liquid, yet they retain the metallic luster and the high reflectivity of continuous silver films. The basic structure of these silver particles based films has been studied in the past [10, 11] as well as the optical properties like the Raman scattering [12] or mechanical ones like viscoelastic properties [13] or the effect of surfactants [14]. Furthermore, previous works concerning silver metal liquid-like films showed that these films exhibit a SHG behavior which is different from that of smooth silver films or electrochemically roughened silver surfaces [15]. These studies were performed mainly by a single group who also described [16] these films with spheroidal metal particles, introducing the polarisation analysis and the resonance enhancement of the SHG intensities as a function of the eccentricity of the particles. UV-visible reflectance spectroscopy of these MELLFs [17] to measure the filling factor and the radius of the particles forming the MELLFs were also performed. Recently, SHG studies at the water/2-octanone interface [18] using gold nanoparticles in an electrochemical cell were performed showing the increase of SHG intensity with the number density of particles at the interface during adsorption but decrease due to aggregation of these particles into large islands.

The present chapter is devoted to the study of MELLFs formed from aggregated silver nanoparticles of diameter 8nm supported at the water/ DCE interface using SHG. The synthesis of the nanoparticles used to form the film is present in chapter 1. Such study is essential in order to study the evolution of the film from a rough one into a smoother one once reorganisation takes place after a certain time of the film formation. This system is chosen in order to investigate the difference in the SHG response of a rough and smooth film. This chapter is divided into several parts : a first part is dedicated to the film kinetics studies using UV–visible absorbance spectroscopy in addition to the resistance measurements of the film, a second part to the nonlinear optical studies with polarisation analysis of SH intensity of neat

interfaces, water/dichloromethane and water/1-2 dichloroethane and interfaces with monodispersed silver nanoparticles in absence of aggregation and a last part to the nonlinear analysis of the evolution of the SH intensity upon the addition of NaCl salt initiating aggregation. The polarisation analysis at different stages of the film formation and the comparison of the films thus formed with thin metallic silver films was also performed.

6.2. Linear optics

6.2.1. Setup

Linear optical studies were performed in order to follow the SPR behaviour during the formation of the film. It is indeed known that the SPR is sensitive to its environment. A white light beam from a halogen deuterium lamp (Ocean Optics) was coupled to the spectroscopic cell through an optical fiber. The light exiting from the cell was collected by another optical fiber and sent to the UV-visible spectrometer (Ocean Optics, USB2000). A diode array integrated in the spectrometer allowed the direct recording of the full UV-visible absorption spectra between about 400 nm and 800 nm. The absorption spectra were taken in transmission, the light beam going through both the aqueous and the organic phase as well as the interface.

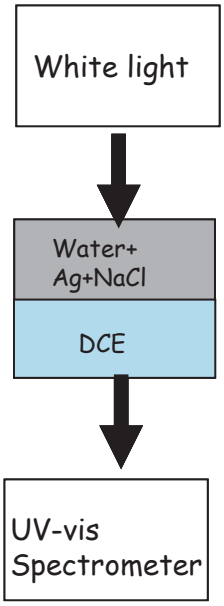

Figure 6.1 : Experimental setup in transmission for the UV-visible absorption measurements

6.2.2.Kinetics of the film formation

The water/1,2-dichloroethane (DCE) interface was prepared by pouring first a precise volume of DCE and then of distilled water into the cell to form a stable interface with the organic phase lying underneath the aqueous one. We first faced problems due to the turbidity of the DCE solution. A high degree of quality of the DCM stock solution, spectroscopic grade, was therefore used. The water/dichloromethane (DCM) interface was prepared following the same procedure since it is a less toxic solvent and is so similar to the DCE. 1 mL of the silver nanoparticles containing aqueous solution was then added to the neat aqueous solution. The aqueous phase turned immediately bright yellow owing to the presence of the particles. The UV-visible absorption spectrum was then recorded. The volume of the aliquot added to the aqueous phase was carefully determined in order to introduce the exact number of particles needed to form a single monolayer at the interface if all the particles were forming a compact arrangement. The cell was rectangular providing a flat surface with dimensions of 2 cm × 4 cm (Hellma, dye-laser cell,101.172.QG). In this calculation, the curvature of the interface was not taken into account. Then, 2.4 mL of a 3 M sodium chloride (NaCl) aqueous solution was added to the aqueous phase. The color of the latter phase rapidly changed from light yellow to grey, signaling the initiation of particle aggregation. The UV-Visible absorption spectra were recorded over time to follow the kinetics of the aggregation in the bulk phase as well as the film formation upon the salt addition. Over time, after aggregation had well proceeded, the aqueous phase was starting to clear as seen from a look at the cell through transmission in a direction perpendicular to the previous one, without looking through the organic phase. Furthermore, a thin shiny grey interfacial layer was formed at the water/DCE interface after few hours. This general process was observed in the absorption spectra through the decrease and broadening with time of the SPR band until it becomes flat altogether as the phase cleared, see Figure 6.2. The aggregation process is initiated by NaCl addition owing to the sudden increase in the ionic strength thereby reducing the Debye length for the particles. These particles, initially protected by a large diffuse layer, are then allowed to come closer to each other owing to the Debye length reduction, hence eventually aggregating. Figure 6.3 presents the absorbance evolution with time at 400 and 700 nm wavelengths adjusted with a fourth order polynomial. This choice was taken referring to reference [19] where a detailed study of adsorbate induced silver nanoparticles aggregate kinetics has been presented. The choice of the 700 nm wavelength was made in order to record the absorbance away from the SPR, to get a clearer picture of the aggregation evolution. However, we notice that the curve at 400

nm is so similar. Upon the addition of the NaCl salt, the nanoparticles aggregated in the bulk of the aqueous phase, starting also to sediment at the interface. A complex process where the kinetics is expected to depend on the size of the aggregates is then expected to take place, the aggregation in the bulk phase proceeding further in the meantime. The UV-visible absorbance spectrum of the upper aqueous phase proved the disappearance of the particles from the aqueous phase within an hour of the salt addition. The SPR associated with the monodispersed suspension of the silver particles therefore vanished owing to aggregation and eventually formation of an interfacial film. Out of Figure 6.3 we conclude that the aqueous solution cleans in about 1 hour.

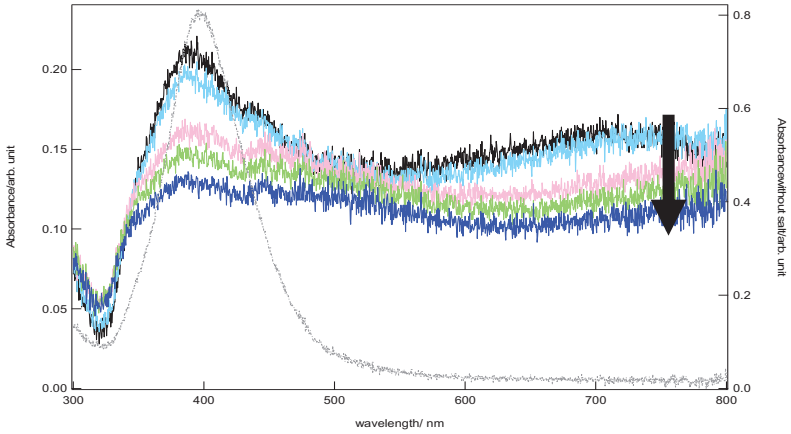

Figure 6.2: UV-visible absorption spectra of 1 mL silver nanoparticles without salt right axis (dotted grey line) and after the addition of salt at 0, 1, 6, 10 and 38 minutes.

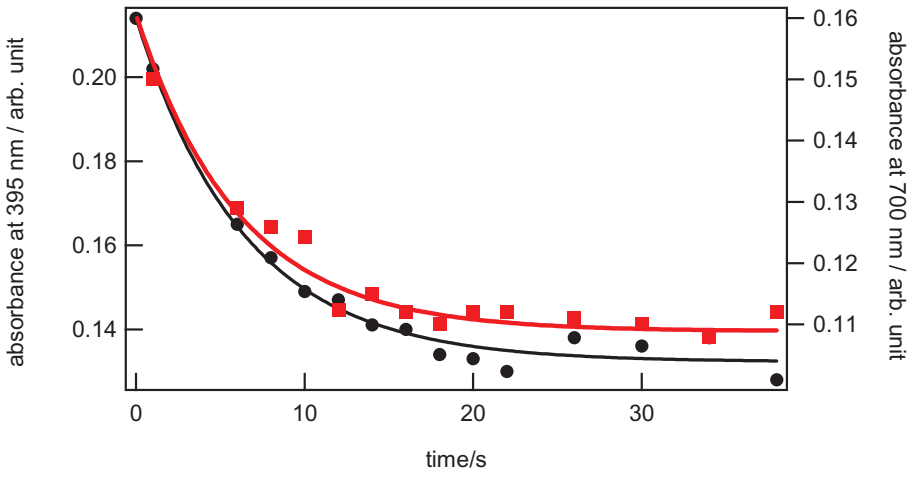

Figure 6.3 : Absorbance at 395nm (●) and 700 nm (■) as a function of time.

6.2.3. Resistance measurements

To complement these studies on the kinetics of the film formation, resistance measurements were also tentatively performed at the interface in order to try to get a picture of the continuous nature of the film. One of the goals of such a study was to record the evolution over time of the in-plane resistance of the film to see whether it decreases, indicating the formation of a rather continuous film, possessing a metallic character. The electrodes were placed at the interface, dipping through the aqueous phase with their ends dipping into the organic solution. It was expected that the resistance in both the aqueous phase and the organic phase would be sufficiently different from that of the interface in the presence of the film, especially if the film presents a metallic character. The resistance measurements were performed using a digital multimeter. We noticed that the resistance did not vary much over time. A decrease of ~3 MΩ was noticed. In fact a sudden drop of about 5 MΩ for a very short time (about 1 minute) followed by a recovery to a value almost identical to that retained before the drop was remarked. This behaviour was observed several times during the recording of the data. Such behaviour is not compatible with the presence of a continuous film presenting a metallic character. A strong drop in resistance should have been observed in that case. We therefore can assume that the film is largely inhomogeneous with resistance fluctuations. This is largely compatible with what is expected for a film produced by the tridimensionnal aggregation of silver particles. Besides, it is important to mention too that the number of particles available for the film is rather limited. It was indeed deliberately chosen to seed the upper aqueous phase with the number of particles required to form a single monolayer of particles. Nevertheless, fluctuations occur owing to diffusion and convection, leading to film reorganization and possibly, for short period of time, a drop in resistance due to the formation of temporary contacts. These resistivity measurements variations were in the range of few MΩ.

6.3. Nonlinear optics

6.3.1.Experimental setup

The Second Harmonic Generation (SHG) experimental setup is shown in Figure 6.4. The system is the same as that presented in chapter 5 for the SHG studies at the air/water interface

except that in the latter case the laser light was irradiating from above, whereas for the liquid/liquid interface the laser was irradiating from below. The angle of incidence was set at 75° providing total internal reflection (TIR) from the organic phase to yield the largest SHG intensities possible. The average power at the cell delivered by the fundamental beam ranged between 0.42 and 0.5 W. The beam was precisely focused in the middle of the cell where the interface lies horizontally flat in the laboratory frame. This ensured that the polarisation states selected for the input beam was properly set with respect to the interface. In fact, curvature of the interface arises because of the non negligible meniscus. The main experimental problem with the use of films at liquid/liquid interfaces was the development of bubbles at the centre of the cell because of laser heating. To avoid the formation of these bubbles, an optimum position of the focusing lenses was searched.

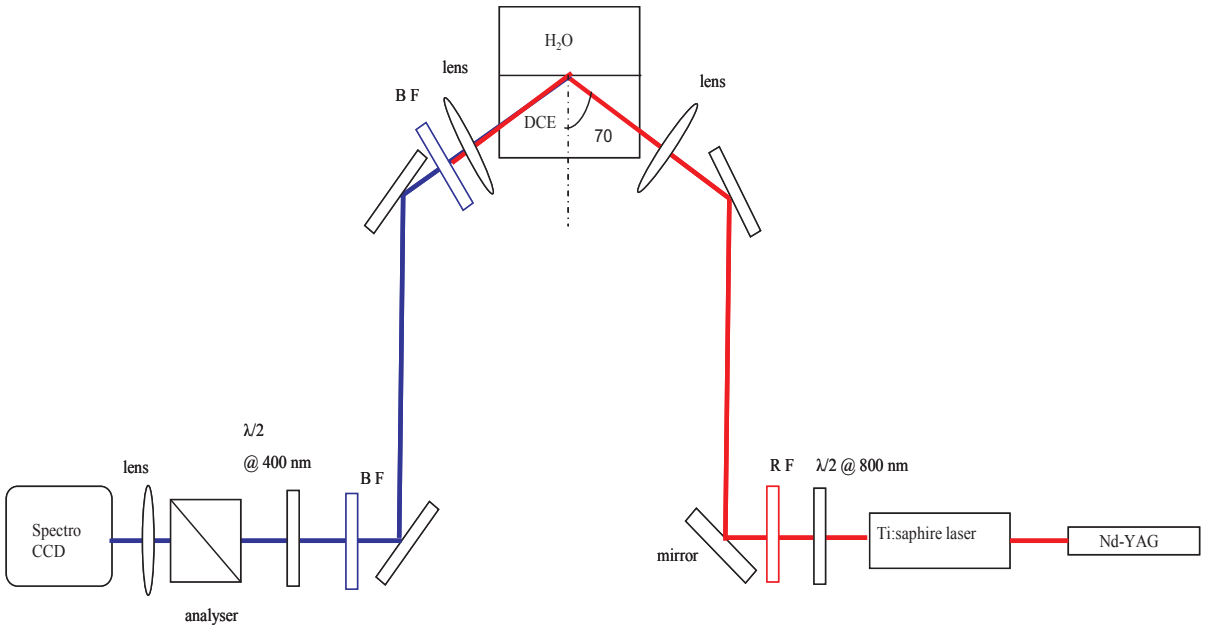

Figure 6.4: Experimental setup for the liquid-liquid interface SHG experiments

Verification of the power dependence of the SHG intensity was done, see Figure 6.5. The average power was measured using a standard wattmeter. The plot, presenting the SH intensity variation as a function of the square of the input average power, indeed exhibits the expected linear behaviour. This plot was obtained for the neat water/DCE interface and showed that an optimum position of the focusing lenses was found, the system being stable for long periods of time. Similarly, the inset shows the SHG line adjusted with a Gaussian

function. Note that any point on the linear graph is the result of the adjustment of a Gaussian line.

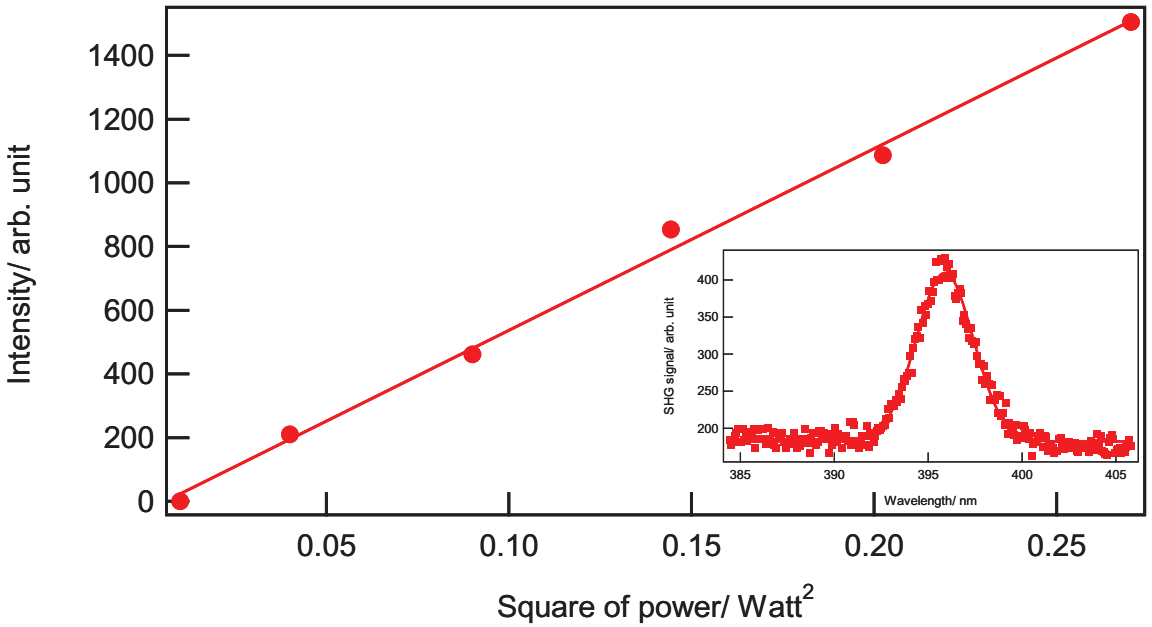

Figure 6.5 : Intensity versus square of laser power fitted with a line. The inset is the SHG line (■) generated at the water/DCE interface fitted by a Gaussian fit.

These results ensured that indeed a SHG signal was collected from this liquid/liquid interface and that a control of the power was available in order to avoid the formation of bubbles at the interface.

6.3.2.Results

6.3.2.1. Polarisation study for the neat liquid/liquid interface

Prior to any further measurements in the presence of particles, light polarization curves for the neat liquid/liquid interface were performed. The quadratic susceptibility tensor elements were then determined with the adjustment to the polar curves. Two neat liquid/liquid interfaces were investigated, namely the water/DCM and the water/DCE interfaces. Figure 6.6 presents the SHG polarisation curves of the water/DCM versus the input polarisation angle.

The model presented in details in Chapter 3 was used to adjust the SHG intensities since it describes the SHG response from an interface between two centrosymmetric media. The equation of the SHG intensity recorded for both the S- and P- polarization configurations are recalled from chapter 3 and given as follows:

$$I_s \propto \left| a_1 \chi_{xzx} \sin(2\gamma) \right|^2 \tag{6.1}$$

and

$$I_p^{DE} \propto \left| (a_2 \chi_{xzx} + a_3 \chi_{zxx} + a_4 \chi_{zzz}) \cos^2 \gamma + a_5 \chi_{zxx} \sin^2 \gamma \right|^2 \tag{6.2}$$

Coefficient	Real value	Imaginary value
a_1	-0.661	-3.832
a_2	-0.081	0.017
a_3	0.034	0.163
a_4	-0.728	-3.476
a_5	-0.527	-3.872

Table 6. 1: Value of the a_i coefficients presented in equations (6.1) and (6.2) at a neat water/DCM interface.

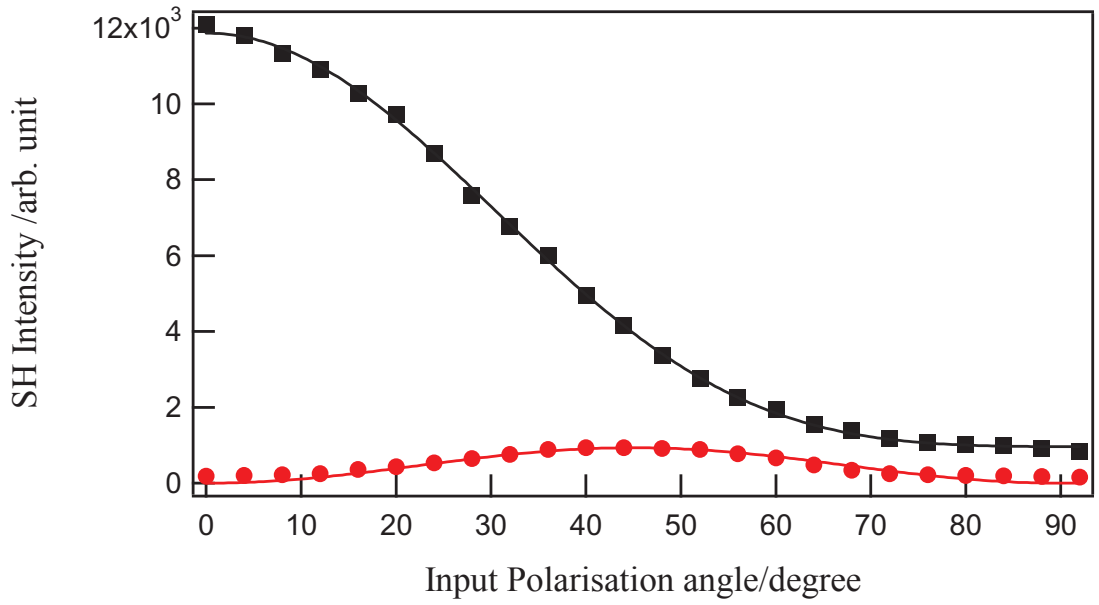

Figure 6.6 : P- (■) and S- (●) polarized SH Intensities as a function of the input polarisation angle of the fundamental incoming beam for the neat water/DCM interface and the corresponding adjustments (solid lines) using equations (6.1) and (6.2).

In Eqs.(6.1) and (6.2), the a_i (I = 1…5) coefficients were calculated using for the dielectric constant of the interface an average value of the optical dielectric constants of the two adjacent phases. From the S-polarised curve, the element $\chi^{(2)}_{eff,XXZ}$ was deduced and from the P-polarized one, the two other elements $\chi^{(2)}_{eff,ZXX}$ and $\chi^{(2)}_{eff,ZZZ}$ were obtained. These elements were assumed real because the system was made from two non absorbing media and because only the relative values of the elements are determined, a normalisation to the element $\chi^{(2)}_{eff,ZZZ}$ was made. For the neat water/DCE interface, the experimental data yielded $\chi^{(2)}_{eff,ZXX} = 0.18$ and $\chi^{(2)}_{eff,XZX} = 0.32$, values similar to those found by Luca *et al.* [7]. For the water/DCM interface, the data yielded the values of $\chi^{(2)}_{eff,ZXX} = 0.19$ and $\chi^{(2)}_{eff,XZX} = 0.23$. These values do not obey Kleinman rule which requires the equality of the elements $\chi^{(2)}_{eff,XXZ}$ and $\chi^{(2)}_{eff,ZXX}$. This indicates the presence of non negligible contributions from the bulk of the two adjacent phases. Table 6.2 presents the tensor elements for the two neat interfaces. It is interesting to note that despite the similarity of the two organic liquids, dichloromethane and dichloroethane, the coefficients are rather different. This difference can indicate differences in the structure of the interface at the molecular level. In particular, the water/DCE interface possess a larger contribution from the volume of the phases, the

kleinmann rule is not obeyed at all, probably indicating a larger degree of ordering as compared to the water/DCM interface.

	$\chi^{(2)}_{eff,XXZ}$	$\chi^{(2)}_{eff,ZXX}$	$\chi^{(2)}_{eff,ZZZ}$
water/DCM	0.23	0.19	1
water/DCE	0.32	0.18	1

Table 6.2: Relative values of the susceptibility tensor elements for the water/DCM and water/ DCE interfaces

6.3.2.2. SHG dependence versus concentration

Since it is known that the SHG intensity scales with the square of the number of particles present at the interface, the SHG intensity was monitored as a function of the increase of number of particles present at the interface. This would be true for an assembly of independent particles, without interactions, their hyperpolarizability being constant. The plots presented in Figure 6.7 clearly show indeed that the SHG intensity increases with the nanoparticles concentration and then saturates. This plot closely resembles isotherms where the surface pressure of the interface is measured as a function of the particle concentration. As expected, with the addition of silver nanoparticles in the bulk of the aqueous phase, partitioning between volume and the interface occurs and the surface concentration increases yielding an increase of the SHG intensity. This increase was modeled with a Langmuir isotherm of the following form [20]:

$$\Gamma = \frac{\Gamma_{max} Kc}{1 + Kc} \tag{6.3}$$

where c is the particle aqueous concentration, Γ is the surface density, Γ_{max} is the maximum surface density adsorbed and K is the equilibrium constant. In agreement with Eq.(6.3), at particle low concentrations, the SHG intensity increases linearly with the concentration and then saturates at higher concentrations. The saturation value of the SHG intensity corresponds to the maximum number of particles possible to pack at the interface. This value depends in particular on the repulsion forces between the negatively charged particles.

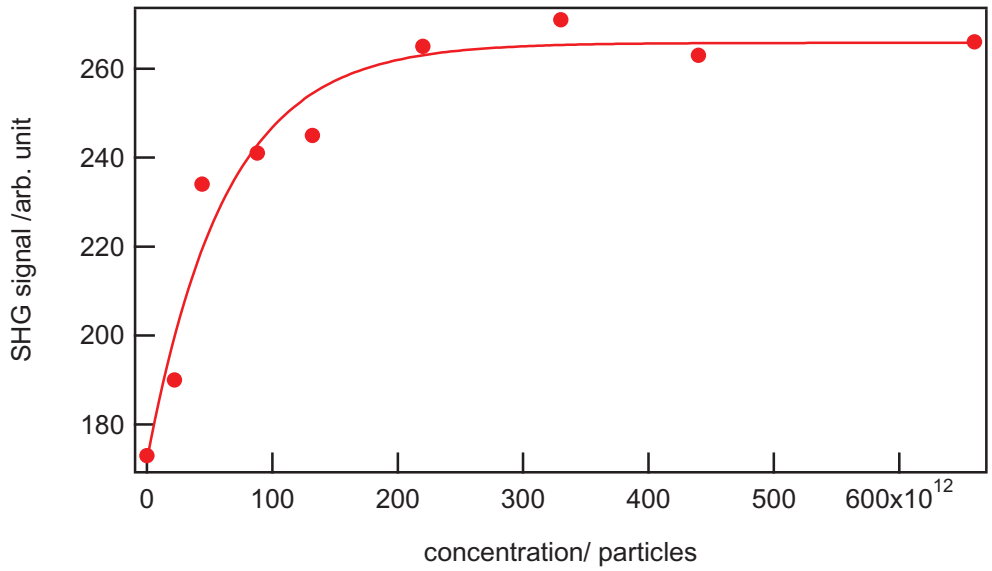

Figure 6.7: SH intensity versus the bulk particle concentration (●) recorded for the pP polarization configuration adjusted with Eq.(6.3)

6.3.2.2.1. Polarisation study of monodispersed particles

Polarization curves were then recorded similarly to the ones recorded for the neat liquid/liquid interfaces. This measurement was performed for the minimum number of particles present at the interface in order to investigate the response of independent particles, see Figure 6.8. Because of the SHG signal fluctuations, long acquisition times were required. The tensor elements of the interface in the presence of monodispersed nanoparticles were deduced using Eqs.(6.1-6.2). If the contribution from the solvents is neglected, then the surface susceptibility tensor $\chi_S^{(2)}$ is related to the particle hyperpolarizability tensor β and the number of particles per unit surface N_S at the interface through:

$$\chi_S^{(2)} = \frac{1}{\varepsilon_0} N_S \langle \beta \rangle \tag{6.4}$$

where the brackets indicate an ensemble average over all orientation taken by the particles. It is interesting to note at this stage though that we cannot assume a complete randomization of the orientation taken by the particles since this would lead to a vanishing value of the susceptibility tensor. Hence, without any assumption on the orientation of the particle frame with respect to the interface, we can introduce the three Euler angles θ, ϕ and ψ to get [21]:

$$\chi^{(2)}_{S,ZXX} = \chi^{(2)}_{S,XZX} = \frac{1}{2}\frac{N_S}{\varepsilon_0}\langle \cos\theta \sin^2\theta \rangle \beta_{zzz} \tag{6.5}$$

$$\chi^{(2)}_{S,ZZZ} = \frac{N_S}{\varepsilon_0}\langle \cos^3\theta \rangle \beta_{zzz} \tag{6.6}$$

Here, the angle ϕ is averaged over 2π to account for the isotropy of the liquid surface and the influence of the angle ψ is neglected, its value being fixed to 90°. Hence, Eqs.(6.5) and (6.6) assume that the particle nonlinearity mainly arise from a single direction. From Figure 6.8, and to first approximation, it can be concluded that the susceptibility elements $\chi^{(2)}_{S,ZXX}$ and $\chi^{(2)}_{S,XZX}$ are almost zero. Hence the only dominating element is $\chi^{(2)}_{S,ZZZ}$. According to Eqs.(6.5)-(6.6), it can be concluded that θ ~ 0, that is, that the nonlinearity stems from the interface and not from the particles themselves. Indeed, if the nonlinearity arises from the particles, the random orientation of the latters would lead to a vanishing value of the susceptibility tensor. On the opposite, if the nonlinearity stems from the interface, arising from the induced polarization of the particles at the heterogeneous interface, a nonlinearity along the normal to the interface can be indeed observed.

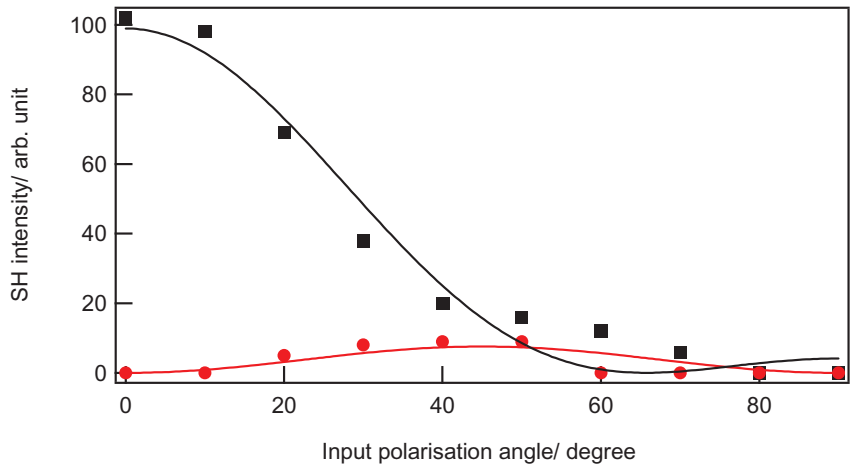

Figure 6.8: The S (●) and P (■) polarized SH Intensity as a function of the input polarisation angle of the fundamental incoming beam of 1 ml monodispersed silver nanoparticles at the interface and the fit (solid lines) using equations (6.1) and (6.2).

6.3.2.3. Evolution of the SHG signal with time

The kinetics of the film formation was then monitored by SHG. After the addition of 1mL of silver nanoparticles and 2400 μL of NaCl, the SHG signal was monitored for a duration about 48 hours, owing to the slow time evolution. Figure 6.9 shows that the SHG signal first increases then reaches a maximum before slowly decreasing. The maximum SH intensity is reached in about 4 hours, a length of time much longer than that of the evolution of the UV-visible absorbance of the bulk solution. Even though the plasmon resonance was lost by about one hour, the signal kept in increasing for about four hours. This time evolution of the *pP* SHG signal is therefore attributed to the sedimentation of the particles at the liquid/liquid interfaces and the kinetics observed indicating that, indeed, we are monitoring the interface instead of the bulk solution. Upon the addition of the NaCl salt, the nanoparticles aggregation in the volume of the aqueous phase is initiated as well as the sedimentation at the interface. As seen from the different kinetics between the volume and the surface, it can be concluded that the process of sedimentation yields an increase of the SHG intensity and that rearrangaments within the film occur, leading to the subsequent loss of the SHG intensity. Similar works have been performed in the past. However, the time duration of the experiments was approximately 8 hours, a much shorter period of time as compared to our set of experiments lasting about 48 hours [15, 21, 22] As a result, all these works have reported just the leveling-off for the SHG intensity instead of both the leveling off and the decrease observed here. In order to get a better understanding of these results, polarisation curves at several stages of the film formation were performed.

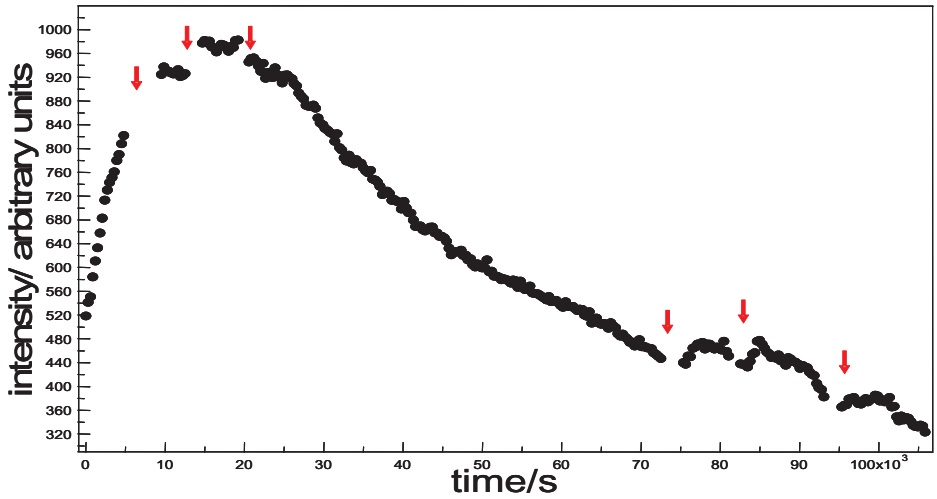

Figure 6.9: The evolution of the SH Intensity with time with the arrows representing the several polarisation curves registered at different times during the film formation.

6.3.2.3.1. Polarisation study during the film formation

Both *P*- and *S*- polarization curves were registered at several stages of the film formation, as seen with the small arrows in Figure 6.9. In Figure 6.10, three S and P polarization curves are presented. The first one is the polar curve obtained at the beginning of the experiment, just after the addition of the salt and the nanoparticles. The second polar curve is recorded at the plateau of the SHG signal obtained at about 4 hours of the film formation. The third is the polar curve recorded just at the end of the experiment, when a grey shiny film is formed at the interface. We further notice that the *sP* SHG intensity value has increased at the end of the experiment as compared to its value at the beginning, before the formation of the film at the interface and at the maximum value of the SHG. It is also noted that the 45S intensity value increased after 4 hours of the film formation and then decreased. In order to underline the polarisation changes, a comparison was made with the intensity values normalized to the value *pP* intensity. Figure 6.11 presents the *sP/pP* polarisation versus time. We notice a decrease, an almost constant value, and then an increase in the value of the sP/pP ratio. Comparing this curve with that of the evolution of the SHG with time, see Figure 6.9, we notice that the minimum in the sP/pP value corresponds to the maximum of the SHG intensity recorded. The general increase of the SHG intensity is therefore simultaneous to a change in polarisation. Figure 6.11 shows the presence of three different regimes and confirms the evolution of the system even at the final stages of the film formation. Another interesting remark is the increase and then the decrease of the value of the 45S. This value gives an idea about the roughness of the film. In fact it is expected to tend to almost zero once

a smooth film is formed at the interface. The increase in this value signifies the formation of a rough film together with the increase of the SH signal expected for such film nature.

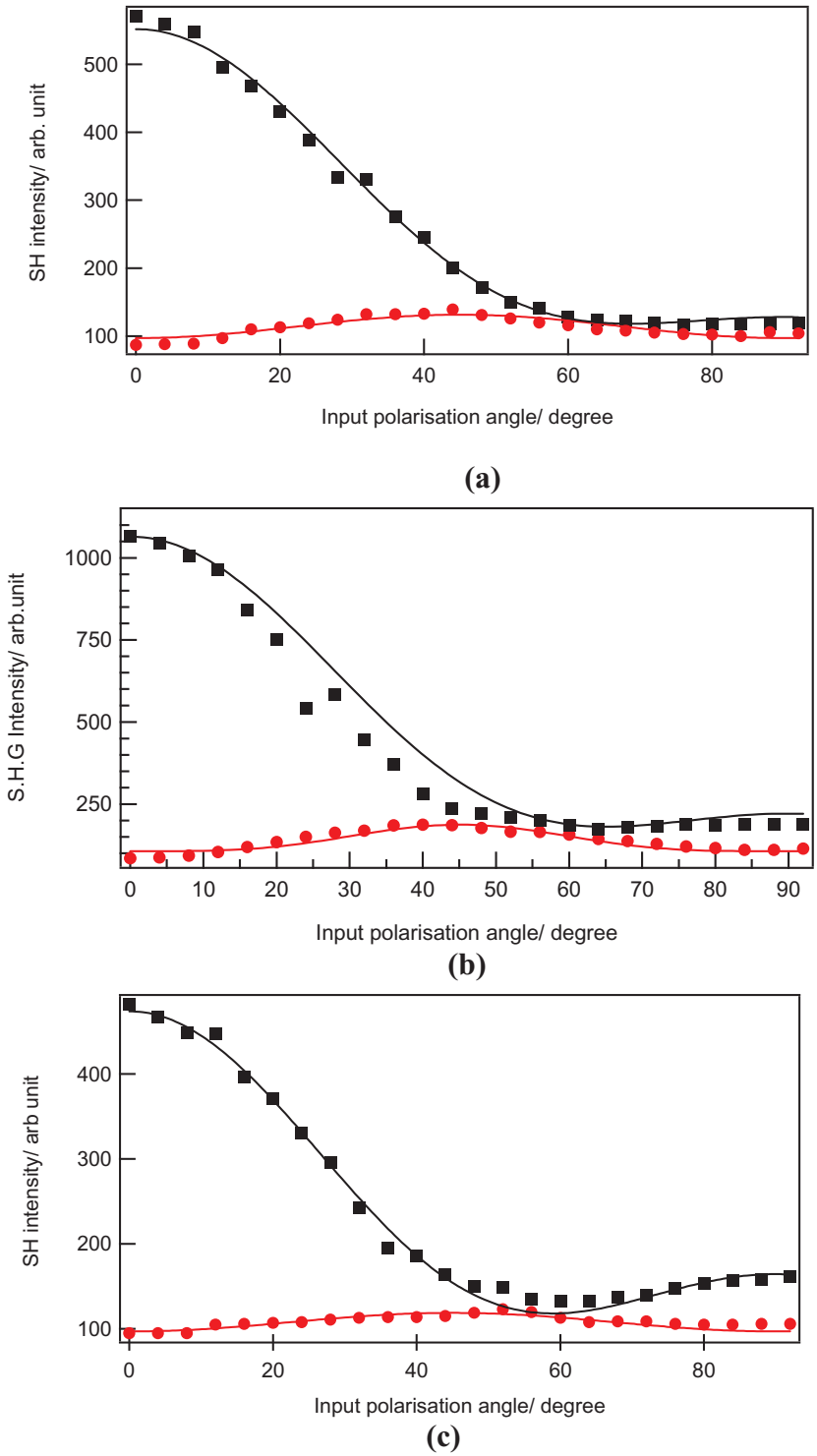

Figure 6.10: Polar curves of the SHG intensity as a function of the incoming fundamental beam polarisation angle: (a) is the S (●) and P (■) polarisation experimental data at the beginning of the film formation fitted with equation (6.1) and (6.2) respectively. (b) at the level of the peak. (c) at the end of the film formation

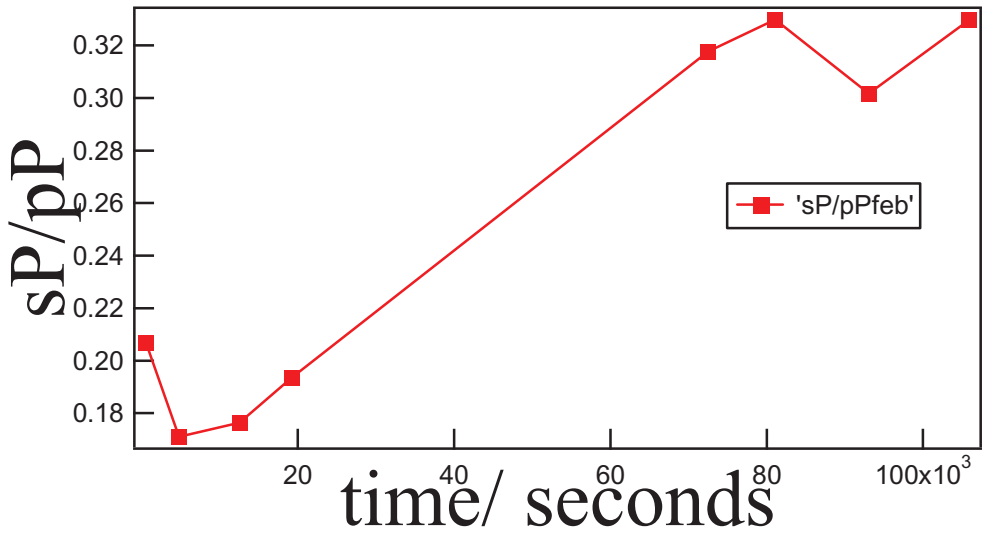

Figure 6.11: sP/pP value with time shows the presence of three different regimes.

The experimental data were adjusted according to Eqs.(6.1) and (6.2) for the *S* and *P* polarisation configurations respectively registered at the different stages of the experiment and the susceptibility tensor elements $\chi^{(2)}_{eff,ZZZ}$, $\chi^{(2)}_{eff,ZXX}$ and $\chi^{(2)}_{eff,XXZ}$ extracted. We notice that the element $\chi^{(2)}_{eff,ZZZ}$ always dominates over the other two elements, $\chi^{(2)}_{eff,ZXX}$ and $\chi^{(2)}_{eff,XXZ}$. Furthermore, the decrease of the *sP/pP* ratio indicates the increase of the nonlinearity along Oz axis, in agreement with the reinforcement of the breaking of the interface along this direction. The element $\chi^{(2)}_{eff,ZXX}$ had a negative value over all its evolution with time. Table 6.3 presents the evolution of the three tensor elements with time.

Time/seconds	0	9240	14400	20280	75060	82260	95040
$\chi^{(2)}_{eff,XXZ}$	0.792	1.1515	1.1584	1.1016	0.511	0.6228	0.58325
$\chi^{(2)}_{eff,ZXX}$	-0.246	-0.897	-0.984	-1.006	-0.681	-0.786	-0.735
$\chi^{(2)}_{eff,ZZZ}$	2.66	3.5819	3.5533	3.7645	2.3243	2.438	2.296

Table 6.3: The evolution of the three tensors elements with time.

A simple look at the evolution of the element $\chi^{(2)}_{eff,XXZ}$ shows that this value increases, stabilizes and then decreases. This behaviour confirms the changes occurring in the nature of the film. The evolution in the $\chi^{(2)}_{eff,XXZ}$ can be explained as follows: at the beginning of the film formation, the surface density of the particles at the interface is rather low. The SH intensity increases and the roughness is rather weak, of the order of that given by a film of monodispersed nanoparticles. It is also interesting to note that initially, only small aggregates can sediment because the time allowed for aggregation within the bulk of the solution is short. After a while, all the particles are present at the interface under the form of aggregates. The roughness is expected to be maximal at this stage since the aggregates are tri-dimensional. With time, these aggregates will collapse at the interface and the SHG response will decrease. Eventually, a rather smooth film is formed. Though the S polarization registered at the end of the experiment isn't completely vanishing, its small value is in agreement with such a smooth film. The enhancement of the SHG intensity is therefore attributed to the local field enhancement at a roughened silver-air interface, the latter reaching three times that at the end of the experiment where a smooth film is formed [10, 15]. We therefore finally conclude that the SHG intensity increases with the adsorption process and the sedimentation of large aggregates yielding a rough film and then decreases while a semi continuous film gets formed. Figure 6.12 illustrates the evolution of the film with the three main stages.

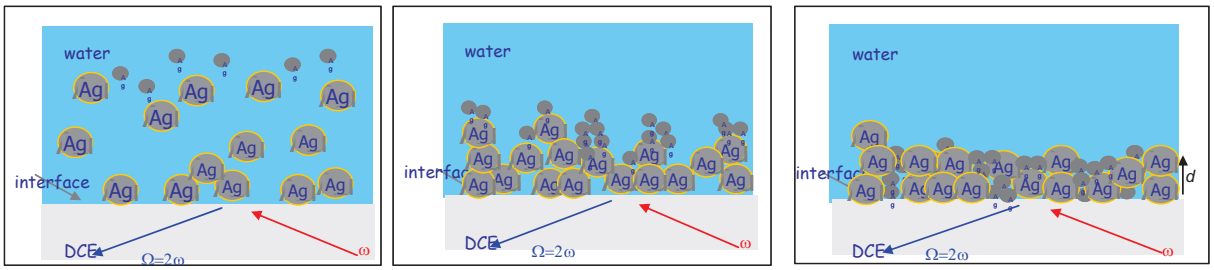

Figure 6.12: The illustration figure of the film evolution

Comparing the polar curves obtained with our film and that of a thin silver metallic film [23] of 500 nm thick, we conclude that the film formed is not a smooth metallic one, see Figure 6.13. A simple comparison between the two polar curves shows that the *sP* value is zero and the 45S negligible compared to the *pP* value for the perfectly smooth film whereas this is not the case for the film here. We conclude that the film still evolves at long times and never reaches a state close to that of a perfectly continuous film.

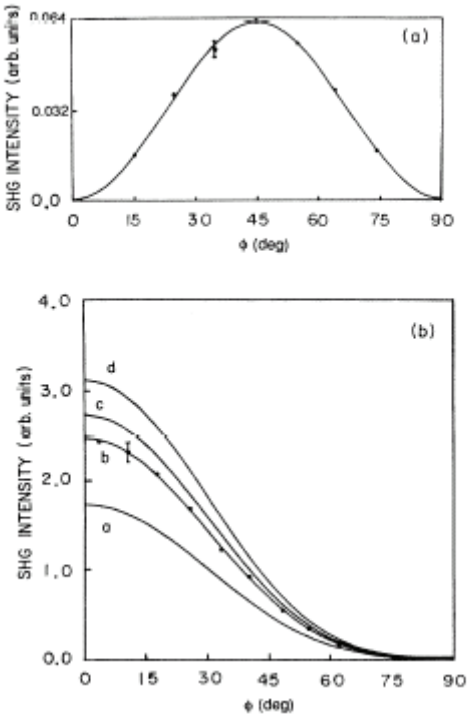

Figure 6.13: The S (a) and P (b) Polarisation curves of a thin silver metallic film. The experimental data are fit using a hydrodynamic model[23] (line)

6.4. Conclusion

We have studied the nature of a film formed from silver nanoparticles the diameter of which is about 8 nm at the water/DCE interface using second harmonic generation. The film obtained is rather a semi-continuous film as compared to a thin silver metallic film. UV-visible absorption spectra provided information about the kinetics of the system and the SPR resonance of the particles vanished confirming the formation of a film and not of dispersed particles. The initial increase of the SHG signal is due to the increase of the nanoparticles number density at the interface, reinforcing the breaking of the interface. A rough film is therefore formed leading to a roughness induced enhancement of the SHG intensity. At longer times the aggregates start to reorganize themselves thus forming a smoother film causing the decrease in the signal. In order to underline the difference in the SHG response of rough and smooth silver films, a detailed study of the growth of an electrodeposited silver film at a Glassy carbon electrode is monitored using SHG in the coming last chapter.

References:

[1] D. Krause, C. W. Teplin, and C. T. Rogers, "Optical surface second harmonic measurements of isotropic thin-film metals: Gold, silver, copper, aluminum, and tantalum," *J. Appl. Phys.,* vol. 96, pp. 3626-3634, 2004.

[2] J.-P. Abid, J. Nappa, H. H. Girault, and P.-F. Brevet, "Pure surface plasmon resonance enhancement of the first hyperpolarizability of gold core--silver shell nanoparticles," *J Chem. Phys.,* vol. 121, pp. 12577-12582, 2004.

[3] J. M. Hicks, K. Kemnitz, K. B. Eisenthal, and T. F. Heinz, "Studies of liquid surfaces by second harmonic generation," *J. Phys. Chem.,* vol. 90, pp. 560-562, 1986.

[4] C. P. Collier, R. J. Saykally, J. J. Shiang, S. E. Henrichs, and J. R. Heath, "Reversible Tuning of Silver Quantum Dot Monolayers Through the Metal-Insulator Transition," *Science,* vol. 277, pp. 1978-1981, 1997.

[5] Y. R. Shen, "The principles of nonlinear optics," *New York,* 1984.

[6] D. S. Walker, M. G. Brown, C. L. McFearin, and G. L. Richmond, "Evidence for a Diffuse Interfacial Region at the Dichloroethane/Water Interface," *J. Phys. Chem. B,* vol. 108, pp. 2111-2114, 2004.

[7] A. A. T. Luca, P. Hebert, P. F. Brevet, and H. H. Girault, "Surface second-harmonic generation at air/solvent and solvent/solvent interfaces," *J. Chem. Soc., Farad. Trans.,* vol. 91, pp. 1763-1768, 1995.

[8] H. Wang, E. Borguet, and K. B. Eisenthal, "Polarity of Liquid Interfaces by Second Harmonic Generation Spectroscopy," *J. Phys. Chem. A,* vol. 101, pp. 713-718, 1997.

[9] D. Yogev and S. Efrima, "Novel silver metal liquidlike films," *J. Phys. Chem. ,* vol. 92, pp. 5754-5760, 1988.

[10] A. H. R. Al-Obaidi, S. J. Rigby, J. J. McGarvey, D. G. Walmsley, K. W. Smith, L. Hellemans, and J. Snauwaert, "Microstructural and Spectroscopic Studies of Metal Liquidlike Films of Silver and Gold," *J. Phys. Chem.,* vol. 98, pp. 11163-11168, 1994.

[11] D. Yogev, C. H. Kuo, R. D. Neuman, and S. Efrima, "Measurement of the viscoelastic properties of silver metal liquid-like films by laser light scattering,"*J. Chem. Phys.,* vol. 91, pp. 3222-3227, 1989.

[12] D. Yogev and S. Efrima, "Raman scattering from silver metal liquidlike films," *J. Phys. Chem.,* vol. 92, pp. 5761-5765, 1988.

[13] D. Yogev, M. Deutsch, and S. Efrima, "Structural studies of silver metal liquid-like films," *J. Phys. Chem.,* vol. 93, pp. 4174-4179, 1989.

[14] D. Yogev and S. Efrima, "Silver metal liquidlike films (MELLFs). The effect of surfactants," *Langmuir,* vol. 7, pp. 267-271, 1991.

[15] R. Bavli, D. Yogev, S. Efrima, and G. Berkovic, "Second harmonic generation studies of silver metal liquidlike films," *J. Phys. Chem.,* vol. 95, pp. 7422-7426, 1991.

[16] G. Berkovic and S. Efrima, "Second harmonic generation from composite films of spheroidal metal particles," *Langmuir,* vol. 9, pp. 355-357, 1993.

[17] I. Farbman and S. Efrima, "Studies of the structure of silver metal liquid-like films by UV-visible reflectance spectroscopy," *J. Phys. Chem.,* vol. 96, pp. 8469-8473, 1992.

[18] P. Galletto, H. H. Girault, C. Gomis-Bas, D. J. Schiffrin, R. Antoine, M. Broyer, and P. F. Brevet, "Second harmonic generation response by gold nanoparticles at the polarized water/2-octanone interface: from dispersed to aggregated particles," *J. Phys.: Cond. Matter.,* vol. 19, pp. 375108-375108, 2007.

[19] M. Moskovits and B. Vlčkova, "Adsorbate-Induced Silver Nanoparticle Aggregation Kinetics," *J. Phys. Chem. B,* vol. 109, pp. 14755-14758, 2005.

[20] A. W. Adamson and A. P. Gast, *Physical Chemistry of Surfaces, 6-th ed*: Wiley-Interscience: New York, 1997.
[21] P. Galletto, P. F. Brevet, H. H. Girault, R. Antoine, and M. Broyer, "Enhancement of the Second Harmonic Response by Adsorbates on Gold Colloids: The Effect of Aggregation," *The Journal of Physical Chemistry B,* vol. 103, pp. 8706-8710, 1999.
[22] G. Martin-Gassin, Y. E. Harfouch, E. Benichou, G. Bachelier, I. Russier-Antoine, C. Jonin, S. Roux, O. Tillement, and P.-F. Brevet, "Correlation reflectance spectroscopy of heterogeneous silver nanoparticle films upon compression at the air/water interface," *J. Phys.: Cond. Matter.,* vol. 20, pp. 055228-055228, 2008.
[23] H. B. Jiang, L. Li, W. C. Wang, J. B. Zheng, Z. M. Zhang, and Z. Chen, "Reflected second-harmonic generation at a silver surface," *Phys. Rev. B,* vol. 44, pp. 1220-1220, 1991.

Chapter 7

Second Harmonic Response from silver-electrolyte interface

7.1. Introduction

Following on from the experiments at the unpolarized water/DCE interface trying to form a metallic film, it was decided to set up an electrochemical cell in which the application of a controlled applied potential across the interface would enable the formation of a silver metallic film. This latter is a very interesting domain of study in the present time [1]. Moreover, this growth is performed to underline the enhancement of the SHG signal at a rough metallic film with respect to that of a smooth one. Since the film formed at the interface in chapter 6 was concluded to be a semi-continuous film, it was believed that more control on the nature and properties of the film could be provided by electrochemical growth of the film where the control is exercised through the potential. This control allows the formation of either a smooth or a rough film and monitor the variation of the SHG signal from such surfaces. The interest in the silver metallic film is due to its unique optical properties. This stems from the large local field enhancements of such particles arising from the Surface Plasmon Resonance (SPR) excitation and subsequently to the potential applications of these particles for high sensitivity detection of compounds, *e.g.* in surface enhanced Raman scattering (SERS) and surface enhancement resonant Raman scattering (SERRS). The methodologies for the controlled production of aggregated particles starting from mono-dispersed colloidal solutions are now well established [2]. Different methods of production of nano-rough metal film substrates are well known including evaporation, chemical vapor deposition (CVD) and electrodeposition. All these routes aim at developing substrates with the largest local field enhancements but the exact details of relationship between the morphology and the field enhancements remain largely unavailable because of their random nature. Therefore a considerable amount of theoretical and experimental work to investigate the linear and non-linear optical properties of these systems, both in ensembles and at the single particle level were carried out [3]. Surfaces with random roughness are known to have

peculiar spatial areas where field localization yields large magnitude local field enhancements. In order to map these areas, several attempts have been proposed with near-field optical imaging but recent work has demonstrated that far-field measurements could also probe the presence of these hot spots on the surface although with lack of spatial resolution [4]. We chose second harmonic generation (SHG) technique to monitor the growth of an electrodeposited silver layer (from a silver cyanide aqueous solution) to address both the problem of field enhancement at these surfaces and random roughness. There exists several reported studies of SHG on metal surfaces with nanoscale roughness [1, 5]. Boyd et *al.* [1] demonstrated that the local field enhancement at a roughened silver-air interface can lead to large magnitude in the SH signals with enhancement factors of the order of $\sim 10^4$ and power-law dependence on the input intensity in excess of 2. These large factors are largely attributed to the concentration of the electric field at the tip of the structures, the so-called lightning rod effect, maintaining the dominant direction of the nonlinearity nearly perpendicular to the metal surface. In addition, this study provided a basis by which the surface local field enhancement at these nanoscale features could be quantified for several materials, including silver. More recently, Stockman *et al.* [6] reported that the SH field becomes both strongly depolarized and dephased at these features.

In parallel, SHG at the metal-electrolyte interface has also been examined by several authors [7-9]. In their experiments conducted at the flat interface between a Ag(111) single crystal and an inert electrolyte, Guyot-Sionnest *et al* [9] identified the non-linear susceptibility component normal to the sample surface as the one component most sensitive to the applied static potential. In particular they obtained experimentally a linear dependence in the magnitude of the surface nonlinear current, perpendicular to the interface, with the applied static potential. This was also examined by Dzavakhidze *et al* [7] and Schmikler *et al.* [10] who employed electronic density-functional calculations to determine theoretically the variation of the SH signal with the electrode charge in the presence and absence of specifically adsorbed ions.

This chapter is the fruit of collaboration with Dr Leonard Berlouis in Glasgow Strathcylde University and is divided into several parts. The first part is devoted to the procedure for the formation of an electrochemical silver film and then the SHG experimental setup is presented. A third section presents the results starting with the cyclic voltammogram, then the relation between the SHG intensity and the potential applied, after which the SHG versus the film

growth is presented and then, a geometrical model to determine the roughness of the film formed at the electrode is detailed. In addition, a polarisation resolved study for the smooth film at the end of the growth is presented and discussed. To highlight the presence of a rough film during the film growth (and before the decrease of the SHG signal), a film is grown to a certain thickness after which the growth is stopped and the SHG in the p_{IN}-P_{OUT} configuration as well as the p_{IN}-S_{OUT} configuration are registered to study in detail the SH response from such a rough film. The Rudnick and Stern $a(\omega)$ parameter introduced in chapter 3 versus potential is determined where it is shown to deviate from the linear behaviour expected for a smooth film. This parameter is the surface current perpendicular to the interface and is the dominant element in the nonlinear response of the film. By discussing these results we demonstrate that the combination of a random rough metal surface and an electric polarization of the interface yields large SH field enhancements with a dependence on the magnitude of the surface nonlinear current perpendicular to the interface. Moreover, large SH intensities are thus collected for the largest applied fields and these results confirm that unusual SERS spectra can be collected from nanorough substrates polarized with an external static field [11].

7.2. Electrochemical film preparation

Figure 7.1 presents the electrochemical cell used. The cell is a quartz cell of dimension ($28\times28\times28 mm^3$, 700.015-OG). The electric potential at the working electrode-solution interface was controlled by the EG&G Model 361 potentiostat, using custom-written LabVIEW software. The potentiostat was computer controlled. The working electrode (WE) in this three electrode system was a glassy carbon (GC) disc (area = 0.38 cm^2). The WE is so named because it is the electrode on which the reaction of interest takes place. A platinum wire was used as the counter electrode (CE) and a silver wire inserted directly into the solution was used as the reference electrode (RE). The potential was measured and controlled between the RE and the WE whereas the current was measured between the WE and the CE. The film growth was monitored *in situ* using SHG. Two different silver-containing solutions were used to form the silver film. The first consisted of a 1.0×10^{-3} M solution of $AgNO_3$ in 0.1 M KNO_3, and the second, a 5.0×10^{-3} M solution of AgCN in 0.2 M KCN/0.5 M KOH. The experiments were performed at room temperature and the GC disc was polished with several grades of alumina and then rinsed in Millipore water prior to each experiment.

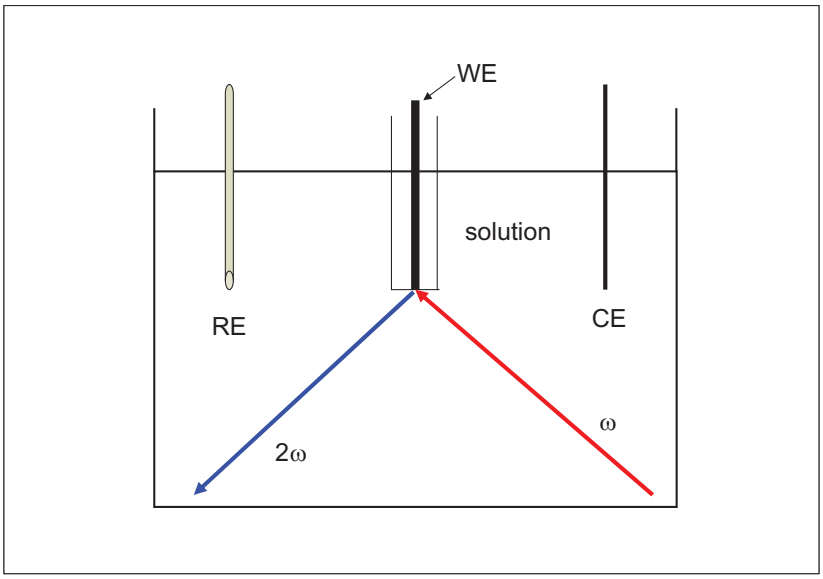

Figure 7.1: Electrochemical cell showing the working electrode (WE), the reference electrode (RE) and the Counter electrode (CE) and the fundamental and harmonic light.

7.3. Experimental setup

The silver deposition on glassy carbon (GC) was performed following the work of Márquez *et al*.[12]. The RE used in the experiments was a Ag wire placed directly into the solution. For direct comparison with previous work, all values of potential in the solutions used here were subsequently referenced with respect to the saturated calomel electrode (SCE) which has a potential of 0.242 V versus the normal hydrogen electrode. In the silver-containing reaction solution used here, the Ag/Ag^+ electrode has a potential of –0.705 V *vs* SCE. The SCE is a reference electrode based on the reaction between elementary mercury (I) chloride. The aqueous phase in contact with the mercury and the mercury chloride (Hg_2Cl_2, "calomel") is a saturated solution of potassium chloride in water.

The non-linear optical studies were performed using the same system shown in figure 6.4 of chapter 6 and the same femtosecond laser source. The average power at the laser exit was about 1 W. The same polarization system as previously employed was used here, a half wave plate at 800 nm was used to change the input polarization angle and a half wave plate at 400 nm and an analyzer set to P position were used to determine the output polarization of the harmonic beam. The incoming fundamental beam was incident at the rough silver-electrolyte

interface at an angle of ~ 45^{o} from the aqueous phase. The SHG band at 400 nm was adjusted with a Gaussian function, thereby removing the background consisting of noise and multiphoton excited luminescence photons.

7.4. Results

7.4.1. Cyclic voltammogram

Cyclic voltammograms were initially carried out in the 3-electrode cell in order to accurately determine the potential region where Ag deposition was initiated. A cyclic voltammogram or CV is a plot of the current versus voltage recorded for a certain working electrode, in our case the glassy carbon GC. In a CV, the working electrode potential is ramped linearly versus time. When cyclic voltammetry reaches a set potential, the working electrode's potential ramp is inverted. The ramp rate shown in Figure 7.2 is named the scan rate and has units of V/s. The potential limits of the ramp depend on the nature of the solution. Here, the starting potential was chosen where no Ag deposition occurred (*e.g.* 0.3 V *vs* Ag/Ag^{+} or –0.405 V *vs* SCE) whilst the other potential limit was selected to be well into the Ag deposition region (*e.g.* –0.2 V *vs* Ag/Ag^{+} or –0.905 V *vs* SCE) for deposition from $AgNO_3$ solutions. For deposition from the AgCN solutions, these potential limits were altered to 0.6 V *vs* Ag/Ag^{+} (–0.105 V *vs* SCE) and –0.6 V *vs* Ag/Ag^{+} (–1.305 V *vs* SCE) due to the strong complexing nature of the CN^{-} to the Ag. The presence of CN^{-} in the solution complicates the deposition of the Ag^{+} on the electrode and the Ag^{+} ions prefer to stay in the solution rather than be deposited. Thus it is harder to deposit Ag from cyanide solution and easy to re-dissolve it, this is because very stable soluble silver cyanide complexes can be formed.

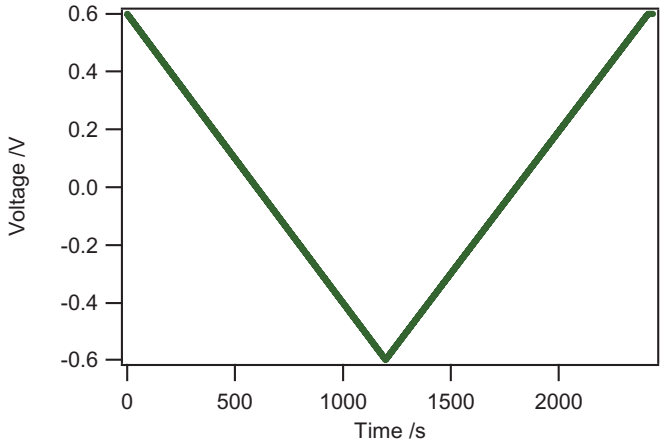

Figure 7.2 : Electrode potential ramp

As noted above, a Ag wire was used as a reference electrode and immersed in the solution containing the Ag^+ ion concentration. Thus, the reversible (or equilibrium) potential of the RE will be given by the Nernst Equation [13]:

$$E_{RE} = E^0_{Ag/Ag^+} + \frac{RT}{F}\ln\left[Ag^+\right] \tag{7.1}$$

where the first term on the Right hand side is the standard potential for the Ag/Ag^+ system, R is the universal gas constant, T is the absolute temperature and F is the faraday constant. Since the reaction here is the deposition of Ag from Ag^+ ions contained in the same solution, the reversible potential for the process measured versus the Ag/Ag^+ RE should be 0.0 V. Thus when the potential is negative with respect to the equilibrium potential, deposition of the Ag ions will occur, whereas to dissolve any deposited Ag, we would have a potential positive of the RE potential.

Scan rates of 20 mV s^{-1} were used in the cyclic voltammograms unless otherwise noted. The position of the peak current was also noted as this signified control of the deposition process by diffusion. The presence of the nucleation loop in the cyclic voltammogram indicated that indeed, a new phase had been formed. Finally, the anodic dissolution of the electrodeposited silver should occur at potentials positive of the reversible potential of Ag/Ag^+. Figure 7.3 shows the cyclic voltammogram for the silver deposition from the 5 mM AgCN / 0.2 M KCN / 0.5 M KOH solution. The scan rate used here was 50 mV/s. We notice the classic controlled

peak at −1.24 V for the reduction of the $[Ag(CN)_2]^-$ complex to yield metallic silver. The nucleation loop at −1.09 V on the reverse scan is consistent with the formation of a new metallic phase on the GC electrode. The onset for the anodic process occurs at −0.81 V yielding a classical surface-controlled symmetrical stripping peak [12, 14]. Thus, a typical deposition/dissolution current-potential curve with a sharp stripping peak is observed in this system where equal charge densities for the Ag deposition and dissolution reactions are found. It is known from literature that deposition from this solution yields hemispheroidal particles with the number density of the nuclei increasing exponentially with the overpotential, up to the peak potential [12]. The application of a potential step into the diffusion controlled region of the electrodeposition process yields the expected falling current-time *I-t* transient (the *I vs* $t^{-½}$ plot is linear) for the film growth [15]. Moreover, it has been demonstrated [12] that an intermediate behaviour between instantaneous and progressive nucleation was recorded on the GC. On Si electrodes, a shift from a progressive nucleation to instantaneous nucleation was observed with increasing deposition potential.

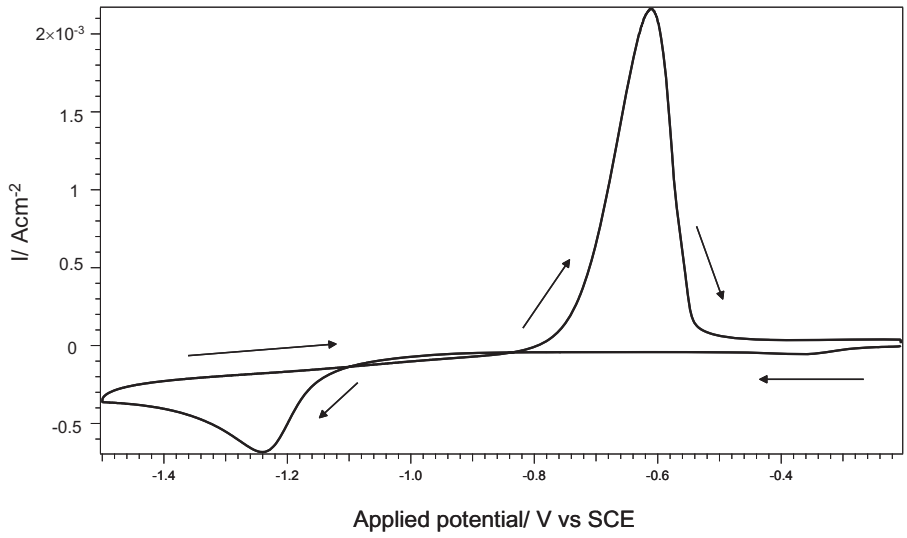

Figure 7.3 : Cyclic voltammogram recorded at the glassy carbon (GC) electrode in a 5.0×10^{-3} *M solution of AgCN in 0.2 M KCN /0.5 M KOH solution where the potential scan rate was 50 mV* s^{-1}.

7.4.2. Dependence of the SHG on the applied potential

Figure 7.4 presents the SHG intensity as a function of the applied potential at the GC electrode interface immersed in a 0.1 M potassium nitrate KNO_3 for a cyclic voltammogram

ramping from –0.55 V to –0.95 V. We notice the parabolic dependence of SHG with applied potential. This is similar to the results of AA Tamburello Luca *et al.*[16], where this parabolic behaviour was demonstrated for several solutions of KCl and KBr as a function of the applied potential and the surface charge. Furthermore, the effect of the anion adsorption on the surface second harmonic generation (SSHG) signal was also examined. A theoretical model was developed (the parabolic model) to show the parabolic relation between the SHG signal and the surface charge. This behaviour confirms that $\chi^{(3)}$ dominates over $\chi^{(2)}$since at the minimum of the parabola, the regime is driven by the polarization of the interface rather than by the intrinsic change of the nonlinear response of the interface. The experimental data were fitted by a polynomial equation which is the solid line in Figure 7.4.

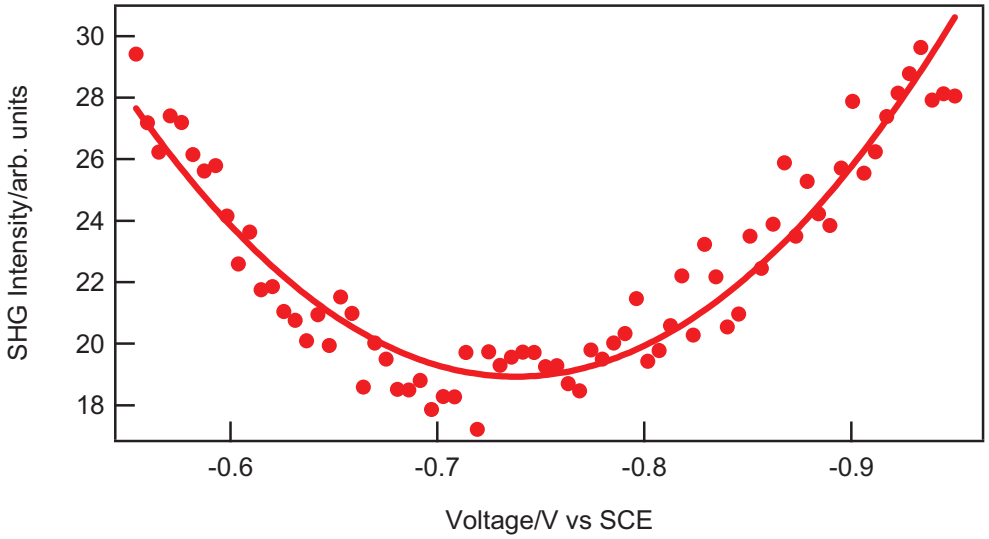

Figure 7.4 : SHG intensity for 0.1M KNO_3 as a function of the applied potential at the GC electrolyte interface (●) fitted with a polynomial equation (line)

7.4.3. SHG signal versus film growth

SHG from polarized metal-electrolyte interfaces has been described in the past through a non-linear current model. Here, the three phenomenological parameters already discussed in chapter 3, also called the Rudnick and Stern parameters *a(ω)*, *b(ω)* and *d(ω)*,[17] are introduced for the three non-linear currents *viz.* the surface currents perpendicular and parallel to the interface and the bulk current perpendicular to the interface arising from the skin layer

effect[17]. In the latter model, the *p*-polarized SH intensity, hereafter referred to as the P_{OUT} intensity, can be written as :[7]

$$\frac{I_{2\omega}}{I_{\omega}} = \frac{8\pi e^2}{m^2\omega^2c^3}\left|\frac{\varepsilon_s(\omega)\varepsilon_s(2\omega)\varepsilon(\omega)\left[\varepsilon(\omega)-\varepsilon_s(\omega)\right]}{\varepsilon(2\omega)+s(2\omega)}\left(P\cos^2\psi + S\sin^2\psi\right)\tan\theta\right|^2 \tag{7.2}$$

where

$$P = \frac{a(\omega)\dfrac{\varepsilon(2\omega)\varepsilon_s(\omega)}{\varepsilon(\omega)}\sin^2\theta - b(\omega)\dfrac{2s(\omega)s(2\omega)}{\varepsilon(\omega)\varepsilon_s(\omega)}\cos^2\theta + \dfrac{1}{2}d(\omega)}{\left[\varepsilon(\omega)+s(\omega)\right]^2} \tag{7.3}$$

$$S = \frac{d(\omega)}{2\varepsilon(\omega)\left[\varepsilon(\omega)+s(\omega)\right]^2} \tag{7.4}$$

and

$$s(\omega) = \frac{\left[\varepsilon(\omega)-\varepsilon_s(\omega)\sin^2\theta\right]^{1/2}}{\cos\theta}\varepsilon_s^{1/2}(\omega) \tag{7.5}$$

Here *e* is the electronic charge, *m* is the electron mass and *c* the speed of light and these three parameters are constant. ω and 2ω are the fundamental and harmonic frequencies respectively. $\varepsilon(\omega)$ and $\varepsilon_s(\omega)$ are the bulk optical dielectric constants of the metal and the electrolyte solution respectively, θ is the angle of incidence and ψ is the angle of the polarization vector with respect to the plane of incidence, with ψ = 0º corresponding to the fundamental *P* polarization, hereafter referred as p_{IN}. The SH response from the metal-electrolyte interface is described principally through the surface current perpendicular to the interface, *i.e.* the $a(\omega)$ coefficient, the dependence of which on the applied static field yields in turn the SH intensity's dependence. For a perfectly smooth interface $b = -1$ and $d = 1$, irrespective of the frequency, and $a(\omega)$ is negative and of the order of unity.

Monitoring the SHG signal in the p_{IN}-P_{OUT} configuration during the deposition process from the solution yields the data shown in Figure 7.5. The scan rate was 1 mV/s and the limits were

from −0.15 V to −1.35 V for this silver cyanide solution. The SH signal is believed to stem from the surface current, which is expressed as a function of the three parameters *a*, *b* and *d*. As noted above, the SHG response at the silver electrode/electrolyte interface is dominated by the surface current perpendicular to the interface expressed by the parameter *a* and parallel to the interface expressed by the parameter *b*. The term *d* accounts for the bulk magnitude contribution and is assumed to remain constant here. Moreover, a theoretical study [6] has shown that the SH local fields at the nanoscale are both strongly depolarized and dephased. The phase curve trajectory obtained confirmed the strong dephasing which is the randomization of the SH polarization phase in the plane of the nanostructure. Moreover, the magnitude of the SHG enhancement is strongly dependent on the morphology of the surface. This was shown for a gold nanostructure surface where local field anisotropy, given by $L_x(\omega)/L_y(\omega)$ where L_x and L_y are the local field factors in the *X* and *Y* direction, respectively, was the parameter indicative of the influence of surface morphology on the SHG enhancement. The local field factor is shape dependent factor and for linear processes, it is equal to the square root of the local field enhancement for metallic thin films. In the case of nonlinear processes, the SH response is proportional to the enhancement factor $\eta^{2\omega}$ where $L(\omega)$ and $L(2\omega)$ are the local field factors at the fundamental and harmonic frequencies [4].

$$\eta^{2\omega} = \left| L^2(\omega) L(2\omega) \right|^2 \tag{7.6}$$

To study in detail the nature of the metallic film that was formed on the GC in our experiment the SHG signal was recorded during the growth of the film in the p_{IN} –P_{OUT} configuration. Several potential steps were performed for the growth of the film and the SH responses are presented in Figure 7.5. The potential step was started from and initial value of –0.35 V and stepped to different limits over the potential range –1.35 V to –1.6 V. An initial sharp increase in the SH intensity was observed before a maximum and decrease at longer times. Note also that there is clear increase in the magnitude of the SH maximum with increasing negative applied potential. This behaviour was observed for all the SH signals recorded as a function of the different potential steps, except for the last potential step where the maximum in the SHG signal found was less than that for −1.55 V. This increase in the SH maximum must be due to effect of the applied potential since the rate of growth in all cases here is controlled by mass transport.

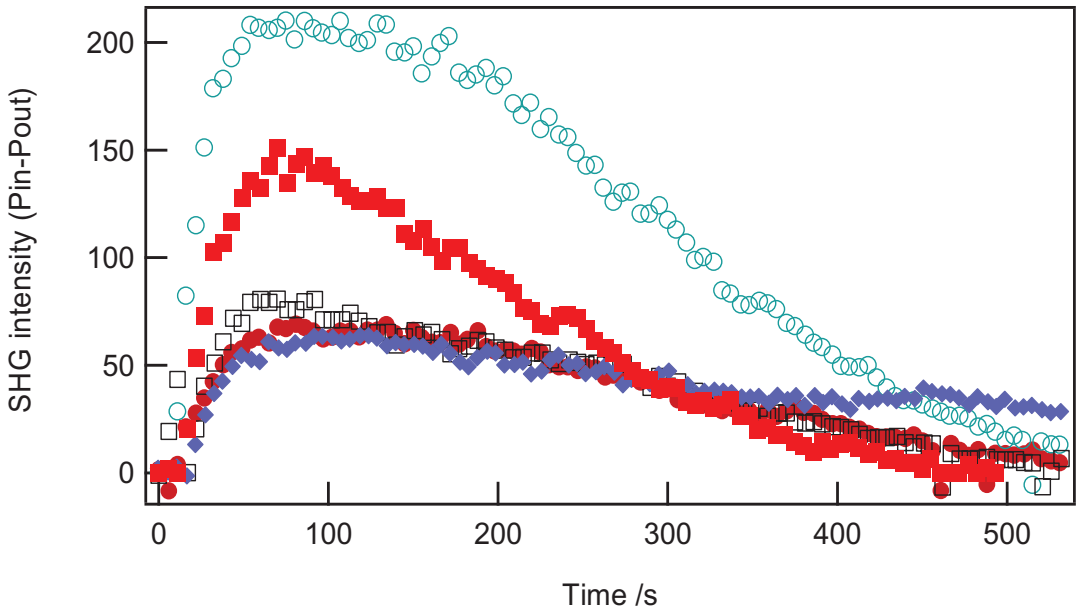

Figure 7.5: The SHG intensity recorded in the $p_{IN} - P_{OUT}$ polarization configuration at a GC electrode during the growth of a Ag film by potential steps: –1.35 V(◆), -1.4V (●),-1.5 V (empty square), -1.55 V(○) and –1.6 V(■) in a 5.0 × 10^{-3} M solution of AgCN in 0.2 M KCN /0.5 M KOH solution.

The rapid initial increase is due to the growth of the silver particles on the GC electrode [12], starting from nuclei densities in the range 10^7 cm^{-2} . The dependence of the SH intensity in this regime depends not only on the amount of silver deposited but also on the morphology of the film and the possible excitation of surface plasmons in the particles. Surface plasmons can be excited in such a nanorough film owing to the loss of the translation invariance along the plane of the interface. Furthermore, the SH radiation at the harmonic wavelength of 400 nm is in close vicinity to the value of the SP resonance excitation of Ag in aqueous solution and can therefore be resonantly enhanced. Beyond an equivalent film thickness of about 60 nm, as determined from the charge consumed during the process, the SH intensity then levels off and a monotonous decrease in the SH intensity with increasing film thickness is then observed. The charge calculation is simply based on application of Faraday's Law of electrolysis which is given as follows:

$$\frac{m}{M} = \frac{I.t}{nF} = \frac{Q}{nF} \tag{7.7}$$

where m is the mass of the substance deposited at an electrode surface, and M is the molar mass of the substance. Thus to deposit one mole of a substance, $n \times F$ coulombs are needed where F is the Faraday's constant which is equal 96 485 C mol^{-1} and n is the number of electrons transferred per ion, (*e.g.* 1 for Ag^{+}). Q is the total electric charge consumed during the deposition process which is the electric current integrated over time. Since we have the current which is measured between the working electrode and the counter electrode and the time t, which is the total time the electrodeposition process, we thus have the charge Q.
We can expand the above equation by using:

$$m = \rho \times V = \rho \times (A \times d) \tag{7.8}$$

where ρ is the density of the metal, A is the electrode surface area and d is the film thickness. Thus we have:

$$d = \frac{Q}{nF} \cdot \frac{M}{\rho A} \tag{7.9}$$

and the thickness d can be then evaluated. As noted above, it was found to be equal to 60 nm at the point of maximum SH signal. This thickness at the maximum of the SH intensity was obtained irrespective of the value of applied potential step as long as this value is in the diffusion controlled growth region. At this SH peak intensity, the roughness must then be maximum. This behaviour is similar to early studies on rough gold surfaces, with diameters in the range 50 μm to 5000 μm, where strong depolarization effects were revealed [5, 18]. In that study, enhancement factors as large as 10^4 compared to continuous gold films were obtained. However, the macroscopic nature of these experiments obscured the local nature of the enhancement. Other experiments by Anceau *et al* [4] provided a detailed study on the influence of local field effects on surface second harmonic generation enhancement of gold nanostructure surfaces of various morphologies using spectral and polarisation studies. It can be concluded that the enhancement mechanism at rough surfaces is dominated by the lightning rod effect [19, 20]. This effect arises when the field tends to concentrate at the tip of the structure perpendicularly to the metal surface. It is a function of the shape of the

hemispheroids, defined by the aspect ratio *a/b*, and the plasmon resonance effects. However, this evolution in the SHG signal is the same as that observed at the liquid/liquid interface for the formation of a film of silver nanoparticles presented in the previous chapter. Thus, the hypothesis proposed for the film at the liquid/liquid interface is reinforced. In this, it is believed that first the signal increase is due to the increase in the number of particles monitored by the laser, forming the rough film. After deposition, the small particles are able to reorganise themselves since they can easily move in the system and start filling the gaps between the particles in the film. This will lead to the formation of a smooth film, causing a decrease in the signal as is indeed observed. A quick comparison to Figure 6.9 of chapter 6 tells that the evolution of the SHG is greatly similar to that presented in Figure 7.5.

7.4.4. The nanoscale roughness model

If we consider the growth to be that of hemispheroids, the film morphology then corresponds to that of touching hemispheroids sitting upwards on a plane [21](see Figure 7.6). At maximum roughness the hemispheroids touch at the base only. Hence, assuming a simple geometrical model where the volume of the hemispheroid is given by:

$$V_{hemispheroid} = \tfrac{1}{2}(\tfrac{4}{3}\pi R^2 h) \tag{7.10}$$

where R is the radius of the particle and h its height. The factor 1/2 is simply because a hemispheroid is half a spheroid. If it is further assumed that all the formed hemispheroids are of the same height h, we then have the following expression:

$$N \times \tfrac{1}{2}(\tfrac{4}{3}\pi R^2 h) = d \times S \tag{7.11}$$

where S equal to:

$$S = N \times \tfrac{1}{2}(4\pi R^2) \tag{7.12}$$

is the area occupied by the N hemispheroids and d is the thickness of the corresponding equivalent flat film. In order to obtain a flat film the gaps between the hemispheroids must be filled. This is done in order to be able to obtain a flat film with a given thickness d. Simple

substitution yields a maximum height of *3d*. The height of the hemispheroids is therefore 180 nm since the film thickness is equal 60 nm as determined above. Such a morphology is similar to that found by Márquez *et al.* [12] in their study of silver deposition on GC and Si(111) from alkali cyanide solutions. Beyond the thickness of 60 nm, the film loses its roughness and so its surface enhancement. The SH intensity eventually falls back to that of a flat continuous silver film. The latter intensity is about 10 times smaller than that observed at the peak for the potential of –1.55 V and 3 times smaller for the –1.35 V. However the thickness at maximum SHG signal is the same irrespective of the applied potential, see Figure 7.5.

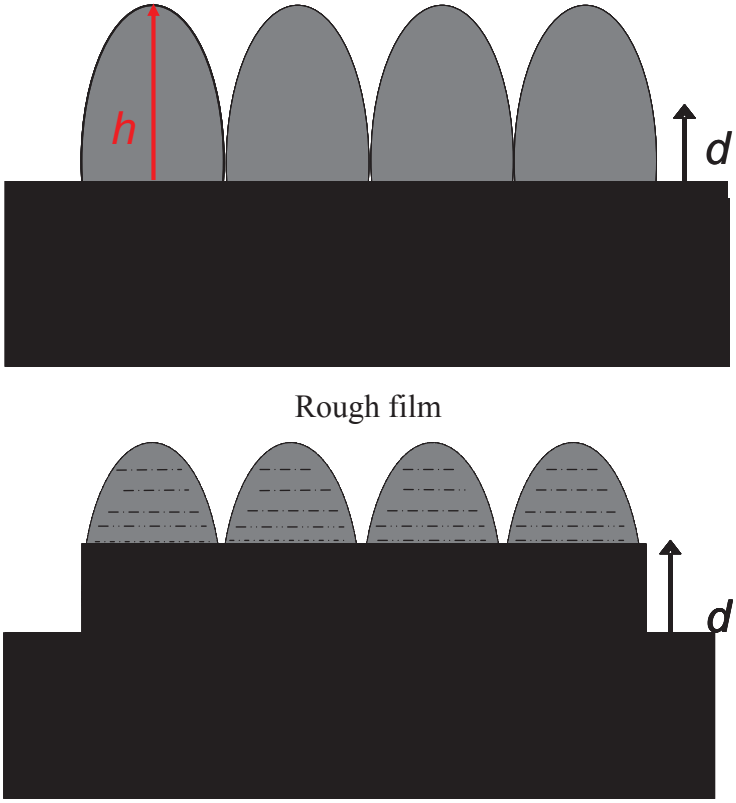

Figure 7.6: Geometrical model

7.4.5.Polarisation resolved study

A polarization resolved study was performed at the end of the film formation to record the polarisation curve for the smooth film formed at the GC electrode and to compare its polar curves with that obtained from a film grown at the liquid/liquid interface. The difference

between this polar curve and that obtained from a smooth thin silver film [22] was also examined. Both the S and P polarisation curves were registered. Figure 7.7 presents the S and P polarisation curves fitted with the equations (3.93) and (3.94) presented in chapter 3. The curves were normalised to 1 second acquisition. We notice that the S polarisation *(●)* is fluctuating and its value is around 5 for any input polarisation angle, whereas for the P polarisation (■) the usual curve was obtained. From the fitting functions, the tensor elements for the film were deduced. The only non vanishing value is $\chi^{(2)}_{eff,ZZZ}$ which is proportional to the value $a(\omega)$ and the relation between them is given in equation (3.98) of chapter 3. In the case of a smooth thin silver film of thickness about 50μm the *S* polarisation was negligible compared to that of the *P* polarisation and this is expected for a smooth thin film. The negligible S polarisation registered for the film formed at the electrode confirms the presence of a thin film as shown in Figure 7.7.

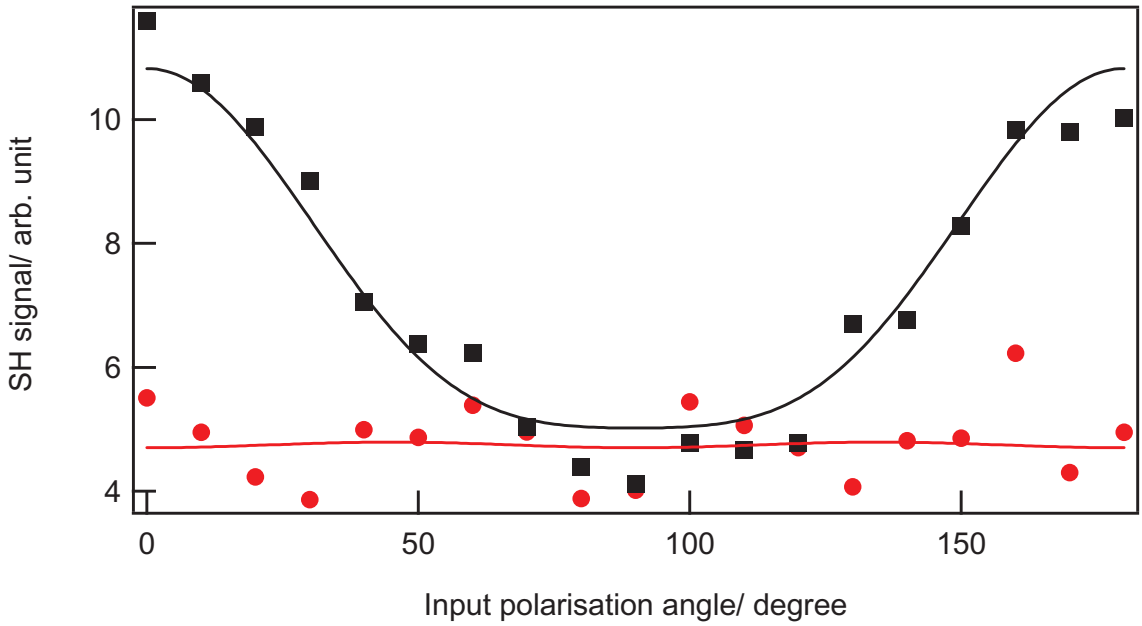

Figure 7.7: The P (■) and S- (●) polarized SH Intensity of the smooth film formed at the GC electrode as a function of the input polarisation angle of the fundamental incoming beam.

7.4.6. Signal versus potential for p_{IN}-P_{OUT} and p_{IN}-S_{OUT}

In order to examine in detail the SH enhancement of a rough film, the growth of the silver deposit to an equivalent thickness of only ~37 nm (which corresponds to ~111 nm roughness height) was carried out using the potential step method. This film thickness was chosen to ensure that the SH intensity enhancement regime is dominated by the surface roughness principally. The film, once grown, was then removed from the growth solution and

placed in the KOH/KCN electrolyte, without Ag^+ ions, and the SHG intensity from this surface was then investigated as a function of the applied potential over the range –0.85 V to –1.55 V *vs* SCE. Figure 7.8 shows the variation in the SH intensity as a function of the potential measured in the p_{IN}-P_{OUT} and p_{IN}-S_{OUT} polarization configurations. The SH signal increases exponentially, as expected, since the number of particles themselves increase with potential during the deposition process. In the p_{IN}-S_{OUT} polarization configurations, the non vanishing SHG intensity collected confirms that the film is rough at the nanoscale since no signal is expected for a perfectly smooth metal-electrolyte interface. This configuration also yields a SHG intensity sensitive to the applied static field. In the p_{IN}-P_{OUT} polarization configuration, where the response is dominated by the $a(\omega)$ parameter, the sharp rise in the SH intensity at the extreme voltages underlines that the nonlinear surface current perpendicular to the interface is greatly affected by the film roughness and the electric polarization, as seen in Figure 7.9, obtained by inverting Eq. (7.1) using a real valued $a(\omega)$ parameter with a normalisation to the polarized flat film and a fundamental wavelength of 800 nm. Then, for each SH signal value of Figure 7.8 the $a(\omega)$ parameter was evaluated and plotted as a function of the potential.

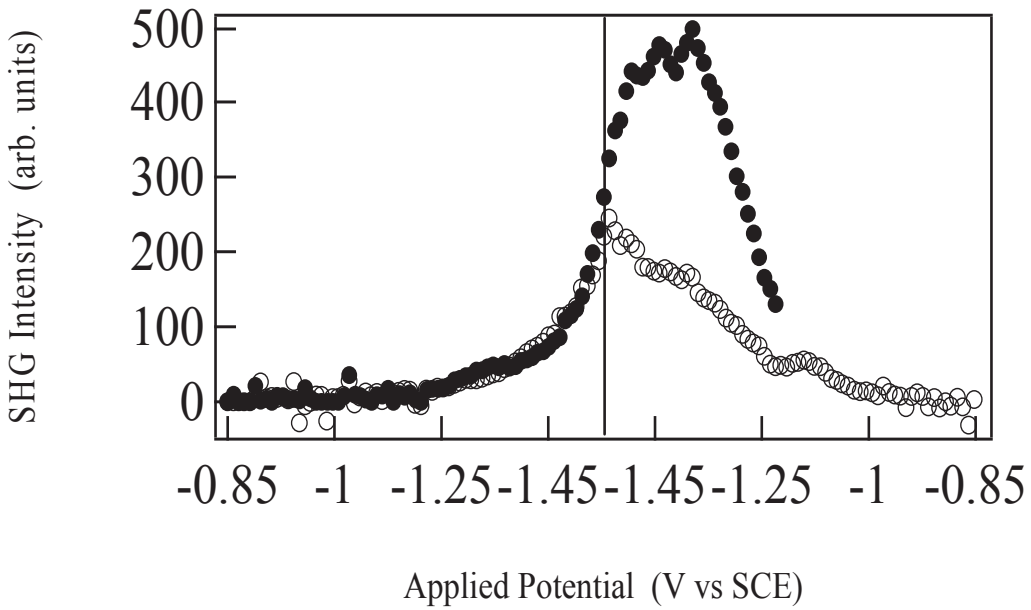

Figure 7.8: SHG intensity recorded in the $p_{IN} - P_{OUT}$ (●) and $p_{IN} - S_{OUT}$ (○) polarization configurations in a 0.2 M KCN /0.5 M KOH solution for an electrodeposited Ag film (37 nm) as a function of the applied potential. The potential was scanned from -0.85 V to -1.55 V (the vertical line marks the potential -1.55 V)

It is found that the applied static field dependence of the *a(ω)* parameter for the rough film strongly deviates from the linear dependence observed for the smooth silver film, where values in the range +0.7 to –10 were estimated [9]. Assuming a value for $b = -1$, Guyot-Sionnest *et al* evaluated the value of *a(ω)* as a function of the potential. A linear relationship was found over the voltage range of 0 V to –1.2V. The small range in potential above –1.0 V limited these authors from quantifying the deviation from a linear behaviour for higher potentials as recorded in our case, see Figure 7.9. A hysteresis is also observed with the applied potential and this is attributed to the non-negligible role of the adsorbing CN^- ions on the Ag electrode surface. In particular, it is expected that with cyanide desorption (dependent on the relative stability of AgCN, $Ag(CN)_2$ and $Ag(CN)_3$ surface complexes) at these negative potentials [14, 23], the electronic tail gets more polarizable. It is therefore concluded that the combination of surface roughness and electrical polarization yields overall SHG intensities much larger than when only one enhancement factor, either roughness or field, is present. The direction normal to the electrode interface is still dominant, as evidenced from the higher dependence of the SH intensity with the applied potential in the p_{IN}-P_{OUT} polarisation

configuration in contrast to that observed for the p_{IN}-S_{OUT}. The non vanishing intensity recorded in this latter polarization configuration also calls for an extension of the SHG intensity dependence with the surface currents. In particular, the nanoscale roughness will yield a dependence of the p_{IN}-S_{OUT} intensity with the two parameters $a(\omega)$ and $b(\omega)$.

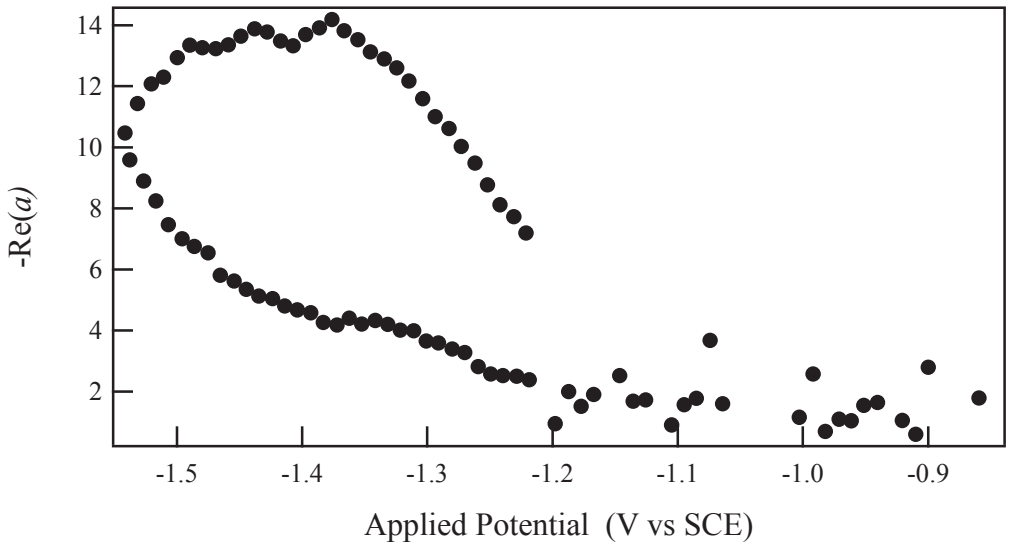

Figure 7.9: The variation of – Re a(ω) with the potential deduced using the real value of a(ω) for a smooth film and the SH signal given in figure 7.5.

7.5. Conclusion

Nanoscale rough silver films have been electrodeposited from a silver–containing aqueous solutions (nitrate and cyanide) and the growth has been monitored by second harmonic generation. SHG is a powerful surface sensitive technique that is able to follow surface change under electrochemical control of the interface. It has been demonstrated that local field enhancements can be greatly increased by the combined action of the electric polarization and the nanoscale surface roughness. These experiments were conducted in a far field configuration where the SH signal is averaged over the whole beam area. The maximum in the SHG intensity was obtained for a film thickness of ~ 60 nm. Moreover, the SH intensity was noticed to decrease once smooth film were formed at the interface regardless of its thickness. The polarisation resolved analysis showed that the film formed at the GC electrode resembles that of a metallic film. Microscopically, it has been shown that the nonlinear surface current perpendicular to the interface expressed by the Rudnick and Stern parameter

a(ω) exhibits a nonlinear dependence with the applied potential due to the combination of the roughness and electric polarization. This rough nature of the film was verified by the non vanishing SHG intensity collected at the p_{IN}-S_{OUT} polarization configurations since no signal is expected for a perfectly smooth metal-electrolyte interface for such polar configuration.

References:

[1] G. T. Boyd, T. Rasing, J. R. R. Leite, and Y. R. Shen, *Phys. Rev. B,* vol. 30, p. 519, 1984.

[2] J. Turkevich, P. C. Stevenson, and J. Hillier, *Discuss. Faraday Soc.,* vol. 11, p. 55, 1951.

[3] J. Nappa, G. Revillod, I. Russier-Antoine, E. Benichou, C. Jonin, and P. F. Brevet, *Phys. Rev. B,* vol. 71, p. 165407, 2005.

[4] C. Anceau, S. Brasselet, J. Zyss, and P. Gadenne, "Local second-harmonic generation enhancement on gold nanostructures probed by two-photon microscopy," *Opt. Lett.,* vol. 28, pp. 713-715, 2003.

[5] C. K. Chen, A. R. B. de Castro, and Y. R. Shen, "Surface-Enhanced Second-Harmonic Generation," *Phys. Rev. Lett.,* vol. 46, pp. 145-145, 1981.

[6] M. I. Stockman, D. J. Bergman, C. Anceau, S. Brasselet, and J. Zyss, "Enhanced Second-Harmonic Generation by Metal Surfaces with Nanoscale Roughness: Nanoscale Dephasing, Depolarization, and Correlations," *Phys. Rev. Lett.,* vol. 92, pp. 057402-057402, 2004.

[7] P. G. Dzhavakhidze, A. A. Kornyshev, A. Liebsch, and M. Urbakh, *Phys. Rev. B,* vol. 45, p. 9339, 1992.

[8] T. E. Furtak, Y. Tang, and L. J. Simpson, *Phys. Rev. B,* vol. 46, p. 1719, 1992.

[9] P. Guyot-Sionnest, A. Tadjeddine, and A. Liebsch, *Phys. Rev. Lett.,* vol. 64, p. 1678, 1990.

[10] W. Schmickler and M. Urbakh, *Phys. Rev. B,* vol. 47, p. 6644, 1993.

[11] B. G. McMillan, L. E. A. Berlouis, F. R. Cruickshank, D. Pugh, and P. F. Brevet, *Appl. Phys. Lett.,* vol. 86, p. 211912, 2005.

[12] K. Márquez, G. Staikov, and J. W. Schultze, "Silver deposition on silicon and glassy carbon. A comparative study in cyanide medium", *Electrochim. Acta,* vol. 48, p. 875, 2003.

[13] H. H. Girault, *Electrochimie physique et analytique*: Presses Polytechniques et Universitaires Romandes (PPUR), 2001.

[14] M. Fleischmann, G. Sundholm, and Z. Q. Tian, *Electrochim. Acta* vol. 31, p. 907, 1986.

[15] A. J. Bard and L. R. Faulkner, *Electrochemical Methods: Fundamentals and Applications*: John Wiley and Sons (WIE), 2001.

[16] P. H. A.A. tamburello-Luca, P. F. Brevet ; H. H. Girault, "Surface second harmonic study of anion adsorption at the mercury | electrolyte interface," *J. electroanal. chem.,* vol. 409, pp. 123-129, 1995.

[17] J. Rudnick and E. A. Stern, *Phys. Rev. B,* vol. 4, p. 4274, 1971.

[18] M. Breit, V. A. Podolskiy, S. Gr□sillon, G. von Plessen, J. Feldmann, J. C. Rivoal, P. Gadenne, A. K. Sarychev, and V. M. Shalaev, "Experimental observation of percolation-enhanced nonlinear light scattering from semicontinuous metal films," *Phys. Rev. B,* vol. 64, pp. 125106-125106, 2001.

[19] J. Gersten and A. Nitzan, "Electromagnetic theory of enhanced Raman scattering by molecules adsorbed on rough surfaces," *J. Chem. Phys.,* vol. 73, pp. 3023-3037, 1980.

[20] P. F. Liao and A. Wokaun, "Lightning rod effect in surface enhanced Raman scattering," *J. Chem. Phys.,* vol. 76, pp. 751-752, 1982.

[21] C. K. Chen, T. F. Heinz, D. Ricard, and Y. R. Shen, "Surface-enhanced second-harmonic generation and Raman scattering," *Phys. Rev. B,* vol. 27, pp. 1965-1965, 1983.
[22] H. B. Jiang, L. Li, W. C. Wang, J. B. Zheng, Z. M. Zhang, and Z. Chen, "Reflected second-harmonic generation at a silver surface," *Phys. Rev. B,* vol. 44, pp. 1220-1220, 1991.
[23] J. Billman and A. Otto, *Surf. Sci.,* vol. 138, p. 1, 1984.

Conclusions

Linear and Non-linear optical properties of metallic nanoparticle films have been studied in this work. First, HRS has been used to characterize the second order nonlinear optical response of silver and gold nanoparticles, both home made and commercial ones. Besides, the hyperpolarisability values and the ζ^V parameter have also been determined through polarisation resolved HRS measurements for spherical silver and gold nanoparticles. From these results, we have been able to compare the role of the capping layer in the enhancement or quenching of the hyperpolarizabilities. It appeared that once the particles are capped with alkylthiol, the nonlinear response is quenched. In addition, it clearly appeared that short alkyl chains are not able to prevent aggregation, contrary to long ones demonstrating the critical role of the alkyl chain length in preventing aggregation. Similarly, the hyperpolarisability values and the ζ^V parameter for nanorods particles have been determined. Same core nanorods capped with various surfactants have been compared. It seems that CTAB capping layer enhanced the hyperpolarizability whereas alkylthiol capping layers on the opposite tended to quench the response. Moreover, it was noticed that the length of the alkyl chain does not provide any effect on the hyperpolarizability since the hyperpolarisability for the same core nanorods capped with dodecanethiol had almost the same value as that capped with octadecanethiol.

The hydrodynamic model has been presented to get an expression for the nonlinear polarisation from both the interface and the bulk metal. An overview of the three layer model was also presented from which the effective tensor elements and the S and P polarisation equations were given. A relation between the $a(\omega)$, $b(\omega)$ and $d(\omega)$ parameters obtained in the hydrodynamic model and the effective susceptibility tensor elements was established. The overall SHG intensity equations were used to adjust the experimental data obtained at the studied interfaces.

Silver and gold nanoparticles both spherical and nanorod geometries were used to form metallic films at the air/water interface of a Langmuir trough. The surface pressure/area isotherm, the reflectance and transmittance of each sample studied were recorded. A drop in the reflectance spectra for commercial dodecanethiol silver nanoparticles was registered,

signature of a transition. This transition looks like the transition reported in literature and was attributed to an insulator to metal transition. At this stage, we don't have a clear evidence of this MI transition; however we had a clear evidence of strong coupling between adjacent particles. In the formation of the films, it also appeared that the size distribution appears to play an essential role. The MI transition required a narrow size distribution in order to favor the compact organization of the film.

The linear studies were followed by a detailed nonlinear study. The nonlinear response of nanoparticles films was studied using a femtosecond laser focused at the air/water interface using the SHG technique. Films formed from dodecanethiol-capped silver spherical nanoparticles the diameter of which was about 10 nm and dodecanethiol- or octadecanethiol-capped gold nanorods with dimensions 64 × 24 × 24 nm were studied in details. The SHG signal evolution upon compression of the film allowed us to underline the change in the properties of the nanoparticles film. A drop in the SH signal for all samples at the highest concentrations was observed. The evolution of the SHG signal for the gold nanorods was partially different than that of the spherical particles. An increase in the SHG intensity for the silver spherical particles with the nanoparticles concentration was observed but the exact dependence is not clear, possibly because of the interactions between particles in the film. For the nanorods, the SHG signal dependence with the nanorods concentration possessed a plateau value, attributed to a phase transition the origin of which remains to clarify. The maximum in the SHG signal corresponded to an enhancement by a factor of ~200 in the case of dodecanethiol nanorods and almost the same factor in the case of octadecanethiol nanorods. The maximum in the SHG signal corresponded to enhancement by a factor of ~20 in the case of silver nanoparticles only. SP resonance enhancement, particle shape and also film morphology may be responsible for such an observation. Polarization curves were also performed in order to investigate the dominant source in the nonlinear response. In all cases, the dominant contribution was the breaking of the inversion symmetry along the normal direction perpendicular to the interface. However, in all cases, the increase of the in-plane contributions was clearly demonstrated indicating that in-plane contributions like particle interactions play a growing role as the compression increases.

These studies were complemented with an experiment performed at the liquid/liquid interface. SHG was used to study the nature of a film formed from silver nanoparticles the diameter of which is about 8 nm at the water/dichloroethane interface. The film obtained was rather a

semi-continuous film as compared to a thin silver metallic film. UV- visible absorption spectra provided information about the kinetics of the system and the SPR resonance of the particles vanished confirming the formation of a film and not of dispersed particles. The initial increase of the SHG signal was attributed to the increase of the nanoparticles number density at the interface, reinforcing the breaking of the interface. A rough film was therefore formed leading to a roughness induced enhancement of the SHG intensity. At longer times the aggregates reorganized themselves thus forming a smoother film where then the signal decreased.

In order to underline the difference in the SHG response of rough and smooth silver films, a detailed study of the growth of an electrodeposited silver film at a Glacy carbon electrode was monitored using SHG. It has been demonstrated that local field enhancements can be greatly increased by the combined action of the electric polarization and the nanoscale surface roughness. These experiments were conducted in a far field configuration where the SH signal was averaged over the whole beam area. The maximum in the SHG intensity was obtained for a film thickness of ~ 60 nm. Moreover, the SH intensity was noticed to decrease once smooth film is formed at the interface regardless its thickness. The polarisation resolved analysis showed that the film formed at the GC electrode resembles that of a metallic film. Microscopically, it has been shown that the nonlinear surface current perpendicular to the interface expressed by the Rudnick and Stern parameter $a(\omega)$ exhibited a nonlinear dependence with the applied potential due to the combination of the roughness and electric polarization. This rough nature of the film was verified by the non vanishing SHG intensity collected at the p_{IN}-S_{OUT} polarization configurations since no signal is expected for a perfectly smooth metal-electrolyte interface for such polar configuration. A complete model should be developed in order to explain the behaviour of the p_{IN}-S_{OUT} polarization.

Laboratoire de Spectrometrie Ionique et Moleculaire, UMR CNRS 5579

Domaine scientifique de la DOUA-Université Claude Bernanrd Lyon1

Batiment A. kastler, 43 boulevard du 11 novembre 1918, 69622 Villeurbanne

RESUME: La technique de la génération de second harmonique (SHG) a été employée pour étudier la réponse non linéaire des assemblées de nano particules métalliques aux interfaces liquides. Les nanoparticules ont d'abord été caractérisées en utilisant la génération de second harmonique incohérente, également nommée diffusion hyper Rayleigh. L'étude de particules d'or et d'argent, nanosphères et des nanobâtonnets, ont permis de mettre en évidence l'influence de la couche protectrice de surfactants sur l'hyperpolarisabilité quadratique de ces particules. Ces particules ont ensuite été placées à l'interface air/eau dans une cuve de Langmuir afin d'étudier le rôle des interactions entre les particules sur la réponse optique linéaire et non linéaire. Celle-ci a révélé dans ces films formés à l'interface la présence de couplages forts entre les particules lors de la compression de la surface. Cela conduit à une transition dans le film une fois que la distance entre les particules passe en dessous d'une distance critique. Ces études ont été complétées par des expériences réalisées à l'interface liquide/liquide et sur une électrode de carbone vitreux pour examiner plus en détail le rôle de la rugosité à l'échelle nanométrique dans l'exaltation de la réponse non linéaire SHG.

MOTS-CLES: Optique linéaire, Optique non linéaire, nanoparticules métalliques, Génération de second Harmonique, Diffusion Hyper Rayleigh, transition, interfaces, interactions, film.

Linear and Nonlinear optics of metallic nanoparticles film

RESUME: In this work, the nonlinear optical response of assembled metallic nanoparticles at interfaces was studied using Second Harmonic Generation. First, the nanoparticles were characterised using incoherent second harmonic generation, a technique also called Hyper Rayleigh Scattering. Thioalkane-capped silver and gold nanoparticles, both nanospheres and nanorods, were investigated and the role of this capping layer on the quadratic hyperpolarisability of these particles was underlined. The particles were then deposited at the air/liquid interface in a Langmuir trough to investigate the role of the interparticles interactions in large assemblies. Both the linear and the nonlinear optical response of these metallic films formed at the surface of the trough provided evidence of a strong coupling between adjacent particles upon compression leading to a phase transition of the film once the interparticle distance is less than a critical value. These studies were complemented with experiments performed at the liquid/liquid interface and at the glassy carbon/electrolyte interface to examine in greater details the role of roughness at the nanoscale on the enhancement of the SHG response.

KEYWORDS: Linear Optics, Nonlinear Optics, metallic nanoparticles, Second Harmonic Generation, Hyper Rayleigh Scattering, transition, interfaces, interactions, film.